FLEXIBLE MEMS SENSORS AND PYROELECTRIC
THIN FILMS

by

MOINUDDIN AHMED

Presented to the Faculty of the Graduate School of

The University of Texas at Arlington in Partial Fulfillment

of the Requirements

for the Degree of

DOCTOR OF PHILOSOPHY

THE UNIVERSITY OF TEXAS AT ARLINGTON

May 2014

Copyright © by Moinuddin Ahmed 2014

All Rights Reserved

To my parents- Md. Gias Uddin and Mrs. Rabeya Begum

Acknowledgements

At first I would like to thank the almighty ALLAH for blessing me with knowledge and patience. I would like to thank my supervising Professor Donald P. Butler for his continuous support, advice and guidance throughout the course of my PhD. I appreciate his patience and intelligence which encouraged me to learn that in research there are good days and bad days, but every day offers a learning experience. His close guidance helped me to explore different areas of research and inspired me to work hard. I had every opportunity to talk with him for any research and non-research related field. I found him helpful and courteous at all aspects. I would like to thank Professor Zeynep Celik-Butler for her insightful comments and innovative ideas which help me a lot in improving the quality of my research work. I really appreciate her patience for listening all research related issues. Both of them supported me to maintain my status as a graduate research and teaching assistant. I would like to thank other members of my dissertation committee Professor Jing-Chih Chiao, Professor Michael Vasilyev, Professor Dereje Agonafer for their time and effort for reviewing my work and making insightful comments. I would like to give special thanks to Dr. Murali, Dr. Shahriar, Dr. Erkin, Dr. Suraj, Dr. Iqbal, Dr. Bhargav, Gaviraj, Rohit, Madhumita, Clement, Sajeeb, Yi Li, Sohel, Mohamed for their help and useful discussions. I would also like to thank all of my colleagues in the cleanroom and all the staff members of the nanofab.

I am eternally indebted to my parents Md. Gias Uddin and Mrs. Rabeya Begum for their support and prayers. The support and inspiration from my sisters Rubina and Ruksana and brother Mohiuddin encouraged me to travel a long path. I will never forget their love and contribution in my life.

April 14, 2014

Abstract

FLEXIBLE MEMS SENSORS AND PYROELECTRIC

THIN FILMS

Moinuddin Ahmed, PhD

The University of Texas at Arlington, 2014

Supervising Professor: Donald P. Butler

MEMS sensors on flexible substrates were developed and fabricated utilizing conventional lithography, deposition and etching tools. All of these sensors were fabricated in a MESA structure on the flexible substrates for tactile sensing, robotic, and biomedical applications. In addition, a new processing technique was developed to release the flexible substrate more easily from the rigid silicon carrier wafer to increase fabrication yield.

Temperature sensors were fabricated on flexible substrates; utilizing amorphous silicon as the sensing material. After releasing from the rigid silicon carrier wafer, the sensors were packaged and characterized for their *I-V*, thermal response and 1/f noise properties. The amorphous silicon showed a temperature coefficient of resistance of 2.88 %/K at room temperature. The average value of normalized Hooge coefficient, $K_{1/f}$ was found to be 1.2×10^{-11} giving a noise equivalent temperature of 5.5 mK over the bandwidth of 1 to 941 Hz.

Relative pressure sensors were fabricated on a flexible substrate using nichrome (Ni-80%/Cr-20%) as the sensing material. The sensors were characterized for *I-V*, pressure sensing, and noise behavior. The average value of normalized Hooge coefficient

$K_{1/f}$ was found to be 1.89 × 10^{-10}. The average sensitivity was calculated to be 0.44 mV/MPa yielding a noise equivalent pressure (*NEPr*) of 58.23 kPa in a bandwidth of 1-8 Hz.

Absolute pressure sensors were fabricated on a flexible substrate utilizing nichrome (Ni-80%/Cr-20%) as a sensing material. The sensors were packaged to create a reference vacuum cavity. The sensors were characterized for *I-V*, pressure sensitivity, and noise characteristics. The average value of normalized Hooge coefficient $K_{1/f}$ was found to be 4.64 × 10^{-11}. The average sensitivity was calculated to be 1.25 nV/Pa producing a noise equivalent pressure (*NEPr*) of 7.8 kPa in the bandwidth of 1-8 Hz.

Modified lead titanate (lead zirconium titanate and lead calcium titanate) was deposited on gold electrodes and characterized for pyroelectric sensor applications. The materials were characterized to analyze the variation of dielectric constant with temperature and the pyroelectric current measurement. The lead calcium titanate showed a pyroelectric coefficient of 40 × 10^{-5} C/m^2-K and lead zirconium titanate demonstrated a pyroelectric coefficient of 28 × 10^{-5} C/m^2-K after poling. It was observed that the poling caused an increase of the pyroelectric coefficient by 10 times.

The incorporation of a low adhesion strength release layer in the fabrication process was investigated. It was observed that depositing a polyimide as a release layer helps to detach flexible substrate from the rigid silicon wafer after fabrication. The release layer can also withstand high processing temperature and survive during lift-off processes.

Microbolometers were designed, fabricated on flexible substrates, and characterized. The design includes several new features such as a nanomesh absorber, a double layer absorber for infrared radiation, a long-pass optical filter, and μm-sized device-level vacuum packaging. The microbolometers showed a maximum responsivity of 3.78 ×

10^3 V/W, detectivity of 4.44×10^6 cmHz$^{1/2}$/W and a minimum *NEP* of 2.78×10^{-9} V/Hz$^{1/2}$ at a chopper frequency of 40 Hz and 1 V dc bias.

Table of Contents

Acknowledgements iv

Abstract……… v

List of Illustrations xii

List of Tables xxiv

List of Symbols xxvi

Chapter 1 Introduction 1

Chapter 2 Fabrication and Characterization of Flexible Temperature Sensors 8

2.1 Introduction 8

2.2 Background 8

2.3 Fabrication 10

2.4 Characterization, Results and Discussions 18

2.4.1 Temperature Sensing in Probe Station 18

2.4.2 Temperature Sensing inside Cryostat 19

2.4.3 Noise Characterization 21

2.5 Figures of Merit 25

2.6 Conclusions 26

Chapter 3 Fabrication and Characterization of Flexible Relative Pressure Sensor 27

3.1 Introduction 27

3.2 Background 27

3.3 Fabrication 30

3.4 Characterization, Results and Discussions 38

3.4.1 Resistance Measurement and Pressure Sensing in Probe Station 38

3.4.2 Pressure Sensing in Load Cell 41

3.4.3 Noise Characterization 43

3.4.4 Gauge Factor Calculation....46
3.4.5 Figures of Merit....47
3.4.5.1 Thermomechanical Noise....51
3.5 Conclusions....52
Chapter 4 Fabrication and Characterization of Flexible Absolute Pressure Sensor....53
4.1 Introduction....53
4.2 Background....53
4.3 Fabrication....54
4.4 Characterization, Results and Discussion....61
4.4.1 Resistance Measurement and Pressure Sensing with a Probe Station....62
4.4.2 Pressure Sensing with a Load Cell....64
4.4.3 Pressure Sensing inside Vacuum Chamber....65
4.4.4 Gauge Factor Calculation....69
4.4.5 Noise Characterization....69
4.4.6 Figures of Merit....70
4.4.6.1 Thermomechanical Noise....71
4.4.7 Effect of Temperature Variation on the Cavity....74
4.4.8 Effect of Bending of the Flexible Substrate....75
4.5 Conclusions....76
Chapter 5 Deposition and Characterization of Pyroelectric Lead Titanate Thin Films....78
5.1 Introduction....78
5.2 Background....78
5.3 Deposition of Modified Lead Titanate Thin Films and Capacitor Fabrication....80

5.4 Characterization..83

5.5 Results and Discussions 84

5.5.1 X-ray Diffraction of the PCT and PZT Thin Films on Gold 84

5.5.2 Dielectric Constant Variation with Temperature...100

5.5.3 Pyroelectric Current Characterization 102

5.5.4 Poling the Ferroelectric Materials...105

5.5.5 Pyroelectric Current Measurements after Poling 109

5.6 Conclusions 114

Chapter 6 Incorporating a Simple Release Layer for Flexible Substrate........................115

6.1 Introduction..115

6.2 Background..115

6.3 Experimental Details..118

6.4 Discussions..121

6.5 Fabricating Multi-Layers MEMS Structure on the Flexible Substrate

and Releasing from Silicon Wafer..124

6.6 Conclusions 127

Chapter 7 Design, Fabrication and Characterization of Uncooled Infrared Detector 129

7.1 Introduction..129

7.2 Designing the Bolometer and Simulating for Optimization..................................131

7.2.1 Designing Thermal Isolation Structure 132

7.2.2 Packaging the Sensor 136

7.2.3 Calculating the Absorption of the Detecting Material 140

7.2.4 Double Layer Absorber for the Infrared Radiation 144

7.2.5 Absorption by the Nanomesh Absorber 147

7.2.6 Optical Filter 152

7.2.7 Different Types of Design 153
7.2.8 Adding a Reference Resistor 155
7.3 Fabrication of the Bolometer 156
7.4 Characterization of Sensors on Flexible Substrate 165
7.4.1 Resistance Measurement 165
7.4.2 IR Response Measurement 165
7.4.2.1 IR Probe Station 166
7.4.2.2 Setup for IR Response Measurement 167
7.4.3 Noise Measurement 168
7.5 Results and Discussions 168
7.5.1 Figures of Merit 173
7.5.1.1 Responsivity 173
7.5.1.2 Detectivity 175
7.5.1.3 Noise Equivalent Power (*NEP*) 177
7.6 Conclusions 181
Chapter 8 Conclusions and Future Directions 183
8.1 Conclusions 183
8.2 Directions for Future Work 186
Appendix A Equations and Parameters for Calculating Responsivity, Detectivity and *NEP* Used in the Microbolometer Simulation 189
References 193
Biographical Information 207

List of Illustrations

Figure 2-1 Passivating Si Carrier Wafer by Si_3N_4 10

Figure 2-2 PI5878 G Flexible Substrate Deposited on Passivation Layer....11

Figure 2-3 Passivating Polyimide by Si_3N_4 11

Figure 2-4 Nomarski Microscope Picture of a 500-μm Au Bondpad 12

Figure 2-5 Ti Right Electrode on Top of Au Protection Layer 13

Figure 2-6 Amorphous Silicon Sensing Element Deposited on Right Electrode 13

Figure 2-7 Al_2O_3 First Insulation Layer....14

Figure 2-8 Ti Left Electrode on Top of Au Protection Layer 14

Figure 2-9 Al_2O_3 Second Insulation Layer 15

Figure 2-10 HD4110 Flexible Superstrate Layer Deposited on the Sensor 15

Figure 2-11 Top Aluminum Layer 15

Figure 2-12 CoventorWare™ 3D Cross-Sectional View of the Temperature Sensor. ©2012 IEEE. Reprinted, with Permission, from Temperature Sensor in a Flexible Substrate by M. Ahmed, M. M.Chitteboyina, D. P. Butler, Z. Celik-Butler, in IEEE Sensors, May 2012 [23]. 17

Figure 2-13 1 cm × 1 cm Die of Flexible Substrate Containing 35 Temperature Sensors .17

Figure 2-14 The Graph is Showing the Resistance and Temperature Coefficient of Resistance Change as a Function of Temperature Plot in the 300-360 K Range. The Arrhenius plot was Drawn from the Resistance versus Temperature Graph for the Same Sensor (Inset). ©2012 IEEE. Reprinted, with Permission, from Temperature Sensor in a Flexible Substrate by M. Ahmed, M. M.Chitteboyina, D. P. Butler, Z. Celik-Butler, in IEEE Sensors, May 2012 [23]. 19

Figure 2-15 Measurement on Leybold ROK 10-300 K Closed-Cycle Refrigerator....20

Figure 2-16 The Graph is Presenting the Resistance and Temperature Coefficient of Resistance Change as a Function of Temperature Plot in the 200-360 K Range. The Arrhenius Plot was Drawn from the Resistance versus Temperature Graph for the Same Sensor (Inset). ©2012 IEEE. Reprinted, with Permission, from Temperature Sensor in a Flexible Substrate by M. Ahmed, M. M.Chitteboyina, D. P. Butler, Z. Celik-Butler, in IEEE Sensors, May 2012 [23]. 21

Figure 2-17 Voltage Noise Power Spectral Density for Four Different Sensors over the Frequency Band from 1 to 1000 Hz. ©2012 IEEE. Reprinted, with Permission, from Temperature Sensor in a Flexible Substrate by M. Ahmed, M. M.Chitteboyina, D. P. Butler, Z. Celik-Butler, in IEEE Sensors, May 2012 [23]. 23

Figure 2-18 Variation of Noise Voltage PSD at 10 Hz with Respect to the Change in Bias Voltage. ©2012 IEEE. Reprinted, with Permission, from Temperature Sensor in a Flexible Substrate by M. Ahmed, M. M.Chitteboyina, D. P. Butler, Z. Celik-Butler, in IEEE Sensors, May 2012 [23]. 24

Figure 3-1 Deposition of Si_3N_4 Passivation Layer 31

Figure 3-2 Flexible Polyimide Substrate Layer 31

Figure 3-3 Deposition of the Second Si_3N_4 Passivation Layer 31

Figure 3-4 Deposition of HD4100 Sacrificial Layer 32

Figure 3-5 Deposition of Al_2O_3 Membrane Layer 33

Figure 3-6 Deposition of Nichrome Piezoresistor 33

Figure 3-7 Deposition of Ti Metallization Layer 34

Figure 3-8 Au Protection Layer 34

Figure 3-9 Deposition of Al_2O_3 Packaging Layer 35

Figure 3-10 Cavity Created by the Removal of Sacrificial Layer 35

Figure 3-11 Flexible Superstrate Layer..36

Figure 3-12 The 3D CoventorWare™ Model of the Cross-Section of the Delta Pressure Sensor. ©2011 IEEE. Reprinted, with Permission, from MEMS Relative Pressure Sensors on Flexible Substrate by M. Ahmed, D. P. Butler, Z. Celik-Butler, in IEEE Sensors, 2011 [50]. 37

Figure 3-13 Micrograph of the Complete Sensor Taken by Confocal Microscope. ©2011 IEEE. Reprinted, with Permission, from MEMS Relative Pressure Sensors on Flexible Substrate by M. Ahmed, D. P. Butler, Z. Celik-Butler, in IEEE Sensors, 2011 [50]. 37

Figure 3-14 The Image is Showing Relative Pressure Sensors Embedded in a 2 x 2 cm^2 Piece of Flexible Substrate. ©2011 IEEE. Reprinted, with Permission, from MEMS Relative Pressure Sensors on Flexible Substrate by M. Ahmed, D. P. Butler, Z. Celik-Butler, in IEEE Sensors, 2011 [50]. 38

Figure 3-15 Layout of Relative Pressure Sensor Showing the Connection of Active and Passive Piezoresistors in a Half Wheatstone Bridge Configuration. ©2011 IEEE. Reprinted, with Permission, from MEMS Relative Pressure Sensors on Flexible Substrate by M. Ahmed, D. P. Butler, Z. Celik-Butler, in IEEE Sensors, 2011 [50]. 39

Figure 3-16 Measured *I-V* Characteristics across the Piezoresistors.................................40

Figure 3-17 Measured Wheatstone Bridge Output Voltage Change under Full Load as a Function of Input Bias Voltage. ©2011 IEEE. Reprinted, with Permission, from MEMS Relative Pressure Sensors on Flexible Substrate by M. Ahmed, D. P. Butler, Z. Celik-Butler, in IEEE Sensors, 2011 [50]. 41

Figure 3-18 Load-Cell Measurement Showing the Change in Output Voltage due the Variation of Applied Load. ©2013 IEEE. Reprinted, with Permission, from MEMS Force Sensor in a Flexible Substrate Using Nichrome Piezoresistors by M. Ahmed, M. M. Chitteboyina, D. P. Butler, Z. Celik-Butler, in IEEE Sensors, October 2013 [49]....43

Figure 3-19 Noise Voltage Power Spectral Density for the Net 1/F Noise of a Pressure Sensor with 1 V Bias on the Wheatstone Bridge. ©2013 IEEE. Reprinted, with Permission, from MEMS Force Sensor in a Flexible Substrate Using Nichrome Piezoresistors by M. Ahmed, M. M. Chitteboyina, D. P. Butler, Z. Celik-Butler, in IEEE Sensors, October 2013 [49]....45

Figure 3-20 Noise Voltage Power Spectral Density for Flicker Noise at 10 Hz as a Function of Bias Voltage Variation. ©2013 IEEE. Reprinted, with Permission, from MEMS Force Sensor in a Flexible Substrate Using Nichrome Piezoresistors by M. Ahmed, M. M. Chitteboyina, D. P. Butler, Z. Celik-Butler, in IEEE Sensors, October 2013 [49]. 46

Figure 4-1 Deposition of First Si_3N_4 Passivation Layer....54

Figure 4-2 Deposition of Flexible Polyimide Substrate Layer....55

Figure 4-3 Deposition of Second Si_3N_4 Passivation Layer....55

Figure 4-4 Deposition of Thin Sacrificial Layer....56

Figure 4-5 Deposition of Thick HD4100 Sacrificial Layer....56

Figure 4-6 Deposition of Al_2O_3 Membrane Layer....57

Figure 4-7 Deposition of Nichrome Piezoresistors....57

Figure 4-8 Deposition of Ti Metallization Layer....58

Figure 4-9 Deposition of Au Protection Layer....58

Figure 4-10 Deposition of Al_2O_3 Encapsulation Layer....58

Figure 4-11 Surface Micromachining to Create Cavity under Selected Region 59

Figure 4-12 Deposition of Packaging Layer and Etching to Open Vias.............................59

Figure 4-13 Deposition of Flexible Superstrate Layer 60

Figure 4-14 CoventorWare^{TM} 3D Picture of the Absolute Pressure Sensor ©2012 IEEE. Reprinted, with Permission, from MEMS Absolute Pressure Sensors on Flexible Substrate by M. Ahmed, D. P. Butler, Z. Celik-Butler, in IEEE MEMS, 2012 [64]..60

Figure 4-15 Micrograph of the Sensor Taken in Confocal Microscope ©2012 IEEE. Reprinted, with Permission, from MEMS Absolute Pressure Sensors on Flexible Substrate by M. Ahmed, D. P. Butler, Z. Celik-Butler, in IEEE MEMS, 2012 [64]..61

Figure 4-16 A 2 x 2 cm^2 Piece of Flexible Substrate Containing an Array of 75 Pressure Sensors. ©2012 IEEE. Reprinted, with Permission, from MEMS Absolute Pressure Sensors on Flexible Substrate by M. Ahmed, D. P. Butler, Z. Celik-Butler, in IEEE MEMS, 2012 [64] 61

Figure 4-17 Measured *I-V* Characteristics for a 424 μm × 424 μm Absolute Pressure Sensor 63

Figure 4-18 Characterized Output Voltage Change as a Function of Input Bias Voltage for Two Different Configurations 64

Figure 4-19 Sensor Characterizations under Load-Cell for Gradual Application and Retraction of a Load and the Corresponding Change in Output Voltage. ©2012 IEEE. Reprinted, with Permission, from MEMS Absolute Pressure Sensors on Flexible Substrate by M. Ahmed, D. P. Butler, Z. Celik-Butler, in IEEE MEMS, 2012 [64]..65

Figure 4-20 Set-up for Characterizing Absolute Pressure Sensor in Vacuum Chamber ...66

Figure 4-21 Characterization of the Sensor inside Vacuum Chamber. The Graph is Showing the Change Output Voltage from Offset Voltage with the Change in Applied Pressure from 100 mTorr to 760 Torr. 67
Figure 4-22 Vacuum Chamber Measurement for One of the Absolute Pressure Sensors, Showing Output Voltage Variation with Chamber Pressure for a 424 μm × 424 μm Device for 10 Cycles. 68
Figure 4-23 Voltage Noise Power Spectral Density for Net 1/F-Noise for the Absolute Pressure Sensors or Two Different Configurations 70
Figure 4-24 Variation of 1/F Noise Voltage Power Spectral Density (PSD) at 10 Hz due to the Variation of the Input Bias Voltage 71
Figure 4-25 Output Offset Voltage as a Function of Temperature Variation for Two Different Configurations. 75
Figure 4-26 CoventorWare^{TM} Simulation of Bending the Flexible Substrate around a Cylinder with Radius of Curvature of 1 cm for 424 μm × 424 μm Device in Order to Calculate the Change in Volume of the Cavity and Hence the Reference Pressure. 76
Figure 5-1 Cross-Sectional View of the Fabricated Capacitor Using Perovskite PZT Thin Films 81
Figure 5-2 (A) Confocal Microscope Micrograph (B) Nomarski Microscope Image of the Top View of the Capacitor 82
Figure 5-3 SEM Micrograph of the Deposited PZT Film 82
Figure 5-4 SEM Micrograph of the Deposited PCT Film 83
Figure 5-5 X-ray Diffraction of the PZT Film, Deposited at 650 ^{o}C Temperature 86
Figure 5-6 X-ray Diffraction of the PZT Film, Deposited at 650 ^{o}C and Annealed for 5 min at 650 ^{o}C 87

Figure 5-7 X-ray Diffraction of PZT Film, Deposited at 650 ^{o}C and Annealed for 10 min at 650 ^{o}C 88
Figure 5-8 X-ray Diffraction of PZT Film, Deposited at 650 ^{o}C and Annealed for 15 min at 650 ^{o}C 88
Figure 5-9 X-ray Diffraction of PZT Film Deposited at 600 ^{o}C 89
Figure 5-10 X-ray Diffraction of PZT Film, Deposited at 600 ^{o}C and Annealed for 10 min at 600 ^{o}C 90
Figure 5-11 X-ray Diffraction of PZT Film, Deposited at 600 ^{o}C and Annealed for 30 min at 600 ^{o}C 90
Figure 5-12 X-ray Diffraction of PZT Film Deposited at 550 ^{o}C 91
Figure 5-13 X-ray Diffraction of PZT Film, Deposited at 550 ^{o}C and Annealed for 10 min at 550 ^{o}C 91
Figure 5-14 X-ray Diffraction of PZT Film, Deposited at 550 ^{o}C and Annealed for 30 min at 550 ^{o}C 92
Figure 5-15 X-ray Diffraction of PZT Film Deposited at 500 ^{o}C 92
Figure 5-16 X-ray Diffraction of PZT Film, Deposited at 550 ^{o}C and Annealed for 10 min at 550 ^{o}C 93
Figure 5-17 X-ray Diffraction of PCT Film, Deposited at 550 ^{o}C Temperature 94
Figure 5-18 X-ray Diffraction of PCT Film, Deposited at 550 ^{o}C and Annealed for 10 min at 550 ^{o}C 95
Figure 5-19 X-ray Diffraction of PCT Film, Deposited at 550 ^{o}C and Annealed for 15 min at 550 ^{o}C 96
Figure 5-20 X-ray Diffraction of PCT Film Deposited at 550 ^{o}C and Annealed for 20 min at 550 ^{o}C 96
Figure 5-21 X-ray Diffraction of PCT Film, Deposited at 550 ^{o}C, 125 mJ Laser Energy 97

Figure 5-22 X-ray Diffraction of PCT Film, Deposited at 550 ^{o}C and Annealed for 10 min at 550 ^{o}C, 125 mJ Laser Energy 98
Figure 5-23 X-ray Diffraction of PCT Film, Deposited at 550 ^{o}C and Annealed for 15 min at 550 ^{o}C, 125 mJ Laser Energy 99
Figure 5-24 X-ray Diffraction of PCT Film, Deposited at 550 ^{o}C and Annealed for 10 min at 550 ^{o}C, 125 mJ Laser Energy 99
Figure 5-25 Change in Dielectric Constant with Temperature for the PZT Films 100
Figure 5-26 Change in Loss Tangent with Temperature for the PZT Films 101
Figure 5-27 Change in Dielectric Constant with Temperature for the PCT Films............101
Figure 5-28 Change in Loss Tangent with Temperature for the PCT Films 102
Figure 5-29 Pyroelectric Current as a Function of Time while Temperature is Changing for the PZT Film (before Poling) 104
Figure 5-30 Pyroelectric Coefficient as a Function of Temperature for the PZT Film (before Poling) 104
Figure 5-31 Pyroelectric Current as a Function of Time while Temperature is Changing for the PCT Film (before Poling)....................105
Figure 5-32 Pyroelectric Coefficient as a Function of Temperature for the PCT Film (before Poling) 105
Figure 5-33 Poling of Capacitors Fabricated by Using PZT Material 107
Figure 5-34 Poling of Capacitors Fabricated by Using PCT Material 108
Figure 5-35 Pyroelectric Current Measurement of PZT Film after Poling at Different Voltage....................110
Figure 5-36 Pyroelectric Current Measurement of PZT Film after Poling at 1 V for 30 min 110

Figure 5-37 Pyroelectric Current Measurement of PCT Film after Poling at Different Voltage 111
Figure 5-38 Pyroelectric Current Measurement of PCT Film after Poling at Different Time 111
Figure 5-39 Pyroelectric Current Measurement of PCT Film after Poling at 3 V for 30 min 112
Figure 6-1 (a) Deposition of 1st Passivation Layer, (b) Wrapping Perimeter of the Wafer with Polyimide Tape, (c) Spin-Coating PI2611 Release Layer, (d) Separating Polyimide Tape before Curing the Polyimide, (e) Spin-Coating PI5878 G Polyimide and Curing, (f) Releasing the Flexible Substrate from the Silicon Wafer. Reprinted with Permission from [88], Copyright [2013], American Vacuum Society. 120
Figure 6-2 (a) Cutting the Edge of the Flexible Substrate by a Cutting Tool to Separate from Silicon Wafer, (b) a Flexible Polyimide Substrate Detached from Carrier Wafer, (c) Polyimide Substrate/Superstrate Combination Containing a Metallization Lines in between Them. Reprinted with Permission From [88], Copyright [2013], American Vacuum Society. 123
Figure 6-3 Die Separated from a Carrier Wafer before Depositing Polyimide Superstrate Layer 125
Figure 6-4 Separation of Superstrate from the Substrate during Dicing 125
Figure 6-5 The Separation of Polyimide Superstrate Layer due to the Stress on the Adjacent Alumina Layer around the Edge. 126
Figure 6-6 The Bolometers Sandwiched between Superstrate and Substrate after Etching Silicon Carrier Wafer from Backside; Dicing Caused the Separation of the Polyimide Substrate and Superstrate (Inset) 127

Figure 7-1 Cross-Section of an Infrared Detector 130
Figure 7-2 A Simple Representation of the Designed Detector Showing the Thermal Isolation of the Detector from the Substrate through the Membrane (Designed by the CoventorWare^{TM})...133
Figure 7-3 Center Part of the Designed Detector Showing the Nanomesh Absorber and the Detector (Designed by CoventorWare^{TM}) 134
Figure 7-4 Steady-State Thermal Analysis of the Designed Detector including Conduction through the Membrane and Radiation of the Entire Structure. 135
Figure 7-5 Displacement of the Detector due to the Application of 1g Acceleration to the Micromachined Structure. 136
Figure 7-6 Displacement of the Packaging Layer due to the Application of 10 atm Pressure. 138
Figure 7-7 New Packaging Layer for the Bolometer 139
Figure 7-8 Displacement of the Packaging Layer due to the Application of 10 atm Pressure. 139
Figure 7-9 Maximum Stress Induced in the Packaging Layer due to the Application of the 10 atm Pressure 140
Figure 7-10 Cross-Sectional Area of the Detector through the Center. 141
Figure 7-11 Cascade Connection of Two Port Networks [104].......................................142
Figure 7-12 Simulated Fractional Absorbed Power in the Double Layer Absorber (a) including the Optical Filter on Top of the Detector; (b) excluding the Long-Pass Optical Filter Layer. 146
Figure 7-13 Measured Fractional Absorption of the Transmitted Power in the Al-Si-Al tri-Layers on Top of the Flexible Substrate. 147

Figure 7-14 (a) Inductive Strip Grating; (b) Capacitive Strip Grating; (c) Inductive Mesh; (d) Equvalent Lump Element Model of Indcutive Mesh....149
Figure 7-15 (a) Part of the Nanomesh Absorber (b) Approximation of the Circular Absorber to Rectangular Absorber....150
Figure 7-16 Cross-Sectional Area of the Detector through the Absorber....151
Figure 7-17 Fractional Absorbed Power in the Double Layer Nanomesh Absorber (a) including the Optical Filter on Top of the Detector; (b) excluding the Long-Pass Optical Filter Layer....151
Figure 7-18 Circular Bolometer with 100-µm Legs....154
Figure 7-19 Rectangular Bolometer....154
Figure 7-20 Addition of a Reference Resistor with the Micromachined Bolometer....156
Figure 7-21 Aluminum Mirror Layer....157
Figure 7-22 Thin Sacrificial Layer....158
Figure 7-23 Thick Sacrificial Layer below Detector....158
Figure 7-24 Membrane on Top of the Sacrificial Layer....159
Figure 7-25 Connection of Bottom Electrode and Metallization Layer....159
Figure 7-26 Si-Al-Al_2O_3 Tri-Layer....160
Figure 7-27 Metallization Layer Connecting Each Detector with Bondpads....161
Figure 7-28 Top Sacrificial Layer....162
Figure 7-29 Encapsulation Layer....162
Figure 7-30 Surface Micromachined Bolometer....163
Figure 7-31 Opening Bondpads by Etching for Electrical Connections....163
Figure 7-32 The Rectangular Shaped Germanium Optical Filter....164
Figure 7-33 HD4110 Flexible Polyimide Superstrate Layer....164

Figure 7-34 1 cm × 1 cm Die Containing 14 Self-Packaged Bolometers on Flexible Substrate 165
Figure 7-35 IR Probe Station for Testing Bolometer....167
Figure 7-36 Electrical Connection of the Bolometer 168
Figure 7-37 *I-V* Characteristics of the Detector Termed as 60TR_10x7 170
Figure 7-38 Output Voltage across the Bolometer with IR 170
Figure 7-39 Noise Voltage PSD with IR....171
Figure 7-40 Noise Voltage PSD for the Device Termed as 60TL_6x6 172
Figure 7-41 Variation of Noise Voltage PSD with the Bias Voltage....172
Figure 7-42 Responsivity versus Chopper Frequency for 60 μm × 60 μm Pixel 174
Figure 7-43 Variation of Responsivity with Bias Voltage (Chopper Frequency 40 Hz) for 60 μm × 60 μm Pixel....175
Figure 7-44 Detectivity versus Chopper Frequency for 35 μm × 35 μm Pixel 176
Figure 7-45 Variation of Detectivity with Bias Voltage (Chopper Frequency 40 Hz) for 35 μm × 35 μm Pixel....177
Figure 7-46 *NEP* versus Chopper Frequency for 60 μm × 60 μm Pixel 178
Figure 7-47 Variation of *NEP* with Bias Voltage (Chopper Frequency 40 Hz) for 60 μm × 60 μm Pixel....179

List of Tables

Table 2-1 Measured Characteristics of the Sensor at Room Temperature. ©2012 IEEE. Reprinted, with Permission, from Temperature Sensor in a Flexible Substrate by M. Ahmed, M. M.Chitteboyina, D. P. Butler, Z. Celik-Butler, in IEEE Sensors, May 2012 [23]. 24

Table 3-1 Comparing Different Piezoresistive Materials. ©2013 IEEE. Reprinted, with Permission, from MEMS Force Sensor in a Flexible Substrate using Nichrome Piezoresistors by M. Ahmed, M. M. Chitteboyina, D. P. Butler, Z. Celik-Butler, in IEEE Sensors, October 2013 [49] 30

Table 3-2 Measured Resistances for Each Devices at Room Temperature. ©2011 IEEE. Reprinted, with Permission, from MEMS Relative Pressure Sensors on Flexible Substrate by M. Ahmed, D. P. Butler, Z. Celik-Butler, in IEEE Sensors, 2011 [50]. 49

Table 3-3 Measured Characteristics and Figures of Merit of Relative Pressure Sensor at Room Temperature..50

Table 4-1 Summary Table Showing Individual Resistances for the Piezoresistors 72

Table 4-2 Measured Response, Noise and Figures of Merit of the Absolute Pressure Sensors at Room Temperature 73

Table 4-3 Comparison of Sensitivity of Pressure Sensors 74

Table 5-1 Summary of PZT and PCT Films..113

Table 6-1 Glass Transition Temperature of the Flexible Polyimides. Reprinted with Permission from [88], Copyright [2013], American Institute of Physics. 118

Table 6-2 Summarizing Coefficient of Thermal Expansion and Young’s Modulus of Different Polyimide and the Silicon <111> Carrier Wafer. Reprinted with Permission From [88], Copyright [2013], American Vacuum Society. 122

Table 7-1 Thickness of Different Layers 144

Table 7-2 Transmission of Visible Light through Germanium...153

Table 7-3 Summary of Different Types of Bolometer 155

Table 7-4 Resistance Values of the Active and Passive Resistors 169

Table 7-5 Summary of the Detectors Characterized for IR Respionse 180

Table 7-6 Comparison of Detectivity...181

List of Symbols

R	Ω	Resistance of temperature sensor
R_o	Ω	Resistance at infinite temperature
E_a	J	Activation energy
k_B	$m^2\ kg\ s^{-2}\ K^{-1}$	Boltzman constant
T	K	Room temperature
β	%/K	Temperature coefficient of resistance (TCR)
f	Hz	Electrical frequency
V	V	Voltage
S_v	V^2/Hz	Noise voltage power spectral density
$K_{1/f}$		Normalized Hooge's coefficient
R_T	μV/K	Temperature sensitivity
V_n	V	Noise voltage
Δf	Hz	Noise frequency bandwidth from f_1 to f_2
NET	mK	Noise equivalent temperature
S_J	V^2/Hz	Johnson noise voltage power spectral density
ρ	Ω-m	Resistivity
L	m	Length of an resistor
A	m^2	Cross sectional area of an resistor
σ		Poisson's ratio
γ_p		Gauge factor
P_1	Ω	Passive resistor 1 of relative pressure sensor
P_2	Ω	Passive resistor 2 of relative pressure sensor
A_1	Ω	Active resistor 1 of relative pressure sensor

A_2	Ω	Active resistor 2 of relative pressure sensor
V_{out}	V	Output voltage across the relative pressure sensor
ΔV_{out}	V	Output voltage change across the relative pressure sensor
V_{in}	V	Input voltage applied across the relative pressure sensor
R_{Pr}	mV/MPa	Pressure responsivity
P	Pa	Applied pressure on the pressure sensor
$NEPr$	kPa	Noise equivalent pressure
ΔR	Ω	Change in resistance
F_{tm}	N	Thermomechanical force
b	Nsm^{-1}	Damping coefficient
p	$Ccm^{-2}K^{-1}$	Pyroelectric coefficient
i	A	Pyroelectric current
A_e	m^2	Area of the pyroelectric detector
η	Ω	Intrinsic optical impedence
η_o	Ω	Intrinsic optical impedence of air
γ	m^{-1}	Propagation constant
d	m	Thickness of particular film
E_{al}	Vm^{-1}	Electric field of radiation on the aluminum
H_{al}	Am^{-1}	Magnetic field of radiation on the aluminum
E_{total}	Vm^{-1}	Total electric field of radiation on the detector
H_{total}	Am^{-1}	Total magnetic field of radiation on the detector
E_i	Vm^{-1}	Electric field of the incident radiation
H_i	Am^{-1}	Magnetic field of the incident radiation

E_t	Vm^{-1}	Electric field of the reflected radiation
p_t		Fractional transmitted power
p_a		Fractional absorbed power
P_{al}	W	Power incident on aluminum
P_i	W	Power incident on detector
r_{fw}		Reflection coefficient
Z_{in}		Impedance of the network
Y_g	Ω^{-1}	Equivalent admittance of a grid
λ	m	Free space wavelength
a	m	Grid width
g	m	Grid width plus spacing between two grids
Z_s	Ω	Resistance of free space
X_l	Ω	Equivalent reactance of inductive grating
X_C	Ω	Equivalent reactance of capacitive grating
ε_0	F/m	Permittivity of free space
c	ms^{-1}	Speed of light
η_b		Grating factor
a_{eff}	m	Effective grating legnth
l	m	Length of a grating
w	m	Width of a grating
t	m	Thickness of a grid
σ_c	S/m	Dc conductivity
ω_0'	Hz	Resonant frequency
ω_0	Hz	Frequency of incident radiation

n_1		Refractive index of medium 1
n_2		Refractive index of medium 2
R_l	Ω	Loss resistance of mesh reactance
R_v	V/W	Voltage responsivity of the bolometer
Φ	W	Incident radiant flux
V	V	Output voltage of the detector
D^*	$cmHz^{1/2}/W$	Detectivity of the bolometer
A_d	m^2	Area of the detector
NEP	W	Noise equivalent power

Chapter 1

Introduction

The introduction of electronics on flexible substrates revealed a new era for the electronics industry; not only for consumer electronics but also the fabrication of sensors for life saving devices as well as prosthetic devices, robotic devices, and military sensors, The development of CMOS compatible processing techniques for the fabrication of MEMS sensors could help to promote large scale fabrication of MEMS sensors.

In recent years, MEMS sensors on flexible substrates has attracted considerable amount of attention from researchers. There are several questions that need to be answered before going into detailed discussions. The questions could be summarized as follows:

- Why sensors need to be on flexible substrate?
- What would be advantages of the flexible substrate over rigid substrate?
- What are the candidates for flexible substrate?
- Does the fabrication technology require to be modified in order to manufacture the sensors on flexible substrate?
- What would be expected performance parameters for these sensors?
- What extra features could be added for the sensors on flexible substrate that could not be possible otherwise?

MEMS sensors on flexible substrate add conformality to the sensors. Rigid substrates have the limitation that they cannot be bent and conform to non-planar surfaces. Most of the structures where MEMS sensors could be applied are not flat; rather there are curved surfaces where sensors need to be attached. For example, if someone wants to measure blood pressure of human body using a pressure sensor, that

sensor needs to be flexible enough to go intimate contact with human body. Since the human body is not straight or flat like a solid block; applying ‘sensors on rigid substrates for pressure measurement is an unrealistic way to get the actual response of blood pressure. MEMS sensors on flexible substrates are not only limited to blood pressure measurements but also many other applications such as structural health monitoring, i.e., aero plane’s ‘temperature and pressure measurement’, bolometer on flexible substrates could be utilized for night vision capability. Moreover, arrays of different types of sensors on a large flexible area with data processing capabilities could enable the sensors to mimic human skin; which could be effectively applied to robotics and smart prosthetic devices, smart wraps and tags. Even these sensors on flexible substrate could be utilized to sense the temperature, flow and pressure of the environment remotely and translate that response to a hand to feel them where hands could not be exposed to that environment [1].

Albert Hanson was the first to introduce flexible circuit board where he printed conductive material on dielectric substrate [2]. The first flexible substrate was developed in 1960 where solar cell arrays were made by thinning single crystalline silicon down to ~100 μm and assembled on a plastic substrate to provide flexibility [3]. Vladimir Lumemski [4], described a sensitive skin with arrays of sensors on flexible substrate which could be used to cover the entire surface of a machine or part of body in order to sense its surroundings. The application of flexible substrate technology for MEMS sensors evolved with the innovation of the flexible substrates and vice versa. The fabrication process for MEMS sensor on flexible substrate dictates or limits the application and choice of candidate. Glass foils produced by downdraw method could be as thin as 30 μm; which have high optical transmittance over 90% in the visible range, higher temperature tolerance up to 600 ^{o}C, high dimensional stability, and low coefficient

of thermal expansion of ~ 4×10^{-6} /^{o}C. But glass substrate is fragile and difficult to handle. On the contrary, polymer based substrates are highly flexible, inexpensive, roll-to-roll fabrication ability; but thermally and dimensionally less stable than their glass substrate counterparts. There are wide varieties of polymer substrates which will be discussed detailed in chapter 6. Metal foil as thin as ~125 nm, i.e., stainless steel is good choice for flexible substrate due to high resistance to corrosion and process chemical; more durable than polymers and glass substrates. But metal foils suffer from higher surface roughness and its high conductivity limits its applications or increases process complexities [3].

The expected performance parameters for the MEMS sensors on flexible substrate should be same as compared to their rigid counterparts. In addition to flexibility, the sensors could add ability to stretch and wrinkle without any further degradation of the sensors performance. So flexibility means many qualities such as: rollable, bendable, conformally shaped, elastic, light weight, nonbreakable. Though there are a lot of expectations from the flexible substrates; there are some requirements that need to demonstrate before replacing rigid substrates with flexible substrates. One of the important properties is the working temperature of the substrate or glass transition temperature of the polymer (in our case) must be compatible with the maximum fabrication process temperature. Alternatively, after forming the flexible substrate, the fabrication steps are limited to the working temperature of the flexible substrate. Another important requirement is that the thermal expansion coefficient should not mismatch more than 0.3% [3], as cracks may result on the structures. The materials of the substrates should be chemically inert for the subsequent steps, i.e., lift-off, etching, photolithography in order to avoid any unnecessary complexity in process. Other

requirements are the high elastic modulus and low surface roughness over short a distance, which also depends on the fabrication processes.

The modification of processing technology is one of the major concerns for fabricating sensors on flexible substrate. Several authors [5, 6] have investigated the fabrication of MEMS sensors on rigid silicon or SOI wafers and subsequent transfer of the sensors to flexible substrates by bonding the sensors on the flexible substrates using sticky materials. While others [7] demonstrated specialized tools to fabricated sensors on flexible substrate directly over large areas. The questions that arise from these techniques could be summarized as follows:

- Are the techniques feasible for manufacturing rather than research?
- What would be the cost of modifying the processing tools?
- What is the minimum feature size that could be achieved in these techniques?
- What is the maximum temperature that these sensors could survive compared to their rigid counterparts?
- Is the fabrication process limiting the application of the sensors?
- Is there any other way to utilize the current fabrication tools while avoiding the necessity of the modification?
- Since the sensors do not need the rigid substrate, is it possible to reduce the overall processing cost?

The detailed answer of all these questions will be discussed later on in chapter 6. But in conclusion, we have developed a fabrication process which can utilize current processing technology to fabricate MEMS sensors on flexible substrate while reducing the cost of overall fabrication process.

The microsensors incorporated with flexible substrates could give the capability of sensing several stimuli including thermal, tactile and flow sensing to mimic a human skin [1]. To accelerate this progress and to incorporate CMOS compatible processing technique for MEMS sensors fabrication on flexible substrates, fabrication of sensors for thermal and pressure sensing on flexible substrate have been developed, fabricated and characterized.

Uncooled infrared detectors for night vision systems and scientific instruments such as spectrometers and radiometers have attracted considerable attention in recent years because of the ability to provide high quality imaging with reduced cost, weight, and size with lower power consumption, compared to cooled infrared detectors. Toward this advancement, the use of e-beam lithography to decrease the thermal conductance of heat away from the detector will help to fabricate high performance uncooled infrared detectors and to shift uncooled detector technology from being a being MEMS technology to NEMS technology. In this work, the design of an uncooled infrared detector, utilizing a micromachined mesh structure to support the detectors has been proposed. Different types of detector including circular and rectangular detectors were designed and fabricated to operate in the long-wave infrared corresponding to the 8-14 μm atmospheric and 6.2-11 μm water transmission windows respectively. The design can be used to fabricate both pyroelectric detector and bolometer.

In order to build a self-exciting thermal detector, pyroelectric material i.e. modified lead titanate was deposited at different conditions and characterized the film. It was observed that deposition and annealing of modified lead titanate thin film requires high temperature (minimum 550 ^{o}C) in order to achieve high pyroelectric response (detailed discussed in chapter 5). This temperature exceeds or closes to the glass transition temperature of the flexible polyimide substrate (PI5878 G). A flexible substrate

that can withstand such high temperature can be used to fabricate the designed detector where the pyroelectric lead titanate can be used. A lot of engineering requires fabricating such flexible substrate. The design also includes optical filter layer, large scale packaging of device which need to work before attempting to build the pyroelectric detector. So efforts were taken to fabricate the designed detector by using amorphous silicon as a sensing material in order to investigate whether the design works or not.

In chapter 2, 3 and 4, the fabrication and characterization of three different types of sensors on flexible substrate have been discussed. The temperature sensor is applicable to wide range of temperature (200 K to 360 K). The relative pressure sensor and absolute pressure sensor used 'MESA' structure compared to the planar structure as discussed in [8]. In planar structure, the cavity inside the pressure sensor is not defined by the design; it is defined by the surface micromachining process. Applying pressure in a sensor then may affect another closely located pressure sensor. The MESA structure that was used also has superior application for tactile sensing since it can go close proximity to any object. The absolute pressure sensor was packaged in device level with a vacuum reference cavity. This pressure sensor can also be used at very wide range of pressure (0.1 Torr to 78 kTorr). This pressure sensors also showed very low noise equivalent pressure (detailed will be discussed in chapter 3 and chapter 4). The noise equivalent pressure is the term that has been introduced here. In chapter 5, deposition and characterization of pyroelectric thin film has been demonstrated. Efforts were to taken to incorporate easy release layer in between rigid silicon substrate and flexible polyimide substrate which has been discussed in chapter 6. In chapter 7, the design, fabrication and characterization of thermal detector on flexible substrate has been discussed. The design has introduced several novel concepts such as double layer absorption of structure, a nanomesh radiation absorber compared the micromesh

radiation absorber [9, 10, 11, 12, 13], device-level packaging of mm sized sensor, and it has an integrated, device-level optical filter for rejecting visible light spectra. Several efforts could be done to fabricate the resistive bolometer on flexible substrate and have been discussed in chapter 7.

The fabrication of self-packaged temperature sensor, relative pressure sensor, absolute pressure sensor, bolometer on flexible substrate accelerate the evaluation of a "smart skin" which can mimic human skin and could be placed in prosthetic devices, robots and many other applications. The incorporation of pyroelectric thin film materials in uncooled infrared detectors will provide unbiased, self packaged detector on rigid and flexible substrates.

Chapter 2

Fabrication and Characterization of Flexible Temperature Sensors

2.1 Introduction

There are several parameters that are used for structural health monitoring such as bridges, roads, aircraft etc and temperature is one of them. Most of the structures possess non-planar and curved surfaces which require the sensor to be placed in the intimate contact with them. Sensors on rigid substrates cannot meet the requirements which motivated the evolution of sensors on flexible substrates. Towards this advancement, amorphous silicon based temperature sensor arrays, embedded in a flexible substrate, have been developed. The use of flexible substrates allows it to conform to non-planar surfaces while a flexible superstrate on top enables flexibility as well as encapsulation of the sensors.

2.2 Background

Amorphous silicon (a-Si) based resistive temperature sensors utilizes the basic material property that their bulk electrical resistivity ρ, and hence resistance R, varies with absolute temperature T. The variation of the resistance with the temperature can be described by the Arrhenius equation [14]:

$$R = R_o \exp\left(\frac{E_a}{k_B T}\right) \tag{2.1}$$

Where, T is the temperature in Kelvin, E_a the activation energy of the carriers, k_B is the Boltzmann's constant, and R_o the resistance at infinite temperature. The activation energy E_a can be calculated from the temperature-dependent resistance profile and hence the temperature coefficient of resistance (TCR), β which is a sensitivity parameter can be calculated [14]:

$$\beta = \frac{1}{R}\frac{dR}{dT} = -\frac{E_a}{k_B T^2} \tag{2.2}$$

The choice of sensing material for temperature sensor depends on the TCR values, ease of deposition, low noise capability etc. There are several materials performed as the sensing element for a temperature sensor, including vanadium oxide (VO_x) [15], amorphous silicon (a-Si) [16], polycrystalline silicon (Poly-Si) [17], yttrium barium copper oxide (YBaCuO) [18] and silicon germanium (SiGe) [19]. The current work utilized utilized radio frequency (rf) sputtered undoped amorphous silicon (a-Si) based due to ease of deposition, larger temperature coefficient of resistance (TCR) value (~13%/K [20]), higher annealing temperature. But the silicon suffers from oxidation at room temperature [21] which inhibits an electrical connection between silicon and metallization layers. HF acid can etch thermal oxide layer from top of the silicon surface, but it might etch the passivation layer (Si_3N_4) below the silicon. HF will also react Al_2O_3 insulation layers and the polyimide layers which will make the fabrication complex. Depositing a sandwich structure of Al-Si-Al at high vacuum helped to overcome the problem of oxidation. Since the sensors were designed to fabricate inside polyimide and top polyimide needed to cure at 250 ^{o}C, a 2-nm of Al in contact with a-Si can cause crystallization of a-Si at a temperature as low as 152 ^{o}C [22]. In order to avoid aluminum-induced crystallization, the thickness of the aluminum has been optimized. There are two metal contact layers which are in contact with the sensor element. Aluminum oxide isolation layer was deposited to electrically isolate top contact layer from bottom metal contact layer. This also helped to protect against electrical connection between contact layers due to lithographic mismatch.

2.3 Fabrication

Three different types of sensors were designed by CoventorWare™ software and simulated for thermal response. For the fabrication process, 4-inch, p-type doped, crystallographic orientation of <100> and double side polished wafer was used. Before starting any deposition, the wafer was cleaned by standard TAMDI process, followed by cleaning in HF and rinsing in DI water. All thin film in the fabrication process were patterned using photolithography and deposited in a rf-sputtering system in the presence of Ar gas environment at room temperature, followed by the liftoff process. At the beginning, Si rigid substrate was passivated by the 200-nm Si_3N_4 passivation layer which was sputtered at 2.8 mTorr pressure and 150 W rf power in the AJA sputtering system. Si_3N_4 also improved adhesion of the subsequent polyimide flexible substrate layer. [Figure 2-1].

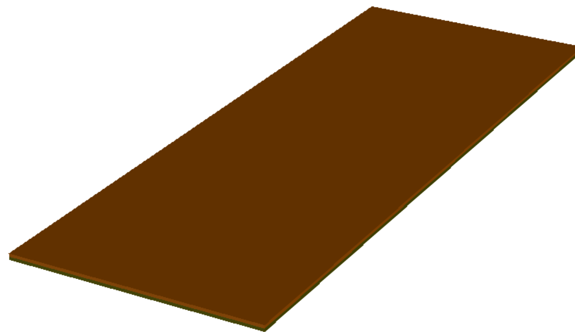

Figure 2-1 Passivating Si Carrier Wafer by Si_3N_4

After that, HD microsystem's polyimdie PI5878 G was spin coated on top of the passivation layer for four times. After each spin coating, the polyimide was soft-baked at 110 ^{o}C for 3 min. Finally, the coated polyimide was cured at 350 ^{o}C for 4 hrs in N_2 gas environment and a final thickness of 35 μm was achieved which formed the flexible substrate for the sensors. [Figure 2-2].

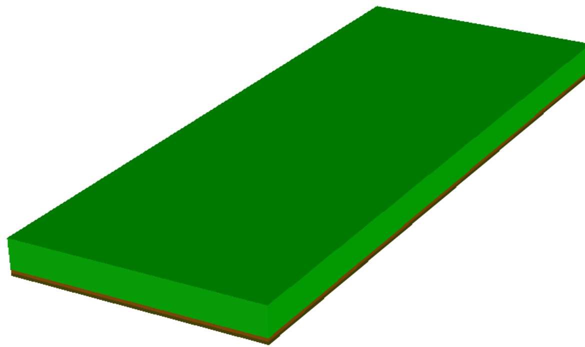

Figure 2-2 PI5878 G Flexible Substrate Deposited on Passivation Layer

Next, 400-nm-thick Si_3N_4 was sputtered on the polyimide to passivate it and protect polyimide from exposing to moisture [Figure 2-3]. This passivation layer also acted as an adhesion promoter for the sensors with the substrate and forms the device plane.

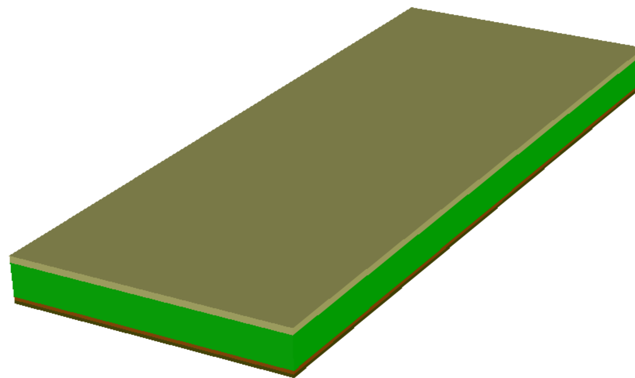

Figure 2-3 Passivating Polyimide by Si_3N_4

The sensor was designed in such a way that backside etching was required so that contact pads are opened from the backside. A 280-nm thick Au was sputtered to form the contact pads which also resist the backside etching to progress through the pads. But Au does not adhere well to the passivation layer, so 20-nm Ti layer was sputtered before the Au deposition. Both of this Au and Ti layers were sputtered using rf-

magnetron sputtering at 10 mTorr pressure in the homebuilt sputtering tool. The rf power was 150 W for Ti and 100 W for Au deposition [Figure 2-4].

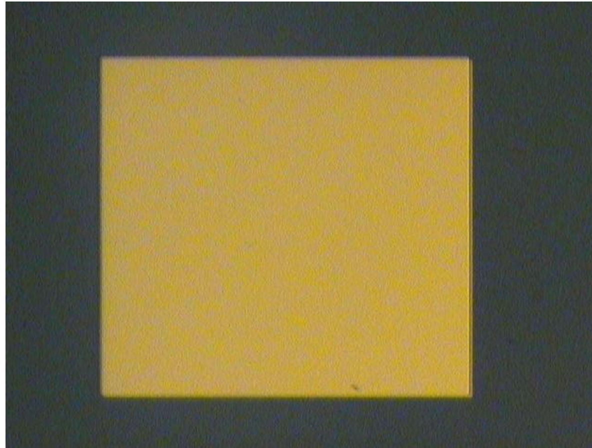

Figure 2-4 Nomarski Microscope Picture of a 500-μm Au Bondpad

Each temperature sensor consisted of two contact pads: left and right contact pads. In order to connect the temperature sensitive material with the right contact pads, a 500-nm-thick Ti layer was sputtered at 10 mTorr pressure and 150 W rf power in the Homebuilt sputtering tool which is termed as the right electrode [Figure 2-5]. After that, the sensing material was deposited on the right electrode. This was done in the AJA sputtering tool, three layers were deposited to form the amorphous Si thermometer and its contacts: a 1.5-nm Al layer, a 500-nm thick Si temperature sensor layer [Figure 2-6] and another 1.5-nm Al layer. The entire deposition process was done consecutively without breaking vacuum. The silicon was sputtered at 5 mTorr chamber pressure and alumina was sputtered at 3.2 mTorr pressure in Ar gas environment. The last Al layer protected the a-Si from thermal oxidation at room temperature. Then, a 150-nm of Al_2O_3 was deposited by rf magnetron sputtering at 150 W rf power in Ar gas environment to insulate the left electrode from the right electrode [Figure 2-7].

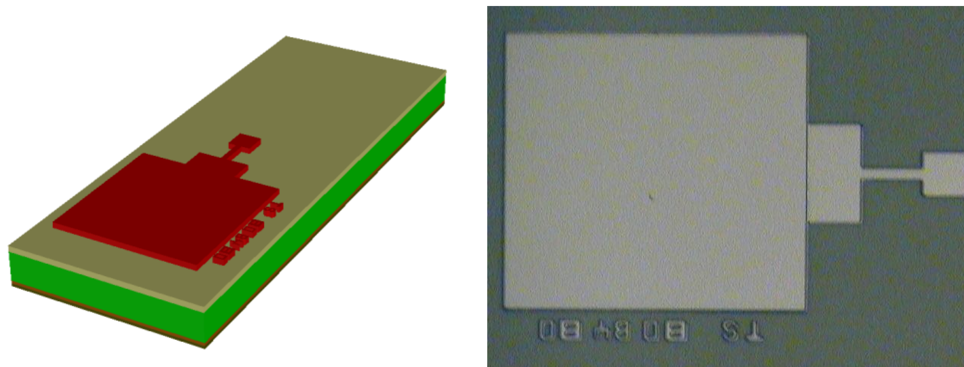

Figure 2-5 Ti Right Electrode on Top of Au Protection Layer

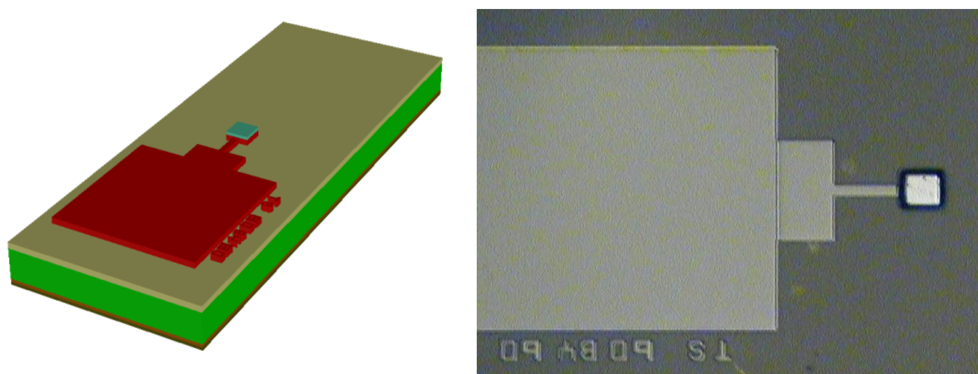

Figure 2-6 Amorphous Silicon Sensing Element Deposited on Right Electrode

Next, in order to connect left cont pad with sensing element, a 500-nm-thick Ti was sputtered to form left electrode [Figure 2-8]. This makes the temperature sensing material to be sandwiched between two electrodes. Then, heat conductor was needed to deposit to make good thermal contact between surrounding with the sensor and transfer heat to temperature sensors. But it required electrically isolate the sensor from the heat conductor, so 150-nm of Al_2O_3 layer was sputtered which provided thermal conductivity to the Si thermometer [Figure 2-9].

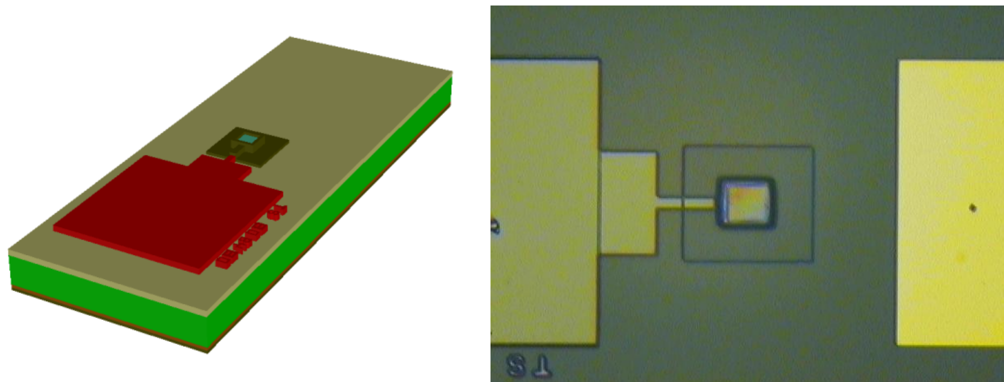

Figure 2-7 Al_2O_3 First Insulation Layer

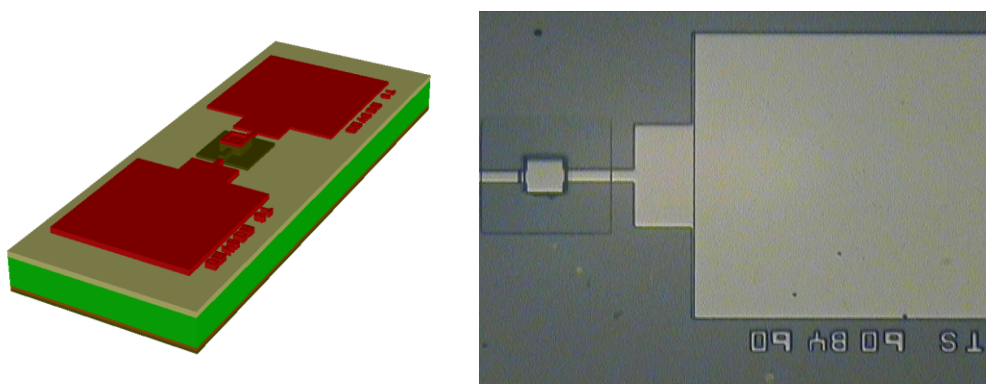

Figure 2-8 Ti Left Electrode on Top of Au Protection Layer

To protect the sensor and provide flexibility on a low stress plane, liquid photo-definable polyimide HD4110 was spin coated on top of the sensors onto the wafer to form the superstrate. Then it was patterned to access the temperature sensor. The polyimide was cured at 250 ^{o}C for 4 hrs in N_2 gas environment and a final thickness of 35 μm was achieved [Figure 2-10]. Next, a 400-nm-thick Al layer was deposited by sputtering to cover entire superstrate layer [Figure 2-11].

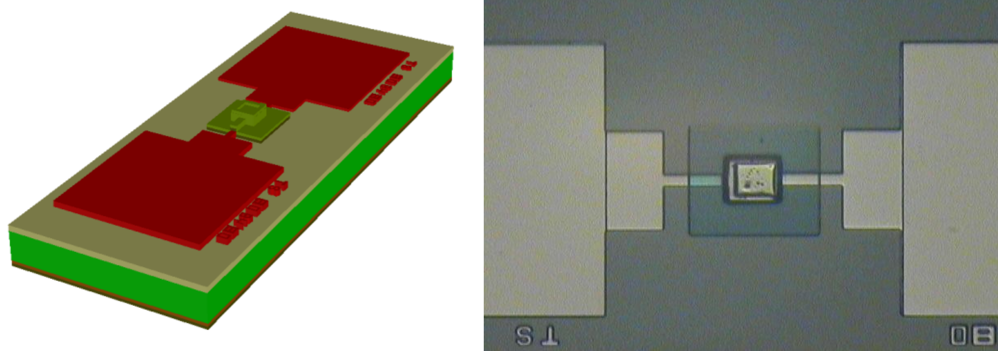

Figure 2-9 Al_2O_3 Second Insulation Layer

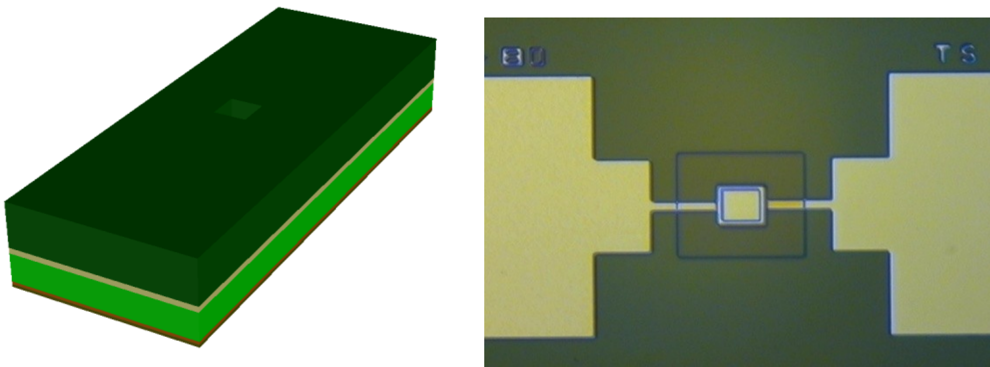

Figure 2-10 HD4110 Flexible Superstrate Layer Deposited on the Sensor

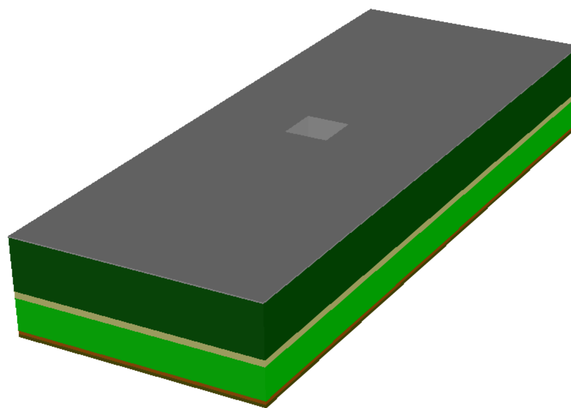

Figure 2-11 Top Aluminum Layer

The next step was to open vias by etching through the Si carrier wafer and polyimide substrate from the backside to reach the buried contact pads. In order to achieve deeper trench cut through wafer, a thick 80-μm SU8 2075 was spin-coated on the back side of the wafer as a mask for the etching. At first, trench was opened through the silicon carrier wafer using a Deep Reactive Ion Etching (DRIE) system in an O_2, SF_6, Ar and He environment. The process was optimized at 50 mTorr pressures and 3000 W ICP power and 50 W RIE power to etch through 300-μm-thick silicon substrate in 3hours in steps of 30 min. This silicon etching process also etched first Si_3N_4 passivation layer. The polyimide substrate and second Si_3N_4 passivation layer were etched using a Reactive Ion Etching (RIE) system, which also removed Ti adhesive layer. The RIE etched process opened the Au contact pads. When the electrical contact pads were exposed, the etching process was terminated. After that, the temperature sensors embedded in the flexible polyimide substrate and superstrate were peeled from the silicon carrier wafer. Then, the sensors were ready for characterization and were cut in into small pieces for packaging. The designed 3D CoventorWare™ model across the cross-section of the temperature sensor is shown in Figure 2-12. Figure 2-13 shows a complete die of temperature sensors in a flexible substrate after removal from the silicon carrier wafer. Each die contains 35 temperature sensors [23] of 3 different sizes.

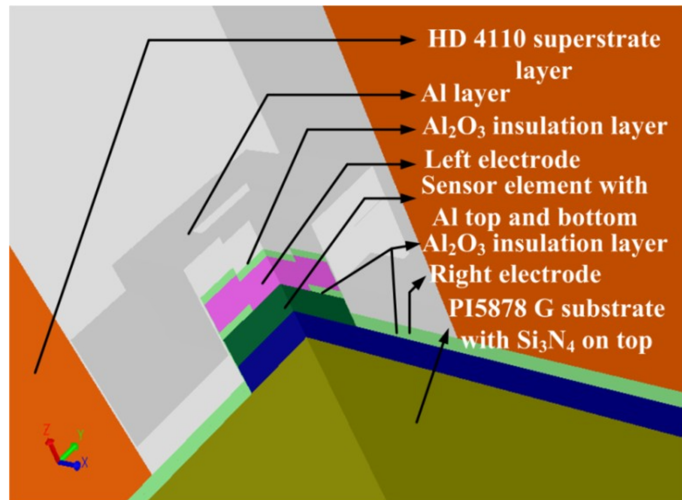

Figure 2-12 CoventorWare™ 3D Cross-Sectional View of the Temperature Sensor. ©2012 IEEE. Reprinted, with Permission, from Temperature Sensor in a Flexible Substrate by M. Ahmed, M. M.Chitteboyina, D. P. Butler, Z. Celik-Butler, in IEEE Sensors, May 2012 [23].

Figure 2-13 1 cm × 1 cm Die of Flexible Substrate Containing 35 Temperature Sensors

2.4 Characterization, Results and Discussions

The characterization of the temperature sensors is divided into two main parts: response measurements and noise measurement. The variation of resistance due to the change in temperature was measured by two methods: response measurements in the probe station and in the cryostat.

2.4.1 Temperature Sensing in Probe Station

The temperature sensors were first characterized in a shielded 8060 series MicroManipulator probe station. The sensor was connected in series with a 1.5 MΩ metal film resistor and the sensor was placed on the stage of the probe station. After that, a dc bias voltage was applied across the series connection. In order to evaluate the sensor's performance due to the variation of the temperature, the temperature of the probe station's heat chuck was varied from 30 ^{o}C to 80 ^{o}C in 5 ^{o}C. The corresponding variation was measured by measuring the voltage across known resistor at each temperature interval and thus the change in the resistance of the sensing element was calculated. The variation of the resistance due to the change in temperature in shown in Figure 2-14. Using Equtation (2.1) and from the Arrhenius plot of *R,* the activation energy was the a-Si for that particular sensor was calculated (Figure 2-14 inset) as 0.2147 eV. The TCR was then computed by three point averaging method for each temperature intervals. The change in TCR due to the variation of temperature is shown in Figure 2-14 for 300 – 370 K. The value TCR was found to be 2.73 %/K at 30 ^{o}C [23].

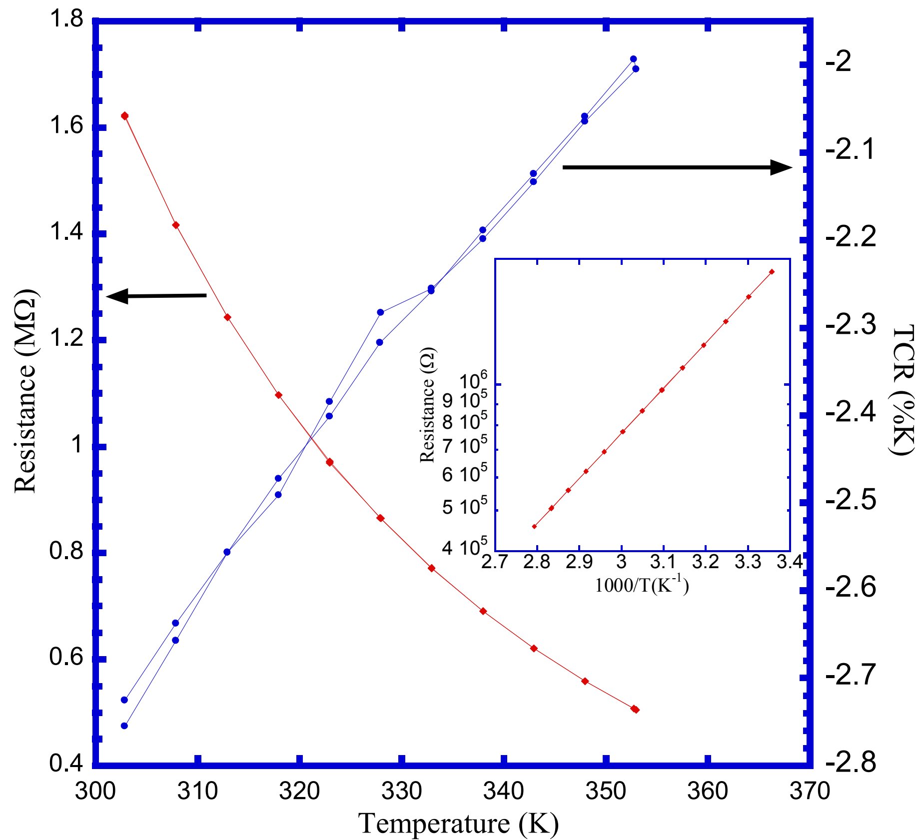

Figure 2-14 The Graph is Showing the Resistance and Temperature Coefficient of Resistance Change as a Function of Temperature Plot in the 300-360 K Range. The Arrhenius plot was Drawn from the Resistance versus Temperature Graph for the Same Sensor (Inset). ©2012 IEEE. Reprinted, with Permission, from Temperature Sensor in a Flexible Substrate by M. Ahmed, M. M.Chitteboyina, D. P. Butler, Z. Celik-Butler, in IEEE Sensors, May 2012 [23].

2.4.2 Temperature Sensing inside Cryostat

In this method, the temperature sensor was fixed inside a Leybold ROK 10-300 K closed-cycle refrigerator and then the chamber was evacuated to 2×10^{-5} Torr pressure (Figure 2-15). Then the temperature of the cryostat's chuck was reduced to 200 K and then temperature was varied from 200 K to 360 K in 5 K intervals using a Lakeshore 331

temperature controller. At each temperature interval, the resistance across the sensing element was measured by two-wire resistance measurement method using an Agilent 34401A multimeter. The change in resistance with the variation of temperature for one temperature sensor was measured using a cryostat over the extended temperature range of 200–360 K as shown in Figure 2-16. From the Arrhenius plot of resistance, the activation energy was calculated (Figure 2-16 inset) to be 0.2208 eV. The TCR versus temperature is shown in Figure 2-16. The TCR was found 2.88 %/K at 300 K.

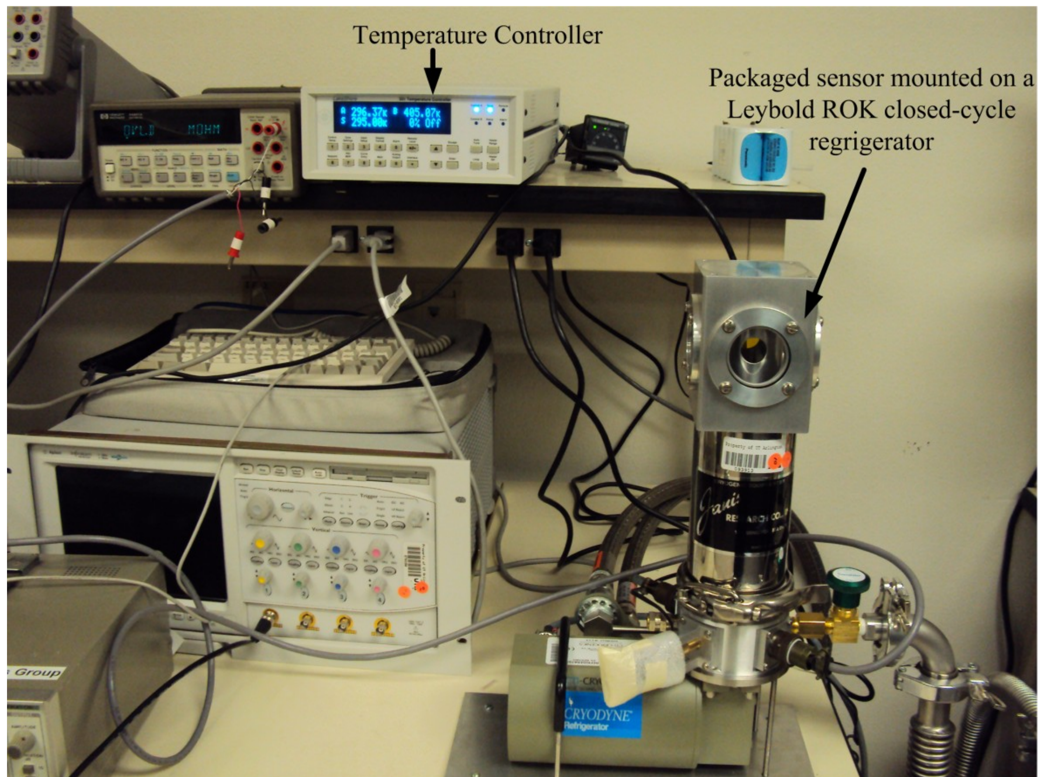

Figure 2-15 Measurement on Leybold ROK 10-300 K Closed-Cycle Refrigerator

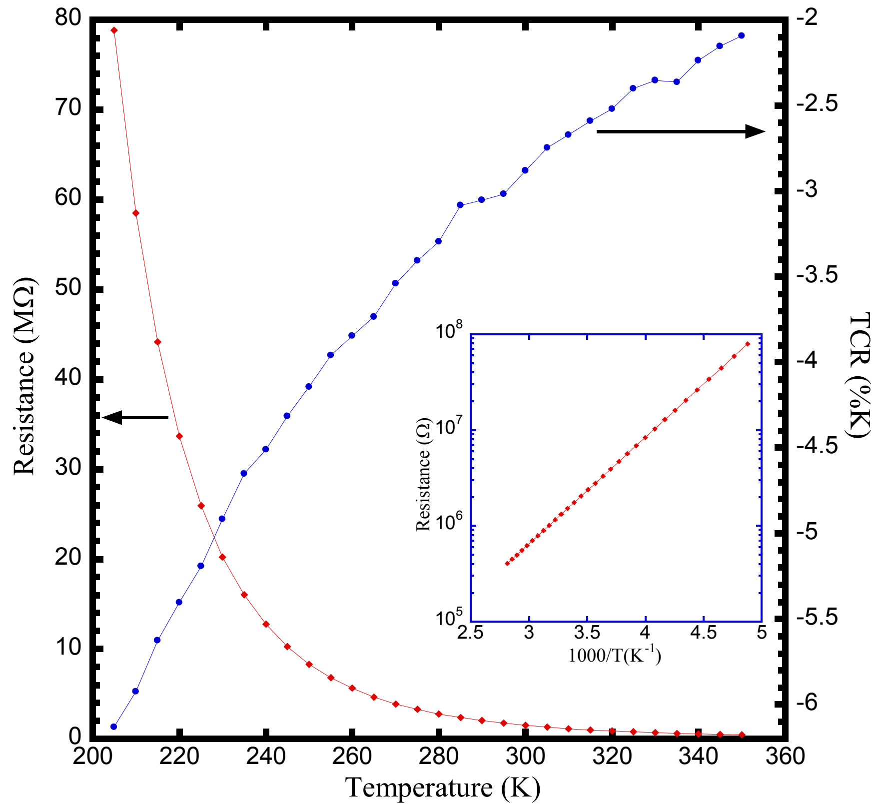

Figure 2-16 The Graph is Presenting the Resistance and Temperature Coefficient of Resistance Change as a Function of Temperature Plot in the 200-360 K Range. The Arrhenius Plot was Drawn from the Resistance versus Temperature Graph for the Same Sensor (Inset). ©2012 IEEE. Reprinted, with Permission, from Temperature Sensor in a Flexible Substrate by M. Ahmed, M. M.Chitteboyina, D. P. Butler, Z. Celik-Butler, in IEEE Sensors, May 2012 [23].

2.4.3 Noise Characterization

The noise put a limit on the sensitivity of the temperature sensor. The sensor was placed on a stage inside the shielded probe station to minimize the influence of extraneous signals. After that, temperature sensor was current-biased by connecting a series resistor of 16.2 MΩ and the voltage across the sensor was amplified 1000 times by

an EG&G PAR113 pre-amplifier. The amplified noise signal from the pre-amplifier was supplied to the Hewlett-Packard 3562A dynamic signal analyzer and voltage noise power spectral density (PSD) across the sensor was recorded over the frequency range of 1 Hz to 1000 Hz. From every measurement, background noise consisting of the amplifier and sensor Johnson noise was subtracted to evaluate net 1/f noise PSD over the entire frequency range for the corresponding device [24]]. Then, normalized Hooge coefficient [25] was calculated from the net 1/f noise PSD.

In order to evaluate the conductance fluctuations of a-Si, a constant current was passed through the sensing material while voltage fluctuation was measured across the sensor. Hooge's expression for 1/f-noise can be expressed as [26]:

$$S_V = \frac{K_{1/f} V^2}{f} \tag{2.3}$$

where, f is the electrical frequency, V is the voltage across the sensor, S_V is the voltage noise PSD and $K_{1/f}$ is the 1/f-noise coefficient or normalized Hooge coefficient which is independent of measuring conditions.

In Figure 2-17, the noise spectral PSD for four temperature sensors are plotted over the frequency range of 1-1000 Hz at the bias voltage of 50 mV and background noise was subtracted. From the 1/f noise spectra of the sensors, magnitude of $K_{1/f}$ value was found to be 1.2×10^{-11}.

The variation of the noise voltage PSD with the bias voltage was characterized by varying the dc voltage across the sensors from 50 mV to 80 mV for all four samples and corresponding noise voltage PSD was recorded. The 1/f noise voltage PSD at 10 Hz for a-Si from all four sensors is shown in Figure 2-18 which depicts a quadratic dependence on bias voltage.

The TCR and 1/f-noise coefficient of four different sensors are summarized in Table 2-1 with their corresponding resistances. The table shows that the TCR values of the temperature sensors are in the range of 2.09 to 2.88 %/K while 1/f-noise coefficients of the sensors are in the range of 8×10^{-12} to 1.6×10^{-11}.

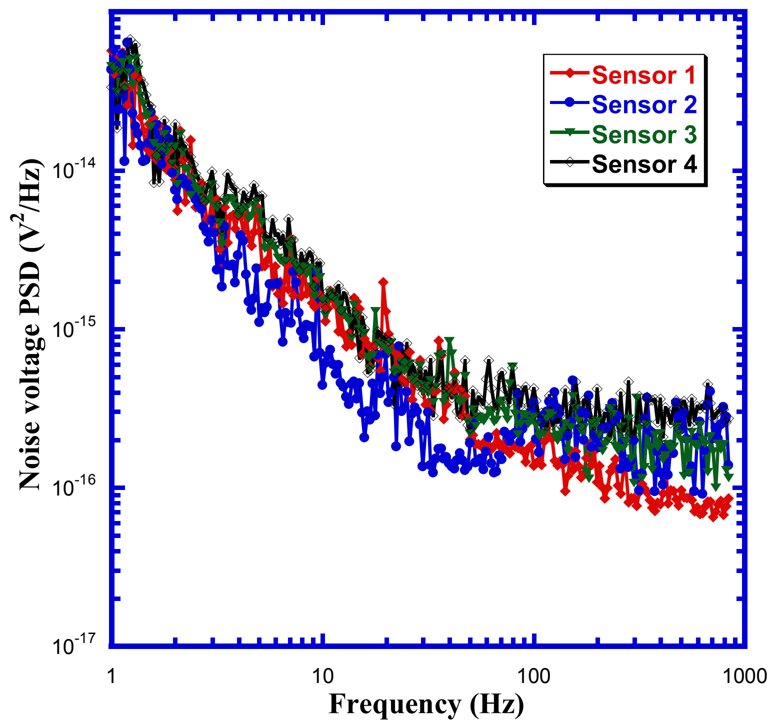

Figure 2-17 Voltage Noise Power Spectral Density for Four Different Sensors over the Frequency Band from 1 to 1000 Hz. ©2012 IEEE. Reprinted, with Permission, from Temperature Sensor in a Flexible Substrate by M. Ahmed, M. M.Chitteboyina, D. P. Butler, Z. Celik-Butler, in IEEE Sensors, May 2012 [23].

Table 2-1 Measured Characteristics of the Sensor at Room Temperature. ©2012 IEEE. Reprinted, with Permission, from Temperature Sensor in a Flexible Substrate by M. Ahmed, M. M.Chitteboyina, D. P. Butler, Z. Celik-Butler, in IEEE Sensors, May 2012 [23].

	Resistance (MΩ)	TCR (1/K)	1/f-noise coefficient
Sensor 1	1.28	0.0227	1.2×10^{-11}
Sensor 2	1.20	0.0209	8×10^{-12}
Sensor 3	1.62	0.0273	1.2×10^{-11}
Sensor 4	1.51	0.0288	1.6×10^{-11}

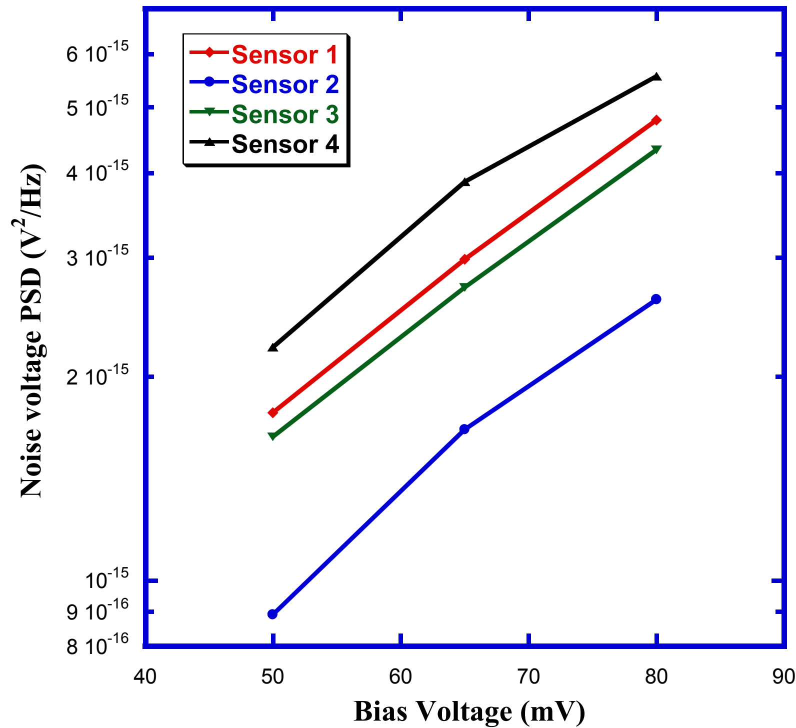

Figure 2-18 Variation of Noise Voltage PSD at 10 Hz with Respect to the Change in Bias Voltage. ©2012 IEEE. Reprinted, with Permission, from Temperature Sensor in a Flexible Substrate by M. Ahmed, M. M.Chitteboyina, D. P. Butler, Z. Celik-Butler, in IEEE Sensors, May 2012 [23].

2.5 Figures of Merit

The temperature sensitivity (R_T) or response of the temperature sensor depends on change in resistance of the sensing material due to the temperature variation and is given as the change in the output voltage with temperature:

$$R_T = \frac{\Delta V}{\Delta T} = I_b R \times \beta \qquad (2.4)$$

where ΔV is the output voltage change for the temperature change ΔT applied on the sensors, I_b is the bias current flowing through the sensing material. The sensitivity of the temperature sensors was measured to vary from 627 μV/K to 1110 μV/K with an average sensitivity of 887 μV/K.

Another important figure of merit is termed as the Noise Equivalent Temperature (*NET*), the amount of temperature changed on the sensor that will produce a signal to noise ratio (SNR) of 1. Therefore, the *NET* can be written as root mean square noise voltage divided by the sensitivity:

$$NET = \frac{V_n}{R_T} \qquad (2.5)$$

where V_n is the root-mean-square noise voltage. The a-Si based temperature sensors exhibited two major noise mechanisms: 1/f noise and the Johnson noise. The 1/f-noise voltage PSD was measured during characterization over frequency bandwidth from 1-941 Hz. The Johnson noise voltage PSD was calculated using following equation [27]:

$$S_J = 4 k_B T R \Delta f \qquad (2.6)$$

where k_B is Boltzmann's constant, T is room temperature in Kelvin, Δf is the noise bandwidth between f_1 and f_2 and taken as 940 Hz for the measurement, R is the resistance of sensing material.

After that, the sum of the noise voltage PSD for flicker noise and Johnson noise gave the total noise voltage power spectral density (PSD), S_v. Then, V_n was calculated from the equation [27]:

$$V_n^2 = \int_{f1}^{f_2} S_v df \qquad (2.7)$$

The noise bandwidth frequencies f_1 and f_2 were chosen to be 1 Hz and 941 Hz for the calculation of the 1/f-noise voltage.

The *NET* of the temperature sensors was calculated vary from 9.37 mK to 13.9 mK with an average value of 11.9 mK in the 1/f noise regime. In the Johnson noise limited regime, the average *NET* was found to be 5.51 mK.

2.6 Conclusions

Undoped amorphous silicon based resistive temperature sensors that are embedded in flexible substrates are presented. The sensors are fabricated while taking into consideration different factors such oxidation and crystallization of the a-Si, proper isolation of the electrical contacts to achieve highest performance from the sensors possible. The sensors are then characterized for measuring temperature coefficient of resistance in two different mechanisms: inside probe station and inside cryostat and noise parameters were also measured. The parameters that are measured from the characterization were used to evaluate the sensitivity and noise equivalent temperature of the temperature sensors encapsulated inside flexible substrate.

Chapter 3

Fabrication and Characterization of Flexible Relative Pressure Sensor

3.1 Introduction

The suitability of MEMS to mass-produce miniature high-performance sensors at low cost has opened up a wide range of applications. MEMS pressure sensor is one of them which is widely used. Pieozoresistive pressure sensors are among the first MEMS devices and comprise a substantial market share of MEMS sensors in the market today [28]. Examples include automotive manifold air and tire pressure, industrial process control, hydraulic systems, microphones, and intravenous blood pressure measurement. Moreover, piezoresistive pressure sensors on flexible substrates allow it to conform to non-planar surfaces and can come to close-contact with the subject. Hence, it enhances the applications of the pressure sensors not limited for rigid body but also for curved surfaces, which in short allows them to apply for structural health monitoring as well as biomedical applications.

3.2 Background

Piezeoresistive effect was first discovered by William Thomson in 1856 [29], since then this effect has been vastly applied in electro-mechanical sensing. At the moment, piezoresistive pressure sensors, mounted on or in a diaphragm are most widely used, where piezoresistor may be diffused in the membrane or deposited on top of the membrane. And, then these resistors are connected in a Wheatstone bridge configuration for temperature compensation. The main advantages of piezoresistive pressure sensor are that simple fabrication process, high linearity and output signal connectivity available as voltage. The main disadvantages are the large temperature sensitivity and drift, low sensitivity of piezoresistors [30]. On the contrary, capacitive pressure sensors based

upon parallel plate capacitors, are less sensitive to temperature variations, higher pressure sensitivity and extremely low power consumption can be obtained. However, it has disadvantages of lower capacitance and complex interface circuit is required. Excessive signal loss from parasitic capacitance is a serious disadvantage, which hindered the development of miniaturized capacitive sensors until on-chip circuitry could be fabricated [30]. Diaphragm-based optical pressure sensors sense the pressure induced deflections by Fabry-Perot interferometry [31, 32] and it has good resolution and sensitivity but sensitivity varies with the temperature [33]. Resonant beam pressure sensors measure pressure by observing the resonance frequency of an embedded doubly clamped bridge [34] or comb drive [35]. It shows high pressure responsivity which does not change with the temperature variation and it has good noise immunity, but the sensors require complex fabrication process [30].

The electrical resistance (*R*) of a homogeneous structure is a function of its dimensions and resistivity (ρ),

$$R = \frac{\rho L}{A} \tag{3.1}$$

where *L* is length, and *A* is the average cross sectional area. The change in resistance due to applied stress is a function of geometry and resistivity changes. The changes in resistance as follows [36]:

$$\frac{dR}{R} = \frac{d\rho}{\rho} - \frac{dA}{A} + \frac{dL}{L} \tag{3.2}$$

Poisson's ratio σ for the material is defined by [36]:

$$\frac{dA}{A} = -\frac{2\sigma dL}{L} \tag{3.3}$$

Consequently [36],

$$\left(\frac{dR}{R}\right)/\left(\frac{dL}{L}\right)=(1+2\sigma)+\left(\frac{d\rho}{\rho}\right)/\left(\frac{dL}{L}\right)\equiv\gamma_p \qquad (3.4)$$

where the dimensionless number γ_p is termed as the electrically resistance-strain coefficient, the strain-sensitivity factor, or the gauge factor.

In Eq. (3-4), the term *(1+2σ)* represents a purely geometrical effect, which corresponds to an increase in length, and a decrease in cross sectional area, of a cylinder under longitudinal tension. The term ($d\rho/\rho$)/(dL/L) represents a physical effect, since it is a change in the resistivity of the material under the applied elastic strain (dL/L).

The change is resistivity term comes into play for the gauge factor calculation due to the alteration in the electron-scattering probability due to change in the thermal vibration amplitude of ions in the stressed crystal. Since the resistivity is a function of mean free path of the electrons and the effective number of free electrons, under strain the mean free path changes which in terms changes resistivity [37]. Resistivity depends exponentially on the separation among grains which is caused by the tunneling effect [38]. Prudenziati *et al.* [39] demonstrated the increment of gauge factor of piezoresistive RuO_2 with the increase of grain size while maintaining sheet resistance constant.

There are several materials that have been utilized for MEMS based piezoresistive pressure sensors, including ruthenium dioxide [40], indium-tin-oxide (ITO) [41], nickel-silver (Ni_x-Ag_{1-x}) [42], palladium, gold and copper [43], tantalum nitride copper [44], germanium [45], amorphous carbon [46] and silicon [47]. Nichrome (Ni –Cr 80/20 wt%) is a good candidate as a piezoresistor due to it’s high resistivity, low temperature coefficient of resistance (TCR), availability and low temperature dependence of gauge factor (GF) and low 1/f noise. The advantage of low 1/f noise allows the sensors to lower the limit of minimum pressure that could be detected by the piezoresistor. The TCR of nichrome films decreases with the increase of the film thickness and a constant GF value

of 2.50 for film thickness 15 nm or above has been shown [48]. The gauge factors of different materials, their TCR values and 1/f noise coefficient is compared in Table 3-1.

Table 3-1 Comparing Different Piezoresistive Materials. ©2013 IEEE. Reprinted, with Permission, from MEMS Force Sensor in a Flexible Substrate using Nichrome Piezoresistors by M. Ahmed, M. M. Chitteboyina, D. P. Butler, Z. Celik-Butler, in IEEE Sensors, October 2013 [49]

Materials	Gauge factor	TCR (%/K)	1/f noise coefficient $K_{1/f}$
RuO_2	2-30	0.005-0.035	1.2×10^{-11}
ITO	2.36-131	0.008-0.18	-
Ni_x-Ag_{1-x}	2.2-2.4	0.04	-
Pd	4.06	0.055	-
Au	4.48	0.16	1×10^{-15}
Cu	3.30	0.43	1×10^{-14}
TaN-Cu	2.3-4.3	~0.001	6.94×10^{-16}
Poly-diamond	17.9-22	0.19	-
Ge	33-42	0.2	-
a-C	36-46	0.5	-
Poly-Si	15-27	0.07-0.3	3.52×10^{-12}
Ni-Cr	Current work	0.0085	$1.89\mathrm{x}10^{-10}$

3.3 Fabrication

A 400-μm-thick, p type <100> 4 inch silicon carrier wafer was used in the fabrication of the pressure sensors so that conventional semiconductor processing equipment could be employed. First, three layers of the device were the same as the temperature sensors to create flexible polyimide substrate and passivate the rigid and flexible substrate. Again, 200-nm-thick Si_3N_4 [Figure 3-1]- 35 μm PI5878 G polyimide [Figure 3-2]- 400-nm-thick Si_3N_4 [Figure 3-3] were deposited on the silicon wafer as the same process described in section 2.3.

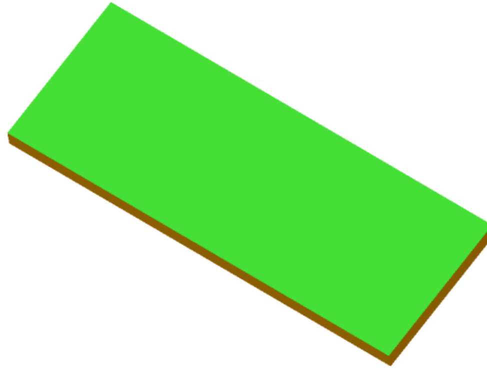

Figure 3-1 Deposition of Si_3N_4 Passivation Layer

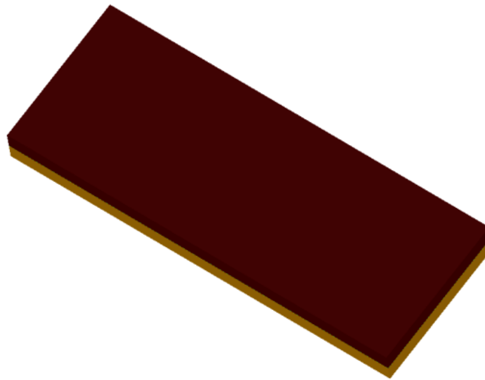

Figure 3-2 Flexible Polyimide Substrate Layer

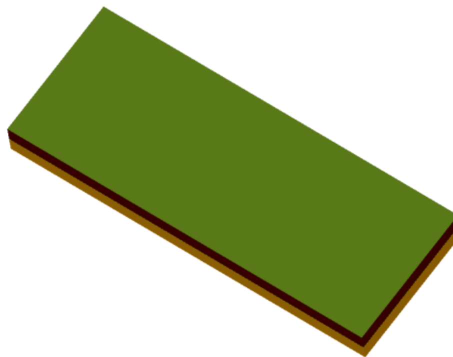

Figure 3-3 Deposition of the Second Si_3N_4 Passivation Layer

In order to suspend the sensing material from substrate a temporary layer needed to be deposited between the sensor and the substrate, which is known as a

sacrificial layer and removed later from the device as a part of the fabrication process. Next stage of the fabrication process, a sacrificial layer was deposited by spin-coating photo-definable liquid polyimide HD4100 onto Si_3N_4 passivation layer and exposed to UV light and developed to pattern [Figure 3-4]. The polyimide was cured at 250 ^oC for 4 hours in the Blue-M Oven to yield a final thickness of 7 µm.

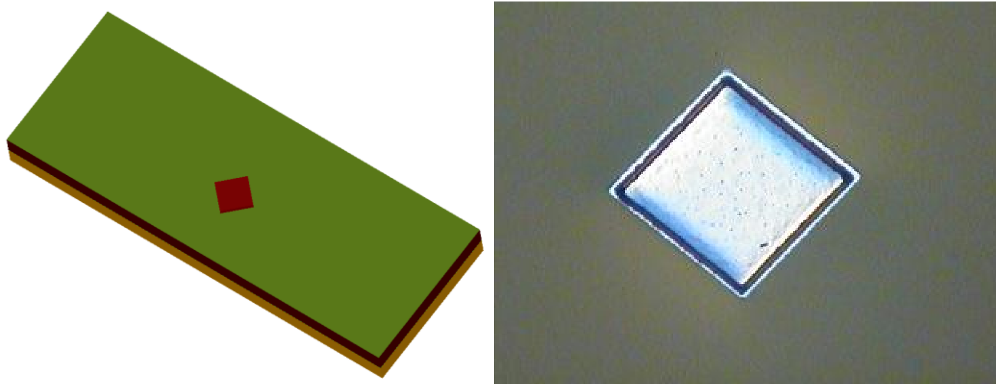

Figure 3-4 Deposition of HD4100 Sacrificial Layer

Next, photoresist was spin coated on the wafer and patterned by photolithography which was followed by the deposition of 1.25-µm of Al_2O_3 membrane layer in the AJA rf sputtering tool at Ar gas environment [Figure 3-5], then lift-off process was done. This membrane layer is an important part of the pressure sensor and undergoes deflection with the applied pressure and attached to the sensing material.

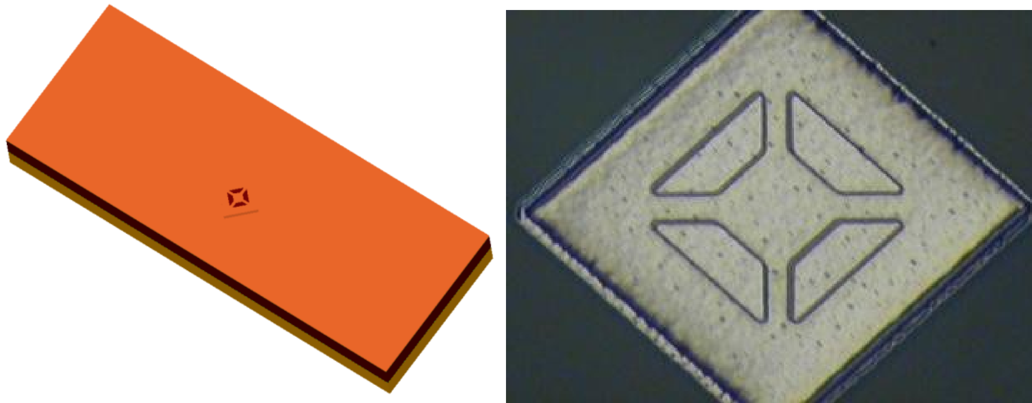

Figure 3-5 Deposition of Al_2O_3 Membrane Layer

After that, the 35-nm-thick nichrome (Ni-80%/Cr-20%) piezoresistor layer was deposited in the Home-built sputtering tool and patterned by lift-off process [Figure 3-6]. This nichrome served as a piezoresistive sensitive material. Then, 2.5-μm of Ti metallization layer was in the Home-built sputtering tool and patterned by lift-off process to connect the active and passive piezoresistors in a Wheatstone bridge geometry [Figure 3-7]. This was followed by depositing 200-nm of Au on top of the contact pads of the metallization layer to facilitate device wire-bonding [Figure 3-8], in the Home-built sputtering tool and patterned by lift-off process. Subsequently, 150-nm of Al_2O_3 layer was sputtered using rf-magnetron sputtering [Figure 3-9].

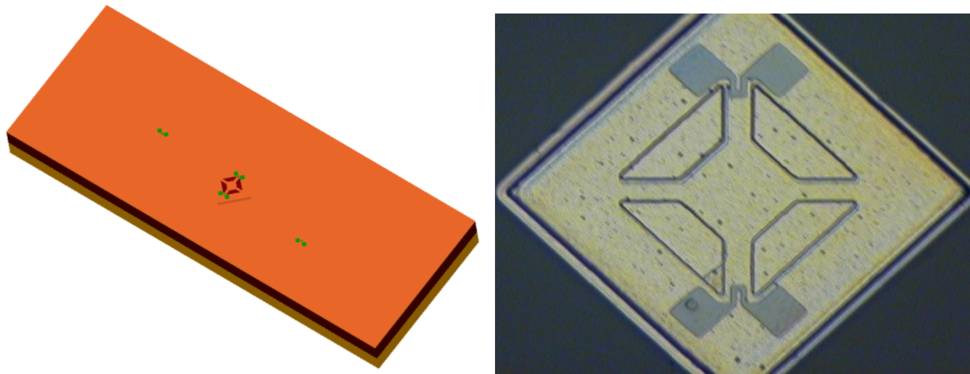

Figure 3-6 Deposition of Nichrome Piezoresistor

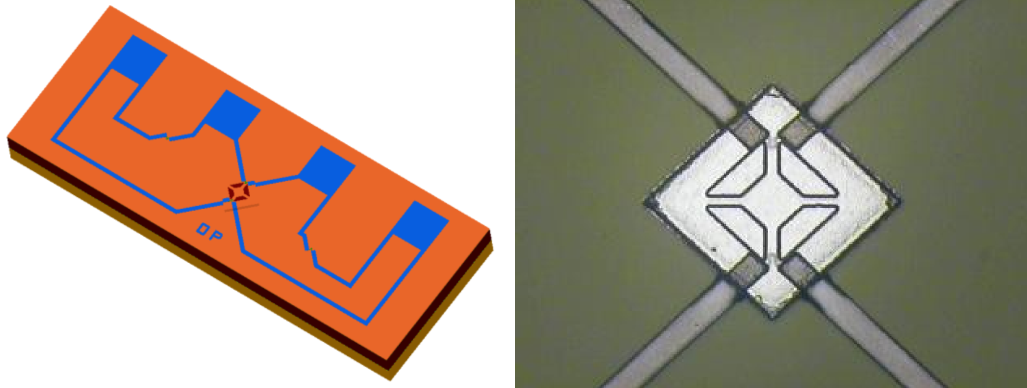

Figure 3-7 Deposition of Ti Metallization Layer

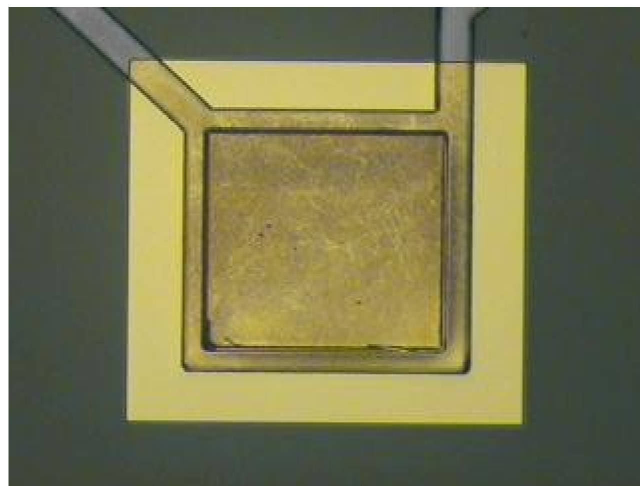

Figure 3-8 Au Protection Layer

This layer holds the openings that was required for surface micromachining step and also served to protect the piezoresistors and metallization from oxidation during polyimide etching. The HD4100 sacrificial layer was removed by surface micromachining in an O_2 gas environment, to create a cavity under the membrane layer in the patterned region [Figure 3-10].

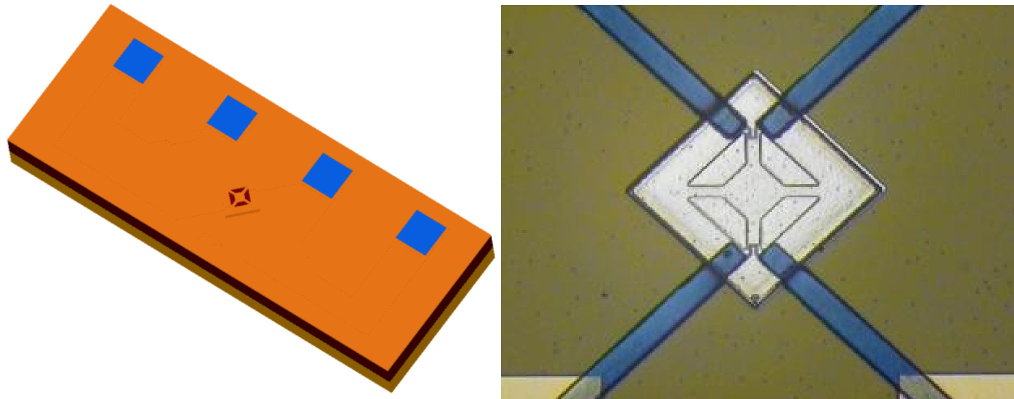

Figure 3-9 Deposition of Al_2O_3 Packaging Layer

The superstrate layer was then deposited by spin-coating photo-definable liquid polyimide HD4110. The superstrate layer was then exposed to UV light and developed to open vias for wire bonding and to expose the entire membrane. The polyimide superstrate was cured at 250 ^{o}C for 4 hrs to yield thickness of 35 μm [Figure 3-11] which created a low stress plane for the sensors [45].

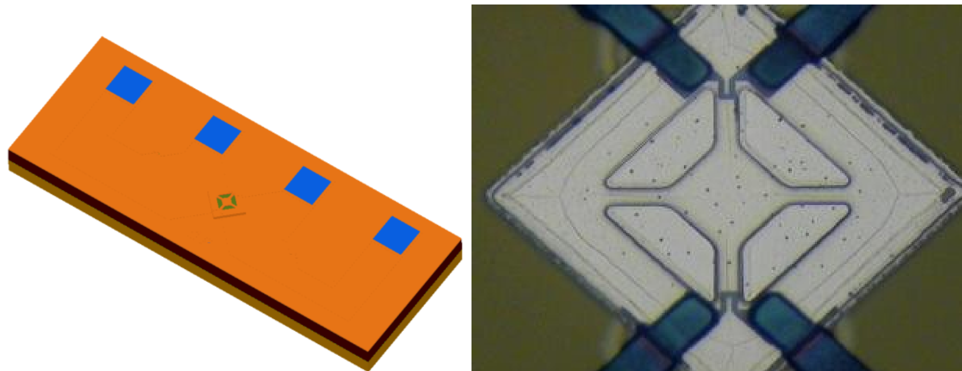

Figure 3-10 Cavity Created by the Removal of Sacrificial Layer

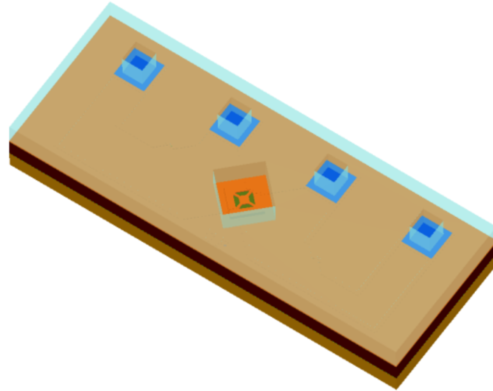

Figure 3-11 Flexible Superstrate Layer

The 3D CoventorWare^{TM} model of the cross-sectional tilted view of the relative pressure sensor is shown in Figure 3-12. The wafer was cut into dies, which were packaged, and wire bonded for characterization. The confocal microscope image of the complete devices is depicted in Figure 3-13. A 2 x 2 cm^2 piece of flexible substrate which was removed from the rigid substrate and containing an array of 48 pressure sensors is shown in Figure 3-14.

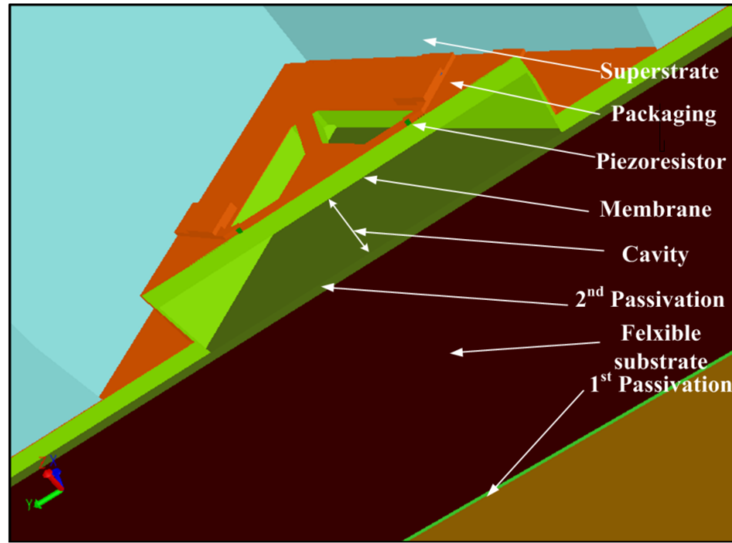

Figure 3-12 The 3D CoventorWare™ Model of the Cross-Section of the Delta Pressure Sensor. ©2011 IEEE. Reprinted, with Permission, from MEMS Relative Pressure Sensors on Flexible Substrate by M. Ahmed, D. P. Butler, Z. Celik-Butler, in IEEE Sensors, 2011 [50].

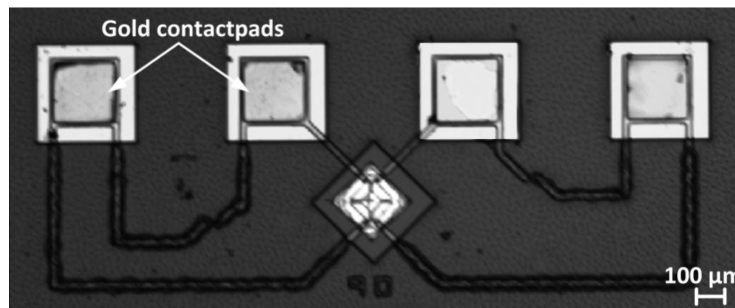

Figure 3-13 Micrograph of the Complete Sensor Taken by Confocal Microscope. ©2011 IEEE. Reprinted, with Permission, from MEMS Relative Pressure Sensors on Flexible Substrate by M. Ahmed, D. P. Butler, Z. Celik-Butler, in IEEE Sensors, 2011 [50].

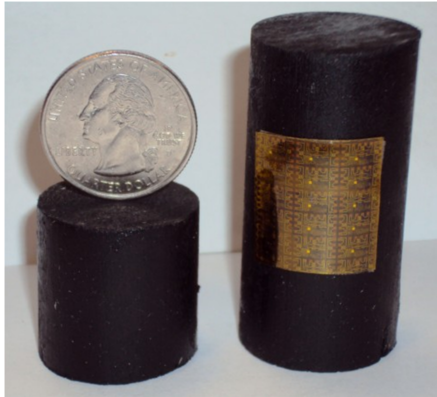

Figure 3-14 The Image is Showing Relative Pressure Sensors Embedded in a 2 x 2 cm^2 Piece of Flexible Substrate. ©2011 IEEE. Reprinted, with Permission, from MEMS Relative Pressure Sensors on Flexible Substrate by M. Ahmed, D. P. Butler, Z. Celik-Butler, in IEEE Sensors, 2011 [50].

3.4 Characterization, Results and Discussions

Once the fabrication was completed, the wafer was cut into small dies and the devices in the die were packaged, wire bonded and characterized. The sensors were characterized in three different stages: measuring resistance values of the individual piezoresistors in the probe station, then response measurement in the probe station and load-cell and finally noise characterization.

3.4.1 Resistance Measurement and Pressure Sensing in Probe Station

The relative pressure sensors were characterized to measure resistance of the each individual piezoresistors. The piezoresistors are declared as active or passive resistors. The resistors, located on top of the cavity and attached to the membrane, are called active piezoresistors. Resistors which were placed outside active region are called passive resistors and they are not substantially affected by the applied pressure. As shown in Figure 3-15, P_1 and P_2 are the passive piezoresistors and A_1 and A_2 are active piezoresistors. To evaluate the current-voltage characteristics, sensors were fixed on the

stage of the probe station equipped with a HP 4155C semiconductor parameter analyzer. The bias voltage applied across bondpads was swept from -0.5 to 0.5 V and the current was measured with the parameter analyzer for the corresponding voltages. The *I-V* measurements were done across the contact pads connected each piezoresistor of a particular device. Each individual resistor is parallel with a series connection of three other resistors; hence the measurement determines a pseudo resistance. A code written in MATLAB program was used to calculate the actual resistance value from the measured pseudo resistance value.

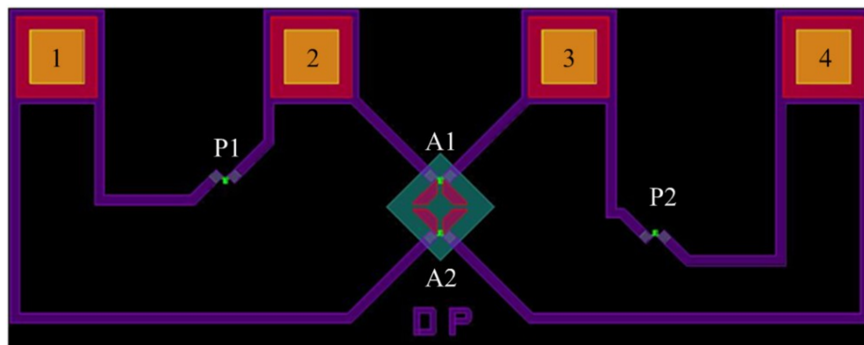

Figure 3-15 Layout of Relative Pressure Sensor Showing the Connection of Active and Passive Piezoresistors in a Half Wheatstone Bridge Configuration. ©2011 IEEE. Reprinted, with Permission, from MEMS Relative Pressure Sensors on Flexible Substrate by M. Ahmed, D. P. Butler, Z. Celik-Butler, in IEEE Sensors, 2011 [50].

The pseudo resistance values for each device measured during *I-V* characterizations are used to calculate individual resistance values presented in Table 1. The measured *I-V* characteristics of the device DP1D15BR is shown in Figure 3-16. The resistance values of the piezoresistors varied from 6 kΩ to 12 kΩ across the wafer, but the variation was less for the resistors of the same device. The variation arose due to lithographic abnormalities occurring during patterning of the nichrome piezoresistor layer and variation of the nichrome thin film. The nichrome thin film was deposited by

Homebuilt sputtering tool which created thickness variation of 20-25% for the deposited thin film for 4 inch wafer.

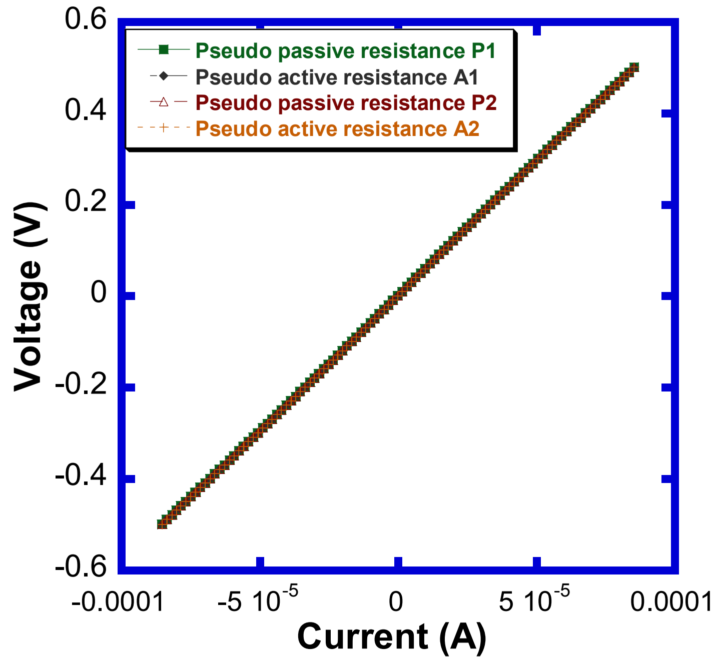

Figure 3-16 Measured *I-V* Characteristics across the Piezoresistors.

After that, a positive input bias voltage was applied across series connection of one active and one passive resistor and output voltage was measured from the other series connection of one active and one passive resistors. At the input port, the bias voltage was applied using Agilent E3620A DC voltage supply and measurements were taken using Keithly 2182A Nanovoltmeter at the output port. Ideally there would not be any output voltage under no load, but due to variations in the resistances for resistors of same device, an offset voltage was observed. Then, the membrane was fully deflected by applying a 20-μm-diameter probe-tip on the membrane surface and the change in output voltage was measured. The bias voltage was varied from 0.25V to 2.5V while applying force in the same process as described above. Then the input and output ports were switched to characterize same device for different configurations.

The response measurement in the probe station for the device named as DP1D15BR is shown in Figure 3-17. The graph shows the change in offset voltage due to the full deflection of the membrane. According to the experimental results, it was observed that with the increment of the bias voltage, the output voltage changed linearly from the offset voltage for full deflection of membrane. This means that linear change of resistance for piezoresistors which is related with change in output voltage.

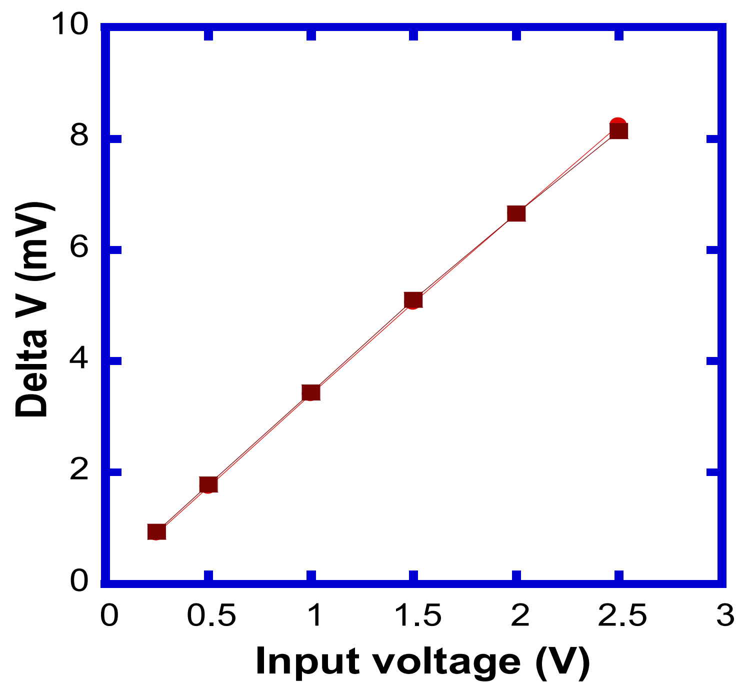

Figure 3-17 Measured Wheatstone Bridge Output Voltage Change under Full Load as a Function of Input Bias Voltage. ©2011 IEEE. Reprinted, with Permission, from MEMS Relative Pressure Sensors on Flexible Substrate by M. Ahmed, D. P. Butler, Z. Celik-Butler, in IEEE Sensors, 2011 [50].

3.4.2 Pressure Sensing in Load Cell

The sensors were then placed on the XYZ manipulator stage which could be moved along three axes and also be tilted. In order to apply varying loads on the sensors,

a tensile GS0-10 load-cell was utilized and it has a range of loads from 0 to 10 g. A PI620-ZCD nanopositioner equipped with a probe tip was served to displace the probe tip precisely using a E-665 PZT Controller, from 0 to 50 μm in vertical direction. The diameter of the probe tip was 10 μm which was utilized for this characterization. The sensor was electrically connected similar to the connection in the probe station. An input bias of 1 V was applied through the series connection of one active and one passive resistors and the output offset voltage was measured without applied pressure. The probe tip was then gradually engaged onto the diaphragm surface by controlling the nanopositioner to deflect the membrane in steps of 0.2 μm. The output voltage was measured for each step of loading. The probe tip was moved up gradually and output voltages were recorded for each load [47]. The measurements were performed again after switching input and output connections.

The sensor response measured for the device termed as DP2D12AT is shown in Figure 3-18. For the full deflection of the membrane, the average change output voltage from offset voltage was measured to be 4.072 mV at 2.49 mN applied force or 7.08 MPa pressure [50]. The sensor response was linear for small application of the load or small deflection of the membrane. As the deflection of the membrane increased the relative change in output voltage was saturated since the membrane reached the bottom of the cavity which also caused maximum strain on the active piezoresistors [45].

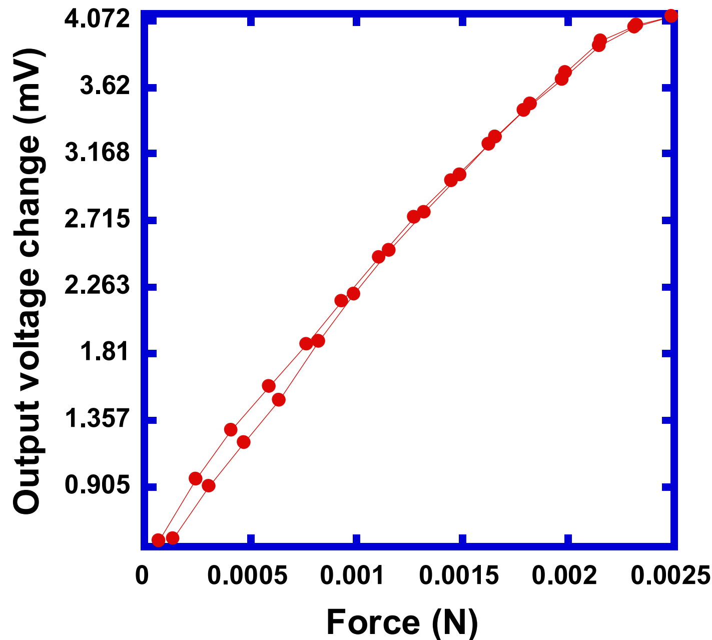

Figure 3-18 Load-Cell Measurement Showing the Change in Output Voltage due the Variation of Applied Load. ©2013 IEEE. Reprinted, with Permission, from MEMS Force Sensor in a Flexible Substrate Using Nichrome Piezoresistors by M. Ahmed, M. M. Chitteboyina, D. P. Butler, Z. Celik-Butler, in IEEE Sensors, October 2013 [49].

3.4.3 Noise Characterization

The noise characteristics of the sensors were measured by current-biasing the sensor by connecting a 100 kΩ series resistor and a NiCd battery source. A bias voltage across bond pads 1 & 3 and the output voltage noise power spectral density (PSD) as evaluated from the bond pads 2 & 4. Again, an EG&G PAR113 pre-amplifier use to amplify the voltage across the device and the gain was set to 1000. The amplified noise signal was passed through a Hewlett-Packard 3562A dynamic signal analyzer to evaluate the noise PSD over the frequency range of 1 Hz to 1000 Hz. The dc voltage across the sensors was varied from 0.25 V to 1.25 V to demonstrate the quadratic voltage dependence of the measured voltage noise PSD. After subtracting the background noise

consisting of the amplifier and device Johnson noise, the normalized Hooge coefficient [25] was determined from the net 1/f portion of the noise spectral density [24]. The characterizations were performed inside a shielded probe station to limit the effect of extraneous signals. The measurements at different bias voltage were performed again after switching input and output ports.

The noise spectra after subtracting the background noise for the sensor termed as DP3D14AR at the bias voltage of 1 V are plotted in Figure 3-19 for two different configurations. The 1/f noise spectra were plotted as a function of frequency and the average Hooge coefficient $K_{1/f}$ value was obtained to be 6.86×10^{-11}. To demonstrate the voltage dependence of the noise PSD, the bias voltage was varied from 0.25 V to 1.25 V and the corresponding 1/f-noise was measured for eight different pressure sensors. The noise voltage PSD for one of the sensor at 10 Hz is shown in Figure 3-20 which demonstrates a quadratic dependence of 1/f noise on bias voltage. The average value of normalized Hooge coefficient $K_{1/f}$ for 8 different pressure sensors was found to be 1.89×10^{-10} [Table 3-3].

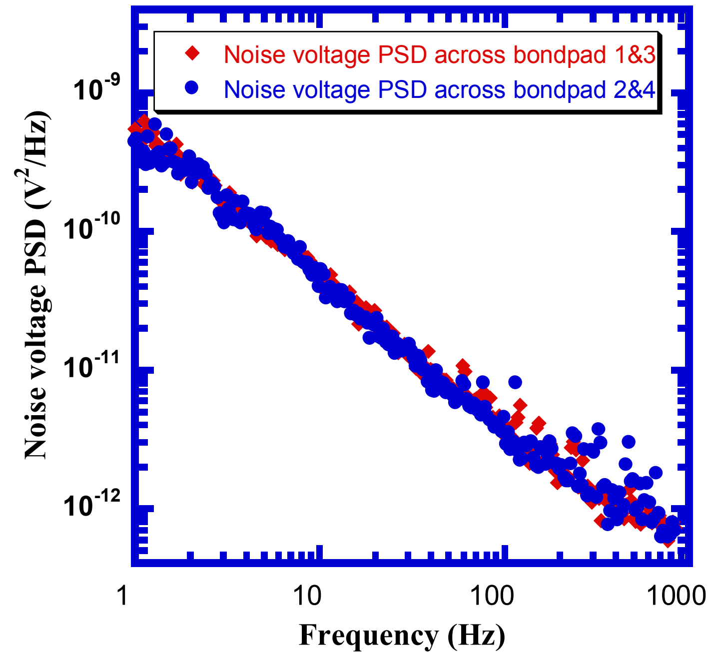

Figure 3-19 Noise Voltage Power Spectral Density for the Net 1/F Noise of a Pressure Sensor with 1 V Bias on the Wheatstone Bridge. ©2013 IEEE. Reprinted, with Permission, from MEMS Force Sensor in a Flexible Substrate Using Nichrome Piezoresistors by M. Ahmed, M. M. Chitteboyina, D. P. Butler, Z. Celik-Butler, in IEEE Sensors, October 2013 [49].

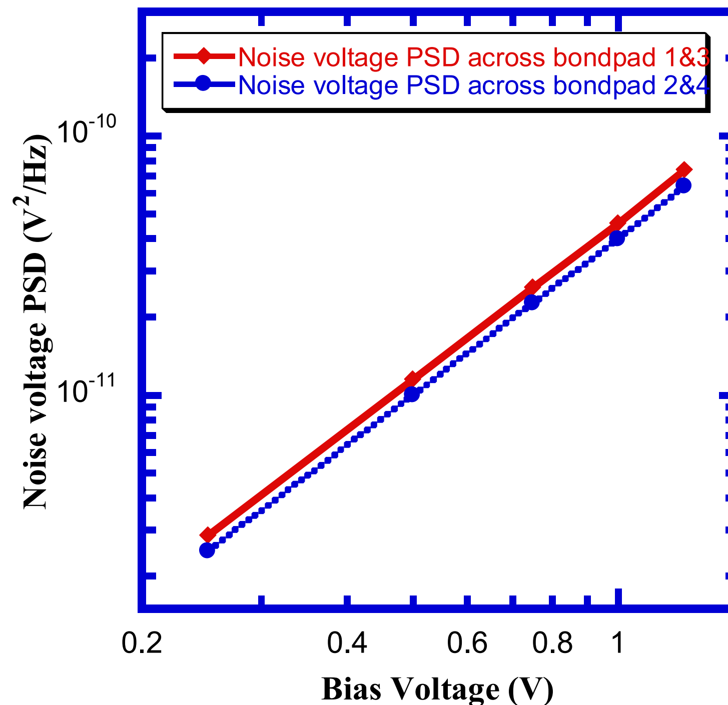

Figure 3-20 Noise Voltage Power Spectral Density for Flicker Noise at 10 Hz as a Function of Bias Voltage Variation. ©2013 IEEE. Reprinted, with Permission, from MEMS Force Sensor in a Flexible Substrate Using Nichrome Piezoresistors by M. Ahmed, M. M. Chitteboyina, D. P. Butler, Z. Celik-Butler, in IEEE Sensors, October 2013 [49].

3.4.4 Gauge Factor Calculation

In order to evaluate the gauge factors of the sensors, the pressure response results were combined with simulations that were performed in the MemMech module of CoventorWare™. For the simulation purpose, a patch created at the center of the membrane for the designed sensor and a force was applied on the patch to mimic the experimental conditions. The pressure values and Young's modulus were varied to deflect the membrane fully by 7 µm. The average strain over the piezoresistor area was

calculated with the aid of CoventorWare™. Then, the normalized change in resistance $\Delta R/R$, was calculated in MATLAB by using the equations below [50]:

$$V_{out} = \frac{P_1 P_2 - A_1 A_2}{(A_1 + P_2)(A_2 + P_1)} V_{in} \tag{3.5}$$

$$V_{out} + \Delta V_{out} = \frac{P_1 P_2 - (A_1 + \Delta A_1)(A_2 + \Delta A_2)}{(A_1 + \Delta A_1 + P_2)(A_2 + \Delta A_2 + P_1)} V_{in} \tag{3.6}$$

where P_1, P_2 are passive resistances, A_1, A_2 are active resistances and the corresponding change in resistors under applied pressure were ΔA_1 and ΔA_2 respectively, ΔV_{out} is the change in output voltage and V_{in} is input bias voltage. In ideal case where resistances are the same i.e., $P_1=A_1=P_2=A_2=R$, the equation can be summarized as:

$$\Delta V_{out} = \frac{\frac{\Delta R}{R}}{2 + \frac{\Delta R}{R}} V_{in} \tag{3.7}$$

Finally, gauge factor for the individual sensor was calculated using Equation (3.4), by dividing calculated value of normalized resistance change by simulated average strain. The values of normalized change in resistance, average strain, and gauge factors of the piezoresistors and the simulated value of Young's modulus for the aluminum oxide membrane are given in Table 3-3. Average gauge factor was calculated to be 1.75 which was comparable to the gauge factor calculated by Kazi *et al.* (1.95) [48] and average value of Young's modulus for the Al_2O_3 was found to be 405.81 MPa [50].

3.4.5 Figures of Merit

The pressure responsivity (R_{Pr}) is one of the important figures of merit of the sensors and the pressures sensors responsivity was calculated using the equation:

$$R_{\mathrm{Pr}} = \frac{\Delta V_{out}}{P} \tag{3.8}$$

where ΔV_{out} is the output voltage change for the pressure P applied on the diaphragm which could be calculated from the slope of output voltage change vs. applied pressure curve. For our pressure sensors responsivity was calculated from 0.094 mV/MPa to 0.79 mV/MPa with an average sensitivity of 0.44 mV/MPa. Another important figure of merit is the noise equivalent pressure (*NEPr*), the amount of pressure applied on the sensor that will produce a signal-to-noise-ratio of 1. Therefore, *NEPr* can be written as root mean square noise voltage V_n divided by the responsivity:

$$NE\,\mathrm{Pr} = \frac{V_n}{R_{\mathrm{Pr}}} \tag{3.9}$$

The root-mean-square noise voltage V_n can be calculated by the equation [27]:

$$V_n^2 = \int_{f_1}^{f_2} S_v df \tag{3.10}$$

where S_v is the noise voltage power spectral density (PSD) which takes consideration of the noise voltage PSD for both flicker noise and Johnson noise. The frequencies f_1 and f_2 were selected as1 Hz and 8 Hz as used during characterization in the Keithley nanovoltmeter. Flicker noise voltage PSD was determined by the noise characterization and Johnson noise voltage PSD was determined by the equation below [27]:

$$S_J = 4k_B TR \tag{3.11}$$

where k_B is the Boltzmann constant, T is the room temperature in Kelvin, R is the equivalent resistance of the piezoresistors. For our pressure sensors noise equivalent pressure (*NEPr*) was calculated from 25.1 kPa to 132.2 kPa with an average value of 58.23 kPa. The average value of the Johnson noise voltage was 3.15×10^{-8} V while the average value of 1/f noise voltage was 1.84×10^{-5} V.

Table 3-2 Measured Resistances for Each Devices at Room Temperature. ©2011 IEEE. Reprinted, with Permission, from MEMS Relative Pressure Sensors on Flexible Substrate by M. Ahmed, D. P. Butler, Z. Celik-Butler, in IEEE Sensors, 2011 [50].

Device name	Passive resistor 1 (kΩ)	Active resistor 1 (kΩ)	Passive resistor 2 (kΩ)	Active resistor 2 (kΩ)
DP1D15BR	6.08	6.60	7.00	7.41
DP1D24CR	6.13	7.23	7.18	9.97
DP1D32CR	10.77	10.71	9.30	9.71
DP2D12AT	7.73	9.20	7.16	8.95
DP2D24BR	10.86	12.67	10.73	13.67
DP3D14AR	8.01	10.59	7.81	7.18
DP3D22BR	7.82	8.33	7.87	7.02
DP3D32BL	7.64	8.21	7.59	9.75

Table 3-3 Measured Characteristics and Figures of Merit of Relative Pressure Sensor at Room Temperature

Device Name	Avg. ΔV (mV) for 1 V input [50]	Avg. maximum pressure measured (MPa) [50]	Avg. ΔR/R (%) [50]	Young modulus for Al_2O_3 GPa [50]	Calculated strain [50]	Gauge factor [50]	$K_{1/f}$ Hooge coefficient [50]	Sensitivity mV/MPa	Noise voltage V [50]	*NEPr* KPa
DP1D15BR	1.895	7.48	5.15	404	0.0311	1.643	5.68×10^{-11}	0.253	1.09×10^{-05}	43.03
DP1D24CR	0.67	7.14	4.533	386	0.0314	1.444	7.37×10^{-11}	0.094	1.24×10^{-05}	132.2
DP1D32CR	6.032	7.95	4.995	429.5	0.03097	1.613	1.74×10^{-10}	0.759	1.90×10^{-05}	25.10
DP2D12AT	5.89	7.44	6.01	402	0.0307	1.958	4.29×10^{-10}	0.792	2.99×10^{-05}	37.74
DP2D24BR	4.473	7.1	4.517	383.5	0.0314	1.439	3.32×10^{-10}	0.630	2.63×10^{-05}	41.74
DP3D14AR	3.422	7.51	6.12	405.5	0.0312	1.96	6.86×10^{-11}	0.456	1.19×10^{-05}	26.29
DP3D22BR	0.918	7.79	5.704	421	0.0312	1.828	6.50×10^{-11}	0.118	1.17×10^{-05}	98.93
DP3D32BL	3.243	7.69	6.672	415.5	0.0312	2.138	3.15×10^{-10}	0.422	2.56×10^{-05}	60.73

3.4.5.1 Thermomechanical Noise

Any micromechanical systems processed through micromachining suffers from mechanical-thermal noise due to the Brownian motion of the gas surrounding the structure. If the temperature around the system is finite and if the system is in thermodynamic equilibrium then the structure will undergo some level of random movement. The random movement of the molecules in gas at a certain temperature and surrounding mechanical structure leads to random fluctuations which is referred as thermomechanical noise [51, 52]. In order take into consideration thermomechanical noise, the damping coefficient of the relative pressure sensors was measured with the aid of finite element analysis in CoventorWare^{TM} software and DampingMM module and "squeeze or slide film flow" for air was utilized. The damping coefficient was found to be 1.03×10^{-4} N/ms^{-1} and the corresponding thermomechanical force was calculated to be 3.45×10^{-12} from the equation [53]:

$$F_{tm} = \sqrt{4k_B T b \Delta f} \tag{3.12}$$

where F_{tm} is the thermo-mechanical force, k_B is the Boltzmann constant, T is the room temperature, b is the damping coefficient and Δf is bandwidth.

The thermomechanical noise power of the relative pressure sensors was measured and the average value was calculated to be 4.31×10^{-5} Pa which is very small compared to the noise equivalent pressure. The equivalent noise voltage for thermomechanical noise calculated from Eq. 3-9 is 1.84×10^{-14} V. Comparing the different noise mechanism, i.e., the 1/f noise, Johnson noise and thermomechanical noise it could be concluded that the pressure sensors are 1/f noise limited.

3.5 Conclusions

This chapter discussed the fabrication and characterization of piezoresistive relative pressure sensors on flexible substrate. Nichrome (Ni-80%/Cr-20%) was utilized as the sensing element and rf sputtered Al_2O_3 was utilized as a membrane material. The average value of the gauge factor for nichrome piezoresistor was found to be 1.75 and the Young's modulus of the Al_2O_3 was calculated to be 405.81 GPa by the finite element analysis using Coventorware™. The average value of normalized Hooge coefficient $K_{1/f}$ was found to be 1.89×10^{-10}. The thermomechanical noise was also calculated. The total noise voltage was found to be 1.84×10^{-5} V. For our pressure sensors sensitivity was calculated from 0.094 mV/MPa to 0.79 mV/MPa with an average sensitivity of 0.44 mV/MPa. The pressure sensors noise equivalent pressure (*NEPr*) was calculated from 25.1 kPa to 132.2 kPa with an average value of 58.23 kPa.

Chapter 4

Fabrication and Characterization of Flexible Absolute Pressure Sensor

4.1 Introduction

The need for pressure measurement inside human body as well as measuring absolute pressure change in structures requires pressure sensor to be packaged and sealed so that the structural integrity can be maintained. The advancement of miniaturization of MEMS sensors forces the fabrication of MEMS pressure sensors. Since the structures, the human body, smart prosthetic devices are curved, sensors needed to be flexible enough to conform to those surfaces and come in intimate contact with the surfaces. In addition, a hermetic sealed pressure sensor on a flexible substrate is can detect absolute pressure compared to a reference pressure inside human body and large structures. In this chapter, the fabrication and characterization of MEMS piezoresistive absolute pressure sensors on flexible substrates have been discussed.

4.2 Background

The absolute pressure sensors that are found in literature can be divided into two categories based on the fabrication technique used: bulk micromachined or surface micromachined absolute pressure sensors. For bulk micromachined sensors, a cavity is created on the substrate by etching and then a diaphragm is bonded with substrate which can be either silicon [54, 55], glass [56, 57, 58, 59, 60, 61] or polymer [62] substrate. The bonding is usually accomplished by either direct silicon bonding [54] or glass-silicon anodic bonding [56, 57, 58, 59, 60, 61] or thermocompression-bonding [62]. The bonding of diaphragm with the substrate forms a reference cavity that is hermetically sealed. This reference cavity operates at the atmospheric pressure. In the surface micromachining

sensors, wet chemical etching [63] was used to remove dielectric sacrificial layer which created the reference cavity between substrate and the membrane.

In this chapter, surface micromachined absolute pressure sensor has been discussed. The polyimide was used as sacrificial layer and dry etching was used to create cavity. The reference cavity was sealed in a deposition system, under vacuum. The current work discussed on fabrication of absolute pressure sensor on flexible substrate.

4.3 Fabrication

A 400-μm-thick, p type <100> 4 inch silicon carrier wafer was used as the starting substrate for the pressure sensors so that conventional thin film deposition and etching technique could be utilized. First, three layers of the device were the same as the temperature sensors and relative pressure sensors to create flexible polyimide substrate and passivate the rigid and flexible substrate. Again, 200-nm-thick Si_3N_4 [Figure 4-1]- 35 μm PI5878 G polyimide [Figure 4-2]- 400-nm-thick Si_3N_4 [Figure 4-3] were deposited on the silicon wafer as the same process described in section 2.3 and section 3.3.

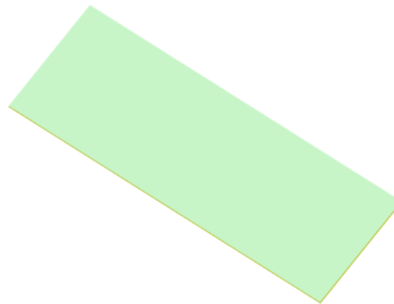

Figure 4-1 Deposition of First Si_3N_4 Passivation Layer

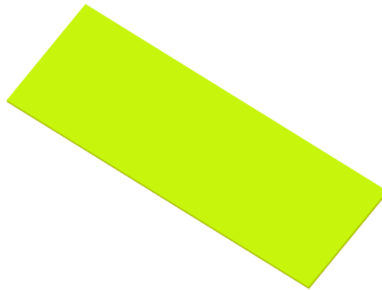

Figure 4-2 Deposition of Flexible Polyimide Substrate Layer

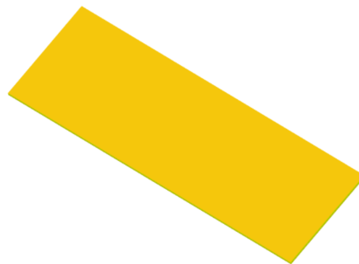

Figure 4-3 Deposition of Second Si_3N_4 Passivation Layer

In order to facilitate surface micromachining process, a thin and photo-definable polyimide sacrificial layer was spin-coated and patterned to form rectangular structure by exposing to UV light and development [Figure 4-4]. The polyimide was cured at 250 ^oC for four hours to yield 0.5-μm thickness. This sacrificial layer served to accelerate the surface micromachining while helped to reduce the thickness packaging layer required for sealing the reference cavity. Next, a thicker polyimide was deposited on the thin polyimide which defined the depth of the cavity the pressure sensors [Figure 4-5]. This was also patterned by photolithography and cured at 250 ^oC for 4 hrs to yield 7-μm thickness.

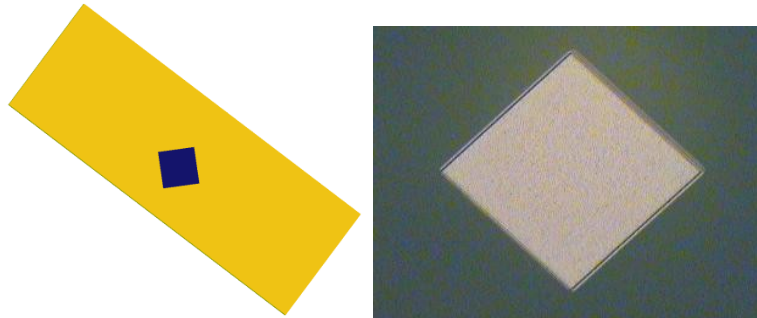

Figure 4-4 Deposition of Thin Sacrificial Layer

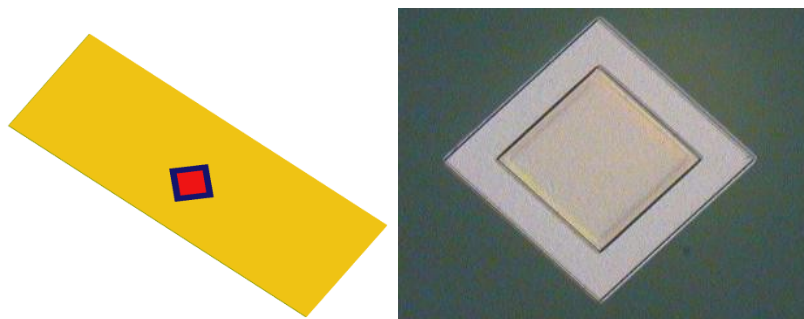

Figure 4-5 Deposition of Thick HD4100 Sacrificial Layer

Next, Negative photoresist NR9-1500 PY was spin coated on the wafer and patterned by photolithography which was followed by the deposition of 150-nm of Al_2O_3 membrane layer [Figure 4-6]. Then, lift-off process was done to keep the patterned portion of the membrane. This membrane layer played a crucial part in the fabrication by which hold the windows required for the surface micromachining process and attached to sensing element and response to the deflection due to applied pressure. Next, the nichrome (Ni-80%/Cr-20%) piezoresistor layer was grown and patterned by lift-off process [Figure 4-7] to achieve a thickness of 38-nm. Then, Ti metallization was deposited to electrically connect the nichrome resistors in a half Wheatstone bridge structure. The 2.15-µm-thick Ti layer was deposited by sputtering and patterned by lift-off process [Figure 4-8]. Then, 200-nm of Au was sputtered on the patterned region of the metallization layer to make the contact pads which helped to wire bond the sensor for

electrical connection and characterization process [Figure 4-9]. Before starting the surface micromachining stage, the piezoresistors and the metallization lines needed to be encapsulated to protect them from oxidation. To meet the necessity, 900-nm of Al_2O_3 layer was sputtered using rf-magnetron sputtering and patterned [Figure 4-10]. Next, the polyimide layers were etched inside oxygen plasma with a Deiner Asher system and a cavity was formed under the membrane [Figure 4-11].

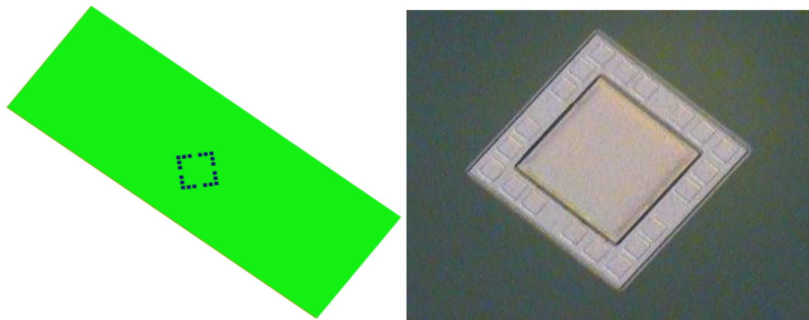

Figure 4-6 Deposition of Al_2O_3 Membrane Layer

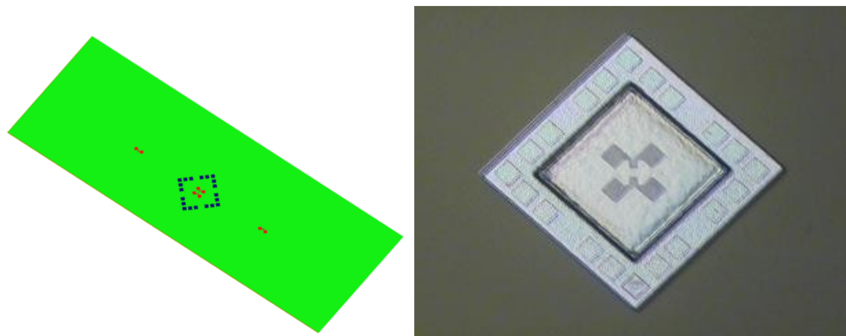

Figure 4-7 Deposition of Nichrome Piezoresistors

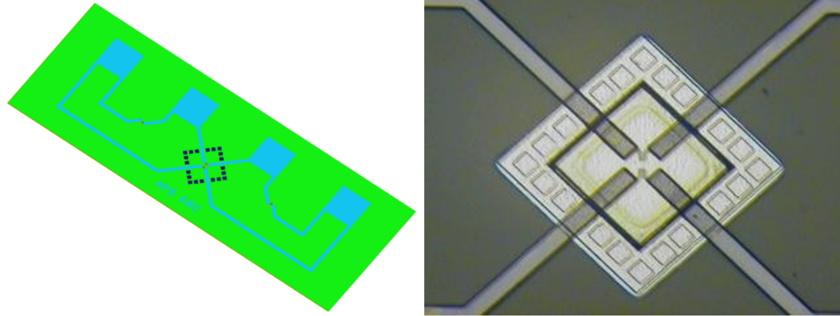

Figure 4-8 Deposition of Ti Metallization Layer

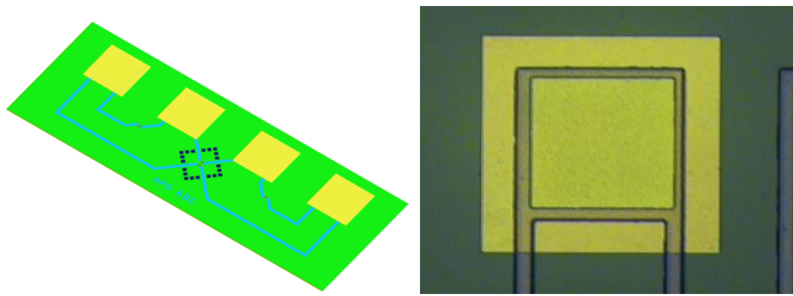

Figure 4-9 Deposition of Au Protection Layer

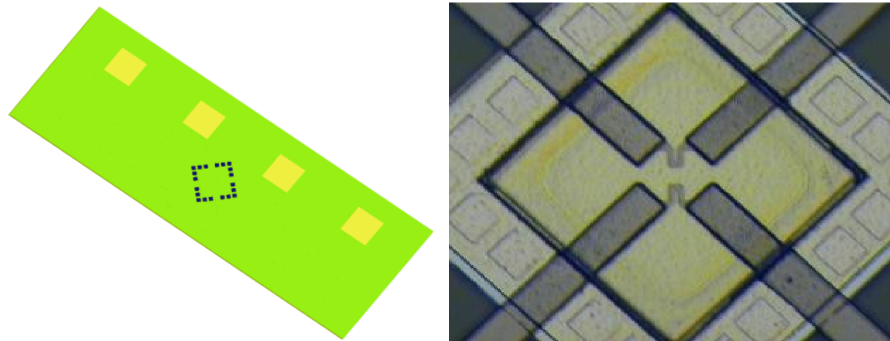

Figure 4-10 Deposition of Al_2O_3 Encapsulation Layer

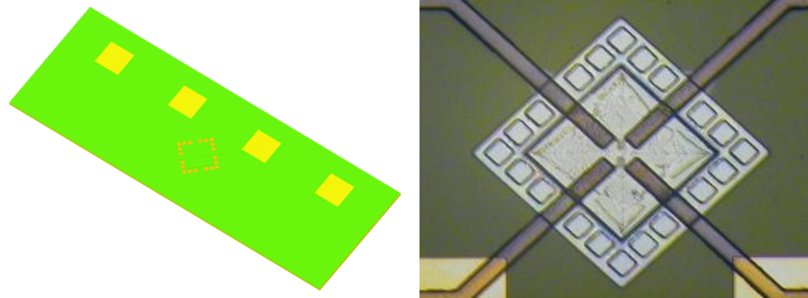

Figure 4-11 Surface Micromachining to Create Cavity under Selected Region

Next, the openings in the membrane and encapsulation layers were sealed by a 3.5-μm-thick Al_2O_3 packaging layer; which was sputtered at 5 mTorr chamber pressure. The sputtering pressure also defined the reference pressure for sensor. In order to open vias for electrical connection HF acid was used to etch Al_2O_3 [Figure 4-12]. At the final stage of the fabrication, HD4110 liquid polyimide was spin-coated, patterned to open contact pads and sensing area; then cured at 250 ^{o}C to yield a thickness of 35 μm [Figure 4-13].

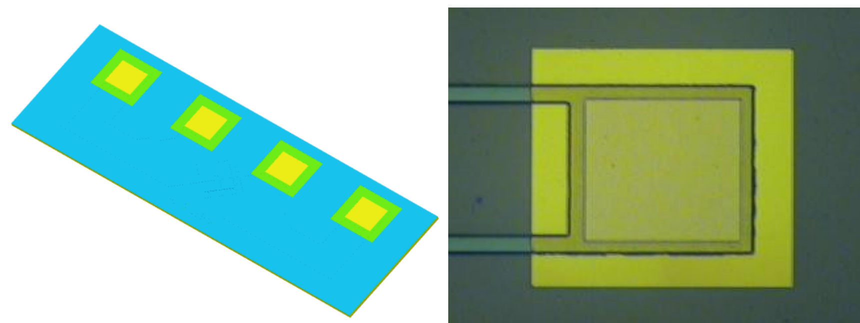

Figure 4-12 Deposition of Packaging Layer and Etching to Open Vias

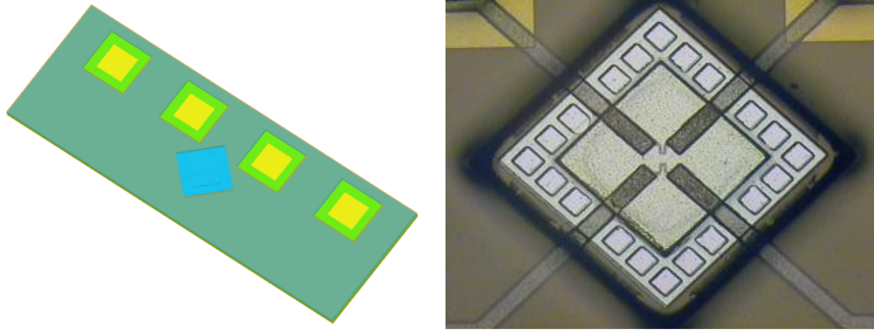

Figure 4-13 Deposition of Flexible Superstrate Layer

In Figure 4-14 is showing a CoventorWare™ 3D cross-sectional view of the sensor inside the polyimide substrate. After fabrication, the wafer was cut into small dies and packaged for measurements. The Confocal microscope micrograph of one completed sensor is demonstrating in Figure 4-15. In Figure 4-16, an array of 75 absolute pressure sensors fabricated on flexible substrate is shown.

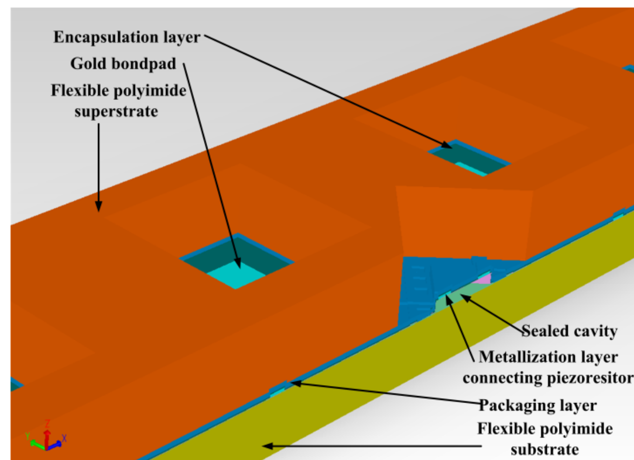

Figure 4-14 CoventorWare™ 3D Picture of the Absolute Pressure Sensor ©2012 IEEE. Reprinted, with Permission, from MEMS Absolute Pressure Sensors on Flexible Substrate by M. Ahmed, D. P. Butler, Z. Celik-Butler, in IEEE MEMS, 2012 [64]

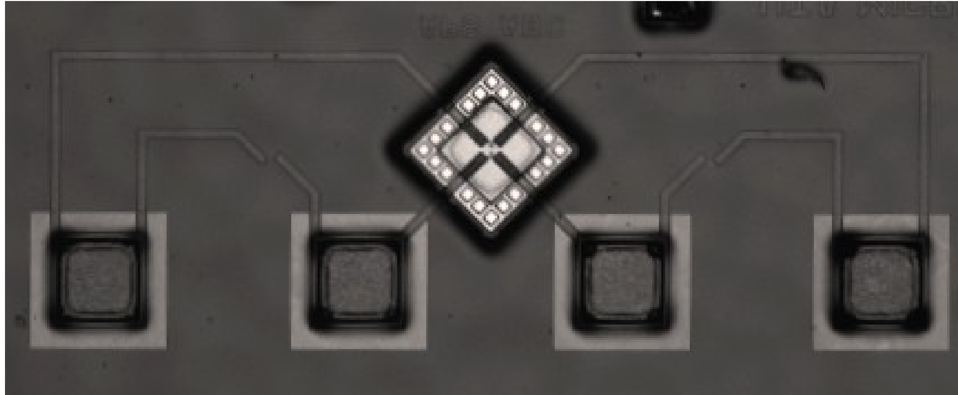

Figure 4-15 Micrograph of the Sensor Taken in Confocal Microscope ©2012 IEEE. Reprinted, with Permission, from MEMS Absolute Pressure Sensors on Flexible Substrate by M. Ahmed, D. P. Butler, Z. Celik-Butler, in IEEE MEMS, 2012 [64]

Figure 4-16 A 2 x 2 cm^2 Piece of Flexible Substrate Containing an Array of 75 Pressure Sensors. ©2012 IEEE. Reprinted, with Permission, from MEMS Absolute Pressure Sensors on Flexible Substrate by M. Ahmed, D. P. Butler, Z. Celik-Butler, in IEEE MEMS, 2012 [64]

4.4 Characterization, Results and Discussion

After fabrication of the devices, the wafer was cut into small pieces to package, wire bond and characterize. The characterizations could be divided into six fold: measuring resistance values of the piezoresistors and response measurement in the probe station, pressure response measurement in load-cell and vacuum chamber and

noise characterization, effect of temperature variation on the offset voltage and simulating effect on reference cavity by bending flexible substrate.

4.4.1 Resistance Measurement and Pressure Sensing with a Probe Station

The absolute pressure sensors were characterized to measure resistance of the each individual piezoresistors. First, resistances values were measured in the procedures as described in section 3.4.1. Similar to the relative pressure sensors, the piezoresistors are termed as active and passive resistors and are connected in a half Wheatstone bridge geometry. The pseudo resistance values for each device were measured from the *I-V* characterization while the actual resistance values were calculated by MATALB [Table 4-1]. The measured *I-V* characteristics of the device AP1D2-2A-ABC-R is shown in Figure 4-17. The resistances varied from 8 kΩ to 12 kΩ across the 4 inch wafer, the variations occurred mainly due to lithographic abnormalities during patterning of the nichrome layer and variation in thickness during deposition in the sputtering tool.

After that, the sensor response due to the full deflection of the membrane was characterized in the probe station as described in the section 3.4.1. The device response measurement in the probe station for the device termed as AP1D2-2A-ABC-R is shown in Figure 4-18. The graph shows change in the output voltage compared to the offset voltage under full deflection of the membrane. From the experimental results it could be observed that due to the variation of the bias voltage the output voltage change from the offset voltage is linear for the applied pressure. This indicates the linear response of the piezoresistor that are connected in a half Wheatstone bridge structure since the change in resistance is related with change in output voltage. This experiments also demonstrates the range of bias voltage that the pressure sensors are applicable is 0.25 V to 2.5 V.

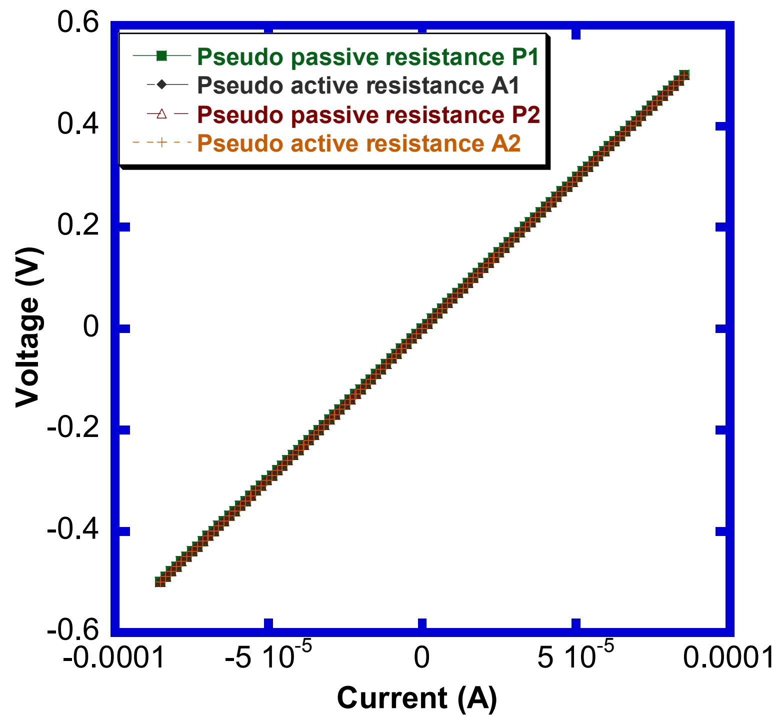

Figure 4-17 Measured *I*-*V* Characteristics for a 424 μm × 424 μm Absolute Pressure Sensor

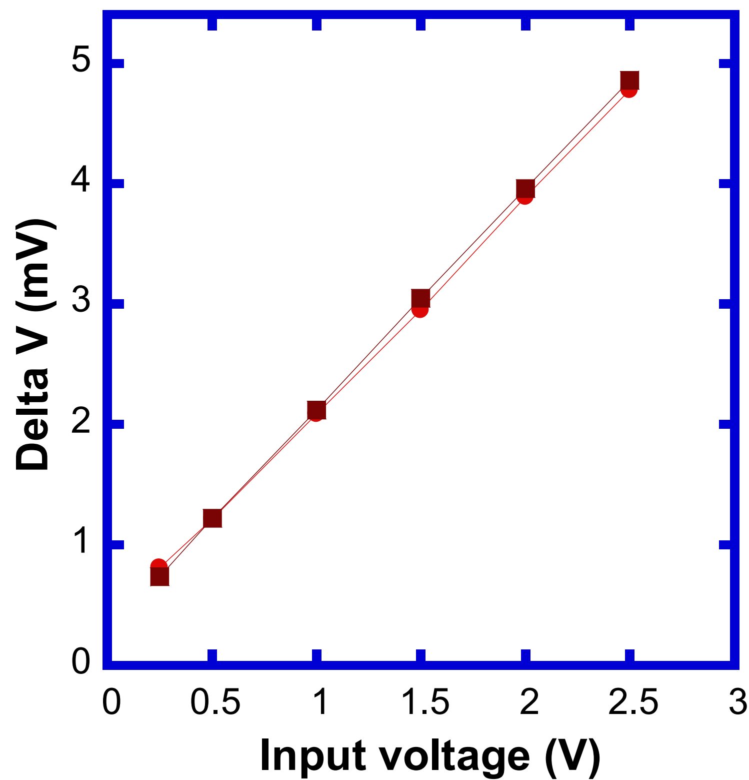

Figure 4-18 Characterized Output Voltage Change as a Function of Input Bias Voltage for Two Different Configurations

4.4.2 Pressure Sensing with a Load Cell

The second characterization setup consisted of the Load cell and same measurement procedures were followed as described in section 3.4.2. The sensor termed as AP1D1-1A-ABCL, characterized for response evaluation under load-cell setup is shown in Figure 4-18. From the graph, it could be observed that due to the applied force (also applied pressure) the output voltage changes linearly from the offset voltage which indicates the linear characteristics of the piezoresistors. The change in output voltages saturated for higher load when the membrane reached bottom of the cavity. The

two curves demonstrated the gradual application (left one) and retraction (right one) of applied force.

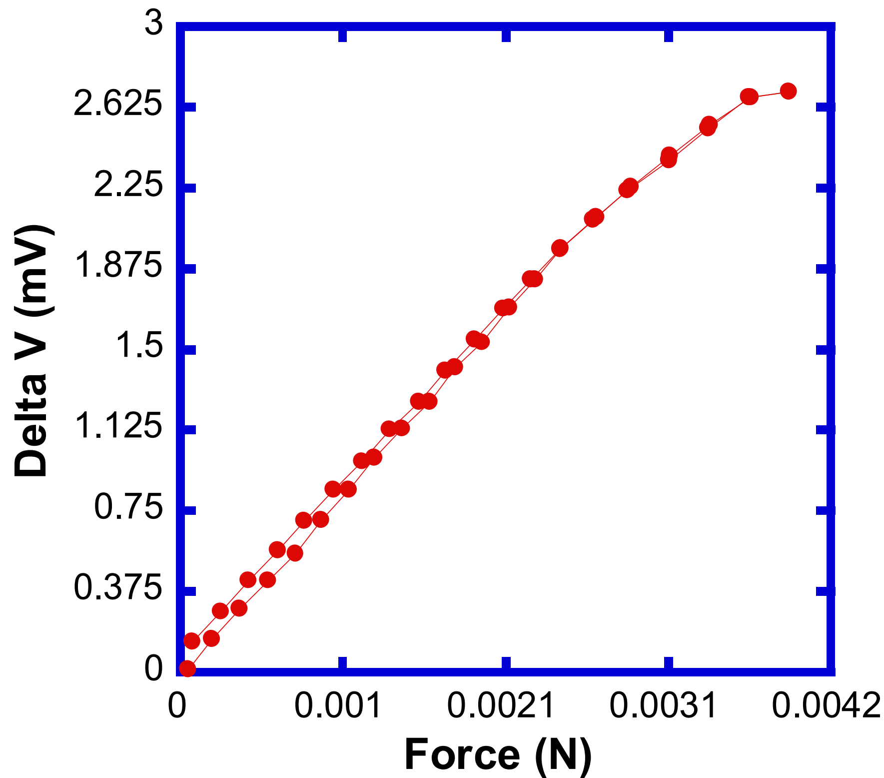

Figure 4-19 Sensor Characterizations under Load-Cell for Gradual Application and Retraction of a Load and the Corresponding Change in Output Voltage. ©2012 IEEE. Reprinted, with Permission, from MEMS Absolute Pressure Sensors on Flexible Substrate by M. Ahmed, D. P. Butler, Z. Celik-Butler, in IEEE MEMS, 2012 [64].

4.4.3 Pressure Sensing inside Vacuum Chamber

In the third response measurement step, the sensor was placed inside a chamber and a Welch duo-seal vacuum pump was utilized to lower the pressure inside the chamber [Figure 4-20]. A Varian 715 vacuum pressure gauge was used to continuously observe the chamber pressure. Once the chamber pressure reduced to 100 mTorr, the pump was turned off. The pressure inside the chamber slowly raised from 100

mTorr due to a leak in the system and hence the applied pressure on the membrane too. The Wheatstone bridge structure was connected to 1 V input bias voltage and output ports were connected voltmeter to measure the voltage. Due to the increment of the chamber pressure, the change in output voltage was measured by a Keithly 2182A Nanovoltmeter. The characterization was done by switching input and output ports to utilize two different configurations.

The device response in the vacuum chamber for the device termed as AP1D2-2A-ABC-R is shown in Figure 4-21. The graph is showing the linear change in output voltage from the offset voltage with the increase of pressure in the range of 100 mTorr to 760 Torr. The application of pressure sensor below the atmospheric pressure demonstrates the integrity of the absolute cavity and the linearity of the graph indicates the reliability of the sensors' response for a short range to long range of applied pressure.

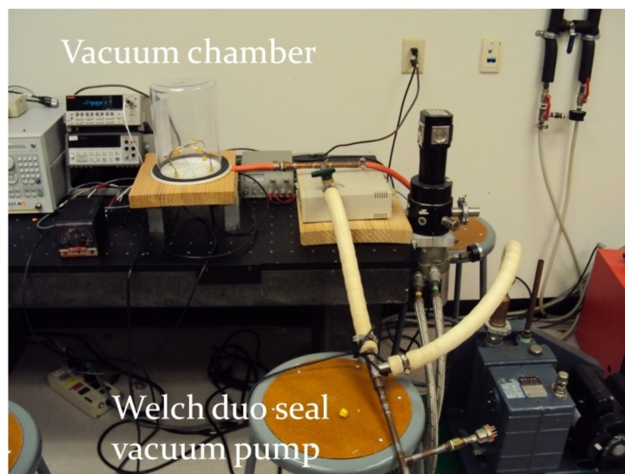

Figure 4-20 Set-up for Characterizing Absolute Pressure Sensor in Vacuum Chamber

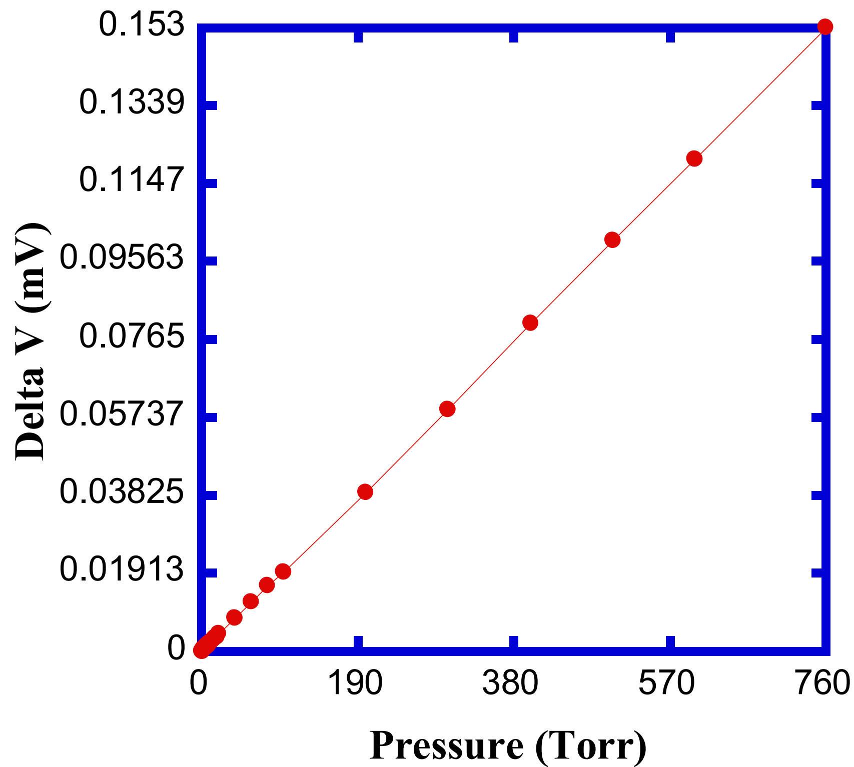

Figure 4-21 Characterization of the Sensor inside Vacuum Chamber. The Graph is Showing the Change Output Voltage from Offset Voltage with the Change in Applied Pressure from 100 mTorr to 760 Torr.

One of the sensor was then characterized for evaluating the repeatability as described above (sensor characterization) for 10 cycles inside the vacuum chamber. The pressure inside the chamber was varied from 100 mTorr to 760 Torr and change in output voltage across the sensor was measured. After each cycle there was a pause of 15 mins before next cycle. The output voltage change with respect to the change in pressure is shown in Figure 4-22. The output voltage at a certain pressure showed approximately similar values for all 10 cycles. The output voltage change (ΔV) was calculated from by subtracting the output voltage at a particular pressure from the offset

voltage at 100 mTorr pressure. Then the standard deviation and average ΔV of each cycle were calculated which were used to evaluate the relative error of the measurements. The average of the relative error from 0.1 to 760 Torr pressure gave average relative error. The average relative error of the voltage variation for 10 cycles was calculated to be 0.074% from the characterization results.

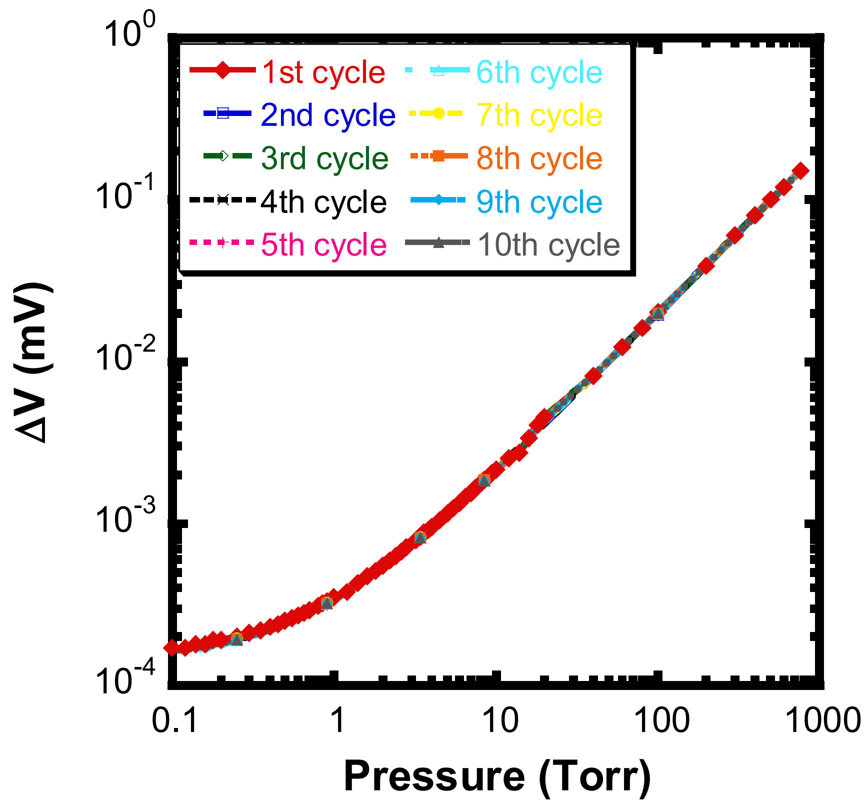

Figure 4-22 Vacuum Chamber Measurement for One of the Absolute Pressure Sensors, Showing Output Voltage Variation with Chamber Pressure for a 424 μm × 424 μm Device for 10 Cycles.

4.4.4 Gauge Factor Calculation

The gauge factor for nichrome and Young's modulus was calculated as described in section 3.4.4. The average value of the gauge factor for nichrome was found to be 1.95 and the Young's modulus of the rf sputtered Al_2O_3 was calculated to be 406.67 MPa by Coventorware™ software.

4.4.5 Noise Characterization

The 1/f noise and Johnson noise characteristics of the sensors were measured by current-biasing the device in the same way as described in section 3.4.4. The net 1/f noise voltage PSD for the sensor termed as AP2D3-1B-FG are plotted in Figure 4-23 for two different configurations. The device was biased at 1 V. From the noise spectra, the average $K_{1/f}$ value of calculated to be1.98 × 10^{-11} for this particular sensor. After that, the input bias voltage was varied from 0.25 V to 1.25 V and the net 1/f-noise spectra was recorded for six different absolute pressure sensors. The purpose of the experiment was to check the dependence of the 1/f noise on the input bias voltage. From the noise voltage PSD at 10 Hz as shown in Figure 4-24 demonstrated a quadratic variation on bias voltage. For the six absolute pressure sensors that were characterized, the average value of 1/f noise coefficient $K_{1/f}$ was evaluated to be 4.64 × 10^{-11}.

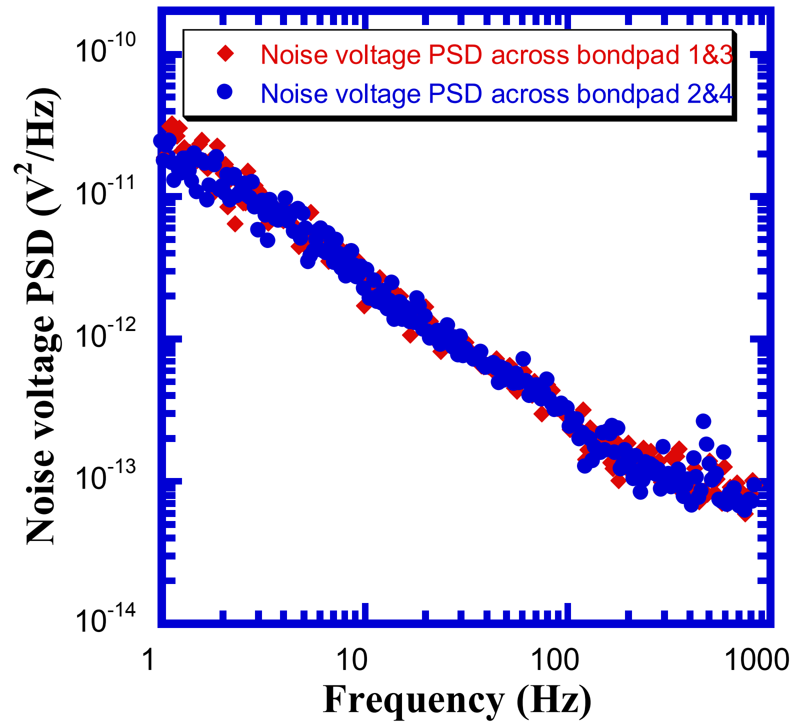

Figure 4-23 Voltage Noise Power Spectral Density for Net 1/F-Noise for the Absolute Pressure Sensors or Two Different Configurations

4.4.6 Figures of Merit

The sensitivity of the absolute pressure sensors was calculated as described at 4.4.6 and found to vary from 1.06 nV/Pa to 1.51 nV/Pa with an average sensitivity of 1.25 nV/Pa. The noise equivalent pressure (*NEPr)* of the absolute pressure sensors was calculated to vary from 3.5 kPa to 15 kPa with an average value of 7.8 kPa in the 1/f-noise regime assuming a noise bandwidth from 1-8 Hz. Table 4-3 compares the sensitivity of the pressure sensors with some other absolute pressure sensors.

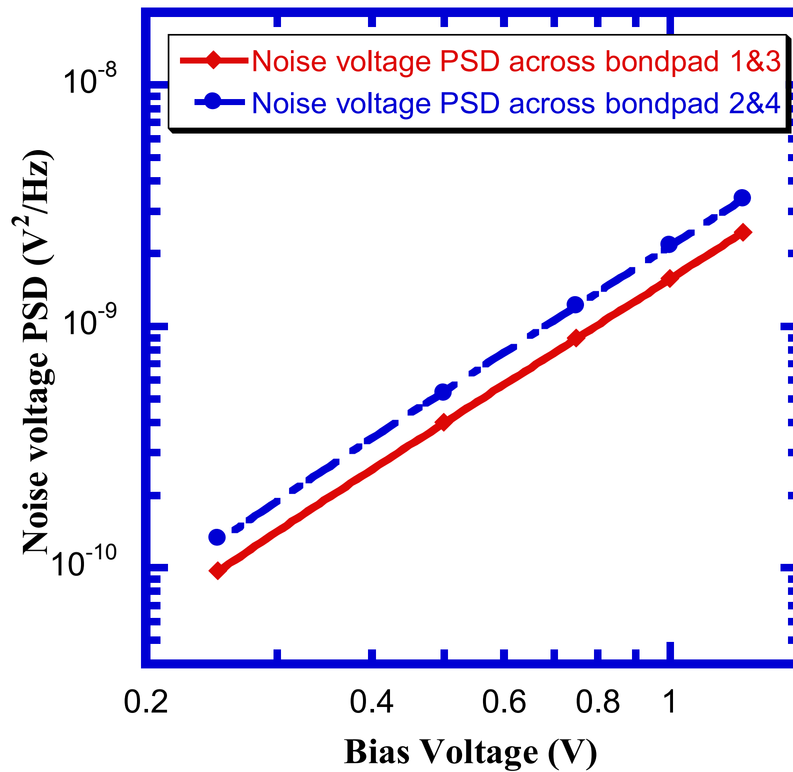

Figure 4-24 Variation of 1/F Noise Voltage Power Spectral Density (PSD) at 10 Hz due to the Variation of the Input Bias Voltage

4.4.6.1 Thermomechanical Noise

Since absolute pressure sensors are mechanical structures, they possess thermal-mechanical noise. Thermomechanical noise of the absolute pressure sensors was calculated as described in the process in section 3.4.5.1. The thermal-mechanical noise power of the absolute pressure sensors was calculated with the help of finite element analysis in CoventorWare™ software and DampingMM module and “squeeze or slide film flow” for argon gas was utilized. The average value of thermal-mechanical noise pressure was calculated to be 1.1×10^{-9} Pa for the six absolute pressure sensors which is much less than the 1/f noise and Johnson noise limited value.

Table 4-1 Summary Table Showing Individual Resistances for the Piezoresistors

Device Name	Area of the membrane (µm × µm)	Passive resistor 1 (Ω)	Active resistor 1 (Ω)	Passive resistor 2 (Ω)	Active resistor 2 (Ω)
AP1D1-1A-ABCL	424 × 424	9345.9	9639.3	11642.3	9185.2
AP1D2-2A-ABCR	424 × 424	10853.2	12275.8	11555.2	12299.1
AP2D3-1B-FG	390 × 390	9408.9	10505.7	10508.8	10481.7
AP2D4-4A-H	381 × 381	11969.3	12207.4	10734.9	12712.6
AP3D5-1A-D	381 × 381	8299.8	8686.3	8182.3	8757.9
AP3D6-3A-E	381 × 381	7906.8	8072.4	7947.4	8148.3

Table 4-2 Measured Response, Noise and Figures of Merit of the Absolute Pressure Sensors at Room Temperature

Device name	Avg. ΔV for 1 V input (full deflection) [mV]	Avg. maximum pressure applied by load cell [MPa]	Avg. ΔR/R (%)	Young modulus for Al_2O_3 [GPa]	Calculated strain under maximum load	Gauge factor	$K_{1/f}$ Hooge coefficient	Sensitivity from vacuum chamber [nV/Pa]	Noise Voltage in 1-10 Hz bandwidth (1/f-noise limit) [ΔV]	*NEPr* (1/f-noise limit) [kPa]	*NEPr* For Johnson noise limit [Pa]
AP1D1-1A-ABC-L	2.79	8.4	7.65	410	0.0311	1.90	1.18×10^{-11}	1.50	5.2	3.5	8.5
AP1D2-2A-ABC-R	2.11	8.3	6.66	408.5	0.0314	2.03	1.59×10^{-11}	1.51	6.06	4.0	9.3
AP2D3-1B-FG	1.82	9.9	7.32	405	0.03097	1.93	1.98×10^{-11}	1.06	6.76	6.4	12.3
AP2D4-4A-H	1.34	9.7	7.28	402	0.0307	1.87	6.91×10^{-11}	1.06	12.6	11.9	13.3
AP3D5-1A-D	2.33	10.3	7.48	406.5	0.0314	1.93	1.40×10^{-10}	1.20	18.0	15.0	9.9
AP3D6-3A-E	1.20	10.4	7.81	408	0.0312	2.04	2.16×10^{-11}	1.20	7.04	5.9	9.6

Table 4-3 Comparison of Sensitivity of Pressure Sensors

Reference	Minimum pressure measured	Sensitivity (nV/Pa)
Current work	100 mTorr	1.25
Wang *et al.* [54]	760 Torr	1.13×10^6
Esashi et al. [65]	760 Torr	97.5
Esashi et al. [61]	2.5 mTorr	100-200

4.4.7 Effect of Temperature Variation on the Cavity

The performance of the absolute pressure sensors relies on the integrity of the encapsulated cavity. Any change in the environment's temperature will cause a change in volume of the cavity. The proposed operating temperature of the absolute pressure sensor is 25 ºC to 80 ºC. Since the sensor was sealed at a 5 mTorr Ar gas pressure, that amount of change in temperature (25 ºC to 80 ºC) will cause the pressure inside the cavity to changes from 5 mTorr to 5.92 mTorr, taking into consideration that the volume of the cavity will not changed. In order to characterize, the change in the output voltage with temperature was measured over the range of 25 ^{o}C to 80 ^{o}C with a 1 V bias applied. In Figure 4-25, the change in output voltage due to temperature variation has been demonstrated for two different configurations by interchanging input and output ports. It has been observed that the change is minimum due to the change in temperature which reflected insignificant change in pressure inside the cavity. Also, the Wheatstone bridge geometry served to reduce the change in output voltage and thus the effect of temperature change.

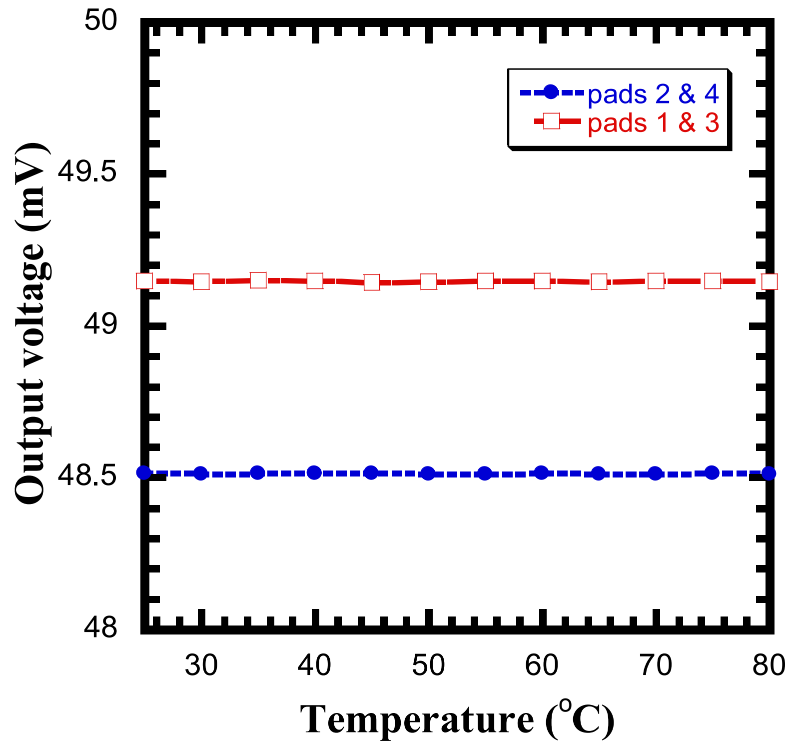

Figure 4-25 Output Offset Voltage as a Function of Temperature Variation for Two Different Configurations.

4.4.8 Effect of Bending of the Flexible Substrate

The absolute pressure sensors were designed to operate on the curved surface and fabricated on flexible substrate. Due to the curvature of the surface the volume of the cavity undergoes a change and hence it affects the reference pressure. The effect of the bending the flexible substrate and the ultimate change in strain of the sensors was evaluated by CoventorWare™ simulations. In the simulation, the change in the volume of the cavity was measured for bending flexible to roll around a cylinder with a 1 cm radius of curvature at atmosphere. The volume was changed to 5.49×10^{-13} m^3 from 6.03×10^{-13} m^3 (without any bending), which causes a change of reference pressure around 0.47 mTorr. The equivalent change in the strain of the piezoresistor was found to be to be 3 ×

10^{-6} which is negligible compared with the average strain of the piezoresistors. From this simulation, it could be concluded that bending the flexible substrate for small radius of curvature does not impact its performance.

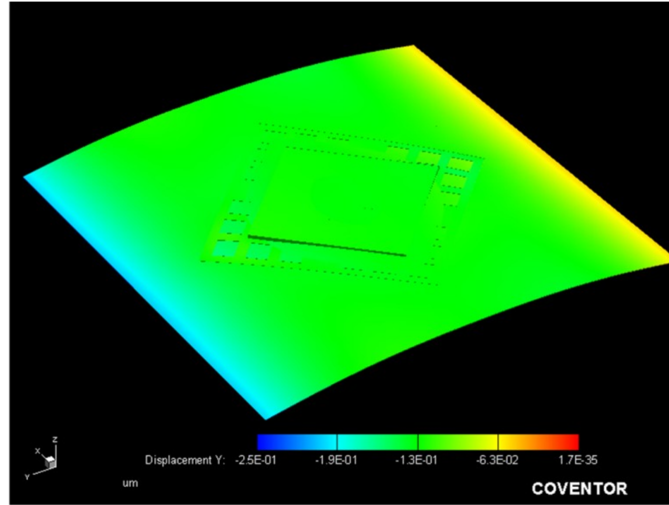

Figure 4-26 CoventorWare™ Simulation of Bending the Flexible Substrate around a Cylinder with Radius of Curvature of 1 cm for 424 μm × 424 μm Device in Order to Calculate the Change in Volume of the Cavity and Hence the Reference Pressure.

4.5 Conclusions

In this chapter, the fabrication and characterization of the absolute pressure sensor on flexible polyimide substrate has been described. The sensors were characterized for evaluating resistance value for the nichrome piezoresistors, response measurement on the probe station, on the load-cell and inside vacuum chamber. The noise exhibited by the sensors was also evaluated and thermomechanical noise of the sensors was calculated using CoventorWare™ software. The figures of merit such as the noise equivalent pressure and the responsivity of the sensors were calculated from the results of the characterized sensors. Finally, the sensors were characterized for the

analyzing the effect of temperature variation and bending the flexible substrate on the reference pressure and the sensors performance.

Chapter 5

Deposition and Characterization of Pyroelectric Lead Titanate Thin Films

5.1 Introduction

Lead zirconium titanate (PZT) and lead calcium titanate (PCT) offer high pyroelectric, piezoelectric, and ferroelectric properties which made them suitable candidate for a number of applications such as non-volatile memory, dynamic random access memory, sensors, transducers , accelerometers and other applications [66].Thin film applications of lead titanate offer it as an excellent candidate for MEMS devices such as pyroelectric infrared detectors which can enable camera systems to be developed with reduced size, weight, and power consumption. The objective of this research is to investigate the pulsed laser deposition technique and characterize lead titanate thin films in order to apply them to uncooled pyroelectric detectors that utilize a nanometer size mesh or truss to support the micromachined detector.

5.2 Background

Pyroelectric materials, i.e. PZT, PCT are inherently polarized, even without presence of an electric field. This spontaneous polarization appears at temperatures less than Curie temperature for a particular material. When the polarization (P) is dependent on the temperature, the material is pyroelectric. When incident radiation heats up a detector, the crystal lattice expands and changes the dielectric constant and alters the polarization of the material. Absorption of heat by the crystal results in a motion of bound positive ions, producing a charge on the electrodes mounted on the pyroelectric material, causing current to flow in an external circuit if electrodes are placed on the crystal face perpendicular to the polarization axis. The structure can also be fabricated as a capacitor filled with a ferroelectric material. Any change in polarization results in an output voltage

across the capacitor. Ferroelectric crystals cause a change in spontaneous polarization due to the temperature variation [67].

The rate of change of electric polarization due to the variation of temperature is defined as pyroelectric coefficient, *p* [67]:

$$p \equiv \frac{\partial P}{\partial T} \tag{5.1}$$

The pyroelectric coefficient has units of coulomb $cm^{-2}K^{-1}$ and is a function of temperature. A high pyroelectric coefficient of material is desirable for infrared detector applications.

As the temperature of the material changes with the incident radiation, a pyroelectric current (*i*) flows and can be calculated from pyroelectric coefficient using the following equation [67]:

$$i = p\frac{dT}{dt}A_e \tag{5.2}$$

where, A_e is the area of electrode on the detector.

The deposition of high quality modified lead titanate ensures high pyroelectric coefficient [68]. The lead zirconium titanate has two phases: intermediate pyrochlore phase and the ferroelectric perovskite phase. There are various conditions such as deposition technique, process temperature, ambient pressure and substrate that affect the formation of the perovskite phase [68, 69, 70]. There are different deposition techniques available to grow the PZT and PCT thin films. Pulsed laser deposition has been utilized to deposit high-quality thin films of lead titanate [71, 72].

In this chapter, the deposition of modified lead zirconium titanate ($PbZr_{0.4}Ti_{0.6}O_3$) (PZT) and lead calcium titanate ($Pb_{0.7}Ca_{0.3}Ti0_3$) (PCT) at various temperatures by pulsed laser deposition has been demonstrated. The polycrystalline thin films were used to

fabricate capacitors in order to determine the dielectric properties and measure the pyroelectric current based on the various growth conditions. The thin films were poled to increase the pyroelectric current and coefficient. The repeatability of the behavior was also measured for one PZT and one PCT perovskite thin film.

5.3 Deposition of Modified Lead Titanate Thin Films and Capacitor Fabrication

The sample preparation of the modified lead titanate thin films had two steps: the first step was to deposit the lead titanate thin film and characterize the crystal structure through x-ray diffraction and the next step was to fabricate capacitors using the lead titanate thin films to determine dielectric and pyroelectric properties. A <100> p type silicon wafer was used. First, a Si_3N_4 passivation layer was deposited on top of the wafer with the AJA rf-sputtering. The thickness of this layer was 400-nm. Then, a Ti adhesion layer was deposited on Si_3N_4 prior to the Au layer. The thickness was 20-nm. After that, the Au bottom electrode was deposited and also promoted the formation of perovskite lead titanate thin films. The 100-nm of Au layer was deposited at 100 W rf power and 10 mTorr of Ar gas environment in the "Homebuilt" sputtering tool. After that, the PZT film was deposited by pulsed laser ablation using a KrF excimer laser with a wavelength of 248 nm, repetition rate 10 Hz and laser pulse energy up to 500 mJ in 200 mTorr of O_2. The temperature of the chamber was varied from 500 ^{o}C to 650 ^{o}C. After deposition of the thin film, annealing was carried out at the same temperature as the deposition temperature while annealing time was varied at 5 mins and 10 mins to form polycrystalline perovskite structure of PZT film. After that the film structure was characterized by x-ray diffraction which will be discussed in the next section. The PZT films, deposited and annealed at various temperatures, were used to make capacitors. At the final stage of the sample preparation, a 100-nm-thick gold electrode was deposited and patterned by photolithography and the lift-off process. In order to deposit the PCT

films, pulsed laser ablation was carried out using the same KrF excimer laser, repetition rate 10 Hz, and 200 mTorr of O_2 environment. The energy of the excimer laser pulse was varied from 125 to 175 mJ and annealed at same temperature as the deposition but varying the annealing time at 10, 15 and 20 min to form a polycrystalline perovskite structure in the PCT film. After x-ray diffraction, the PCT films that were deposited at 550 ^{o}C but different laser energies were used to fabricate capacitors. The cross section of the fabricated capacitor is shown in Figure 5-1 and Confocal and Nomarski microscope micrographs of the top view of the capacitors are shown in Figure 5-2.The SEM micrograph of the deposited PZT film at 650 ^{o}C and annealed for 10 min at 200 mTorr O_2 gas environment is shown in Figure 5-3 and the SEM of the deposited PCT film at 550 ^{o}C and annealed for 10 min at 200 mTorr O_2 gas environment is shown in Figure 5-4.

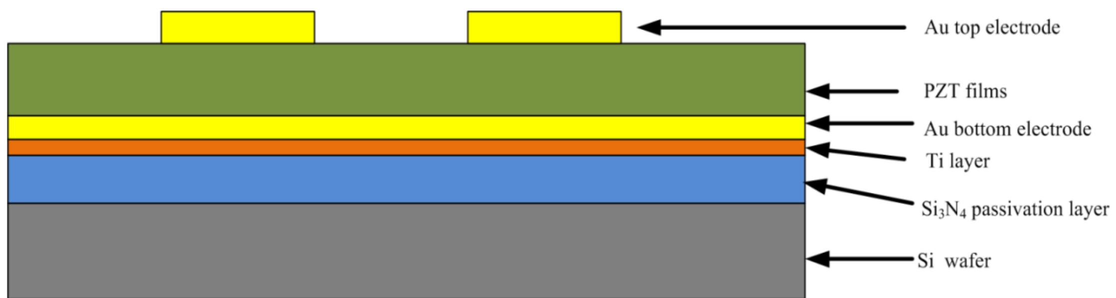

Figure 5-1 Cross-Sectional View of the Fabricated Capacitor Using Perovskite PZT Thin Films

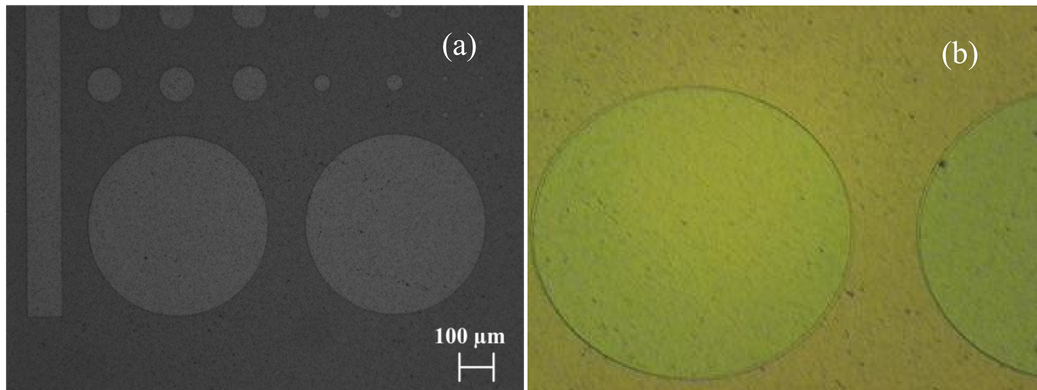

Figure 5-2 (A) Confocal Microscope Micrograph (B) Nomarski Microscope Image of the Top View of the Capacitor

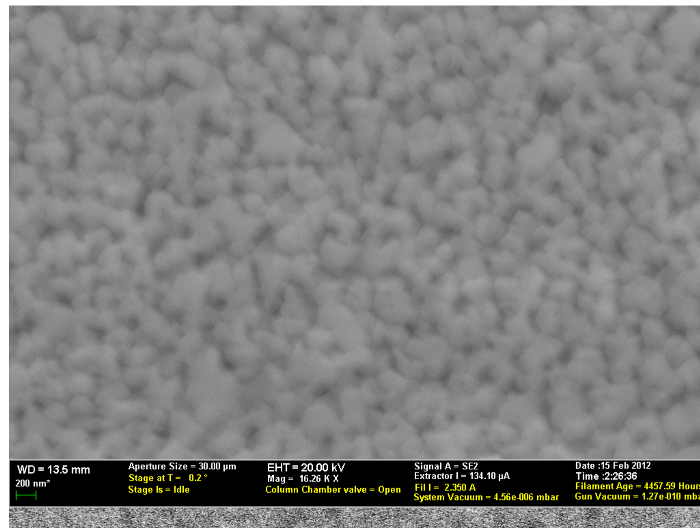

Figure 5-3 SEM Micrograph of the Deposited PZT Film

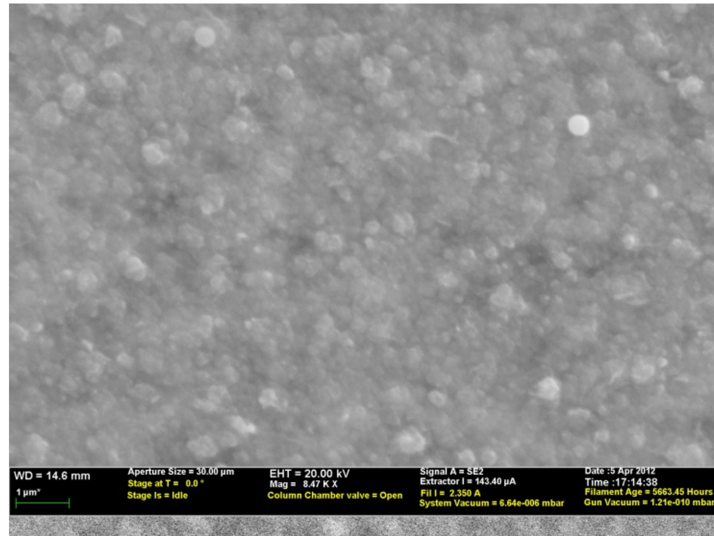

Figure 5-4 SEM Micrograph of the Deposited PCT Film

5.4 Characterization

After deposition of the modified lead titanate thin films, the x-ray diffraction of the samples was done in a Siemens D500 powder diffractometer. The diffractometer uses a Cu-Target to produce x-rays at 1.54 Å. The rate of scan is determined by the step time and the dwell time. Here the step time was set to 0.01 seconds and the dwell time was set to 0.4 seconds. The scan was carried out from 20.0° to 60.0° which is termed as the scan range.

In order to determine the variation of dielectric constant, the capacitance versus temperature characteristics were measured by placing the capacitor on a stage of a shielded 8060 series MicroManipulator probe station. The temperature of the capacitor was varied from 30 °C to 80 °C in 5 °C intervals which were controlled by the micromanipulator probe station's heated chuck. At each interval, the capacitance and corresponding loss tangent was measured by using a HP 4284A precision LCR meter. For this measurement, 200 mV rms ac voltage at 1 kHz was set for the LCR meter. The

capacitors that were fabricated with PZT and PCT films deposited at different temperature were characterized by this procedure.

The characterization for determining the pyroelectric current and pyroelectric coefficients of PZT and PCT films, deposited at different conditions, were done in two steps. In the first step, the capacitor (diameter of 500 μm) was placed on a stage of a shielded 8060 series Micromanipulator probe station. Then, an 11.2 MΩ metal film resistor was connected in parallel with the capacitor. The temperature of the capacitor was varied from 30°C to 80°C by the shielded probe station's heated chuck and the corresponding output voltage was measured by Agilent 34401A multimeter at a regular temperature interval. The time that was required to reach at a certain temperature was also recorded. The pyroelectric current was calculated from the measured output voltage.

In the second stage of characterization, the capacitors were poled and the capacitors were tested again through the same process. Poling helps to align the ferroelectric domains by applying electric field across the material. The poling was done by applying a dc bias voltage across a series connection of capacitor and resistance of 103 MΩ. The resistor was used to limit the current into the capacitor. The dc poling voltage was changed to determine dielectric break down voltage of the thin films as well as to optimize poling effect on the thin films. The poling was accomplished at 150 °C while placing the capacitor fixed on the probe station's chuck. In this stage of characterization, the capacitors used had 100-μm-diameter.

5.5 Results and Discussions

5.5.1 X-ray Diffraction of the PCT and PZT Thin Films on Gold

The x-ray diffraction of PZT film that was deposited at 650 ^{o}C temperature is shown in Figure 5-5. The diffraction result showed peaks at different scanning angles,

which mainly appeared due to polycrystalline nature of the film. It has been observed that there was a peak at 21° which corresponds to <100> crystal orientation of the perovskite peaks. There are peaks between 25° to 30° which correspond to the crystal orientation of the pyrochlore structure and hexagonal $PbO_{1.37}$ and orthorhombic α-PbO_2 scrutinyite. The peak at 30.2^{o} depicts <100> crystal orientation of the perovskite structure of the PZT film. The peak associated with 34.6^{o} indicates <440> crystal orientation of the pyrochlore structure of the PZT film. The peak that appeared at 38.2^{o} corresponds to the <111> crystal orientation of the perovskite of the PZT film and also for gold film which was used as substrate. The peak that appeared at 44.2^{o} (not sharp and distinct) corresponds to the <200> crystal orientation of the perovskite PZT film as well as the gold film. The peak that appeared at 50.56^{o} (not sharp and distinct) indicates the <501> crystal orientation of the hexagonal $PbO_{1.37}$ structure. There could be another pyrochlore phase of PZT film's peak that could appear near 49° but was not observed in this case. The peak that appeared at 58.6^{o} (not sharp and distinct) indicates the <622> crystal orientation of the pyrochlore structure of the PZT film [69]. The perovskite structure of the PZT showed higher pyroelectric coefficient than pyrochlore structure (will be discussed in later sections). So the purpose of the x-ray diffraction was to search for the perovskite structure's peaks or perovskite peaks on the grown PZT film.

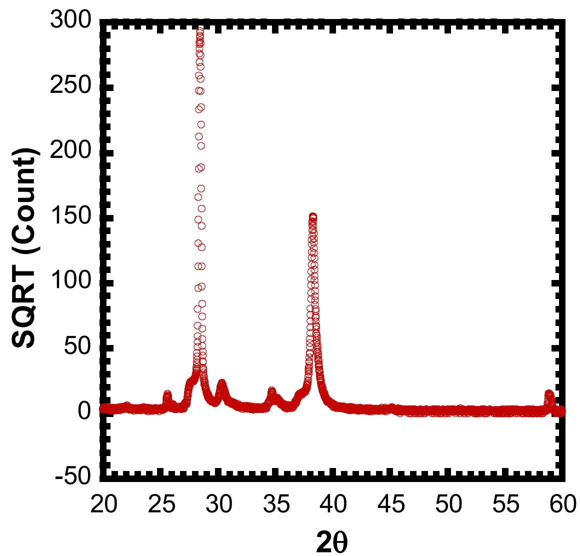

Figure 5-5 X-ray Diffraction of the PZT Film, Deposited at 650 ^{o}C Temperature

The x-ray diffraction of PZT film, deposited at 650 ^{o}C and annealed for 5 mins in 200 mTorr of O_2 gas ambient at 650 ^{o}C temperature is shown in Figure 5-6. The graph shows those peaks that are associated with perovskite structure of the PZT films. But only one peak that was appeared at 34.6^{o} related to the <440> crystal orientation of the pyrochlore structure of the PZT film. The broader peak indicates smaller grain size of the grown film.

Figure 5-7 shows the x-ray diffraction of PZT film that was deposited at 650 ^{o}C and annealed for 10 mins in 200 mTorr of O_2 gas ambient at 650 ^{o}C temperature. From the graph, the peaks that are observed, associated with the perovskite phase of the PZT film. But only one peak that corresponds to <440> crystal orientation of the pyrochlore structure of PZT film was appeared at 34.6^{o}. The sharper peak compared with the graph shown in Figure 5-6 depicts bigger grain size of the grown film.

Figure 5-8 shows the x-ray diffraction of PZT film deposited at 650 ^{o}C and annealed for 15 min in 200 mTorr of O_2 gas ambient at 650 ^{o}C temperature. There are

peaks associated with the perovskite and pyrochlore structure of the PZT film and lead oxide. The presence of the pyrochlore peaks and lead oxide peak indicate that the phase transformation from perovskite phase took place due to the longer annealing time.

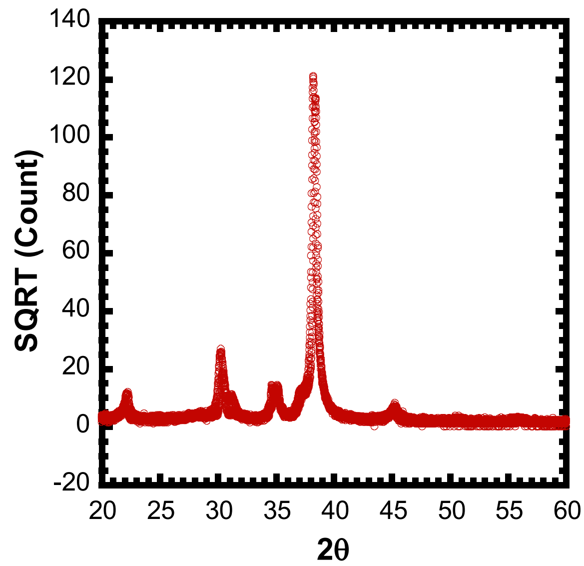

Figure 5-6 X-ray Diffraction of the PZT Film, Deposited at 650 ^{o}C and Annealed for 5 min at 650 ^{o}C

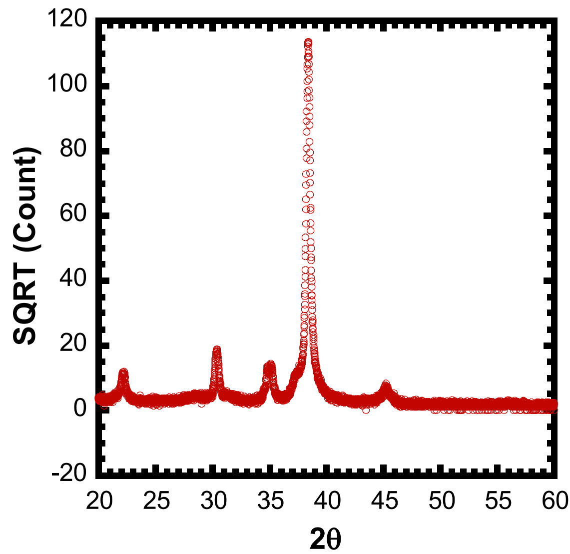

Figure 5-7 X-ray Diffraction of PZT Film, Deposited at 650 ^{o}C and Annealed for 10 min at 650 ^{o}C

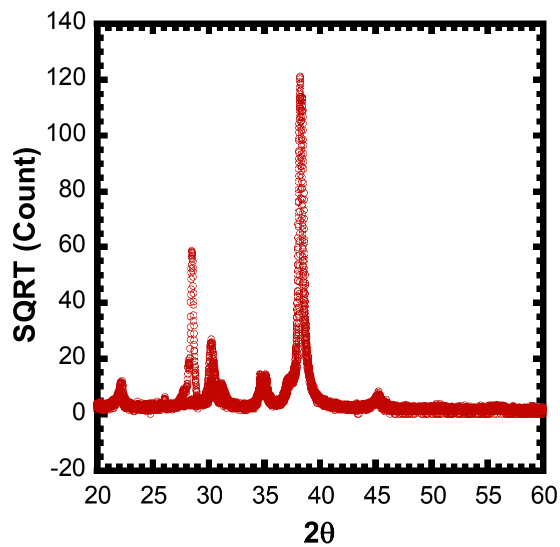

Figure 5-8 X-ray Diffraction of PZT Film, Deposited at 650 ^{o}C and Annealed for 15 min at 650 ^{o}C

The x-ray diffraction of PZT films deposited at 600 ^{o}C temperature and annealed at different time lengths in 200 mTorr of O_2 gas ambient at 600 ^{o}C are shown in Figure 5-

9 to Figure 5-11. From the graphs, there is no distinct peak observed that corresponds to the perovskite structure of the PZT film. Peaks associated with the pyrochlore structure of the PZT film and lead oxide were appeared. Only one peak associated with <110> crystal orientation of the perovskite structure was appeared for the film deposited at 600 ^{o}C and annealed for 10 mins in 200 mTorr of O_2 gas ambient at 600 ^{o}C temperature.

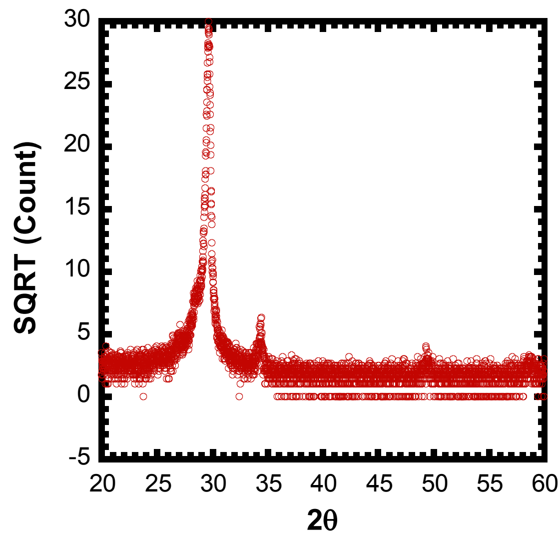

Figure 5-9 X-ray Diffraction of PZT Film Deposited at 600 ^{o}C

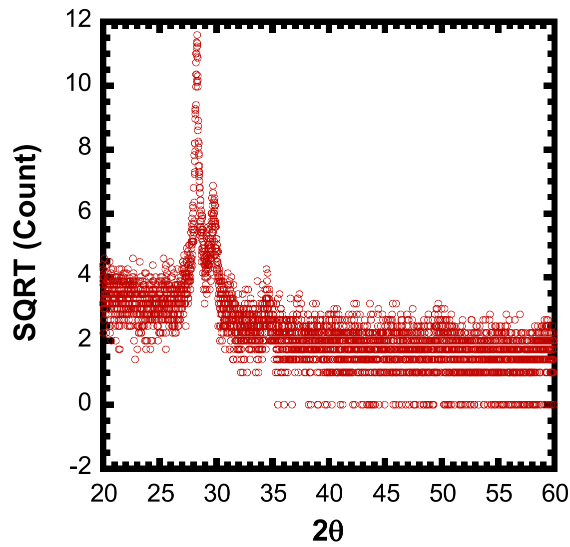

Figure 5-10 X-ray Diffraction of PZT Film, Deposited at 600 ^{o}C and Annealed for 10 min at 600 ^{o}C

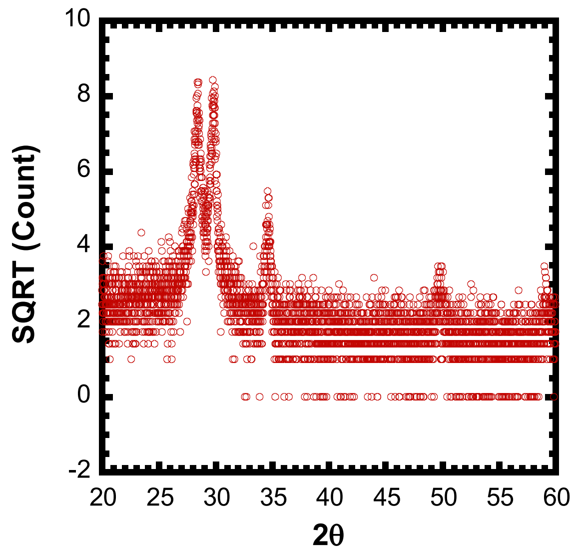

Figure 5-11 X-ray Diffraction of PZT Film, Deposited at 600 ^{o}C and Annealed for 30 min at 600 ^{o}C

The x-ray diffraction of PZT films deposited at 550 ^{o}C temperature and annealed for different time lengths in 200 mTorr of O_2 gas ambient at 550 ^{o}C are shown in Figure 5-

12 to Figure 5-14. There is no distinct peak observed here that corresponds to the perovskite structure of the PZT film, but only peaks associated with the pyrochlore structure of the PZT film and lead oxide were appeared.

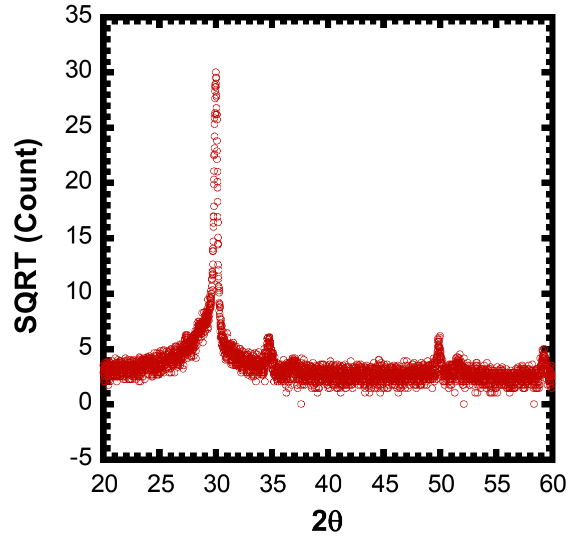

Figure 5-12 X-ray Diffraction of PZT Film Deposited at 550 °C

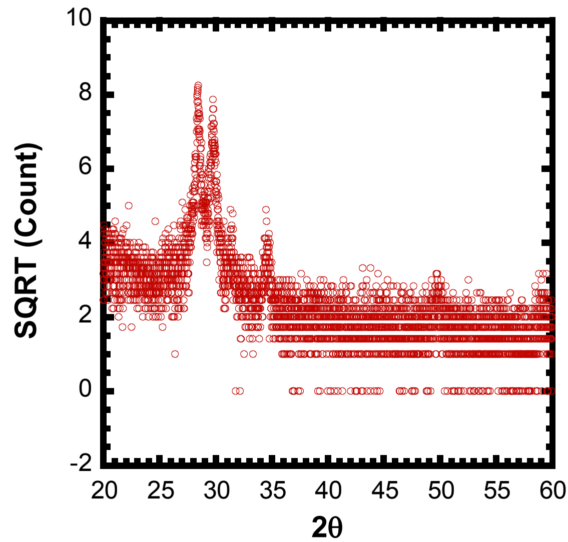

Figure 5-13 X-ray Diffraction of PZT Film, Deposited at 550 °C and Annealed for 10 min at 550 °C

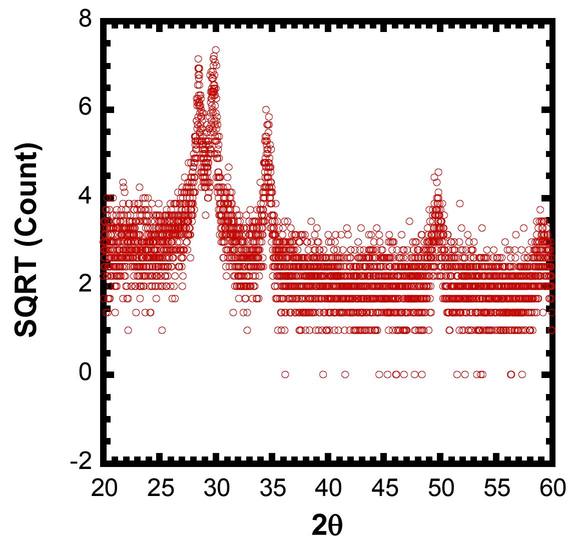

Figure 5-14 X-ray Diffraction of PZT Film, Deposited at 550 ^{o}C and Annealed for 30 min at 550 ^{o}C

The x-ray diffraction of PZT film deposited at 500 ^{o}C temperature and annealed for 10 min in 200 mTorr of O_2 gas environment at 500 ^{o}C are shown in Figure 5-15 to Figure 5-16. They show similar results as the film grown at 600 ^{o}C and 500 ^{o}C.

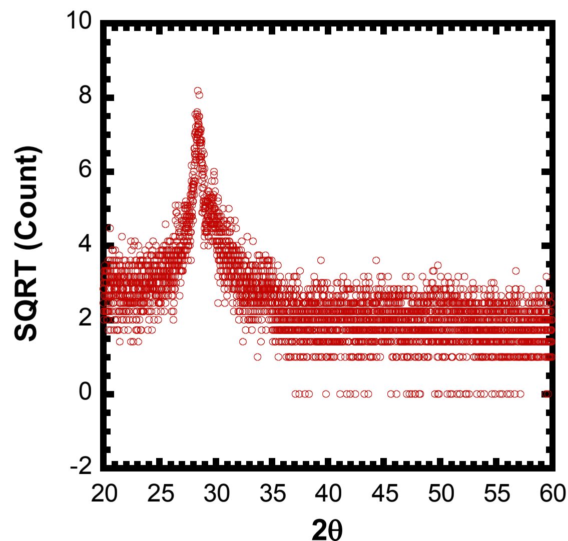

Figure 5-15 X-ray Diffraction of PZT Film Deposited at 500 ^{o}C

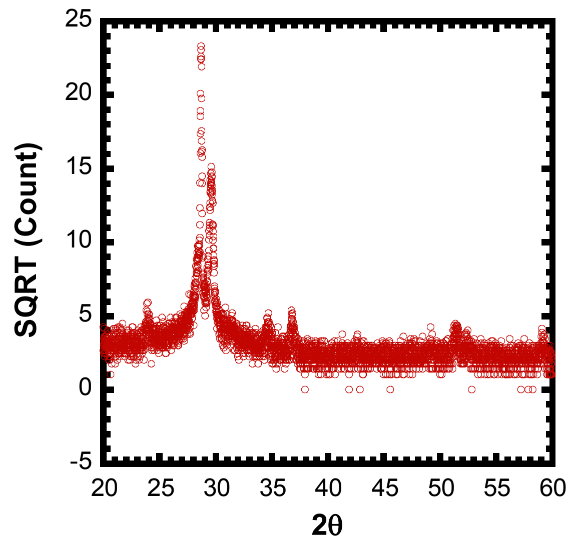

Figure 5-16 X-ray Diffraction of PZT Film, Deposited at 550 °C and Annealed for 10 min at 550 °C

From this section it could be concluded that, the PZT film that was deposited at 650 °C and annealed for 10 min in 200 mTorr of O_2 gas ambient at 650 °C showed different crystal orientations of perovskite structure with bigger grain size compared to other films, thus it's a good condition to deposit this pyroelectric material.

The x-ray diffraction of PCT film deposited at 550 °C, 175mJ laser energy is shown in Figure 5-17. The graph shows peaks which depicts the polycrystalline nature of the grown film. The graph shows peak appeared at 22.84° which indicates<100> crystal orientation of the perovskite structure. The peaks appeared between 25° to 30° scanning angles, correspond to the crystal orientation of the pyrochlore structure and hexagonal $PbO_{1.37}$ and orthorhombic α-PbO_2 scrutinyite. The peak at 32.33° indicates the<100> crystal orientation of the perovskite structure of the PCT film. The peak associated with 34.62° (not sharp and distinct) demonstrates the <440> crystal orientation of the pyrochlore structure of PCT film. The peak that observed at 38.6° indicates the <111> crystal orientation of the perovskite PZT film as well as gold film which was used as

substrate. There are peaks observed at 44.88° and 46.9° which demonstrate the <200> crystal orientation of the perovskite structure of the PCT film. The peak observed at 50.56° (not sharp and distinct) demonstrates the <210> crystal orientation of perovskite structure of the PCT film. There is another peak of pyrochlore structure of the PCT film could appear near 49° but it is absent here. The peak that associated with 57.7° (not sharp and distinct) demonstrates the <211> crystal orientation of the pyrochlore structure of the PCT film [69,73].

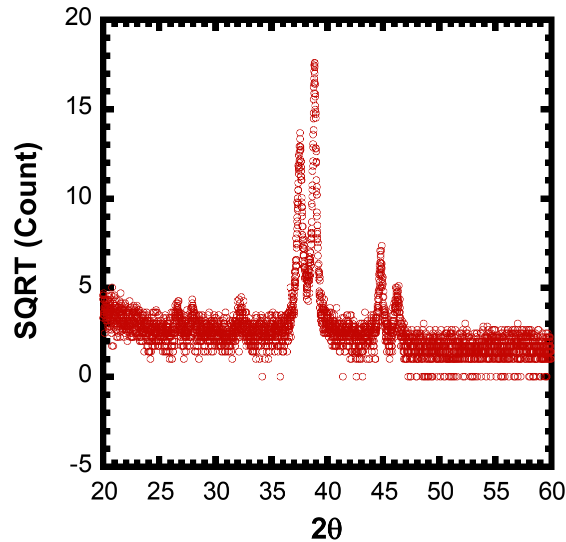

Figure 5-17 X-ray Diffraction of PCT Film, Deposited at 550 °C Temperature

The x-ray diffraction of PCT film deposited at 550 °C, 175 mJ laser energy and annealed for 10 min in 200 mTorr of O_2 gas ambient at 550 °C temperature is shown in Figure 5-18. The graph shows different peaks that reflects the polycrystalline nature of the perovskite structure of the PCT films. But only one peak that appeared at 34.6° that reflects the <440> crystal orientation (not sharp) of the pyrochlore structure of PCT film. The peak broadening indicates small grain size of the grown film in this particular direction.

The x-ray diffraction of the PCT film, deposited at 550 °C, 175 mJ laser energy and annealed for 15 min in 200 mTorr of O_2 gas ambient at 650 °C temperature is shown in Figure 5-19. The graph shows different peaks that reflects the polycrystalline perovskite structure of the PCT film. Compared with the PCT film annealed for 10 mins, it showed peak broadening which means smaller grain size of the grown film.

The x-ray diffraction of PCT film, deposited at 550 °C, 175 mJ laser energy and annealed for 20 min in 200 mTorr of O_2 gas ambient at 550 °C temperature is shown in Figure 5-20. The graph shows peaks that were associated with both the perovskite structure of the PCT films and the pyrochlore structure and lead oxide. The appearance of the pyrochlore peaks and lead oxide indicates that the phase transformation took place for longer annealing time.

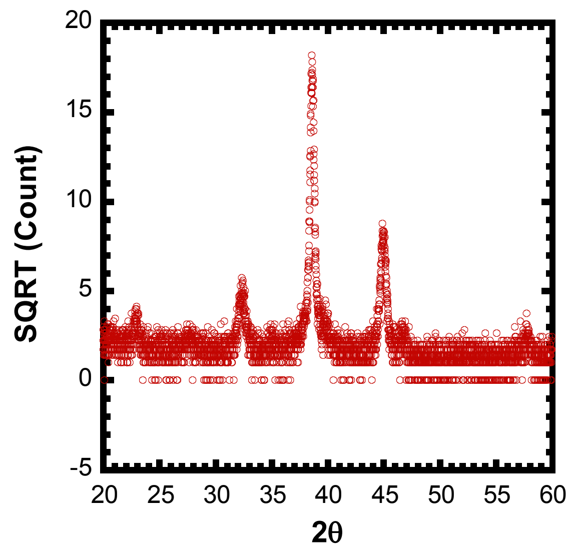

Figure 5-18 X-ray Diffraction of PCT Film, Deposited at 550 °C and Annealed for 10 min at 550 °C

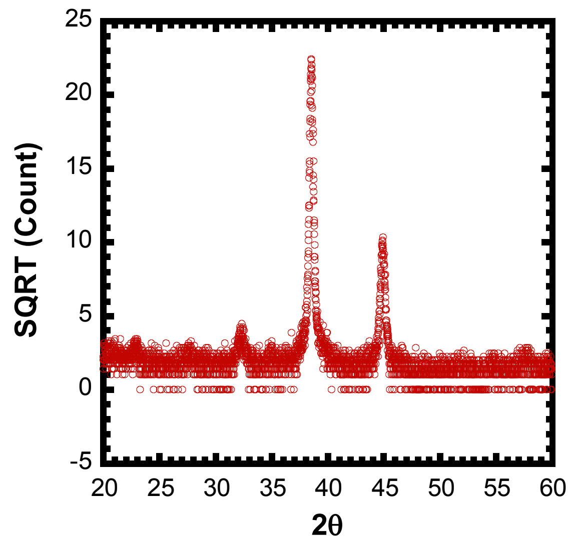

Figure 5-19 X-ray Diffraction of PCT Film, Deposited at 550 °C and Annealed for 15 min at 550 °C

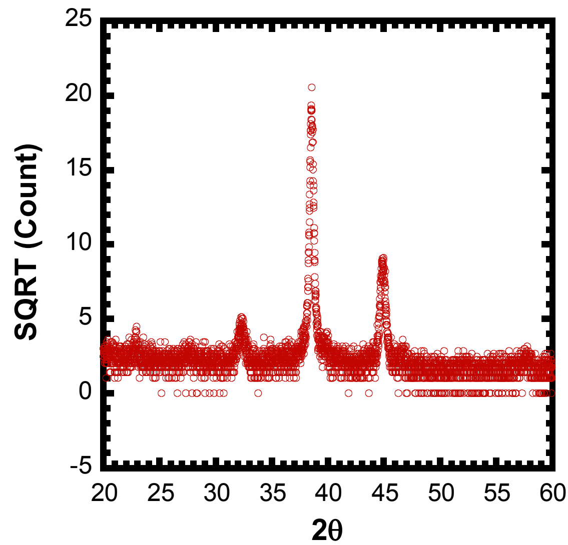

Figure 5-20 X-ray Diffraction of PCT Film Deposited at 550 °C and Annealed for 20 min at 550 °C

The x-ray diffraction of PCT film, deposited at 550 °C, 125 mJ laser energy in 200 mTorr of O_2 gas ambient at 550 °C temperature is shown in Figure 5-21. The graph

shows peaks that correspond to the perovskite structure of the PCT films. The graph also shows the lead oxide peaks which demonstrates laser energy was not sufficient enough to give rise of perovskite PCT structure.

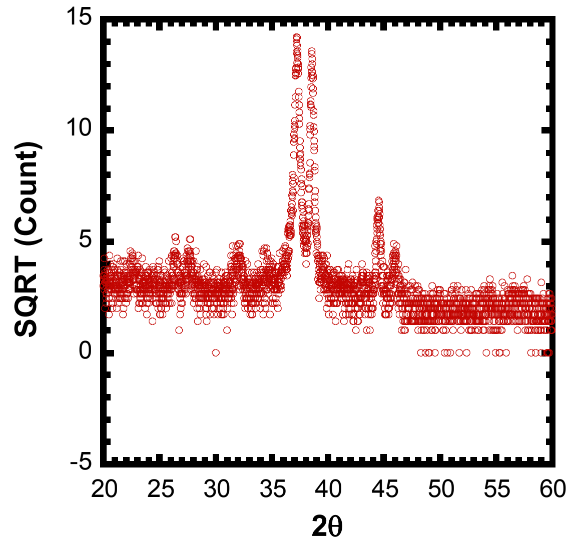

Figure 5-21 X-ray Diffraction of PCT Film, Deposited at 550 °C, 125 mJ Laser Energy

The x-ray diffraction of PCT film, deposited at 550 °C, 125 mJ laser energy and annealed for 10 min in 200 mTorr of O_2 gas ambient at 550 °C temperature is shown in Figure 5-22. The graph shows different peaks which reflect the formation of polycrystalline nature of the perovskite PCT film.

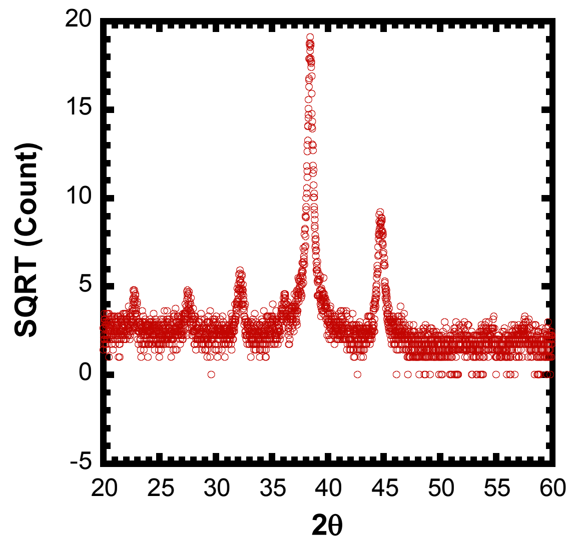

Figure 5-22 X-ray Diffraction of PCT Film, Deposited at 550 °C and Annealed for 10 min at 550 °C, 125 mJ Laser Energy

The x-ray diffraction of PCT film deposited at 550 °C, 125 mJ laser energy and annealed for 15 min in 200 mTorr of O_2 gas ambient at 550 °C temperature is shown in Figure 5-23. The graph also indicates the polycrystalline nature of the perovskite PCT film. The peak broadening demonstrates small grain size of the grown film.

The x-ray diffraction of PCT film, deposited at 550 °C, 125 mJ laser energy and annealed for 20 min in 200 mTorr of O_2 gas ambient at 550 °C temperature is shown in Figure 5-24. The graph shows the peaks that demonstrate the formation of perovskite PCT structure by annealing. The multiple peaks near 25°, 45° position demonstrate the breaking of PCT structure and formation of various oxides.

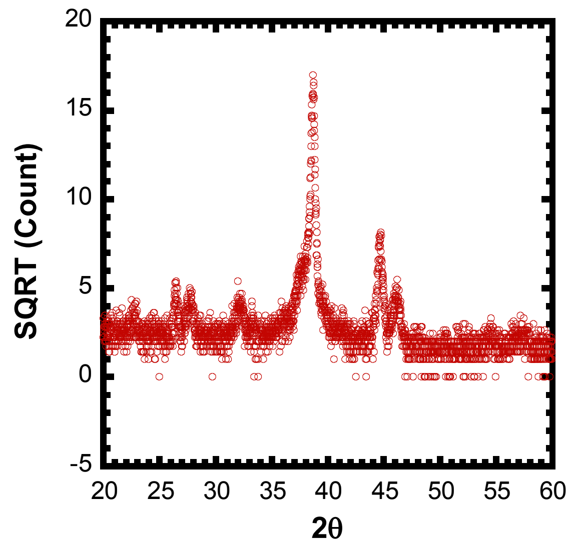

Figure 5-23 X-ray Diffraction of PCT Film, Deposited at 550 °C and Annealed for 15 min at 550 °C, 125 mJ Laser Energy

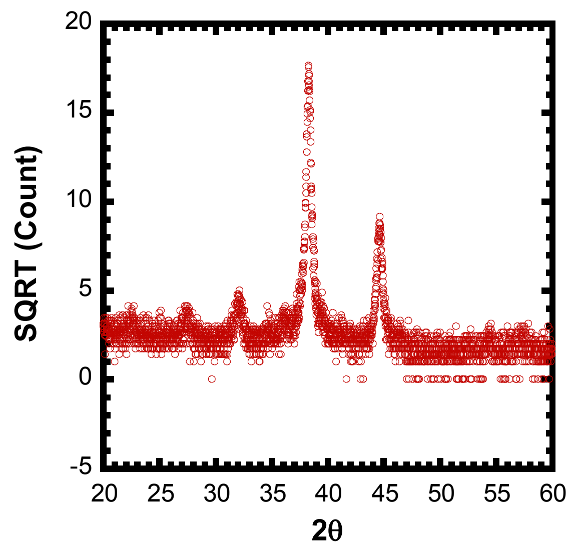

Figure 5-24 X-ray Diffraction of PCT Film, Deposited at 550 °C and Annealed for 10 min at 550 °C, 125 mJ Laser Energy

5.5.2 Dielectric Constant Variation with Temperature

The variation of the dielectric constant with temperature is shown in Figure 5-25 and 5-27. The graphs show approximately linear increment of dielectric constant with temperature variation for both PZT and PCT thin films. From the Figure 5-26 and Figure 5-28, it could be observed that the loss tangent of the PZT and PCT films did not show any significant variation with the change in temperature. Viehland *et al.* [74] also showed increase in dielectric constant of PZT films for different Zr/Ti contents in the temperature range of -50 °C to 150 °C, where the PZT thin films were deposited on gold surface.

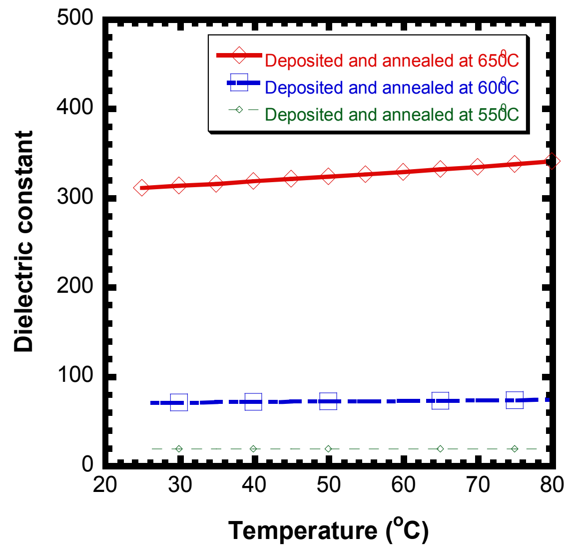

Figure 5-25 Change in Dielectric Constant with Temperature for the PZT Films

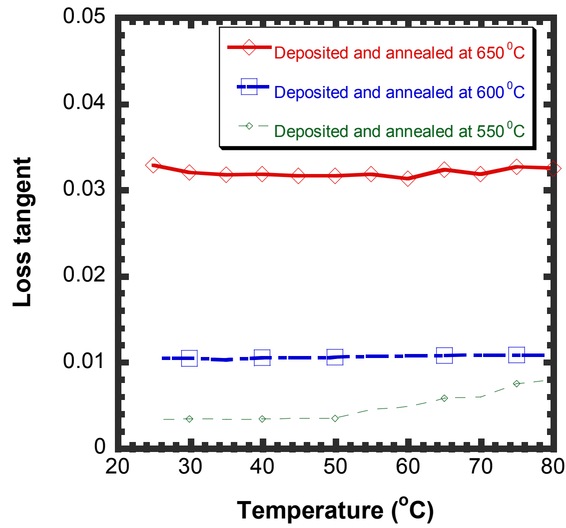

Figure 5-26 Change in Loss Tangent with Temperature for the PZT Films

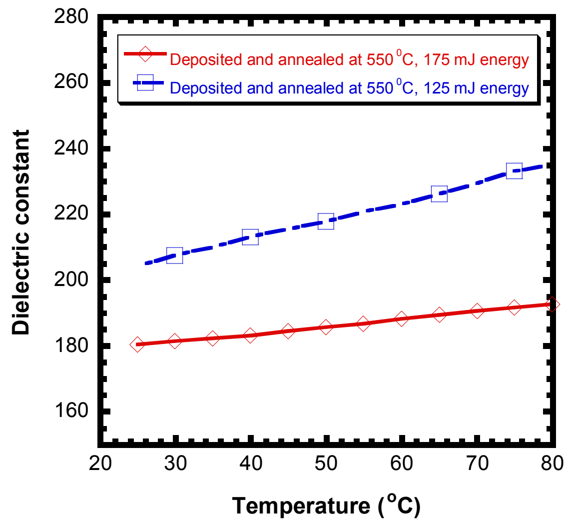

Figure 5-27 Change in Dielectric Constant with Temperature for the PCT Films

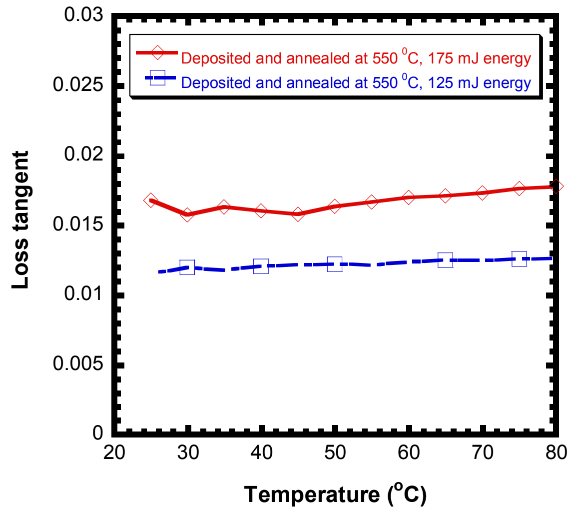

Figure 5-28 Change in Loss Tangent with Temperature for the PCT Films

5.5.3 Pyroelectric Current Characterization

As the procedure discussed in section 5.4, the pyroelectric current for the PZT films was measured which were deposited and annealed at different temperature and it is shown in Figure 5-29. From the graph, it was observed that as the rate of temperature change increased, the value of pyroelectric current also increased until it reached to a maximum value at 80 °C and then it reduced. This characteristic only observed for the PZT film that was deposited and annealed at 650 °C. For the PZT film that was deposited and annealed at 600 °C, the value of current was low and the variation of current was random with the rate of change of temperature which might be caused by the absence of any net polarization. The results also indicated that the presence of pyrochlore structure with perovskite structure does not produce any pyroelectric current. The measurement for current of the PZT film that was deposited and annealed at 550 °C showed random change of current with time which demonstrates pyrochlore structure does not produce any pyroelectric current. The pyroelectric coefficient of the film was calculated by using Equation (5.2). The change in pyroelectric coefficient with temperature is shown in Figure

5-30. The PZT film that was deposited and annealed at 650 °C showed significant pyroelectric coefficients compared to the PZT films that was deposited and annealed at 600 °C. The pyroelectric coefficient of the PZT film that was deposited and annealed at 550 °C is neglected due to the random nature of the current and presence of the pyrochlore structure which truly doesn’t reflect pyroelectricity.

The pyroelectric current for the PCT films which were deposited and annealed at different energy, were also measured and the results are shown in Figure 5-31. From the graph, It could be observed that the PCT film that was deposited and annealed at 550 °C, 175 mJ laser energy demonstrated significant pyroelectric current which increased as the rate of the temperature with time was increased and reached to a maximum value at 80 °C and then fallen down. The pyroelectric current of the PCT film that was deposited and annealed at 550 °C, 125 mJ laser energy showed a low value of pyroelectric current (not significant amount) and random variation of current with the rate of change of temperature (not always) with time which demonstrate presence of pyrochlore structure with perovskite structure affects pyroelectric effect of the PCT films. Again, the pyroelectric coefficient of the film was calculated using Equation (5.2). The change in pyroelectric coefficient with temperature is shown in Figure 5-32. The PCT film that was deposited and annealed at 550 °C, 175 mJ laser energy showed significant pyroelectric coefficients compared to the PCT film that was deposited and annealed at 550 °C, 125 mJ laser energy.

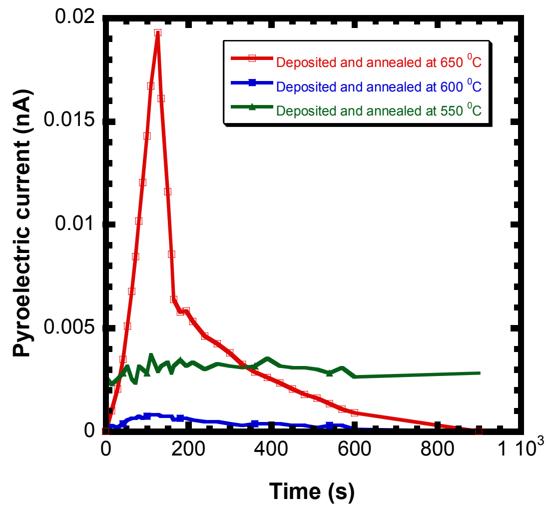

Figure 5-29 Pyroelectric Current as a Function of Time while Temperature is Changing for the PZT Film (before Poling)

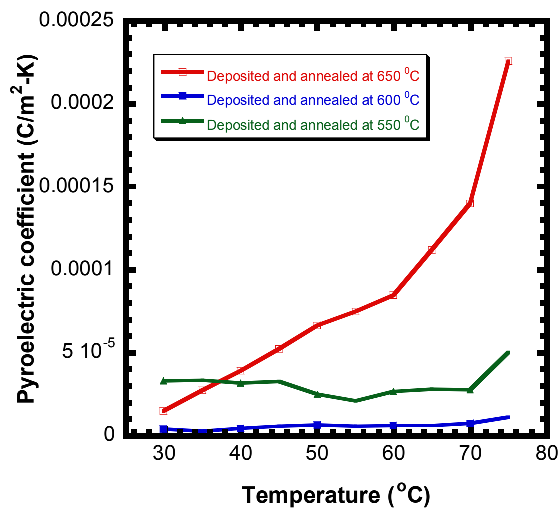

Figure 5-30 Pyroelectric Coefficient as a Function of Temperature for the PZT Film (before Poling)

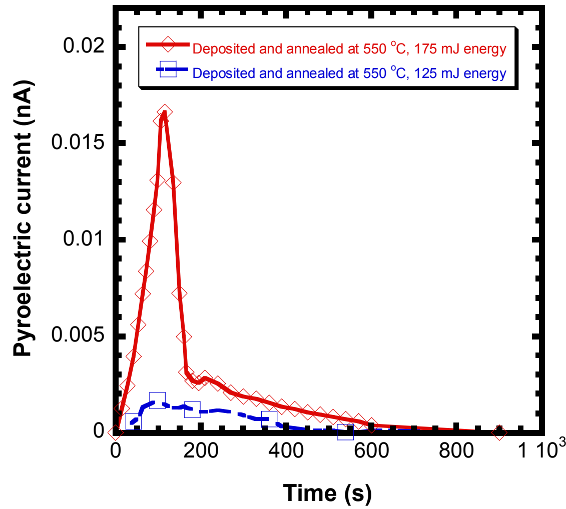

Figure 5-31 Pyroelectric Current as a Function of Time while Temperature is Changing for the PCT Film (before Poling)

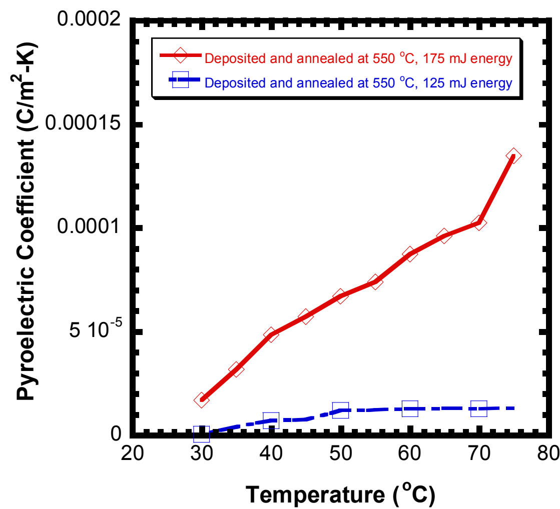

Figure 5-32 Pyroelectric Coefficient as a Function of Temperature for the PCT Film (before Poling)

5.5.4 Poling the Ferroelectric Materials

In order to pole the PZT film, bias voltage was applied across the capacitors made of PZT film (was deposited and annealed at 650 °C) which was varied from 1 V to 4 V. The purpose of poling is to form domains; it also helps to accelerate mobility of the

domain wall which increase domain alignment [75, 76]. In the first stage of poling, the poling voltage was kept constant at 1 V while the poling duration was changed from 30 mins to 60 mins to analyze its effect on the pyroelectric material. The experimental results indicated that higher poling time causes a degradation of dielectric constant of the PZT film. In the second stage of the experiment, the bias voltage was varied which showed reduction of dielectric constant. The high electric field might have caused dielectric degradation of the PZT film. The graph representing results for the capacitors that were poled at 1 V for 30 min and 60 min, it was observed that no variation in capacitance occurred. It means that there was no dielectric degradation of the films took place for these conditions [Figure 5-33].

A bias voltage was applied across the capacitors which are made of PCT film that was deposited and annealed at 550 °C, 175 mJ laser energy. At the beginning, a fixed bias voltage of 3 V was applied across the capacitor while the duration was varied from 30 min to 2 hrs. The experimental result indicates that higher poling time causes a degradation of dielectric constant of the PCT film. In the second stage of poling, the bias voltage was varied from 1 V to 20 V while the time of poling was kept constant at 30 min. It could be observed that higher electric field causes degradation of the dielectric materials. The poling of the film for 3 V at 60 min demonstrates no dielectric degradation of the PCT film, since variation of capacitance became stabilized [Figure 5-34].

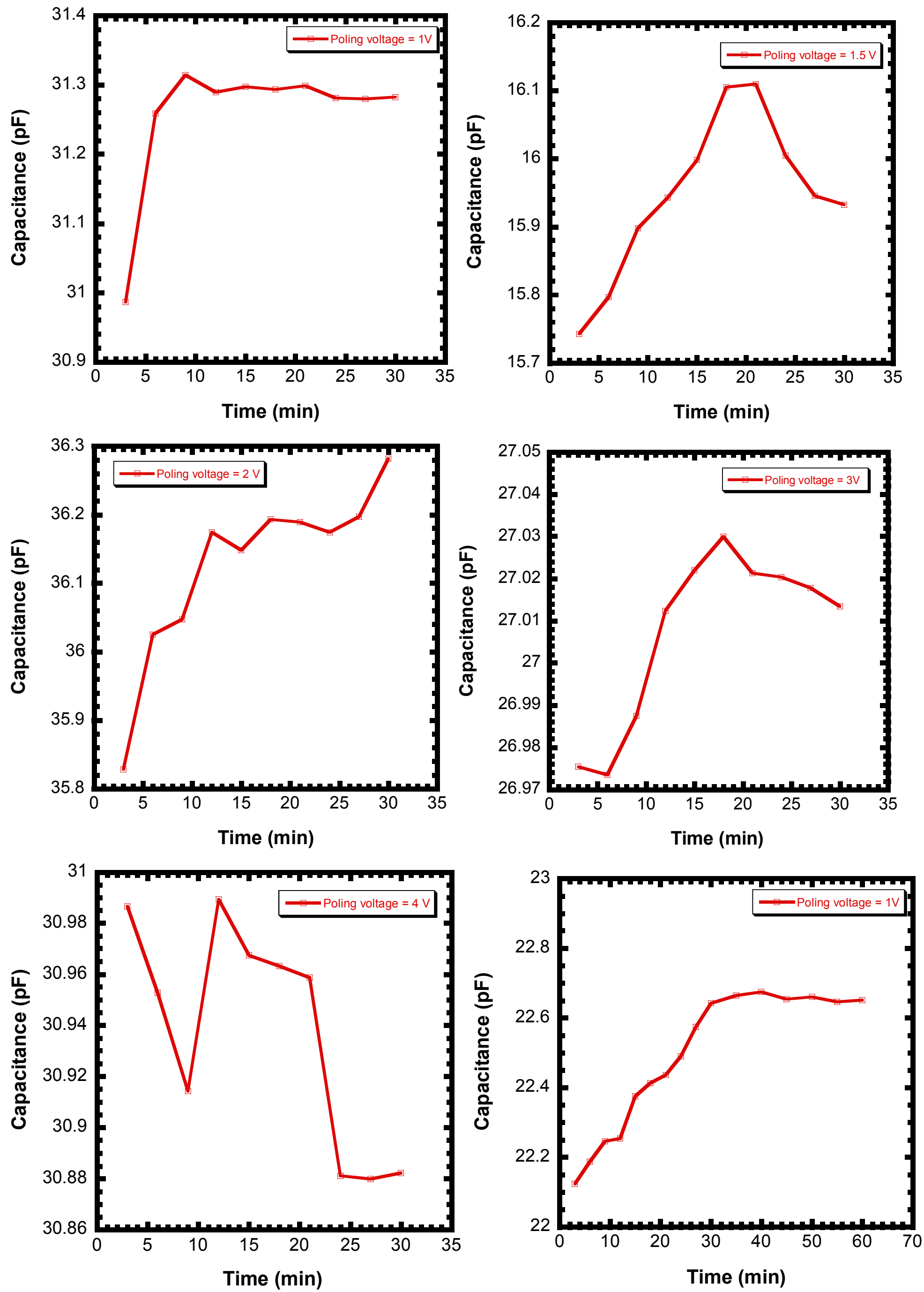

Figure 5-33 Poling of Capacitors Fabricated by Using PZT Material

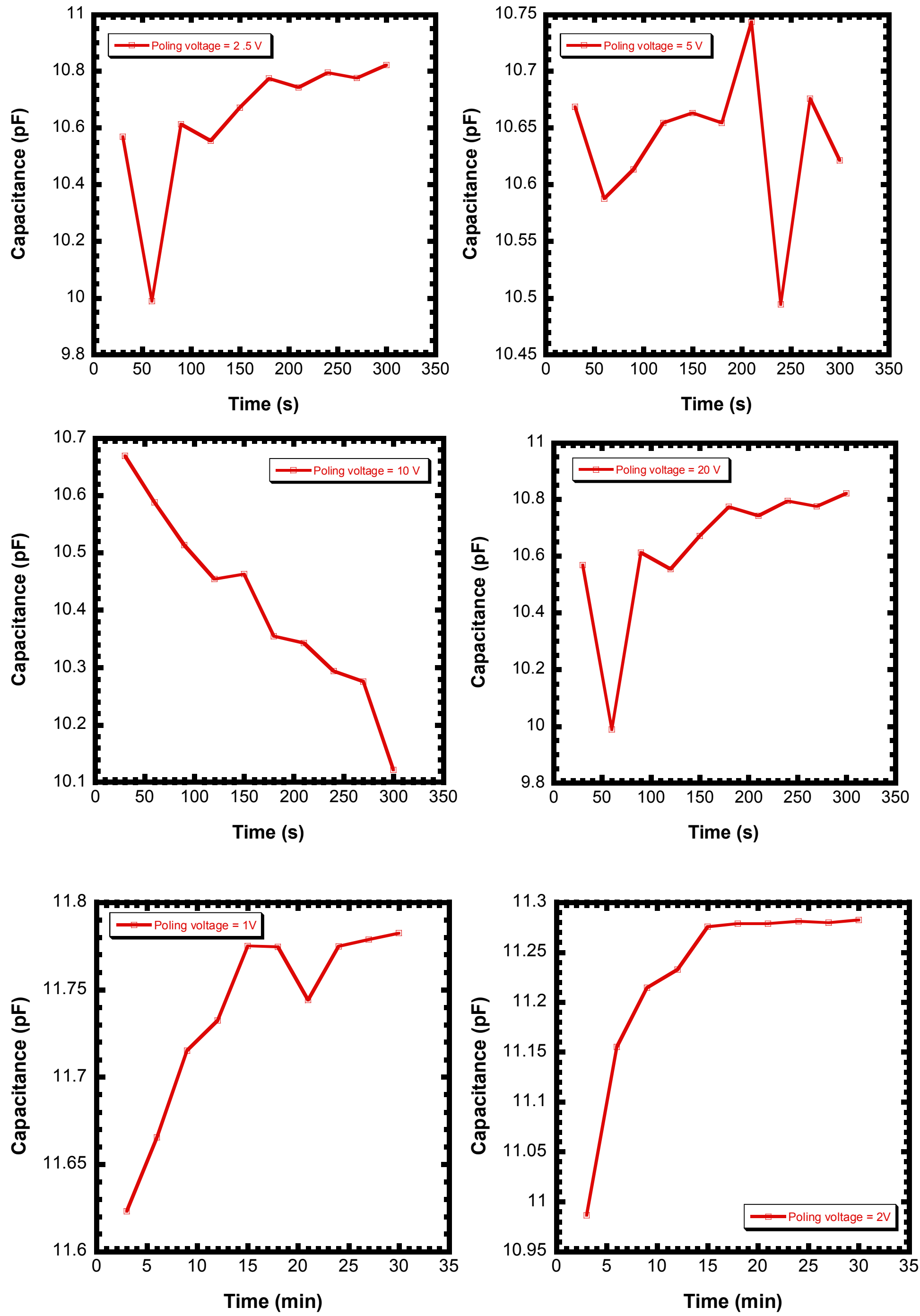

Figure 5-34 Poling of Capacitors Fabricated by Using PCT Material

5.5.5 Pyroelectric Current Measurements after Poling

The pyroelectric current of the PZT film in the capacitors were measured, after poling, as same procedure as discussed in section 5.4.4. From the characterization of the capacitors made with the PZT film, it could be observed that the capacitor that was poled at 1V, 30 mins showed [Figure 5-35] higher value of pyroelectric current compared to other poling conditions (poled at higher voltage). This also reflects that higher voltage causes dielectric degradation of the PZT film. It could be observed that poling at 1V for 60 mins also results in higher pyroelectric coefficient such as 2.5×10^{-5} C/m^2-K. The capacitor that showed higher pyroelectric coefficient were characterized for 10 cycles in order to verify whether the measurement could be repeated or not. These measurements followed each other as shown in Figure 5-36.

In order to measure the pyroelectric current of the PCT films after poling, same procedure was followed as discussed in section 5.4.4. The results indicate that the capacitor that was poled at 3V for 30 mins demonstrates higher pyroelectric current [Figure 5-37 and Figure 5-38]. The capacitor that was poled at 3V for 60 mins also shows high pyroelectric current (at 35°C). The capacitor that demonstrated higher pyroelectric coefficient was characterized for 10 cycles in order to check whether the measurement could be repeated or not. These measurements followed each other as shown in Figure 5-39.

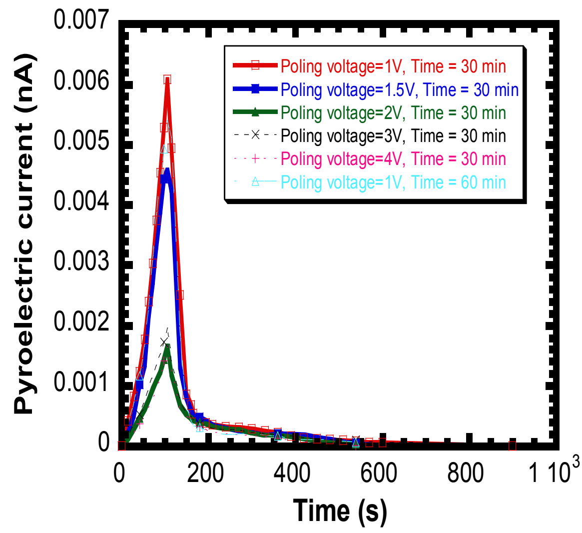

Figure 5-35 Pyroelectric Current Measurement of PZT Film after Poling at Different Voltage

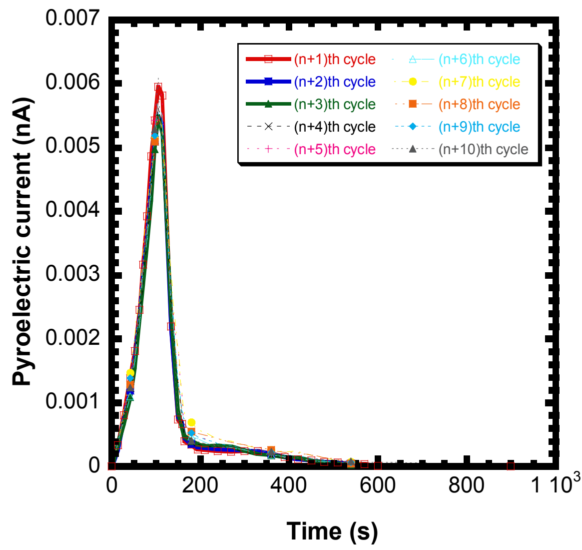

Figure 5-36 Pyroelectric Current Measurement of PZT Film after Poling at 1 V for 30 min

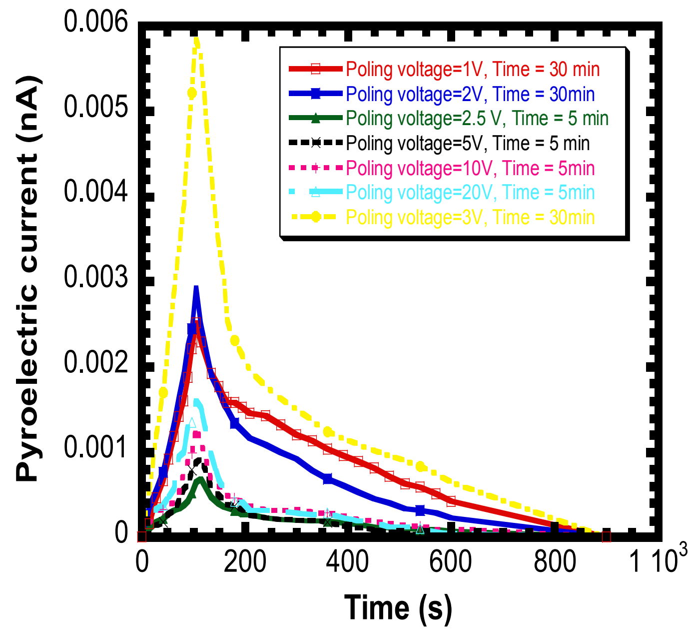

Figure 5-37 Pyroelectric Current Measurement of PCT Film after Poling at Different Voltage

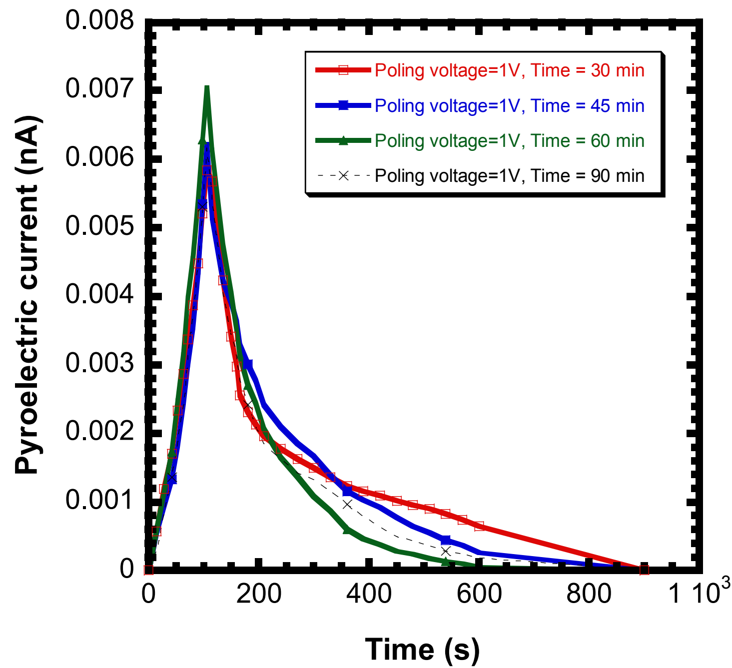

Figure 5-38 Pyroelectric Current Measurement of PCT Film after Poling at Different Time

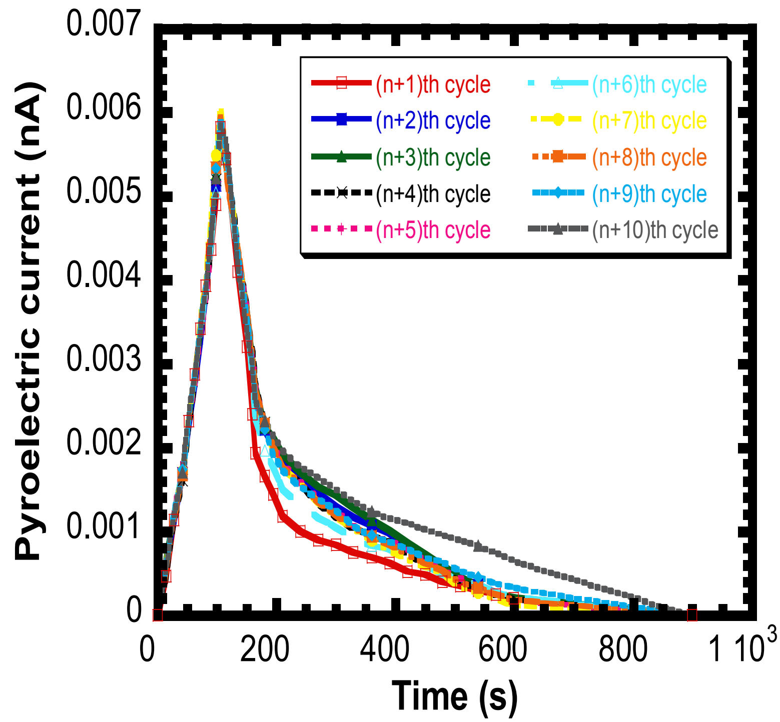

Figure 5-39 Pyroelectric Current Measurement of PCT Film after Poling at 3 V for 30 min

Table 5-1 Summary of PZT and PCT Films

Film	Deposition temperature and annealing time	Laser energy (mJ)	Dielectric constant	Loss tangent	Highest pyroelectric coefficient (C/m^2-K), before poling	Poling electric field for optimum pyroelectric coefficient V/m	Highest pyroelectric coefficient (C/m^2-K), After poling
$PbZr_{0.4}Ti_{0.6}O_3$	650°C, 10 mins	500	133.6 to 777.105	0.0137 to 0.0329	2.71×10^{-5}	3.33×10^{6}	28×10^{-5}
$Pb_{0.7}Ca_{0.3}TiO_3$	550°C, 10 mins	175	90.4 to 388.4	0.0118 to 0.0164	4.77×10^{-5}	12.45×10^{6}	40×10^{-5}

From the experiment described above show the pyroelectric coefficient 28×10^{-5} C/m^2-K for the PZT film and 40×10^{-5} for PCT film C/m^2-K after poling that were deposited on the gold surface. On the contrary, Huang *et al.* [77] prepared PZT film on PT surface by sol-gel method and annealed at 480 ^oC and found pyroelectric coefficient of 18×10^{-5} C/m^2-K. The application of gold as a electrode would reduce the cost for preparing ferroelectric films if compared with platinum. Kang *et al.* [78] deposited PZT film on Pt coated Si surface by metallorganic decomposition and annealed it at 700 ^oC and measured the pyroelectric coefficient of $32 \pm 3 \times 10^{-5}$ C/m^2-K. The grown film was also poled and it showed similar pyroelectric coefficient to our results. Ye *et al.* [79] reported pyroelectric PZT film that was deposited by sol-gel method on p-Si substrate and annealed at 400 ^oC which showed a pyroelectric coefficient 50-80 $\times 10^{-5}$ C/m^2-K. Chang

et al. [80] sputtered PCT film on Pt surface and annealed it at 650 ^{o}C and measured the pyroelectric coefficient of 15 × 10^{-5} C/m^{2}-K. Chopra *et al.* [81] deposited PCT film on ITO surface and found high pyroelectric coefficient of 43 × 10^{-5} C/m^{2}-K. Others [82, 83] also demonstrated high pyroelectric coefficient for PCT film deposited on Pt surface. In this research we focused to use the lead titanate thin film for MEMS detector application at a low cost; so that we utilized gold as a electrode rather than Pt as a electrode and we have found comparable results with the counterparts on Pt surface.

5.6 Conclusions

This chapter discussed about deposition, poling and characterization of modified lead titanate on gold surface for MEMS application. Two different modified lead titanate thin film were utilized: lead zirconium titanate (PZT) and lead calcium titanate (PCT) for The deposition and annealing of PZT material was carried out at 650 °C, 500 mJ laser energy which showed good pyroelectric properties while deposition and annealing of PCT material was carried out at 550 °C, 175 mJ laser which showed good pyroelectric properties. From the investigation of pyroelectric properties of PZT/PCT thin films, it was also observed that the perovskite structure of the film demonstrate good pyroelectric current compared to pyrochlore structure. The thin films were poled afterwards in order to increase the alignment of the domains and it showed improvement of pyroelectric properties. At the final stage of characterization the pyroelectric current was measured for ten repetitive cycles in order to investigate the repeatability of the results.

Chapter 6

Incorporating a Simple Release Layer for Flexible Substrate

6.1 Introduction

The previous chapters described the fabrication of sensors on flexible substrates with the flexible polyimide substrates directly deposited on a rigid silicon wafer. In this chapter, deposition of an intermediate polyimide layer between the flexible substrate and the silicon wafer has been demonstrated. We report a process demonstrated for flexible substrate fabrication on silicon carrier wafers and the subsequent release of the flexible substrate from the carrier wafer. HD Microsystems PI2611 was employed as an intermediate layer to facilitate easy release of the flexible substrate. The deposition process was also defined so that conventional fabrication techniques could be used as well as the release layer could resist common solvents and remover during lift-off or cleaning process.

6.2 Background

The requirement for flexible, foldable, bendable, light-weights sensors and electronics employs attention towards development of fabrication process of flexible substrate. The development of flexible electronics also forces the incorporation of flexible substrates to meet two basic requirements: 1) the fabrication process should utilize the conventional fabrication process; 2) the performance of the flexible devices should be comparable to their rigid counterparts. The requirements are not mandatory but these will help to ensure the development of flexible electronics will not force to replace any deposition tools, will not increase cost or reduce device’s performance.

There are three different approaches towards the fabrication of devices on flexible substrates: 1) fabricating devices directly on the flexible substrate; 2) fabricating

devices on the rigid substrate first and then transferred it to the flexible substrate; and 3) fabricating devices on the flexible substrate coated on rigid wafer and later releasing the flexible substrate containing the devices from the rigid wafer.

The fabrication of electronics directly on the flexible substrates made reel-to-reel fabrication processing possible for large area electronics. One of the major advantages of the reel-to-reel fabrication is that devices are fabricated directly on the flexible substrate which reduces the cost of rigid wafer. But the process needs specialized lithography, etching and deposition tools compatible for large area fabrication, which may cause replacement or modification of conventional tools that are used for costs for MEMS and other electronic systems. Hence, the overall production cost will increase. Moreover, reel-to-reel production has the problem of registering patterned layers with each other and suffers from low dimensional accuracy [7]. Many fabrications systems for producing MEMS device and thin film based transistors do not need large area production, rather 4-18 inches wafers are more convenient for them to utilize conventional fabrication equipments and techniques. For this reason, reel-to-reel production of devices will incorporate more expense and fabrication complexities.

The application conventional equipment to fabricate devices on the silicon wafer and then transfer to flexible substrate may help to overcome most of the problems associated with the reel-to-reel production, since it does not require any specialized tools. The transfer methods mostly use a temporary release layer which dissolves. Kim *et al.* [5] demonstrated the fabrication silicon integrated circuits on thin polyimide which was coated on the rigid wafer. PMMA was used as a sacrificial release layer so that acetone could be used to remove the PMMA and the thin polyimide could be transferred to a thick PDMS film. The PMMA is soluble to most of the solvents so that lift-off or cleaning of the wafer would be difficult for this process. Moreover, low glass transition temperature of

PMMA limits its application for high temperature process. Cao *et al.* [84] applied polyamic acid between SO_2-Si wafer and polyurethane (PU)-polyimide substrate as a release layer, but its solubility in solvents and low glass transition temperature [85] limits the applications. Lee *et al.* and Sun *et al.* [86, 87] fabricated thin-film transistor on SOI wafer and later transferred them on PDMS substrate after etching SOI wafer. This process eventually sacrificed rigid wafer and employed flexibility. Kim *et al.* [6] described application of photoresist to bond parylene based flexible membranes to the silicon carrier wafer. Later, he used a razor blade to make opening near the edge of the membrane and removed photoresist by acetone to separate the wafer from parylene. The photoresist is soluble to solvents and it has low glass transition temperature which makes it inconvenient for most of the MEMS fabrication process. The transfer and bonding mechanism helps to overcome the disadvantages of the reel-to-reel fabrication process; this process need flexible substrate and release layer to be insoluble to solvent in order to overcome complex fabrication process.

The temperature sensors and pressure sensors described in the earlier chapters have been fabricated on the flexible substrate coated rigid wafer so that conventional MEMS fabrication process could be utilized. The glass transition temperature of the polyimide (~400 ^oC) determines the highest process temperature of the sensors. The cured polyimide is not soluble to any solvent or remover which provides an advantage for this polyimide. In order to remove the flexible substrate from the silicon carrier wafer, the wafer's immersing into water helped to decrease the bond strength of the polyimide substrate to the silicon carrier wafer by hydrophilic polyimide/hydrophobic Si_3N_4 interaction with the water.

In this chapter, a process is described where HD Microsystems PI2611 was used between flexible polyimide substrate/superstrate combination (HD Microsystems PI5878

G/4110) and silicon carrier wafer to create low bond strength between them and later release the flexible substrate from the carrier wafer after completion of the fabrication. The purpose of developing the process is to release the sensors fabricated on the flexible substrate by applying a low force which will not cause any stress-induced defect on the device. The process does not need any specialize tools or skills to remove the flexible substrate. Another advantage of this process is that the carrier wafer could be reused after releasing the flexible substrate and cleaning the wafer. The glass transition temperature of the different polyimides are shown in Table 6-1.

Table 6-1 Glass Transition Temperature of the Flexible Polyimides. Reprinted with Permission from [88], Copyright [2013], American Institute of Physics.

	Glass transition temperature (°C)	Reference
PI2611	360	89
PI5878 G	> 400	90
Polyamic	107	85
PDMS	-125	91
PMMA	<124	92
Polyureth	<65	93
Parylene	<90	94

6.3 Experimental Details

An n-type, <111> and 4-inch silicon was used as a carrier wafer where the fabrication was processed. The fabrication steps are shown in Figure 6-1. After cleaning the wafer by standard TAMDI process, a 200-nm-thick Si_3N_4 was deposited on the carrier wafer by rf-magnetron sputtering in a AJA sputtering tool [Figure 6-1(a)]. The Si_3N_4 is used to passivate the wafer and improve adhesion of the subsequent polyimide films. Next, the edge of the wafer was wrapped by a polyimide tape to prevent coating of next polyimide layer [Figure 6-1(b)]. After that, HD Microsystems liquid polyimide PI2611 was spin coated at 3000 rpm for 30 sec on the wafer [Figure 6-1(c)] and after the deposition

the tape was removed [Figure 6-1(d)] to avoid any spin coating of PI2611 around the perimeter. Then, the wafer was pre-baked at 130°C for 90 sec followed by the curing at 350°C for 30 min inside N_2 gas environment in Blue-M oven. The PI2611 provides low adhesion for the flexible polyimide substrates where MEMS devices were fabricated. The polyimide taper allowed the subsequent spin coated flexible substrate to create a seal with the Si_3N_4 layer so the PI2611 would not be attacked by solvents or "remover" used during subsequent process steps. Next, HD Microsystems liquid polyimide PI5878G was spin-coated onto the wafer in 4 steps [Figure 6-1(e)] which formed the flexible substrate. In each step, after spin coating the polyimide at 1500 rpm for 60 sec, wafer was pre-baked for 3 min at 110 ^{o}C. Finally, the wafer was cured at 300 ^{o}C for four hours to achieve a total thickness of 35 μm. The PI5878G polyimide also covered the perimeter of the wafer which protected the PI25611 from exposing to any solvent or remover in any stage of the fabrications. Here, the flexible "substrate" is mostly combination of substrate/superstrate in order to place device at a low stress plane near the center of the film [95].

After curing, a 400-nm-thick Si_3N_4 was sputtered on the polyimide to increase adhesion for the subsequent layers and passivate the polyimide. The passivation layer also defines the device plane for the MEMS devices. Then, 150-nm-thick Ti was sputtered on the passivation layer, followed by the lift of process. This lift-off process also indicates that the flexible substrate can undergo conventional MEMS fabrication techniques. Next, HD Microsystems liquid photo-definable polyimide HD4110 (superstrate) was spin-coated at 1500 rpm for 30 sec on top of the wafer in 2 steps and patterned to provide open vias for electrical connection. In each step, the polyimide was prebaked for 110 ^{o}C for 180 sec and cooled for 60 sec before starting next spin-coating. Then, the polyimide was cured at 250 ^{o}C for 4 hrs to achieve thickness of 35 μm.

Finally, the flexible substrate containing Si_3N_4 passivation layer and the Ti-metal layer was removed from the silicon carrier wafer. It was accomplished by a sharp cutting tool to cut the polyimide substrate around the perimeter of the wafer as shown in Figure 6-1(f) and Figure 6-2. Then, the flexible polyimide substrate was separated from the silicon wafer by a low force. The wafer could be cleaned for reusing another batch of flexible substrate production.

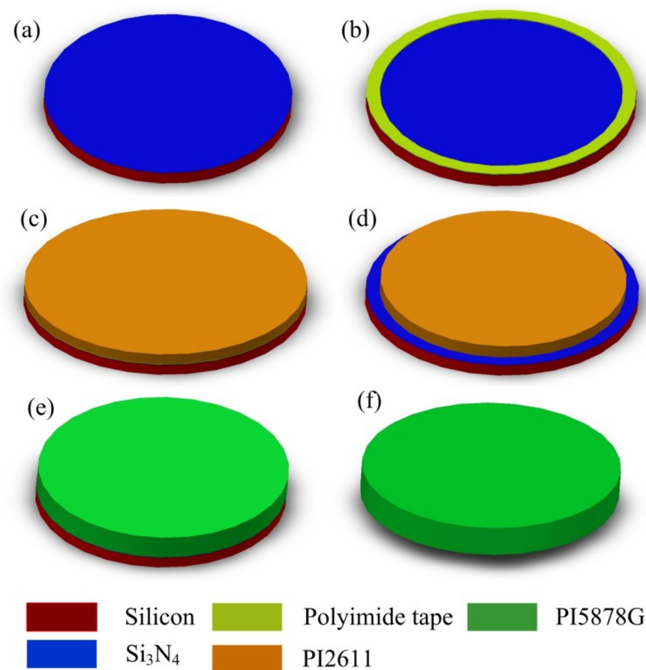

Figure 6-1 (a) Deposition of 1st Passivation Layer, (b) Wrapping Perimeter of the Wafer with Polyimide Tape, (c) Spin-Coating PI2611 Release Layer, (d) Separating Polyimide Tape before Curing the Polyimide, (e) Spin-Coating PI5878 G Polyimide and Curing, (f) Releasing the Flexible Substrate from the Silicon Wafer. Reprinted with Permission from [88], Copyright [2013], American Vacuum Society.

6.4 Discussions

The processing (curing) temperature of the release layer dictates the maximum temperature that could be used for the fabrication of the device. If the processing temperature exceeds curing temperature it will cause outgasing and bubble formation in between the PI2611 polyimide and the subsequent layers. It also indicates that any annealing or curing steps (for polyimide) above 350 ^{o}C may delaminate the flexible substrate from the release layer.

The application of polyimide tape before spin coating release layer and removing it before curing the PI2611 polyimide, helped the following polyimide PI5878 G to protect the edge of the wafer. Eventually it served to prevent any solvent or any chemical reagent to get into contact with the release layer to cause any delamination of the flexible substrate.

After cutting the edge of the flexible substrate, the flexible polyimide substrate could be removed from the wafer by applying a low force. The strain induced defect in the MEMS device due to the force could be avoided by immersing the wafer into n-methyl pyrrolidinone after cutting the polyimide substrate around the perimeter of wafer, which helps to detach the polyimide film from wafer. After releasing the flexible substrate, the silicon wafer could be immersed into HF acid to strip off the polyimide near the edge. Hence the silicon wafer could be used for another batch of device fabrication. Another advantage of the current process described above is that the silicon wafer could be used for the multiple batch of device fabrication. This would reduce tremendous amount of cost for fabrication. This process could be used for fabricating complex MEMS device that has more lithographic, lift-off, wet etching and dry etching steps which will be discussed in the next chapter. The deposition of polyimide substrate on the silicon wafer gives the process flexibility to apply conventional fabrication tools.

The thermal expansion mismatch between the polyimides with the silicon may cause stress in the film. The thermal expansion coefficient (CTE) of the polyimides and silicon wafer is summarized in Table 6-2.

Table 6-2 Summarizing Coefficient of Thermal Expansion and Young's Modulus of Different Polyimide and the Silicon <111> Carrier Wafer. Reprinted with Permission From [88], Copyright [2013], American Vacuum Society.

	Coefficient of thermal expansion (ppm/ °C)	Young's modulus (GPa)	Reference
HD PI2611	3	8.5	89
HD PI5878G	20	2.3	90
HD 4110	35	3.4	96
Silicon <111>	2.6	163	97, 98

From Table 6-2, the close match of CTE between the PI2611 and the silicon helped to cure the release layer without forming any stress on the film or the carrier wafer. The CTE mismatch among PI2611, PI5878 G, and HD4110 are very small, which could not induce any stress on the film or silicon wafer. The CTE mismatch between the flexible substrate (PI5878 G) and the superstrate (HD4110) are comparatively lower than their mismatch with the PI2611 film and silicon. The PI2611 was not a part of the final flexible substrate, hence it effect should be less pronounced. The mismatch would cause curling the polyimide after release, which could be avoided by depositing thick layers of polyimide in the case of temperature sensors. In order to avoid stress induced on the devices in between substrate and the superstrate, the substrate/superstrate needs to be engineered while taking consideration their Young's modulus [95]. The important consideration for the devices to place in a low stress plane in between the flexible substrate/superstrate. Moreover, the curling effect could be utilized to engineer bendable

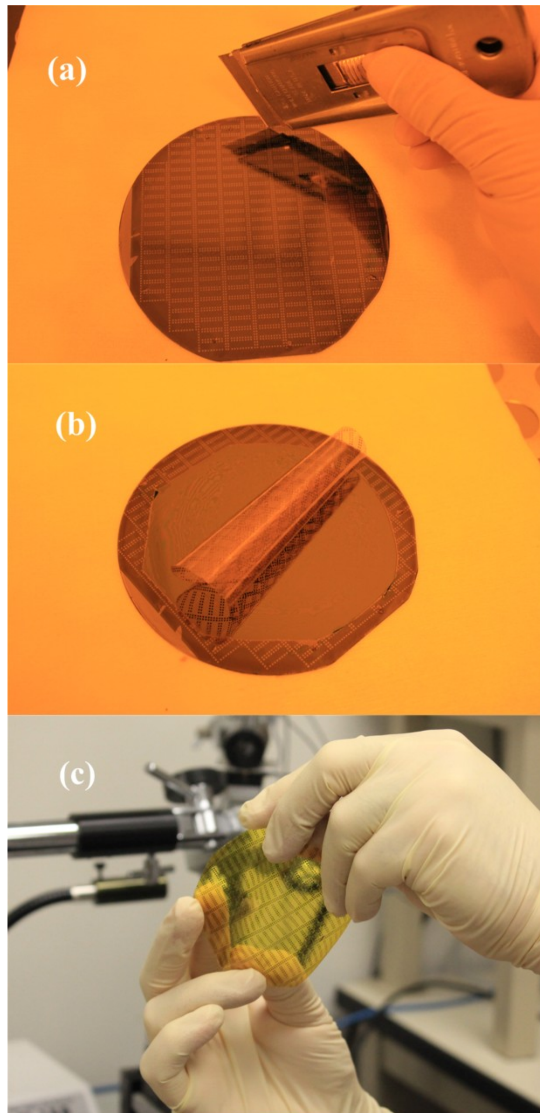

Figure 6-2 (a) Cutting the Edge of the Flexible Substrate by a Cutting Tool to Separate from Silicon Wafer, (b) a Flexible Polyimide Substrate Detached from Carrier Wafer, (c) Polyimide Substrate/Superstrate Combination Containing a Metallization Lines in between Them. Reprinted with Permission From [88], Copyright [2013], American Vacuum Society.

substrate at the particular angle, since the application of the flexible electronics lie on conforming to non-planar or curved surface.

6.5 Fabricating Multi-Layers MEMS Structure on the Flexible Substrate and Releasing from Silicon Wafer

The process discussed above was used to fabricate bolometer which consists of 16 lithographic stage, 9 lift-off process,1 dry etching step and 1 wet etching step (detailed will be discussed in chapter 7). The bolometers were sandwiched between the polyimide substrate and superstrate; similar as the other sensors discussed before.

Before depositing the superstrate layer on the bolometer, an attempt was taken to dice a single die from the wafer by using a scalpel by cutting around the die line. It was successfully separated out from the carrier wafer [Figure 6-3] and rest of the flexible substrate was attached with the silicon wafer. After deposition of the superstrate layer, another attempt was taken to dice a single die. It was possible to separate die from the wafer, but the superstrate and substrate were detached from each other [Figure 6-4]. The possible reason for the problem still needs to be investigated. But after viewing the die periphery through a confocal microscope it was observed that there was crack on the alumina (in between the polyimide superstrate and substrate) due to the cutting by the scalpel which might have caused the separation [Figure 6-5].

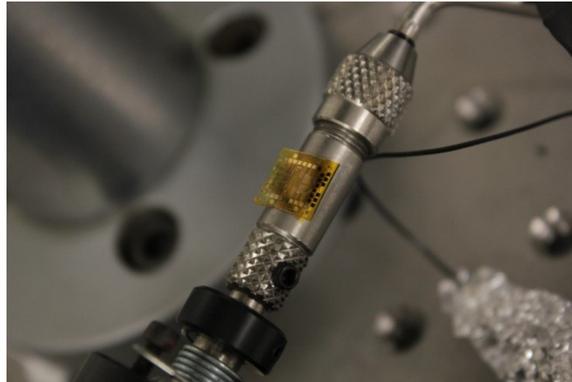

Figure 6-3 Die Separated from a Carrier Wafer before Depositing Polyimide Superstrate Layer

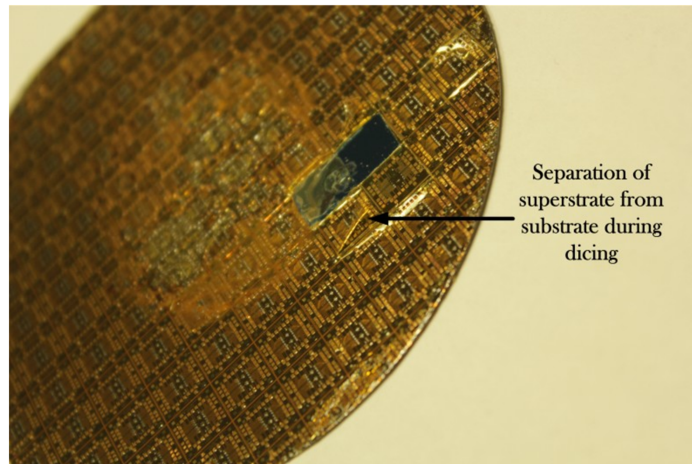

Figure 6-4 Separation of Superstrate from the Substrate during Dicing

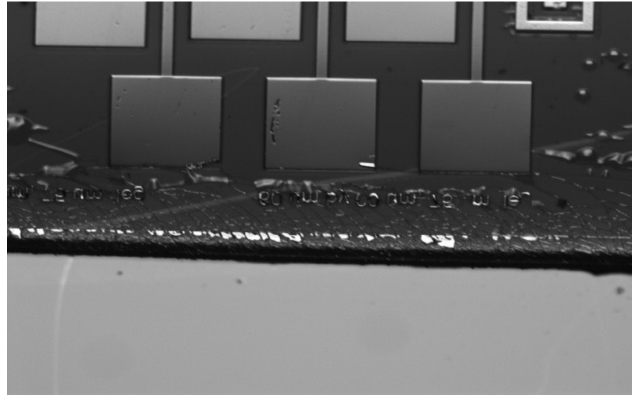

Figure 6-5 The Separation of Polyimide Superstrate Layer due to the Stress on the Adjacent Alumina Layer around the Edge.

Another approach was done to dice by etching the silicon wafer from the backside to reach the flexible substrate by utilizing standard DRIE silicon etch process (as discussed in chapter 2). After that, attempt was taken to dice a die from the flexible substrate, but again superstrate and substrate were detached from each other [Figure 6-6] which is similar to the results that was observed before. So whether the dicing was done with/without etching silicon wafer, an intermediate layer (such as adhesion promoter) is required to hold the superstrate with substrate for complex structure. The complex structure is mentioned here because this separation was not observed for less simple structure such as temperature sensor or pressure sensors. Moreover, etching has a disadvantage over using the easy release layer is that the reactive gas might react with the front side of the wafer during the etching and damage the devices. It needs a good sealing to protect the top side of the wafer from being exposed to the etching gas.

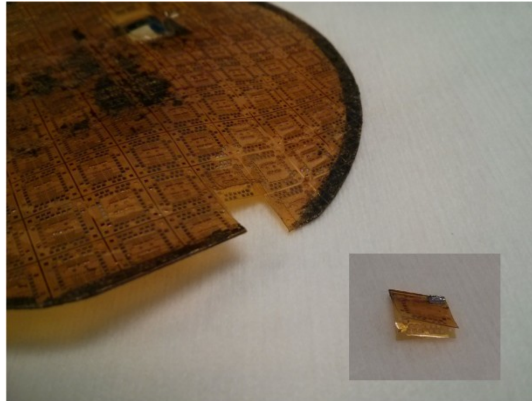

Figure 6-6 The Bolometers Sandwiched between Superstrate and Substrate after Etching Silicon Carrier Wafer from Backside; Dicing Caused the Separation of the Polyimide Substrate and Superstrate (Inset)

The temperature sensors were diced by using a scissor, but there was no delamination observed [Figure 2-13]. For the relative pressure sensors and absolute pressure sensors, also there was no delamination observed.

6.6 Conclusions

In this chapter, deposition of a polyimide release layer has been described and a way to prevent any chemical reaction with the polyimide has been demonstrated. HD Microsystem PI2611 polyimide was used in between the silicon carrier wafer and the flexible substrate/superstrate combination. A lift-off process has been demonstrated to show the application of conventional MEMS technique with the current flexible substrate technology. Finally, the flexible polyimide substrate/superstrate was released from the silicon wafer by cutting near the edge of the flexible substrate and applying a low force to detach the substrate. In comparison with other works on flexible substrate, we demonstrated a process that can be used to fabricate sensors or devices on flexible substrate that requires high temperature process. This incorporation of easy release layer allowed to utilize the existing fabrication technology without adding any kind of

complexity. The process could be extended further to reuse silicon carrier wafer for another batch of fabrication after removal of the flexible substrate.

Chapter 7

Design, Fabrication and Characterization of Uncooled Infrared Detector

7.1 Introduction

Uncooled Infrared detectors transform incident radiation into thermal energy which can create an output electrical signal. They have various applications for night vision, scientific instruments, and health monitoring systems. Infrared detectors on flexible substrates also allow them to be applied to non-planar surfaces such as for robotics applications.

Once the infrared radiation is absorbed by the detecting material, either thermal change of an electrical/electronic property (uncooled thermal detectors) or photo-generation of carriers (photo-detectors) take place. In order to detect photo-generation of carriers the thermal generation of carriers must be suppressed. The current research is focused on the detection 8-14 μm infrared radiation band. In this region, the activation energy of carriers is small enough that thermal generation is more dominant than photo-generation of carriers. At room temperature, the thermal detection of infrared radiation is more convenient since it is less complex than that of a photodetector and more cost effective since cryogenic cooling is not required. There are different types of thermal detectors such as pyroelectric, resistive bolometer, thermopile detector and transition edge super-conducting bolometers [99]. The thermal detector's sensitivity whether it is a bolometer or pyroelectric detector, depends on the maximum change of temperature of the detecting material and the change of an electrical property with temperature. Figure 7-1 shows the cross section of a thermal detector on a flexible substrate. The thermal isolation of the detector from the substrate helps to reduce heat loss from the detector. This creates a temperature gradient from the detector to the substrate which acts as a

driving force for heat flow. Heat flows by conduction and radiation mechanisms, where convection can be suppressed by packaging the detector in vacuum. Packaging the detector in vacuum makes the heat conduction dominate over convection and can be controlled by changing device geometry i.e. arm connecting the pixel/detecting material.

This chapter has focuses on the design, fabrication and characterization of thermal detector. For the design portion, the 8-14 μm infrared radiation detectors were investigated. Both pyroelectric and resistive bolometer types of thermal detectors were designed. For the fabrication, a resistive bolometer on a flexible substrate was emphasized. After fabrication, the bolometers were characterized and their performance has analyzed.

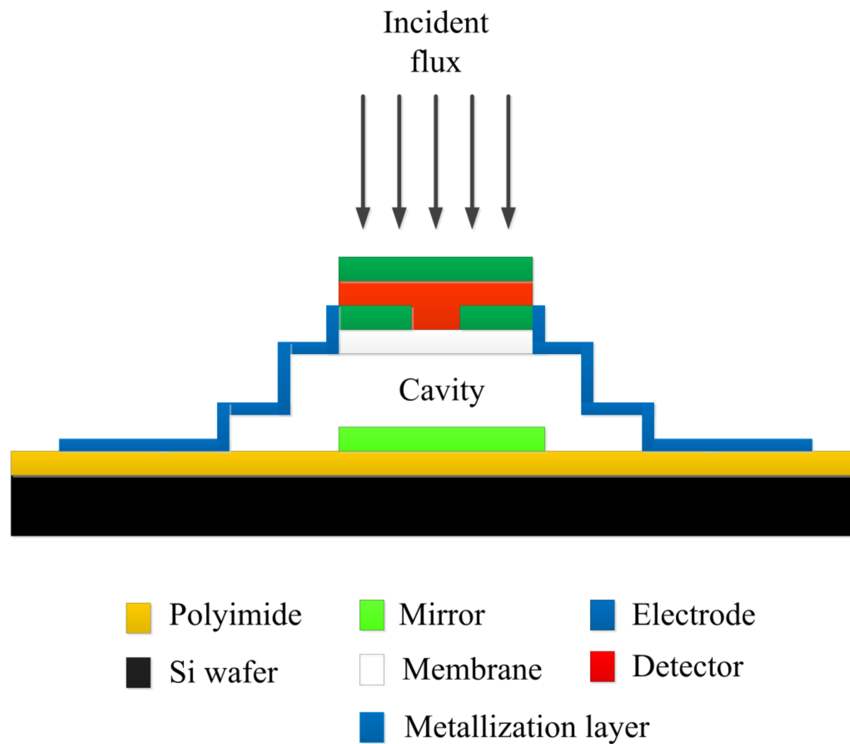

Figure 7-1 Cross-Section of an Infrared Detector

7.2 Designing the Bolometer and Simulating for Optimization

There were four objectives that were determined before starting the design: (a) achieving low thermal conductance; (b) increasing the absorption of infrared radiation in the wavelength range of 8-14 µm; (c) device-level packaging of the detector in order to limit the convection of heat away from it and giving it rigidity against external force; (d) Blocking visible light from the detector.

In order to increase the thermal isolation of the detector area from the heat sink, micromachining is utilized. A good approach is to use a polyimide sacrificial layer, deposited between the detector and substrate and later surface micromachined the polyimide by dry isotropic etching.

The arm that is used to connect the detector with heat sink or substrate needs to have very low thermal conductance. At the same time, it should have high elastic modulus in order to support the detector against the gravitation force. Alumina was used previously for pressure sensors as a membrane material since it offers high Young's modulus and low thermal conductance. The detector material which absorbs radiation and undergoes temperature dependent changes needs to be selected properly. The design of the IR detector was focused on both pyroelectric and resistive bolometer types of IR detectors. But for simulation purpose, silicon was selected as a sensing material for the resistive bolometer. From the fabrication point of view, silicon is easy to deposit, robust against crystallization below temperature of 250 ^{o}C (the maximum temperature that might be used for polyimide curing) and it has a high temperature coefficient of resistance (as discussed in chapter 2). But the design was performed such that pyroelectric materials could be substituted though the thickness of different layers would need to be re-optimized for the pyroelectric detector case.

In order to reduce the heat convection by air, the detector needs to be vacuum packaged. Device-level packaging also helps to protect the detector from damage by external collision or touch. The packaging layer also affects the overall design and can absorb IR radiation. So the thickness needs to optimize to reduce optical energy loss.

The silicon which is used as a thermometer is also affected by visible light. The production of photo-generated carriers can be reduced by using a long-pass optical filter layer on the detector. Germanium has very low extinction coefficient [100] at IR wavelengths while transmitting sub-bandgap infrared radiation through it.

The total number of the layers could be divided into four subcategories: (a) Optical filter layer; (b) structural and metallization layer; (c) packaging layer; (d) detector and reflector layer.

7.2.1 Designing Thermal Isolation Structure

Increasing the absorption of radiation of the detector while reducing the thermal conductance away from it, is challenging from the design point of view. One way to reduce the thermal conductance of the detector is to incorporate a nanomesh structure around the detecting material which offers low thermal conductance, low thermal capacitance and serves as an absorber layer on it to increase the radiation absorption. The circular structure can ensure the maximum absorption of radiation while transferring heat easily to the detecting material which undergoes electrical changes. So the nanomesh structure needs to have two components: the nanomesh membrane and the absorber layer on the membrane. The nanomesh membrane can be connected to the outer membrane (eventually the substrate) through an narrow arm (termed as leg) to reduce the thermal conductivity away from the detecting material. The IR detector that was designed to have 12 circular rings of width 100 nm around the detector which are connected with each other by 2 μm long legs. These small legs are termed as grid legs.

The entire mesh like structure is suspended from the substrate by 6 support legs of width 100 nm and length of 386.6 nm (based on simulation results) which are connected to the outer membrane. The grid size is smaller than the infrared wavelength (8-14 μm) of interest in order to ensure the effective absorption [101].

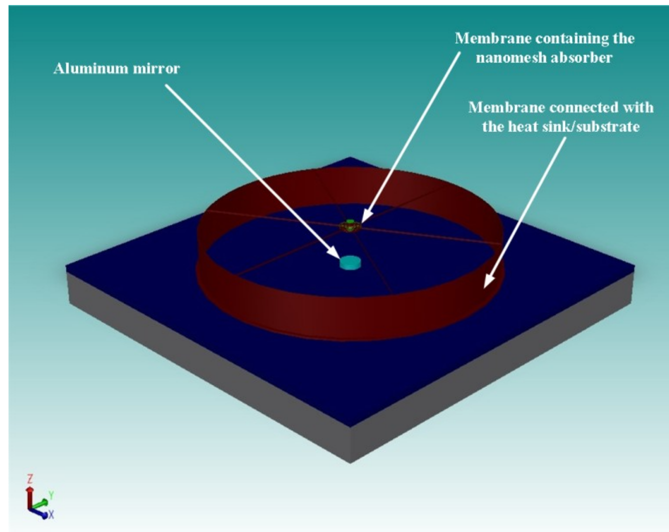

Figure 7-2 A Simple Representation of the Designed Detector Showing the Thermal Isolation of the Detector from the Substrate through the Membrane (Designed by the CoventorWare^{TM}).

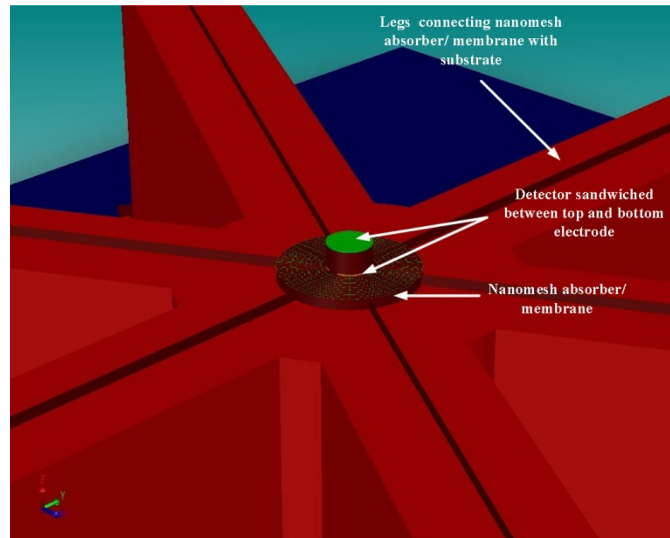

Figure 7-3 Center Part of the Designed Detector Showing the Nanomesh Absorber and the Detector (Designed by CoventorWare^{TM})

The thickness of the alumina was selected to be 100 nm for the simulation purpose. The steady state thermal analysis of the designed detector was done by applying a heat flux of 4.89 nW on the detector area and the absorber while keeping temperature substrate constant at 300 K. The temperature difference from the detector to the substrate was found to be 0.395 K. The thermal conductance was calculated to be 14.1 nW/K including both heat conductance and radiation. The transient analysis of the detector was simulated to find the time constant and it was found to be 31.9 msec. The heat capacity of the detector was calculated to be 44.98 nJ/K from thermal conductance and thermal time constant.

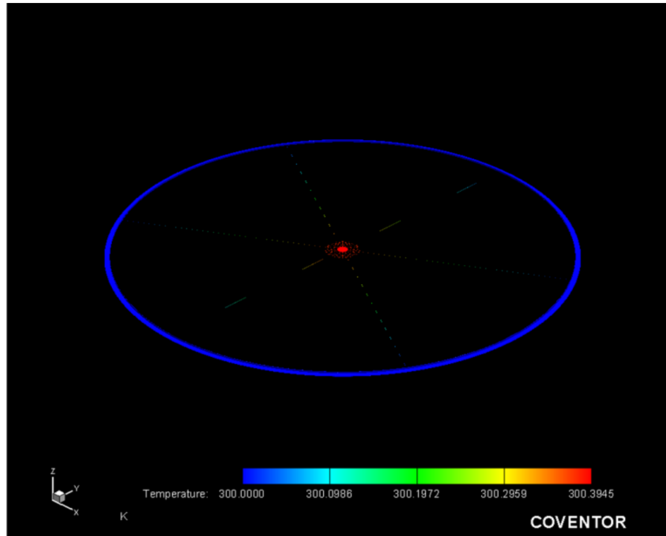

Figure 7-4 Steady-State Thermal Analysis of the Designed Detector including Conduction through the Membrane and Radiation of the Entire Structure.

In order to evaluate the z-axis displacement of the center part of the detector due to the gravitational force, 1g acceleration was applied on the detector and the surrounding membrane and absorber. The maximum displacement near the center area of the detector was found to be 370 nm towards the substrate insignificant compared to the distance between the substrate and the detector material.

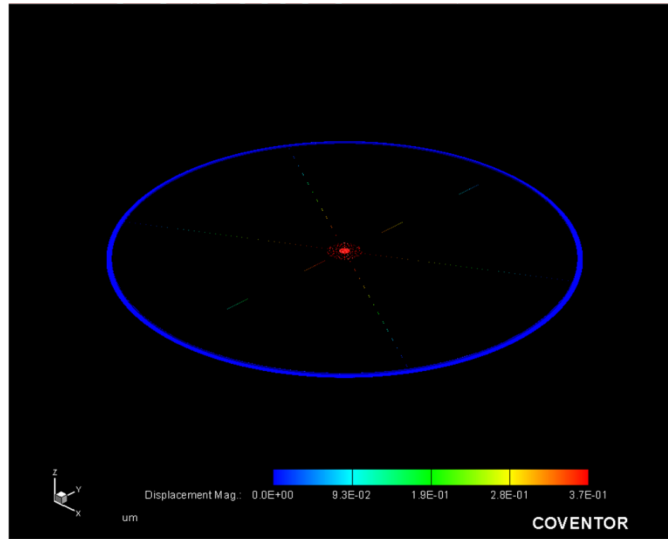

Figure 7-5 Displacement of the Detector due to the Application of 1g Acceleration to the Micromachined Structure.

7.2.2 Packaging the Sensor

The necessity to build a packaging layer around the detector is to reduce heat convection away from the detector by air. At the same time it helps to protect the detector from external forces or touch. Before depositing the packaging layer, the surface micromachining step needs to be done. In order to facilitate surface micromachining, the encapsulation layer needs to be deposited over the detector which contains windows to help etching the sacrificial layer. Later, the windows are sealed by the packaging layer which also covers the detector area. The encapsulation layer involves the deposition of an extra sacrificial layer between detector and encapsulation layer to make a separation between them. This separation is needed since it helps to avoid any thermal conductive path from detector to the substrate through encapsulation layer. The sacrificial layer is etched away by surface micromachining.

There are different approaches that could be utilized to build the encapsulation and packaging layer around the detector. The area around the detector could be either

planar filled or the polyimide could be patterned to form mesa type structure before depositing the encapsulation layer. The planar filling could be easily etched and it doesn't need any additional patterning. But a problem after the isotropic etching step is there will not be any definite structure around the detector which increases the wiring difficulty. On the contrary, the mesa type of structure invokes the polyimide to be patterned which gives a definite shape below the encapsulation layer after etching polyimide. Both type of structure requires a thick layer of packaging layer to completely seal the gap between the substrate and the windows. The deposition of an extra thin sacrificial layer around the top sacrificial layers helps to reduce the thickness of the packaging layer. In this case, the windows of the encapsulation layer are located on the thin sacrificial layer. This thin sacrificial layer serves as a channel for surface micromachining.

In order evaluate the compatibility of the packaging layer; a rectangular packaging layer was designed around the detector. The thickness of the packaging layer was kept constant at 2.5 μm and alumina was selected as a packaging material. After applying a pressure of 10 atm (target pressure that detector could withstand), it was observed that a maximum displacement of 45 μm along z-axis from simulation results. The result indicated, the entire structure would collapse under such pressure and the absorption of radiation would be affected as well.

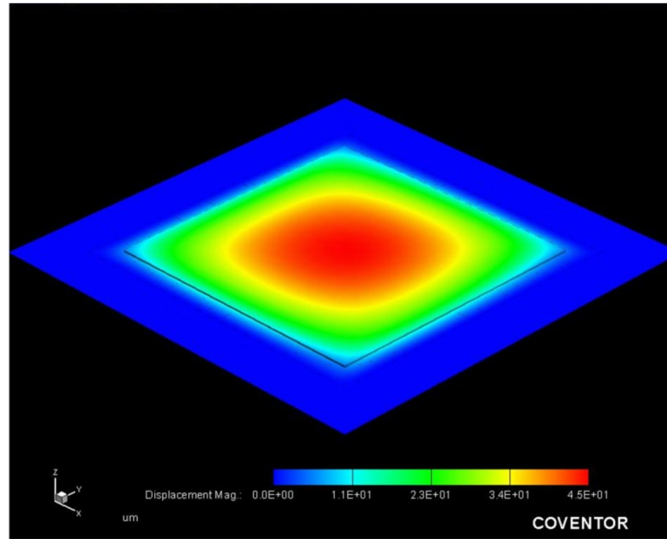

Figure 7-6 Displacement of the Packaging Layer due to the Application of 10 atm Pressure.

The open area around the detector needed to be reduced to minimize the displacement along z-axis. This could be done by designing a circular encapsulation layer around the detector and extending rectangular encapsulation layer on the legs of the membrane. The rectangular legs also contain the opening that is required for the etching. After removing the sacrificial layer below encapsulation layer, the windows could be sealed by the packaging layer create a vacuum around the detector [Figure 7-7]. After designing such a packaging layer, simulations were performed and a displacement of 0.75 µm was observed for the application of 10 atm pressure on the packaging layer. The maximum mises stress was found to be 690 MPa which is below the yield strength of the alumina [102]. This spoked wheel type of packaging layer showed more robust structure compared to the rectangular structure.

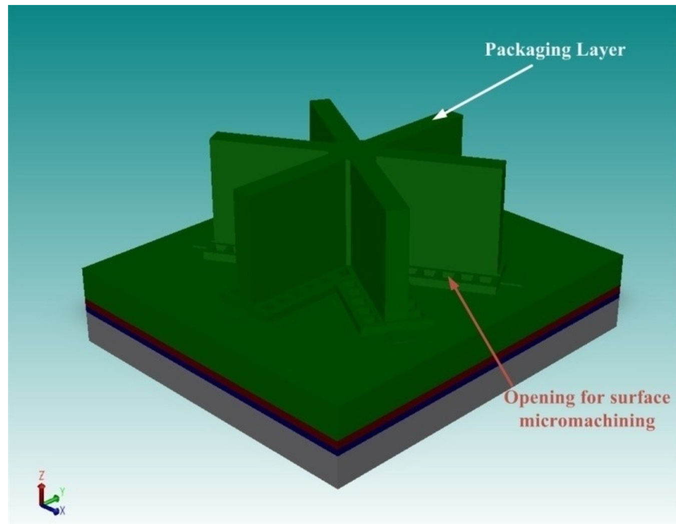

Figure 7-7 New Packaging Layer for the Bolometer

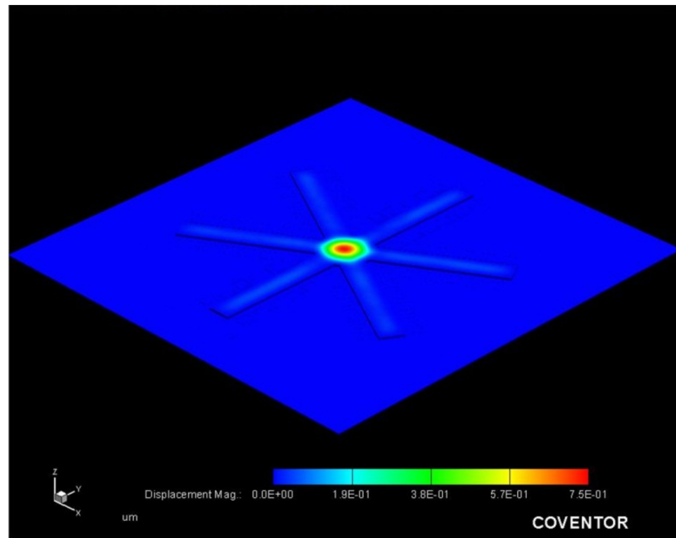

Figure 7-8 Displacement of the Packaging Layer due to the Application of 10 atm Pressure.

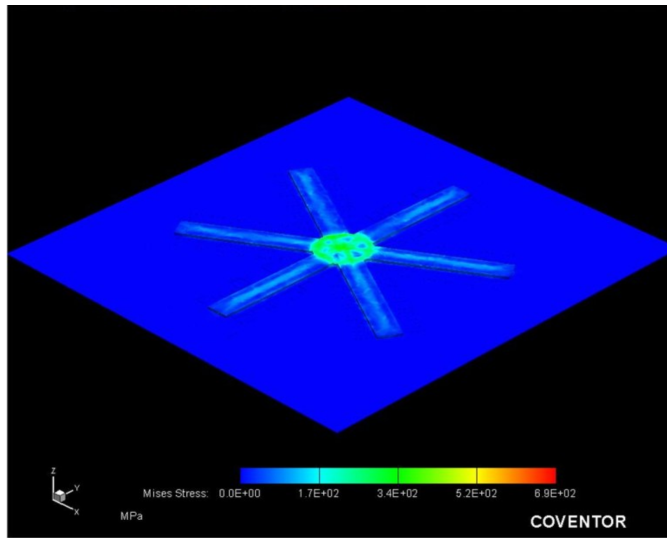

Figure 7-9 Maximum Stress Induced in the Packaging Layer due to the Application of the 10 atm Pressure

7.2.3 Calculating the Absorption of the Detecting Material

Figure 7-10 shows different layers through the cross section of the center part of the detector. The thickness of the different layers needs to be optimized in order to achieve maximum absorption by the detecting material. The detector was planned to be fabricated on flexible substrates and it must have a transparent package in the long-wave infrared wavelength. A reflector medium is required on the flexible substrate to reflect back radiation towards the detecting material and form a resonant cavity. From the simulation, it was observed that a thickness of 300-nm of aluminum would serve as a reflector and would be able to reflect 99.44 % of infrared radiation in the wavelength range of 8-14 μm.

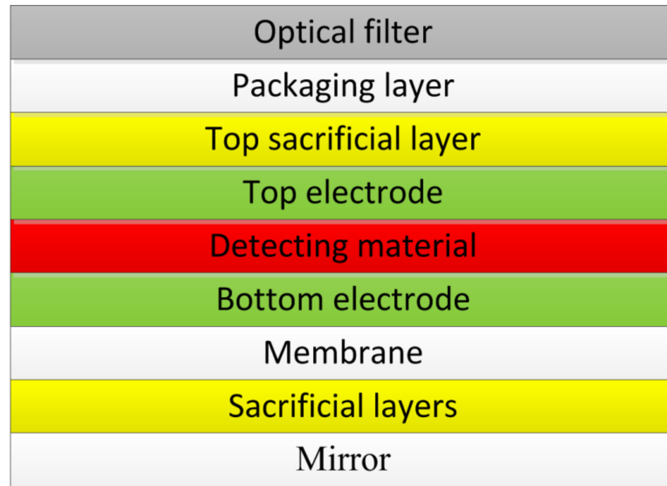

Figure 7-10 Cross-Sectional Area of the Detector through the Center.

During the optimization for maximum absorption, the thickness of the packaging layer and the membrane layer could be kept constant since it will affect the structural strength and the alumina acts as transparent medium for much of the infrared wavelength range. Thus, the thickness of the sacrificial layers, sensor layer, top and bottom electrode and the optical filter layer could be varied to obtain the optimum absorption.

The optimization of the absorption by the detecting material requires minimum transmission and reflection loss through different layers. A convenient approach towards finding the transmission and absorption loss is to transform different layers into equivalent transmission line elements. These layers then could be represented as a cascaded connection of two port networks [Figure 7-11] [103] where each port could be represented as a 2 × 2 ABCD matrix. The multiplication of ABCD matrix of individual layers gives the overall ABCD matrix for the entire network (all layers). The ABCD matrix could be defined as [103]:

$$\begin{bmatrix} A & B \\ C & D \end{bmatrix} = \begin{bmatrix} \cosh \gamma d & \eta \sinh \gamma d \\ (1/\eta) \sinh \gamma d & \cosh \gamma d \end{bmatrix} \tag{7.1}$$

where η is the intrinsic optical impedance of the film, γ is the propagation constant through a film and d is the thickness of that particular film.

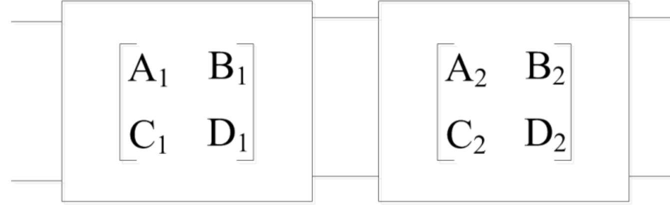

Figure 7-11 Cascade Connection of Two Port Networks [104].

Once the overall ABCD matrix was calculated from the individual matrix, it represented the ABCD matrix for all layers. Then, ABCD matrix could be multiplied by the $[\boldsymbol{E}, \boldsymbol{H}]_{al}$ vector of the reflector (mirror), the $[\boldsymbol{E}, \boldsymbol{H}]_{total}$ vector could be calculated. Here, the $\boldsymbol{E}$ is the electric field and $\boldsymbol{H}$ represents the magnetic field. The $[\boldsymbol{E}, \boldsymbol{H}]_{al}$ vector of the aluminum reflector could be defined easily by setting $\boldsymbol{E}$ as 1 and $\boldsymbol{H}$ as $1/\eta$, where eta represents as the intrinsic impedance of reflector. Once the $[\boldsymbol{E}, \boldsymbol{H}]_{total}$ vector is calculated the impedance, i of the network (considering all layers) could be found by dividing $\boldsymbol{E}_{total}$ by $\boldsymbol{H}_{total}$. Then the reflection coefficient, r_{fw} and the fractional reflected power, p_r could be calculated using the equations [105]:

$$r_{fw} = \frac{(Z_{in} - \eta_0)}{(Z_{in} + \eta_0)} \tag{7.2}$$

$$p_r = |r_{fw}|^2 \tag{7.3}$$

where η_0 is the intrinsic impedance of the free space.

The power incident on the aluminum mirror could be calculated from the magnitude of the Poynting vector:

$$P_{al} = \frac{1}{2} E_{al} * H'_{al} \tag{7.4}$$

Here H'_{al} is the complex conjugate of magnetic field. The electric field and the magnetic field of the incident radiation could be calculated by:

$$E_i = \frac{E_t}{(1 + r_{fw})} \tag{7.5}$$

$$H_i = \frac{E_i}{\eta_0} \tag{7.6}$$

The incident power on the detector then calculated by:

$$P_i = \frac{1}{2} E_i * H_i' \tag{7.7}$$

which is used to calculate the fractional transmitted power, p_t and hence the fractional absorbed power, p_a:

$$p_t = \frac{P_{al}}{P_i} \tag{7.8}$$

$$p_a = 1 - p_r - p_t \tag{7.9}$$

The procedure discussed above was used to find the absorption of the infrared radiation. But in order to maximize the absorbed power, the thickness top and bottom electrodes; the detector, the germanium filter and the sacrificial layers thickness needed to be optimized. As the total number of variable is five, a Monte Carlo simulation with simulated annealing method [106] was used to optimize the absorption. The Monte Carlo method is useful to achieve approximated thickness of different layers, the Newton-Raphson method was used to get the final optimum thickness values. The thickness of these layers is listed in Table 7-1 which was found for the maximum absorption of radiation in the center detector area. The reason for selecting the maximum absorption in the center detector instead of the absorber region is that radiation in the center part can directly impact the detector performance while the absorber's heat needs to conduct to the detector. There is always some heat loss while conducting heat from the absorber to detector and heat might conduct to the heat sink. So finding the maximum absorption of radiation in the center detector area helps to achieve a greater change in temperature.

Table 7-1 Thickness of Different Layers

Layer name	Thickness (nm)
Mirror (Al)	300
Thin sacrificial layer	500
Thick sacrificial layer below detector	3200
Bottom, top electrode (Al)	30
Membrane (Al_2O_3)	100
Detector (Silicon)	500
Absorber (Ti)	1
Top sacrificial layer above detector	3700
Encapsulation plus the packaging layer (Al_2O_3)	2500
Optical filter layer (Ge)	720

7.2.4 Double Layer Absorber for the Infrared Radiation

The micromachined bolometers discussed in various literature, focused on the absorption of radiation by a single metal layer which is then conducted to the thermal detector area to heat up and change its characteristics [101, 9, 10, 11, 12, 13]. The characteristics could be either change in the resistance of the thermometer or the generation of a pyroelectric current due to changes in the spontaneous polarization in response to temperature variation. Gildemeister *et al.* [12] mentioned absorption that took place due to the destructive interference between incident and reflected wave in the absorber for a transition edge bolometer. A tri-layer structure of Ti-Al-Ti thermistor was used to control the transition temperature. It was mentioned that the upper two layers

were removed from the absorber to increase the optical efficiency which would not affect the absorption since the destructive interference took place at a single plane. The literature mentioned above, demonstrated the absorption of heat by the detector from the surrounding structure; which means the detector indirectly absorbs heat. In conclusion, effective infrared absorption takes place only in a single plane in the entire structure. While Nivelle *et al.* [107] and Mahmood *et. al.* [108] demonstrated the direct absorption of the infrared radiation by a single layer of detector.

On the contrary, in this design, a double layer absorber structure was designed where the thermometer material was sandwiched between top and bottom electrodes. Once the radiation pass through the electrodes, they could absorb heat and would heat up the detector that is intimate contact with them [Figure 7-2 & 7-3]. Besides this direct heating of the detector an absorber structure was surrounded the detector which could also absorb radiation (will be discussed in later section). From the simulation, it was observed that this tri-layers could able to absorb a fractional power of 99.44% at the wavelength of 11.4 μm, but could absorb an average absorbed power of 18.5% in the entire bandwidth from 8-14 μm [Figure 7-12]. Note that, the Ge optical filter mostly acts as barrier which effects total absorption of infrared radiation. Without the filter average fractional absorption of power was around 32.67%.

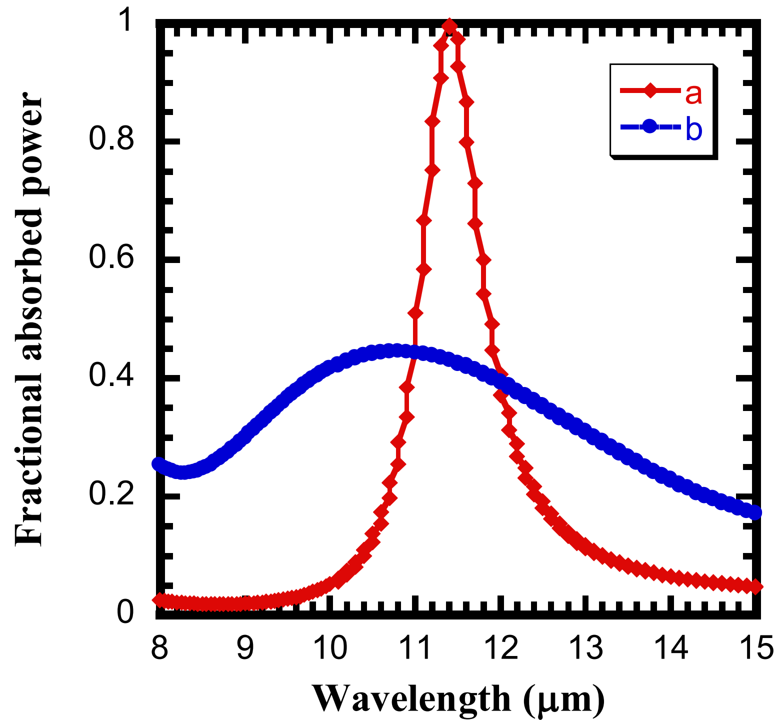

Figure 7-12 Simulated Fractional Absorbed Power in the Double Layer Absorber (a) including the Optical Filter on Top of the Detector; (b) excluding the Long-Pass Optical Filter Layer.

The fractional absorbed power of the Al (30 nm)-Si (500 nm)-Al (30 nm) tri-layers on the flexible substrate was characterized and the results is shown in Figure 7-13. The maximum power of infrared radiation that could be absorbed by these tri-layers was 70% in the wavelength of 10 μm. There was no packaging layer or the reflector layer in this experiment. The packaging layer also serves to trap the radiation inside the detector and the radiation that is reflected from the detector, bounce back by the packaging layer. The reflector layer also helps to block the radiation to pass through the flexible substrate and reflects the light back to the detector. These two effects increase the absorption of the detector as observed in the simulation results.

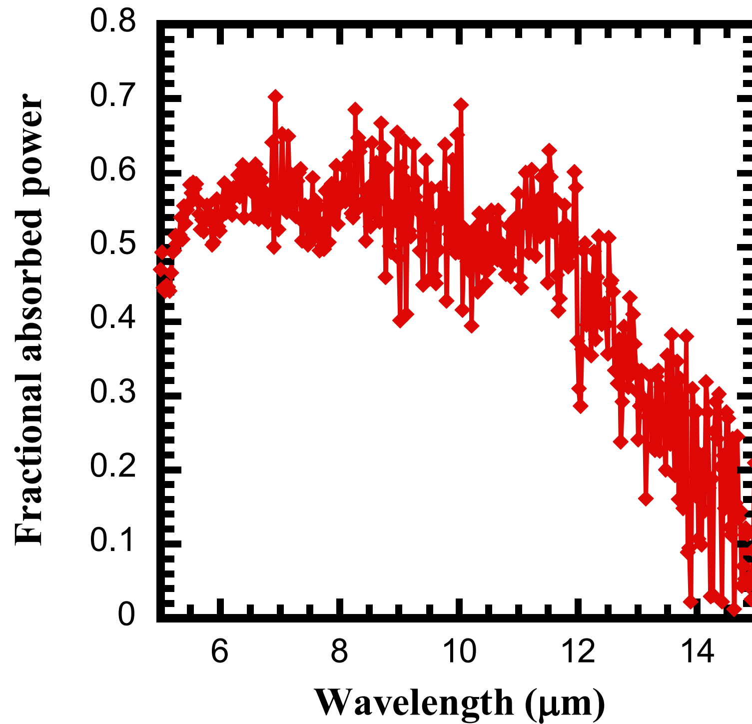

Figure 7-13 Measured Fractional Absorption of the Transmitted Power in the Al-Si-Al tri-Layers on Top of the Flexible Substrate.

7.2.5 Absorption by the Nanomesh Absorber

The nanomesh absorber also absorbs infrared radiation which needs to account in order to find total absorption by the detector for the entire wavelength range of 8-14 μm. In order to count its absorption, the grids need to be accounted as an equivalent thin film and consider it as one more layer (two layers; one for nanomesh membrane and other for absorber) [109]. These grids then could be treated as a lumped circuit element of admittance Y_g the equivalent ABCD matrix is [109]:

$$\begin{bmatrix} A & B \\ C & D \end{bmatrix} = \begin{bmatrix} 1 & 0 \\ Y_g & 0 \end{bmatrix} \qquad (7\text{-}10)$$

According to Ulrich [110], the transmission and reflection coefficient grids depend strongly on the polarization. If the electric field of a linearly polarized incident

wave is perpendicular to the grid, then it is called capacitive grating; for the opposite orientation, it is called inductive strip grating [Figure 7-14]. Since the metal mesh has square grating; it needs to consider as the superposition of capacitive and inductive gratings. For an inductive grating the equivalent reactance is given by [111]:

$$\frac{X_I}{Z_S} = -\left(\omega_0' \ln \csc \frac{\pi a}{g}\right)\left(\frac{\omega_0}{\omega_0'} - \frac{\omega_0'}{\omega_0}\right)^{-1} \quad (7\text{-}11)$$

where λ is the free space wavelength; the grid parameters *2a* and *g* are shown in Figure 7-14. Here Z_s is the resistance of the free space. For the capacitive grating the equivalent capacitance value is [111]:

$$\frac{X_C}{Z_S} = \frac{2}{(\mathrm{n}_1^2 + \mathrm{n}_2^2)}\left(\omega_0' \ln \csc \frac{\pi a}{g}\right)^{-1}\left(\frac{\omega_0}{\omega_0'} - \frac{\omega_0'}{\omega_0}\right) \quad (7\text{-}12)$$

Here grids are located on plane boundaries between dielectrics of refractive n_1 and n_2 and ω_0' is the resonant, given by [111]:

$$\omega_0' = \omega_0 \sqrt{\frac{2}{(\mathrm{n}_1^2 + \mathrm{n}_2^2)}} \quad (7\text{-}13)$$

The loss resistance of the mesh reactance shunts the transmission lines at their junction which is given by [111]:

$$\frac{R_l}{Z_S} = \sqrt{\frac{4\pi\varepsilon_0 c}{\lambda \sigma_c}} \frac{\eta_b}{4} \quad (7\text{-}14)$$

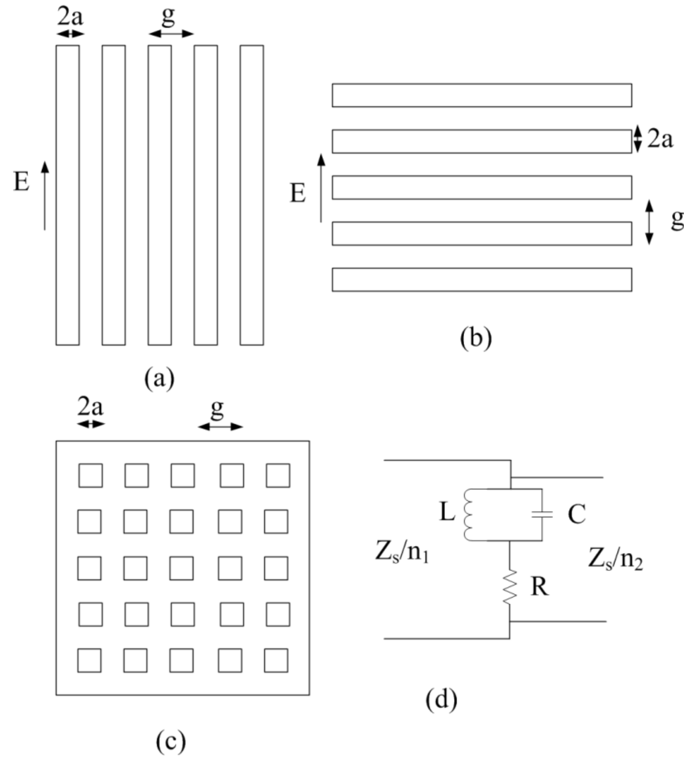

Figure 7-14 (a) Inductive Strip Grating; (b) Capacitive Strip Grating;

(c) Inductive Mesh; (d) Equivalent Lump Element Model of Inductive Mesh.

Where ε_0 is the permittivity of free space, c is the velocity of light and σ_c is taken as one quarter of the bulk dc conductivity of the mesh material , η_b is a factor equal to *1/(1-2a/g)* for capacitive meshes and *g/2a* for inductive meshes. Since in this current design, the thickness of the grid was comparable to the grid width, the grid width *2a* needs to be converted to effective strip width $2a_{eff}$. For an inductive mesh, a_{eff} is given by [110, 111]:

$$a_{eff} = a + \frac{t}{2\pi}\left[\ln\left(\frac{8\pi a}{t}\right) + 1\right] \tag{7-15}$$

For capacitive strip gratings it is given by [111]:

$$a_{eff} = a - \frac{t}{2\pi}\left\{\ln\left[\frac{4\pi(g-2a)}{t}\right] - 1\right\} \tag{7-16}$$

The procedure above described is applicable to square grids/gratings or mesh. The nanomesh structure that was designed has circular mesh, which could be approximated as a rectangular strip of length, *l* and width, *w* where *l* is taken as the average perimeter of the outer and the inner grating and *w* is taken as the distance between two grating (as shown in Figure 7-15). The effective grating parameter *g* could be calculated as:

$$g = \sqrt{l * w} \tag{7-17}$$

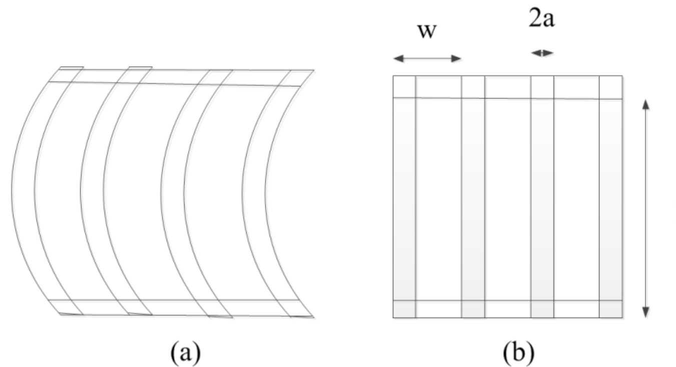

Figure 7-15 (a) Part of the Nanomesh Absorber (b) Approximation of the Circular Absorber to Rectangular Absorber.

The procedure has been described above is applicable to transform a grating mesh to an equivalent lumped circuit model to find equivalent ABCD matrix and thus added to the $[\mathbf{E}, \mathbf{H}]_{total}$ vector.

The cross sectional area though the nanomesh structure of the detector is shown in Figure 7-16. Thickness of the different layers was not optimized near nanomesh area for maximum radiation absorption. Since the center part of the detector was optimized, deposition/optimization of the membrane or absorber for different thickness would create complexities in the fabrication. The fractional absorbed power for the detector is shown in Figure 7-17 after including the nanomesh absorber. The average fractional absorption of power has reduced to 12.54 % while the effective area has

increase (10.9 times) for radiation absorption; eventually total absorption of power increased significantly. Note that, without optical filter the average fractional absorption of power would be 32.44%.

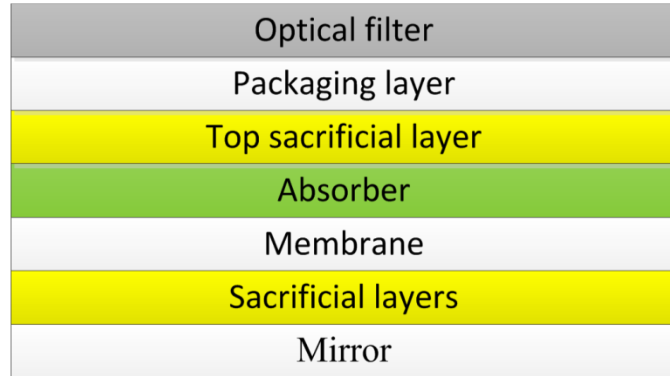

Figure 7-16 Cross-Sectional Area of the Detector through the Absorber

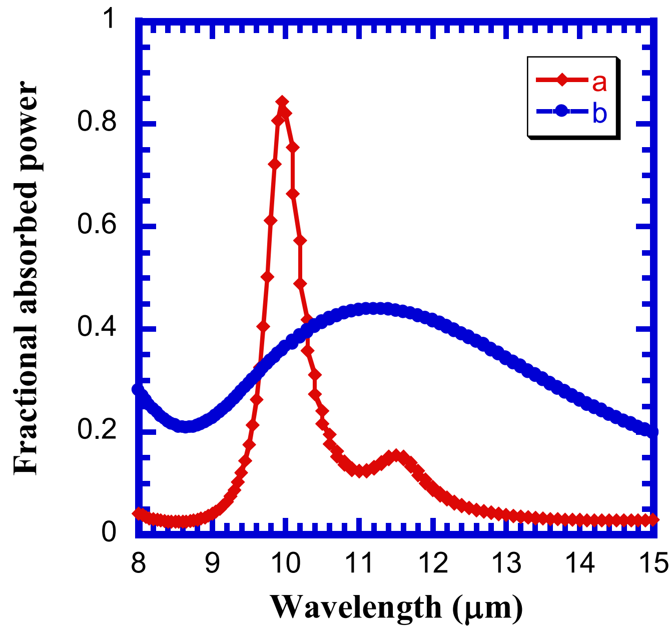

Figure 7-17 Fractional Absorbed Power in the Double Layer Nanomesh Absorber (a) including the Optical Filter on Top of the Detector; (b) excluding the Long-Pass Optical Filter Layer.

Spiderweb (mesh) bolometers that are found in the literature [9, 10, 11, 12, 13, 107] demonstrated gratings (grids) or legs of width more than 1 micrometer in the mesh absorber area utilizing conventional photolithography. These bolometers were designed to operate in the far infrared region (> 200 μm of wavelength) of radiation. In this work, the spiderweb bolometer (nanomesh) has 100 nm of legs/gratings which needs e-beam lithography. The designed bolometer could be able to operate in the 8-14 μm of wavelength. One of the major novelties of the current work is that it will accelerate the transition of MEMS to NEMS technology in bolometer area.

7.2.6 Optical Filter

Beside the infrared radiation, the visible light spectra (400-700 nm) could be accumulated by the detector which would cause generation of photo-carriers. This infrared detector is designed for thermal generation of carriers at a certain wavelength range instead of optical generation. In order to reduce the effect of photo-generation of carrier due to visible light a 720-nm thick Ge-optical filler layer is designed to deposit on the entire detector area. Germanium has very low extinction coefficient [100] for the infrared light. It could be observed from Figure 7-17, there is considerable amount of radiation absorption in the detector area in spite of thick optical filter. In order to evaluate the attenuation loss of visible light through a Ge-layer, a 720-nm-thick Ge was evaporated on top of a flexible substrate. The transmission of visible light at certain wavelength (using LEDs as a source of light) through this film was measured by a photodiode and the corresponding results are shown in Table 7-2. It could be observed that the blue light (430 nm) has been attenuated maximum (5.37×10^{-5}% of transmission) amount while the green light (565 nm) has maximum amount of transmission through the germanium-polyimide film. It should be noted here that

polyimide film has very low absorption and reflection in visible light as well as infrared wavelength range.

Table 7-2 Transmission of Visible Light through Germanium

Light	Wavelength (nm)	Fractional transmitted power
Red	650	2.85×10^{-6}
Yellow	585	3.74×10^{-6}
Green	565	1.08×10^{-5}
Blue	430	5.37×10^{-7}
White	400-700	3.87×10^{-7}

7.2.7 Different Types of Design

Besides designing the nanomesh based bolometer, two other types of bolometer were designed [Figure 7-18 & Figure 7-19]. One of them was designed as circular type of bolometer, but there was no nanomesh structure and the 100-nm legs were replaced by 10-µm legs. Other type of bolometer was designed as a rectangular shape and the detector size (or pixel size) and leg length was varied to change the heat conductivity and thermal time constant of the detectors (Table 7-3). For each detector steady-state and transient thermal analysis was done. The z-axis displacement due to 10 atm pressure or 1g acceleration was negligible for these rectangular sensors (< 50 nm). The z-axis displacement for the circular bolometer due to 1g acceleration was 200 nm.

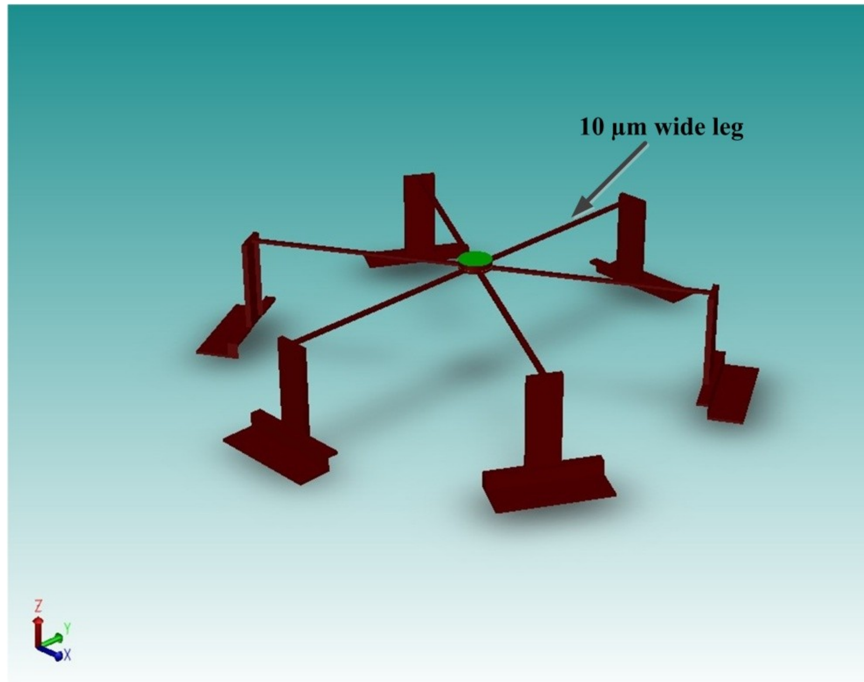

Figure 7-18 Circular Bolometer with 100-μm Legs

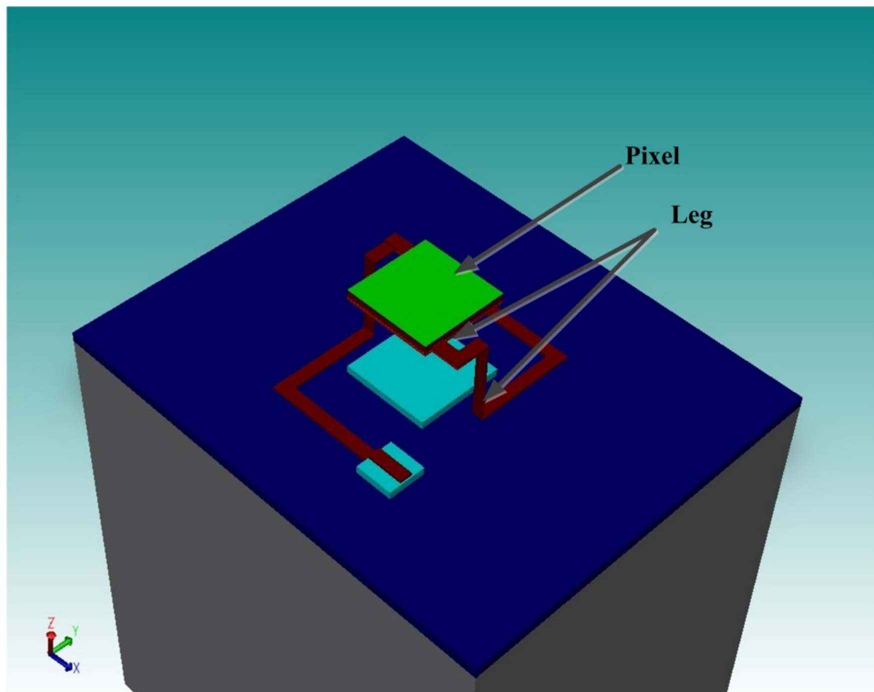

Figure 7-19 Rectangular Bolometer

Table 7-3 Summary of Different Types of Bolometer

Bolometer type and pixel size	Leg length (μm)	Thermal conductance (W/K)	Thermal time constant (msec)
Nanomesh Circular bolometer; diameter-20 μm	386.5	4.69×10^{-9}	78.5
Circular bolometer without nanomesh; diameter-50 μm	386.5	5.37×10^{-7}	9.9
Rectangular; pixel-35 μm× 35 μm	20	8.67×10^{-7}	1.1
Rectangular; pixel-35 μm× 35 μm	50	4.03×10^{-7}	2.82
Rectangular; pixel-35 μm× 35 μm	75	2.89×10^{-7}	4.2
Rectangular; pixel-60 μm× 60 μm	20	10.09×10^{-7}	5.23
Rectangular; pixel-60 μm× 60 μm	50	4.03×10^{-7}	8.83
Rectangular; pixel-60 μm× 60 μm	75	3.13×10^{-7}	11.58
Rectangular; pixel-80 μm× 80 μm	20	10.49×10^{-7}	5.75
Rectangular; pixel-80 μm× 80 μm	50	4.32×10^{-7}	14.75
Rectangular; pixel-80 μm× 80 μm	75	3.11×10^{-7}	20.55

7.2.8 Adding a Reference Resistor

A reference resistor was added with each type of bolometer [Figure 7-20]. The thickness and area of the reference resistor is same as the micromachined resistor (bolometer). The reference resistor would be deposited on the substrate. The purpose of adding reference resistor is to subtract the affect of room temperature heating from the bolometer response. The addition of reference resistor requires each bolometer to have three bond pads for electrical connections.

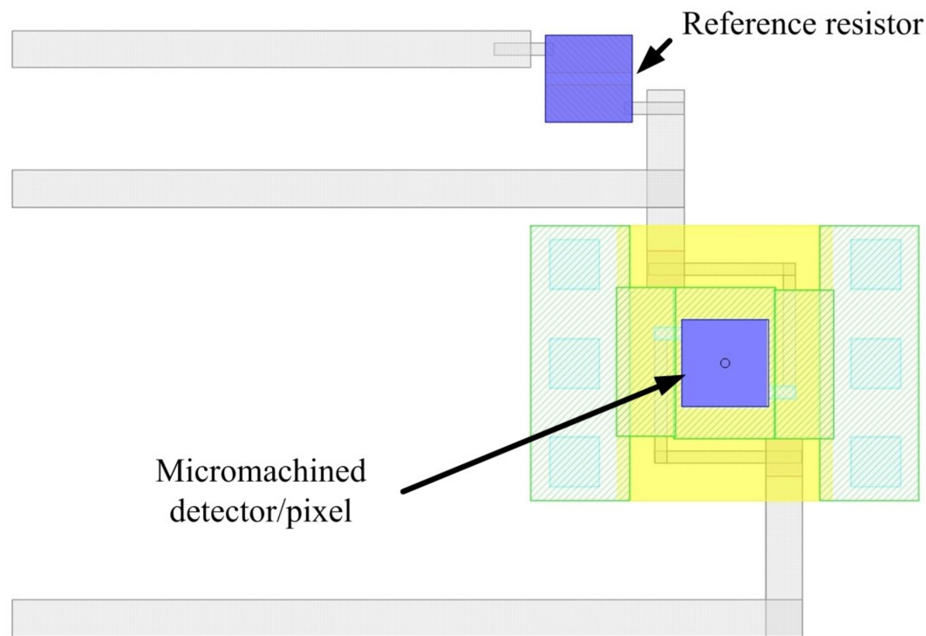

Figure 7-20 Addition of a Reference Resistor with the Micromachined Bolometer.

7.3 Fabrication of the Bolometer

The fabrication of the bolometer was started with the cleaning of a 4-inch <100> p-type wafer by standard TAMDI process followed by the deposition of 200-nm-thick Si_3N_4 passivation layer. After that, PI2611 polyimide release layer was spin coated, patterned and cured at 350 ^oC in N_2 gas environment (detailed discussed in section 6.3). After that, the PI5778 G was spin coated and soft baked for at 105 ^oC. The spin coating was carried out 4 times on this wafer followed by the soft bake. Then, the polyimide was cured at 300 ^oC to achieve a thickness of 70 µm. Next, a 400-nm-thick Si_3N_4 passivation layer was deposited on the polyimide substrate. This passivation layer defines device plane. After that, the sensors were fabricated on this flexible substrate coated silicon wafer. All thin film deposition was accomplished by rf magnetron sputtering followed by the lift-off process. At first, 303-nm-thick aluminum was sputtered on the passivation layer and

patterned [Figure 7-21]. This aluminum acts as a reflector for the bolometer. After that, thinned HD4104 thin polyimide was spin coated, soft-baked and exposed. After developing the polyimide, it was cured at 250 ^{o}C to get a thickness of 548 nm [Figure 7-22]. Next, HD4104 polyimide was spin coated, patterned and cured 250 ^{o}C for 4 hours to get a thickness of 3.27 µm [Figure 7-23]. This polyimide acts as sacrificial layer between the detector and reflector. Then, 109-nm-thick alumina (Al_2O_3) was deposited, patterned by lift-off [Figure 7-24]. The alumina acts as a membrane layer for the detector. After that, 130-nm-thick nichrome (Ni 80%-Cr 20%) was deposited and patterned to connect the bottom electrode with the bondpads. Then, 31.96-nm-thick aluminum bottom-electrode was sputtered on the membrane followed by the lift-off [Figure 7-25]. Then, Si (500nm)-Al (30-nm)- Al_2O_3 (20-nm) layers were deposited one by one and patterned [Figure 7-26].

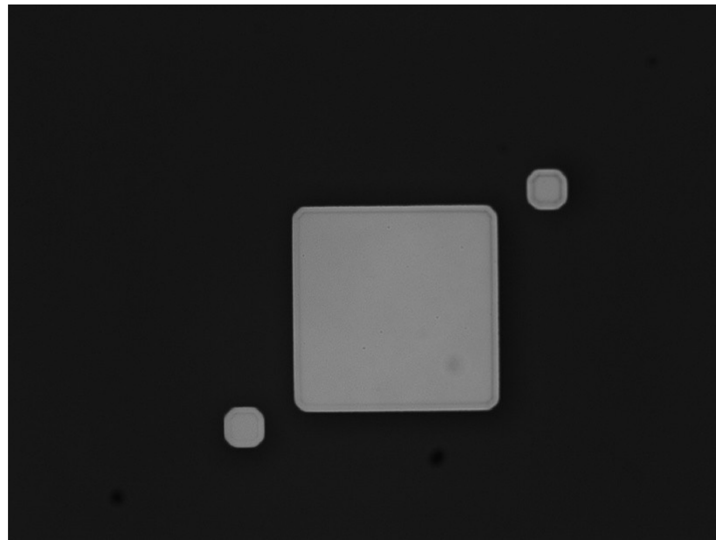

Figure 7-21 Aluminum Mirror Layer

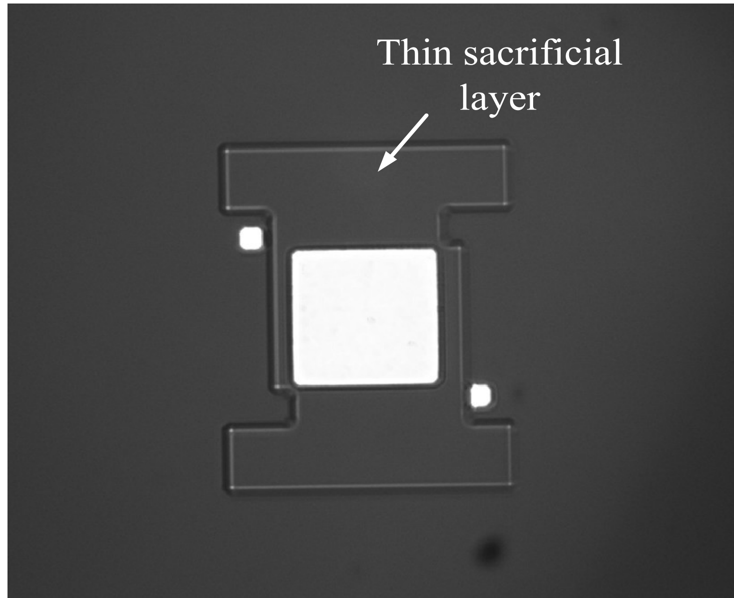

Figure 7-22 Thin Sacrificial Layer

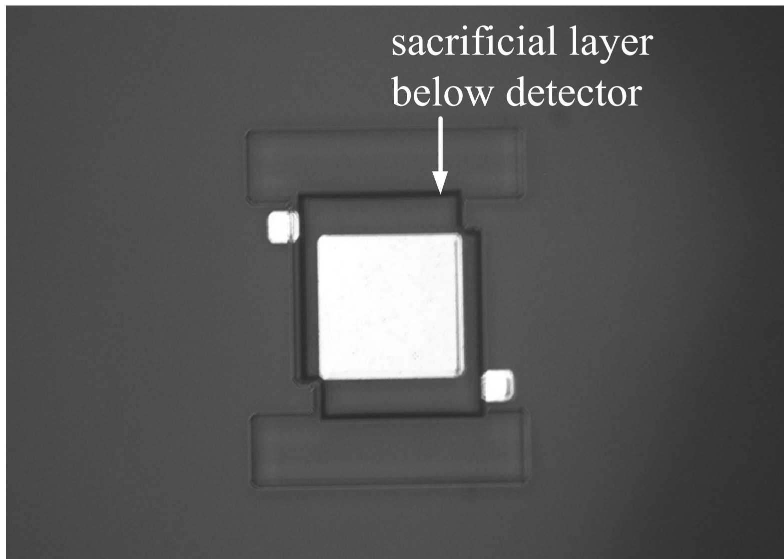

Figure 7-23 Thick Sacrificial Layer below Detector

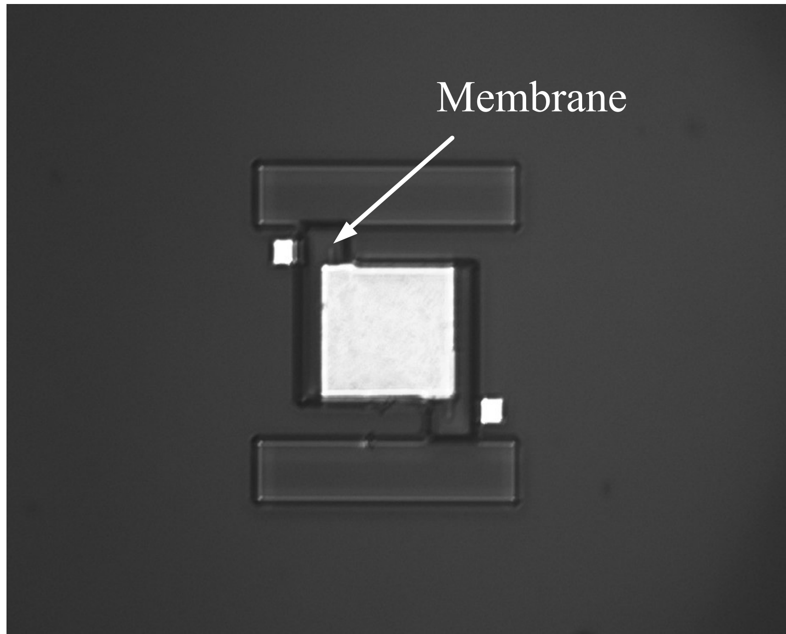

Figure 7-24 Membrane on Top of the Sacrificial Layer

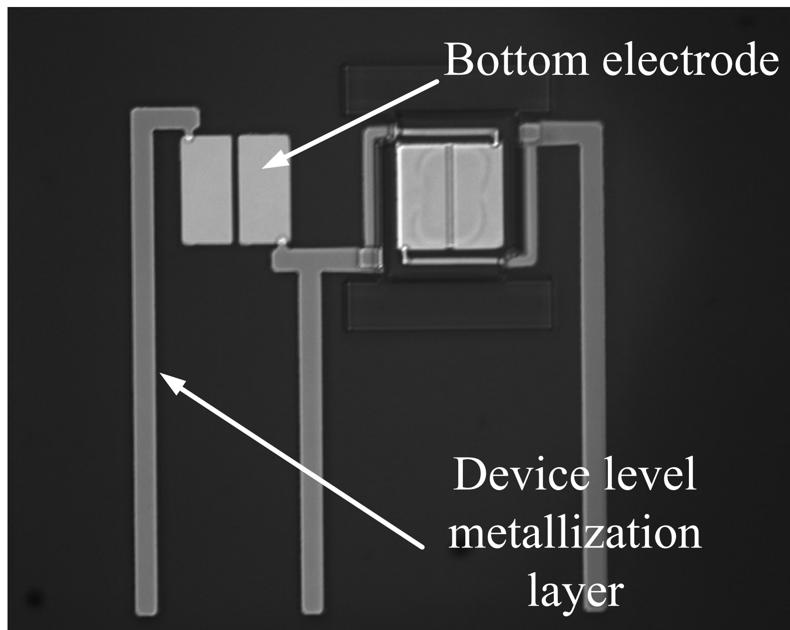

Figure 7-25 Connection of Bottom Electrode and Metallization Layer

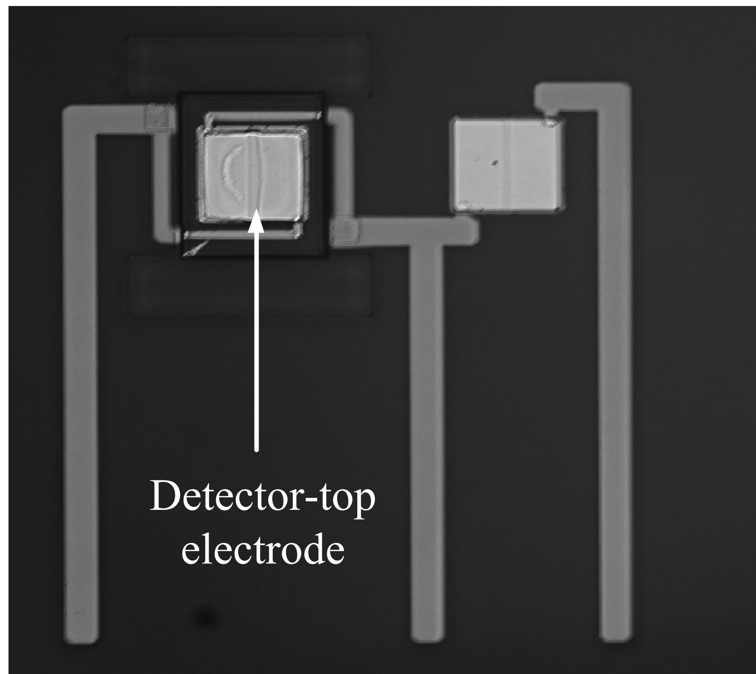

Figure 7-26 Si-Al-Al_2O_3 Tri-Layer

The thin aluminum layer prevents thermal oxidation of silicon at room temperature and also acts the top electrode. The top alumina protects the aluminum from oxidation during surface micromachining. Next, Ti (300-nm)-Au (200-nm) layers were sputtered subsequently and patterned. These layers serve to connect each device with the bondpads for electrical connection and also create the bondpads [Figure 7-27]. After that, HD4104 top sacrificial layer was spin coated, patterned and cured to achieve a thickness of 3.2 μm [Figure 7-28]. Then, 558-nm-thick alumina was sputtered on the structure and patterned which termed as encapsulation layer [Figure 7-29]. This encapsulation layer holds the windows that facilitate surface micromachining. After that, the sacrificial layers were etched in Plasma Therm Asher[Figure 7-30]. Then, the openings of the encapsulation layer were sealed by 2-μm of alumina-packaging layer. Next, the vias were opened near the bondpads area by etching alumina in phosphoric

acid [Figure 7-31]. After that, 720-nm-thick germanium was thermally evaporated on the detector and patterned to form an long-pass optical filter [Figure 7-32]. At last, HD4110 polyimide was spin coated at 1500 rpm for four times, patterned and cured at 250 ^{o}C to achieve a final thickness of 47 μm [Figure 7-33 and Figure 7-34]. This polyimide acts as a superstrate layer to keep the detector at a low stress plane.

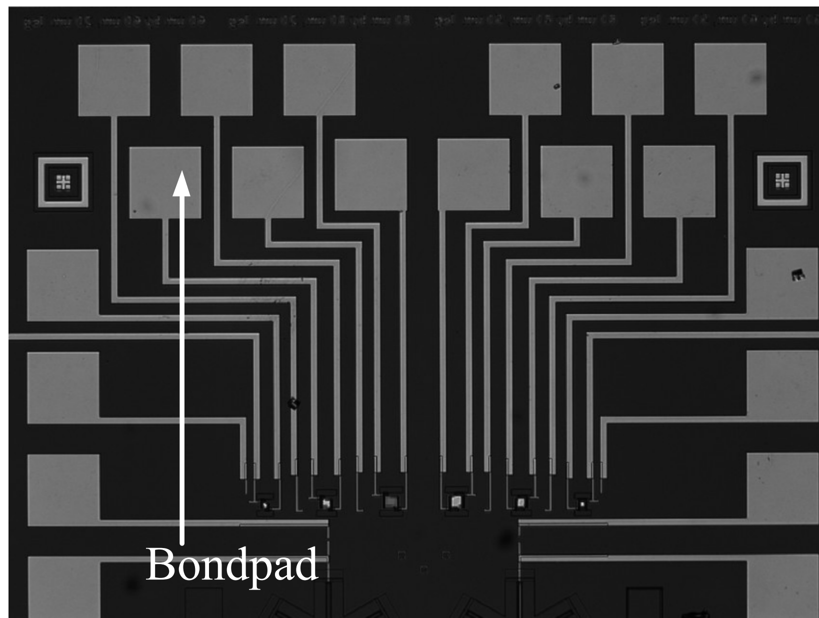

Figure 7-27 Metallization Layer Connecting Each Detector with Bondpads

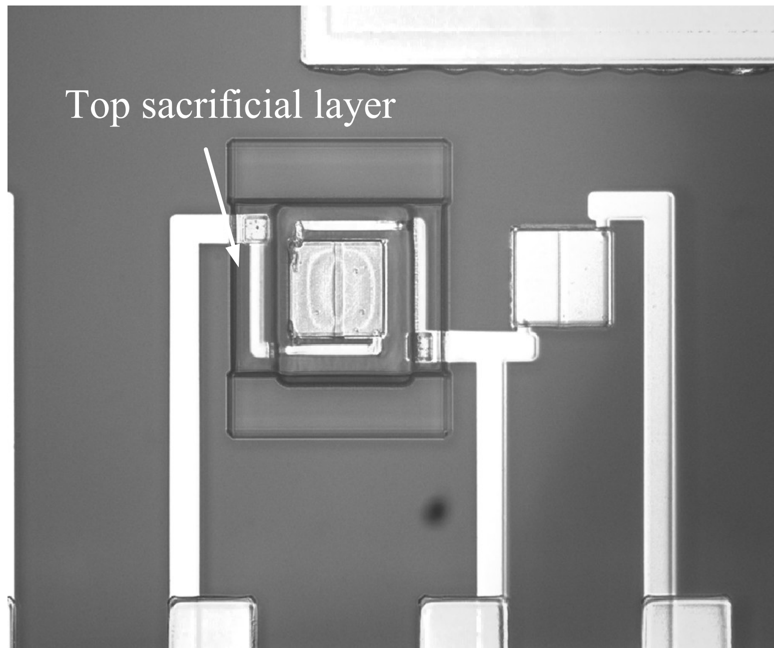

Figure 7-28 Top Sacrificial Layer

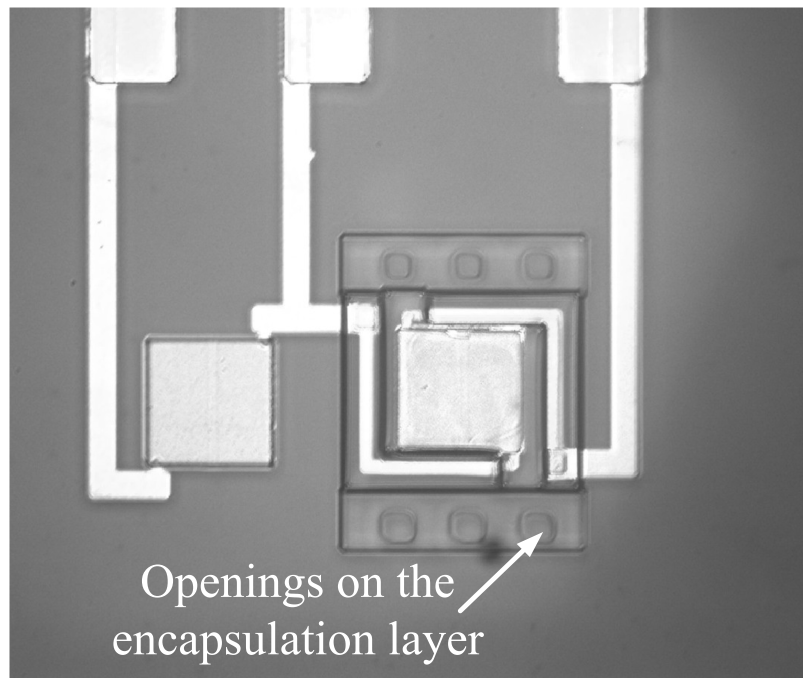

Figure 7-29 Encapsulation Layer

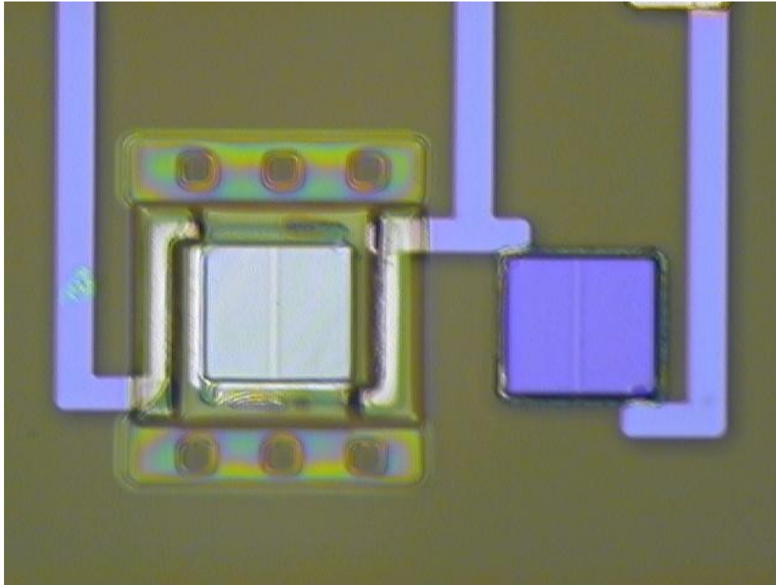

Figure 7-30 Surface Micromachined Bolometer

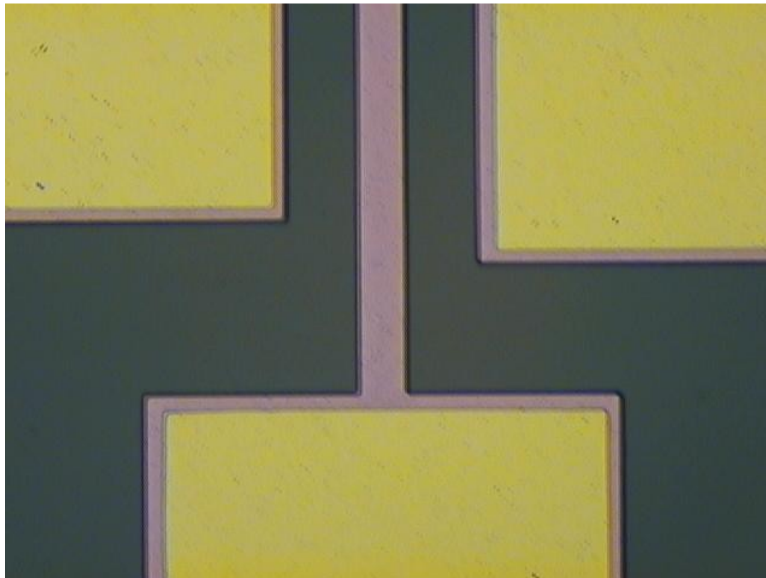

Figure 7-31 Opening Bondpads by Etching for Electrical Connections

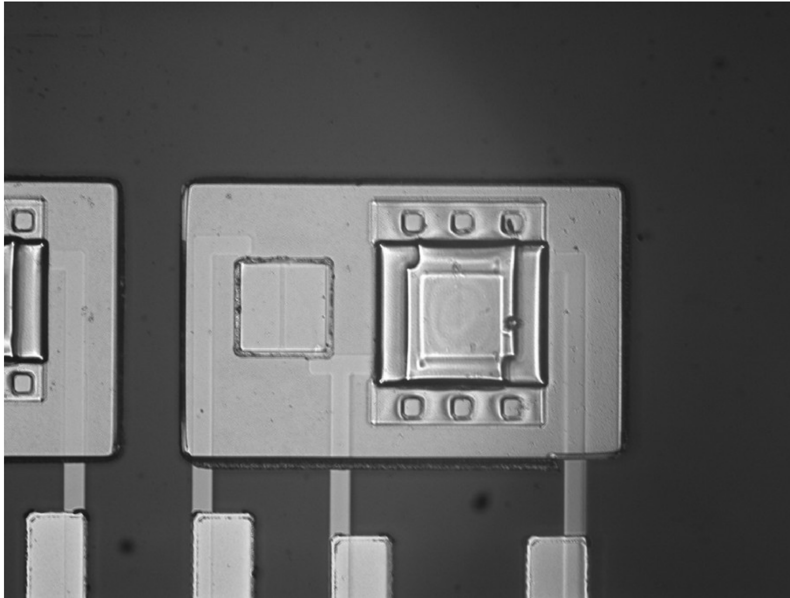

Figure 7-32 The Rectangular Shaped Germanium Optical Filter

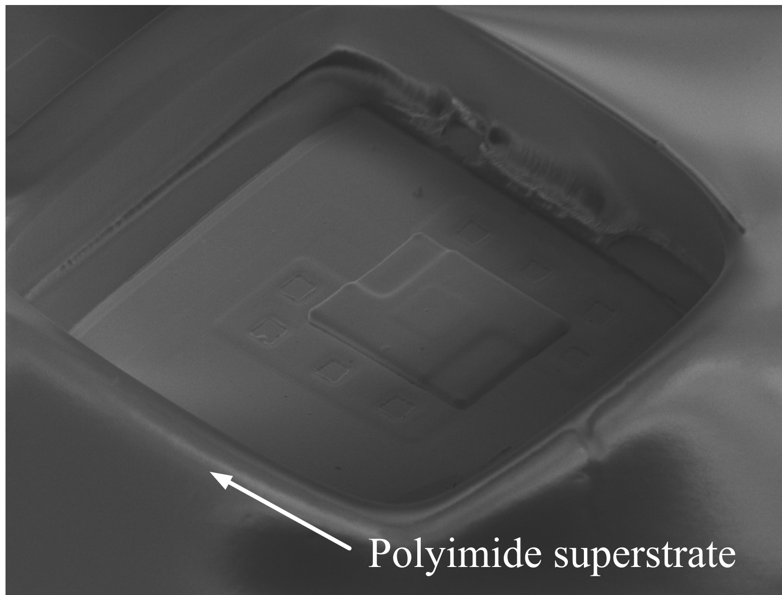

Figure 7-33 HD4110 Flexible Polyimide Superstrate Layer

Figure 7-34 1 cm × 1 cm Die Containing 14 Self-Packaged Bolometers on Flexible Substrate

7.4 Characterization of Sensors on Flexible Substrate

7.4.1 Resistance Measurement

After fabrication of the IR detectors, the resistance of each individual detector was measured in a shielded probe station equipped with HP 4155C semiconductor parameter analyzer. As mentioned earlier, each detector has two resistor, the resistor located inside the vacuum cavity is termed as active resistor (R_a) and the resistor located on the substrate is termed as passive resistor (R_p). The resistance of each individual resistance was measured by *I-V* measurement across each resistor.

7.4.2 IR Response Measurement

The sensors that were fabricated on flexible substrate were characterized for IR response. Since the flexible substrate was attached to the silicon wafer, it was required to characterize the detector by placing the wafer on flat surface. In this case, the IR source was placed in a vertical position. In order to meet this requirement, a specialized tool was

built which is termed as an IR probe station. A total of 7 detectors were characterized to measure the IR response and sensitivity.

7.4.2.1 IR Probe Station

The IR probe station is a custom built probe station as shown in Figure 7-35. A quartz tungsten halogen lamp (operated at 90 W, 8.06 A) was used as the infrared source. The radiation was modulated by passing the IR light through a chopper. A long-pass (5100 nm) was used which blocks the visible light spectra and allow only the infrared radiation to pass through it. A ZnSe lens was used to converge the radiation on the infrared detector that was located on the wafer. The entire set-up was built on an optical bench. The setup was used to measure the irradiance of the infrared radiation by utilizing a reference pyroelectric detector. In order to use the calibrated pyroelectric detector, the set-up was arranged horizontally and the wafer was replaced by the reference pyroelectric detector.

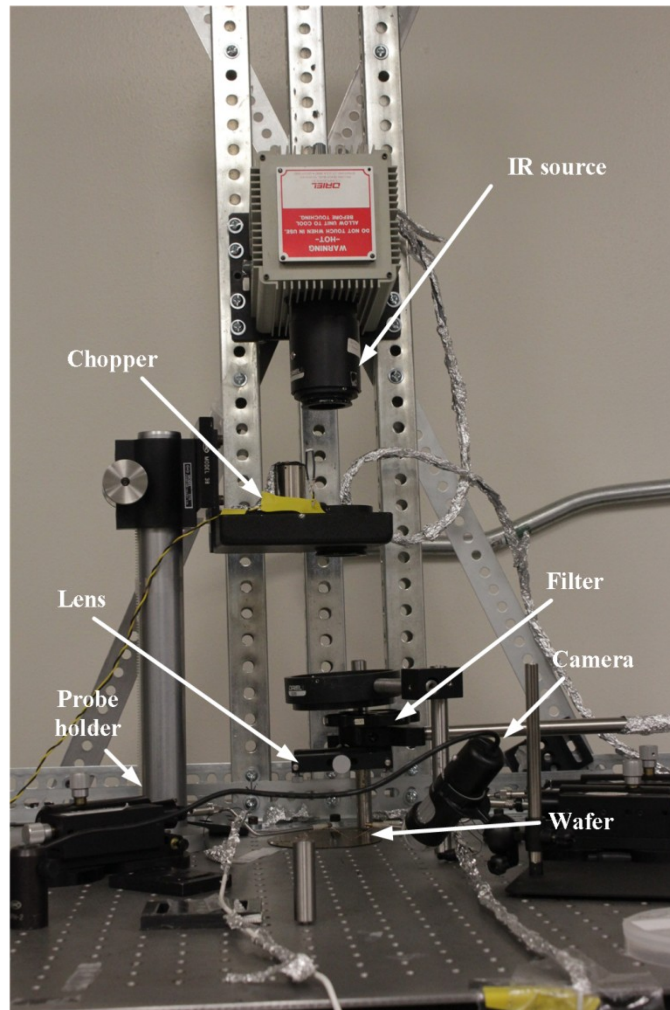

Figure 7-35 IR Probe Station for Testing Bolometer

7.4.2.2 Setup for IR Response Measurement

Once the wafer was placed inside the 'IR probe station', the bolometer was biased by a dc battery source as shown in figure 7-36. The signal from the active resistor was fed to a pre-amplifier (Stanford Research Instruments model SR560) using a gain of 100. The infrared light was modulated to a desired frequency. So, the output across the bolometer was an ac signal. A HP3562A dynamic signal analyzer was used to measure the voltage across the resistor through a pre-amplifier at each frequency and record the

corresponding power spectral density (PSD). Both the rms voltage and PSD were averaged for 10 measurements. The bias voltage of the dc source was varied from ±0.5 V to ±1.25 V in step of 0.25 V. The chopper frequency was varied from 4 Hz to 200 Hz (maximum frequency range of the chopper). At each measurement, a photo-diode was used to measure the variation of the infrared radiation intensity so that the variation of incident flux could be corrected during calculation.

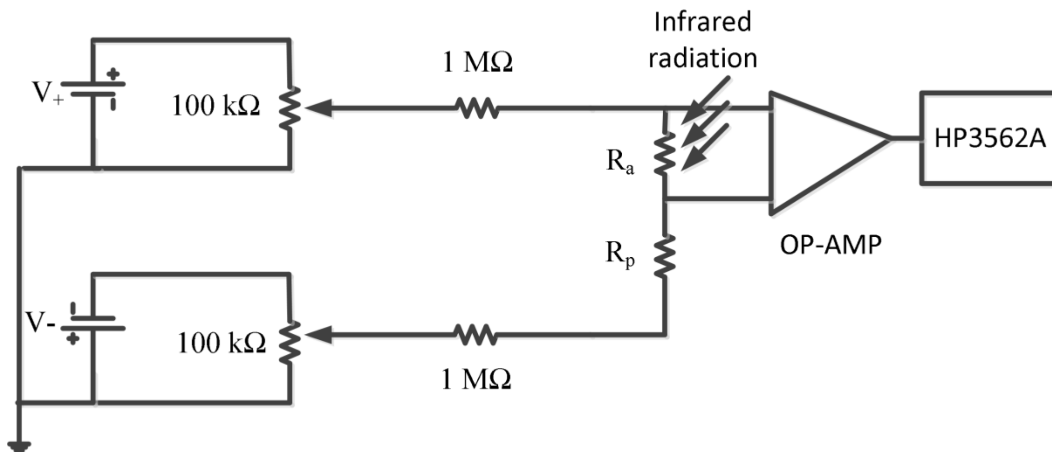

Figure 7-36 Electrical Connection of the Bolometer

7.4.3 Noise Measurement

The noise voltage power spectral density was measured across each active resistor over the frequency range of 10 to 1000 Hz. Since the resistance (Table 7-4) of the bolometer was much larger than the series resistance, the device was voltage biased. The voltage was also varied from ±0.5 V to ±1.25 V in step of 0.25 V. At each bias, the corresponding noise voltage power spectral density was measured with and without infrared radiation. The chopper was turned off during the measurement.

7.5 Results and Discussions

The *I-V* characteristics across the active and passive resistors of a 60 μm × 60 μm pixel with leg length of 20 μm are shown in Figure 7-37. The slope of the *I-V* curve

gives the resistance values of these resistors. Table 7-4 shows the resistance values of active and passive resistor of each detector that was characterized for its IR response. It could be observed here that the resistance value varies for the same sized pixel. The reasons for this variation could be the non-uniformity of the thickness of sensing material over large area, lithographic misalignment of the bottom electrode, oxidation of the electrodes and sensing material around the periphery.

Table 7-4 Resistance Values of the Active and Passive Resistors

Device name	Pixel size (*μm × *μm)	Leg length (μm)	Active resistor (Ω)	Passive resistor (Ω)
35BR_7x4	35 × 35	75	9.00×10^{10}	4.00×10^{09}
35TR_4x6	35 × 35	20	5.00×10^{11}	2.00×10^{11}
60BL_5x2	60 × 60	75	1.00×10^{11}	1.00×10^{09}
60BL_8x7	60 × 60	75	2.00×10^{10}	2.00×10^{10}
60TL_6x6	60 × 60	50	2.00×10^{11}	1.00×10^{11}
60TL_7x9	60 × 60	50	9.00×10^{10}	1.00×10^{09}
60TR_10x7	60 × 60	20	4.00×10^{08}	2.00×10^{08}

The output voltage and power spectral density across the active resistor due to the radiation absorption for the detector termed as 60TL_6x6 is shown in Figure 7-38 and Figure 7-39. The detector was biased at ±1 V and the chopper frequency was set to 40 Hz to modulate the infrared radiation. It could be observed that there is a peak at 39.75 Hz. Even though the chopper was set to run at 40 Hz, the actual chopper frequency always varied slightly. The peak root-mean-square voltage was found to be 1.54×10^{-4} V and noise voltage PSD was found to be 5.54×10^{-11} V^2/Hz.

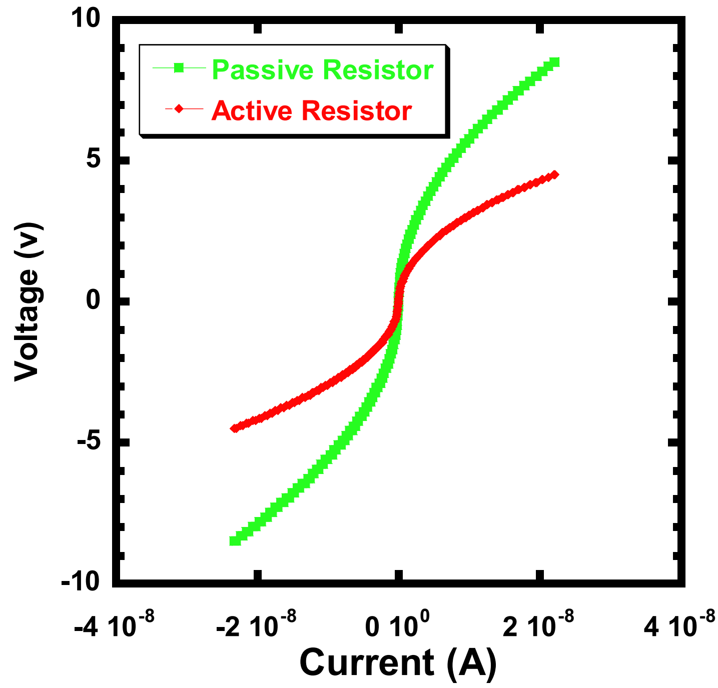

Figure 7-37 *I-V* Characteristics of the Detector Termed as 60TR_10x7

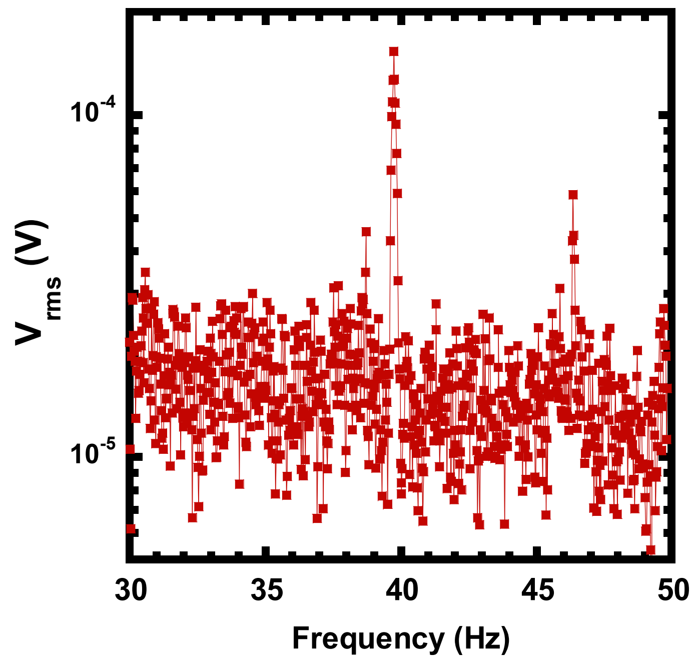

Figure 7-38 Output Voltage across the Bolometer with IR

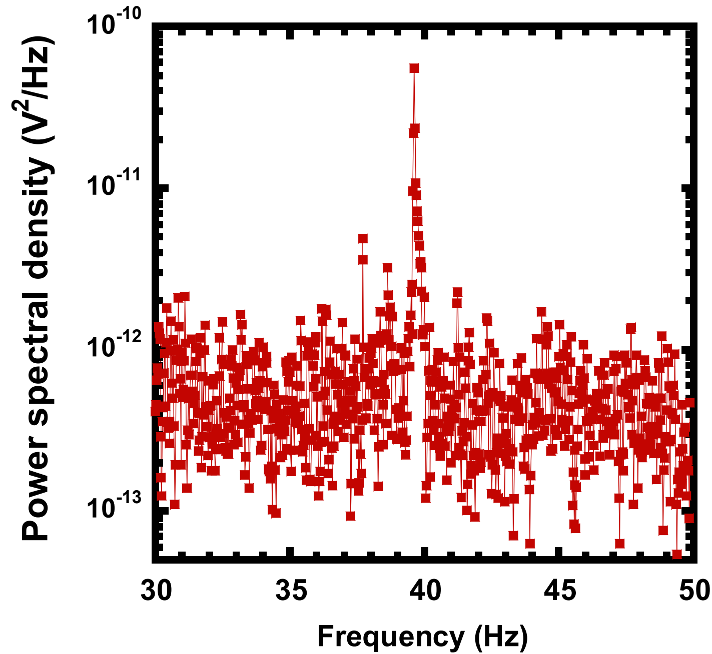

Figure 7-39 Noise Voltage PSD with IR

The noise spectra, after subtracting the background noise, for the detector termed as 60TL_6x6 at the bias voltage of ±1 V are plotted in Figure 7-40 with and without infrared radiation. It could be observed that the PSD with infrared radiation is higher than the PSD without the infrared radiation over the frequency range of 10 to 1000 Hz. Figure 7-41 demonstrates the quadratic voltage dependence of the noise voltage PSD for the detector 60TL_7x9, the normalized Hooge coefficient was calculated to be 1.21×10^{-13}.

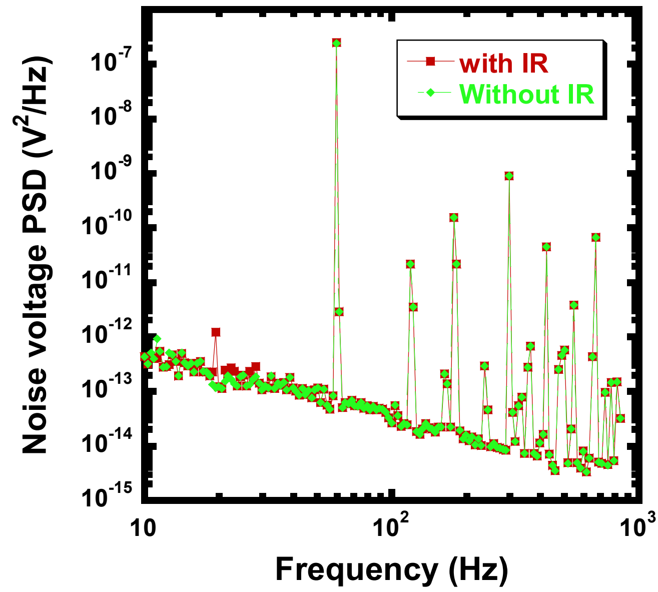

Figure 7-40 Noise Voltage PSD for the Device Termed as 60TL_6x6

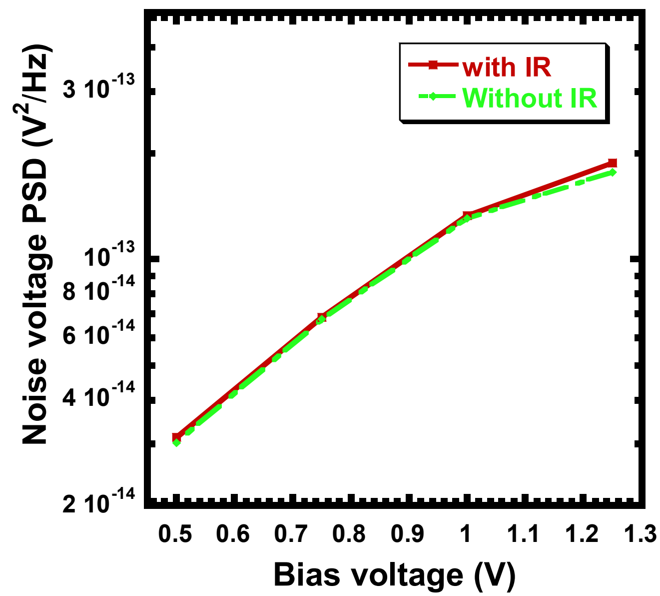

Figure 7-41 Variation of Noise Voltage PSD with the Bias Voltage

7.5.1 Figures of Merit

7.5.1.1 Responsivity

Responsivity is defined as the variation of output signal of the detector with respect to the input radiant power. If the output signal is voltage the responsivity is termed as voltage responsivity, R_v (as in this bolometer) and could be defined as:

$$R_v = \frac{V}{\phi} \tag{7.1}$$

Where Φ is the input radiant flux on the detector which could be calculated from irradiance measured by the reference detector and the area of each detector.

The variation of responsivity with the frequency at ±1 V dc bias for three 60 μm × 60 μm pixel is shown in Figure 7-41. It could be observed here that the responsivity for the detector termed as 60BL_5x2 reduced after 80 Hz and for the detector that was termed as 60TL_6x6 reduced after 100 Hz of the chopper frequency. From the Table 7-2 and Table 7-4, it can be found that the cut-off frequency for the device termed as 60BL_5x2 is 86.35 Hz (simulated), for the device termed as 60TL_6x6 is 113.25 Hz and for the device termed as 60TR_10x7 is 309.6 Hz. So it could be concluded here that those devices showed a reduction after cut-off frequency, due to the heat transfer to the substrate. Figure 7-43 shows the variation of the responsivity with bias voltage for the device termed as 60BL_5x2 at the chopper frequency of 40 Hz. It was observed here that the responsivity is increasing with the bias voltage. In order to demonstrate detail on the variation of responsivity, the bias voltage needs to increase more. But during the experiments, it was observed that above ±1.25 V the bolometer reaches its break down point.

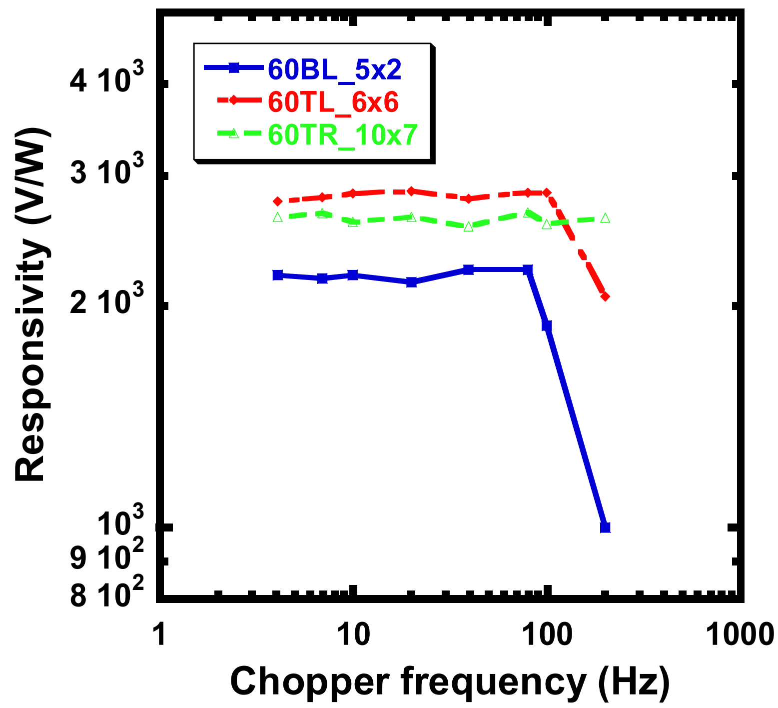

Figure 7-42 Responsivity versus Chopper Frequency for 60 µm × 60 µm Pixel

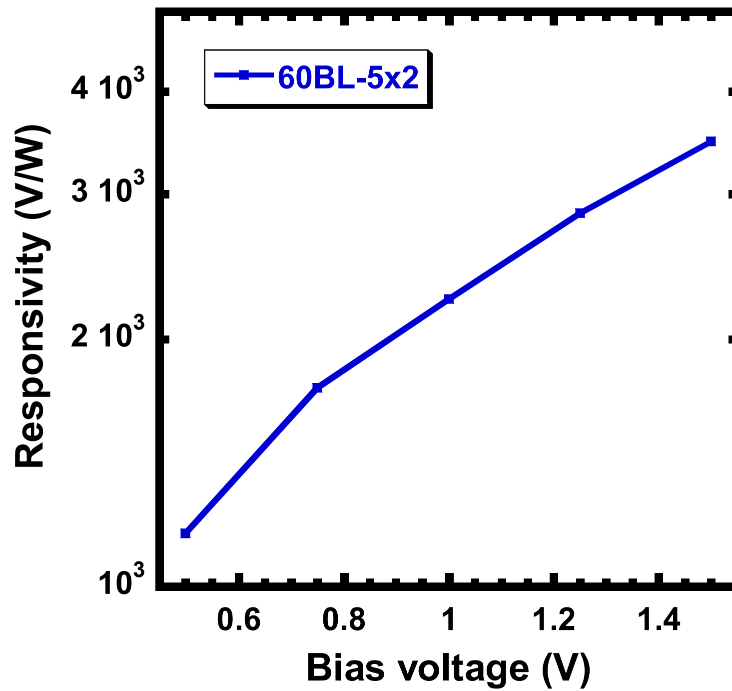

Figure 7-43 Variation of Responsivity with Bias Voltage (Chopper Frequency 40 Hz) for 60 µm × 60 µm Pixel

7.5.1.2 Detectivity

The detectivity, D* is defined as the area normalized signal to noise ratio and can be expressed as:

$$D^* = \frac{R_v \sqrt{A_d \Delta f}}{V_n} \quad (7.2)$$

where V_n is the noise voltage over the electrical bandwidth of Δf and A_d is the area of the detector.

The detectivity over the frequency range of 4 to 200 Hz is shown in figure 7-44 for the bolometer termed as 35BR_7x4 and 35TR_4x6. The detectivity did not show any significant reduction over the frequency range, but showed variation due to the variation of infrared radiation. The cut-off frequency for the detector 45BR_7x4 is 238 Hz

(simulated) and for the detector 35TR_4x6 is 909 Hz which is above the maximum chopper frequency. Figure 7-45 shows the variation of detectivity with the bias voltage for the bolometer termed as 45BR_7x4 at the chopper frequency of 40 Hz. It could be observed here that the detectivity is increasing with the bias voltage. But in order to quantify this variation, bias voltage needs to be increased further.

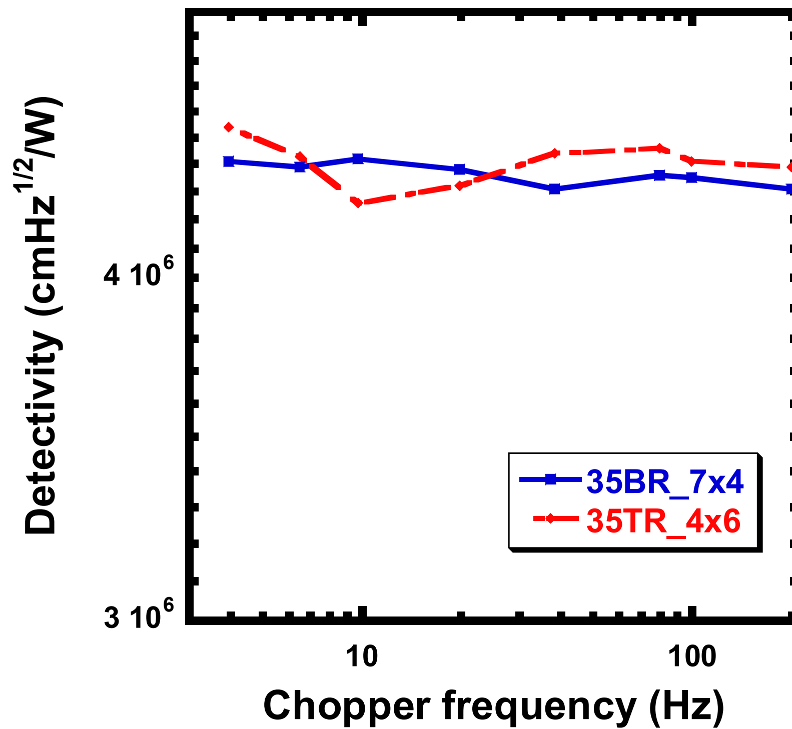

Figure 7-44 Detectivity versus Chopper Frequency for 35 μm × 35 μm Pixel

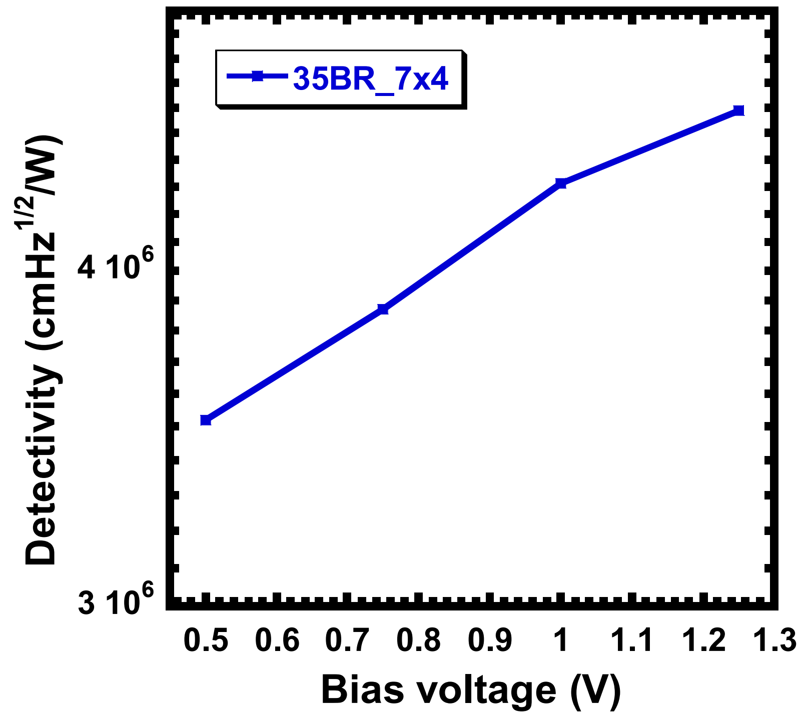

Figure 7-45 Variation of Detectivity with Bias Voltage (Chopper Frequency 40 Hz) for 35 µm × 35 µm Pixel

7.5.1.3 Noise Equivalent Power (*NEP*)

The *NEP* is defined as the incident radiant power necessary to produce a SNR of unity and could be expressed as:

$$NEP = \frac{\sqrt{A_d \Delta f}}{D^*} \quad (7.3)$$

The *NEP* over the frequency range of 4 Hz to 200 Hz is shown in Figure 7-46 for the detector 35BR_7x4 and for the detector 35TR_4x6. It could be observed that the *NEP* decreases once the cut-off frequency was reached. The variation of *NEP* with bias voltage (Figure 7-47) shows that with the increase of voltage the *NEP* is decrease with a

decremented slope. The reason could be the NEP was saturating as the bias voltage was increasing.

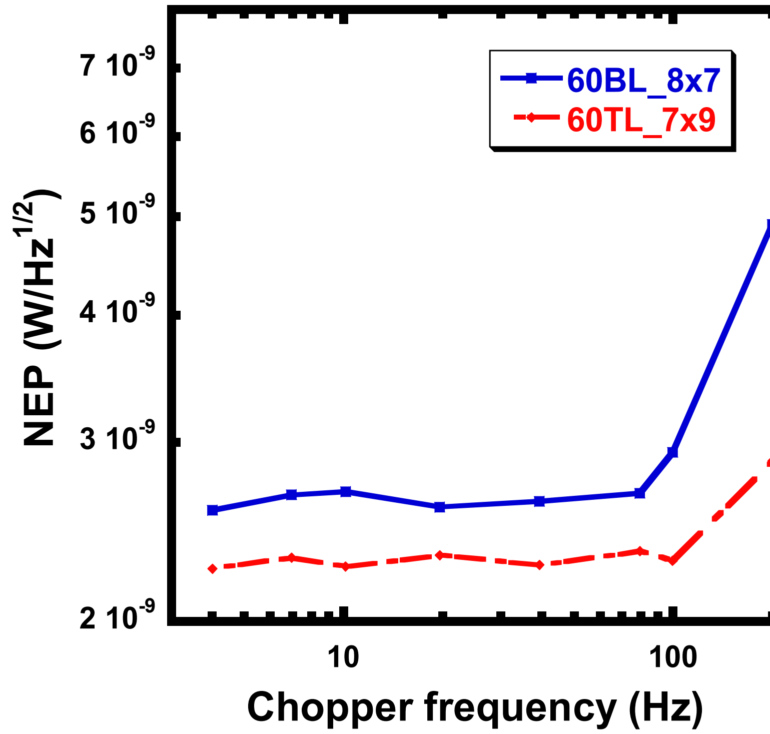

Figure 7-46 *NEP* versus Chopper Frequency for 60 μm × 60 μm Pixel

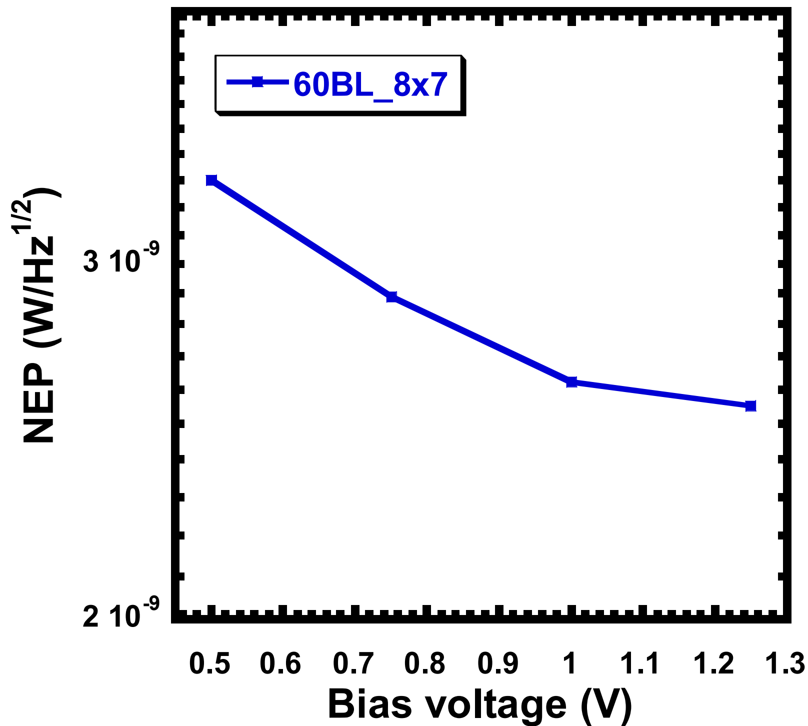

Figure 7-47 Variation of *NEP* with Bias Voltage (Chopper Frequency 40 Hz) for 60 µm × 60 µm Pixel

The measured responsivity, detectivity and *NEP* of the detectors are summarized in Table 7-5.

It was observed that the detectivity of the 35 µm × 35 µm bolometers is higher than the 60 µm × 60 µm bolometers. One of the reasons could be the 35 µm × 35 µm bolometers are surface micromachined completely. For the 60 µm × 60 µm bolometers, there is a chance that some debris of sacrificial layer left which may either absorbing some radiation or creating a conductive path through it. The thickness of different layers was optimized so that some debris of polyimide on the cavity will cause a decrease in the affective absorption of radiation by the detecting material.

Table 7-5 Summary of the Detectors Characterized for IR Respionse

Device name	Simulated cut-off frequency (Hz)	Responsivity at 1 V and 40 Hz (V/W)	Detectivity at 1 V and 40 Hz (cmHz$^{1/2}$/W)	*NEP* at 1V and 40 Hz (W/Hz$^{1/2}$)
35BR_7x4	238	3.71×10^{3}	4.31×10^{6}	8.12×10^{-10}
35TR_4x6	909	3.78×10^{3}	4.44×10^{6}	7.88×10^{-10}
60BL-5x2	86.35	2.24×10^{3}	2.08×10^{6}	2.89×10^{-9}
60BL_8x7	86.35	2.58×10^{3}	2.29×10^{6}	2.62×10^{-9}
60TL_6x6	113.25	2.79×10^{3}	2.25×10^{6}	2.66×10^{-9}
60TL_7x9	113.25	2.89×10^{3}	2.64×10^{6}	2.27×10^{-9}
60TR_10x7	309.6	2.56×10^{3}	2.15×10^{6}	2.79×10^{-9}

One of 60 µm × 60 µm bolometer was characterized (was not mentioned in table) which showed almost 100 times higher responsivity than the detectors mention in the Table 7-5. But the device was destroyed during etching of the silicon wafer. The time spent performing the surface micromachining stage for that particular detector was longer than the detectors that were fabricated later and characterized. So it could be possible that micromachining for longer time would remove polyimide debris completely and increase the responsivity and detectivity. But the longer micromachining time can result in unwanted etching of the Au-bondpads which was observed during fabrication. Depositing a thin layer of alumina on top of Au-bondpads can reduce chance of unwanted etching. The bondpads undergo underwent etching to open the vias and expose the bondpads through the packaging layer. So depositing a thin layer of alumina on top of the bondpads would not increase fabrication complexity or any addition mask.

The maximum detectivity of the detector that was found is compared with some other detectors that are found in literature in Table 7-6.

Table 7-6 Comparison of Detectivity

Reference	Device-level long-pass optical filter	Detecting material	Maximum detectivity ($cmHz^{1/2}/W$)	NEP ($W/Hz^{1/2}$)	Biasing power
Current work	Yes	a-Si	4.54×10^{6} at 4 Hz	7.72×10^{-10} at 4 Hz	5.71 pW
Mahmood *et al.* [108]	No	YBCO	5.2×10^{5} at 398 Hz	7.1×10^{-7} at 5 Hz	597 nW
Rana *et al.* [112]	No	a-$Si_xGe_{1x}O_y$	8.27×10^{6}	4.84×10^{-10}	2.97 μW

From the Table 7-6, it could be observed that the detectivity of the vacuum packaged detector is comparable to the other vacuum packaged detectors found in literature. The incorporation of long-pass filter did not affect the detector performance and the concept of double layer absorption of radiation also works. If there was no long-pass filter (which absorbs and reflects infrared radiation) the absorption would be more and the detectivity would be significantly higher than the counterparts. The bias power was mentioned even though first two works on the table were voltage biased and the last work was current biased. The bias voltage in our case could not be increased since it cause break down of the detector.

7.6 Conclusions

Uncooled resistive microbolometers were designed, fabricated and characterized on flexible substrate. In the design part, a nanomesh absorber was included to study its effect on increasing absorption of radiation. Several other concepts were also studied

and applied in the fabrication step such as: double layer absorber structure, incorporation of device-level long-pass filter, μm-size and mm-size device level packaging of the detector. The detector with nanomesh absorber could not be fabricated since it requires specialized tool such as e-beam lithography for patterning. But the detectors were fabricated on flexible substrate and characterized to check the other three concepts. A reference resistor was utilized to subtract the room temperature heating effect on the detector performance. The detectors were characterized for measuring IR response under custom built IR probe station. The detector showed a maximum responsivity of 3.78×10^3 V/W, detectivity of 4.44×10^6 cmHz$^{1/2}$/W and a minimum *NEP* of 2.78×10^{-9} W/Hz$^{1/2}$ at a chopper frequency of 40 Hz and 1 V dc bias for a 35 μm × 35 μm detector.

Chapter 8

Conclusions and Future Directions

8.1 Conclusions

The temperature sensors were fabricated on flexible substrate where amorphous silicon was used as a sensing material. The amorphous silicon showed a maximum temperature coefficient of resistance of 2.88 %/K. The average value of normalized Hooge coefficient, $K_{1/f}$ was found to be 1.2×10^{-11}, where the noise equivalent temperature was found to be 5.5 mK at a bandwidth of 940 Hz (1-941 Hz).

The relative pressure sensors were fabricated on flexible substrate where nichrome (Ni-80%/Cr-20%) was used as a sensing material. The average gauge factor for nichrome piezoresistor was found to be 1.75 and the Young's modulus of the Al_2O_3 was calculated to be 405.81 GPa. The average value of normalized Hooge coefficient $K_{1/f}$ was found to be 1.89×10^{-10}. The average sensitivity was calculated to be 0.44 mV/MPa. The average value of noise equivalent pressure (*NEPr*) was found to be 58.23 kPa at a bandwidth of 8 Hz (1-8 Hz)..

The absolute pressure sensors were fabricated on flexible substrate where nichrome (Ni-80%/Cr-20%) was used as a sensing material, and the entire sensors were packaged to create a reference cavity. The average gauge factor for nichrome piezoresistor was found to be 1.95 and the Young's modulus of the Al_2O_3 was calculated to be 406.67 GPa. The average value of normalized Hooge coefficient $K_{1/f}$ was found to be 4.64×10^{-11}. The average sensitivity was calculated to be 1.25 nV/Pa. The average value of noise equivalent pressure (*NEPr*) was found to be 7.8 kPa at a bandwidth of 8 Hz (1-8 Hz).

Modified lead titanate was deposited on gold electrode and characterized. The lead calcium titanate showed a pyroelectric coefficient of 40×10^{-5} C/m^2-K and lead zirconium titanate demonstrated a pyroelectric coefficient of 28×10^{-5} C/m^2-K after poling. It was observed that the poling caused an increase of the pyroelectric coefficient by 10 times.

In chapter 6, incorporation of release layer was studied and was observed that depositing a flexible polyimide as a release layer helps to detach flexible substrate from the rigid silicon wafer after fabrication. The release layer can also withstand high processing temperature and survive during lift-off process.

At last, bolometer was designed, fabricated on flexible substrate and characterized. The design includes nanomesh absorber, double layer absorber for infrared radiation, long-pass optical filter, and mm-sized device-level packaging. The characterization results showed a maximum responsivity of 3.78×10^3 V/W , detectivity of 4.44×10^6 cmHz$^{1/2}$/W and a minimum *NEP* of 2.78×10^{-9} W/Hz$^{1/2}$ at a chopper frequency of 40 Hz and 1 V dc bias.

Different types of sensors were fabricated on flexible substrate toward building a smart skin. In order to characterize those sensors specialized characterized tools were also built. All these sensors were fabricated as MESA structure for ease of tactile sensing, but they could be applicable to robotics, biomedical and smart devices.

The utilization of conventional fabrication technology to fabricate flexible, bendable sensors gives direction to future fabrication technology without any increase in cost. Moreover, the incorporation of high temperature release layer will allow increasing the yield during separation of flexible substrate (containing sensors and devices) from rigid wafer. The process doesn’t restrict application of any solvent or acids. The demonstration of dicing of the detectors for easy removal from the wafer will help to save

the wafer. The process could be accelerated further to reuse same wafer, which in turn can be cost effective and may bring a new era “green technology”. The application of device-level packaging layer will help to reduce cost and complexities of packaging sensor, which makes the device to be self-packaged. In broader sense, this research will give future direction to build self-packaged sensors on rollable, bendable flexible substrate which will reduce the cost of fabrication.

Several questions were asked in chapter 1; it would be good time to answer those questions based on the research that has been conducted. Those are as follows:

- Are the techniques feasible for manufacturing rather than research?
- What would be the cost of modifying the processing tools?
- Even though there was no need to use any specialized tool for fabrication, but the incorporation of easy release layer may
- What is the minimum feature size that could be achieved in these techniques?
- What is the maximum temperature that these sensors could survive compared to their rigid counterparts?
- Is the fabrication process limiting the application of the sensors?
- Is there any other way to utilize the current fabrication tools while avoiding the necessity of the modification?
- Since the sensors do not need the rigid substrate, is it possible to reduce the overall processing cost?

From the current research, it could be explained that the fabrication of sensors on flexible substrate could be manufactured in batch; chapter 6 gives direction how to fabricate the sensors on flexible substrate and separate easily without any complexities. But a tool that can remove easy sacrificial layer from the edge of the wafer after spin-

coating will help to get more control over batch production. Otherwise, no specialized tool is required which may increase cost of modification, implementation of the process. The minimum feature size that was achieved was 2 μm; the proximity lithography was utilized. In order to pattern smaller feature and achieve uniformity and high resolution step-by-step lithography could be used. This is also obvious for their rigid counterparts. Since the sensors were fabricated on flexible substrate and the flexible substrate has lower melting temperature (around 550 ^{o}C) than most of the rigid substrates, they can not apply to high temperature applications. It somewhat limits the sensors application; but the flexibility increases sensor's overall application which could not imagined for the sensors on rigid wafer.

8.2 Directions for Future Work

The temperature sensor sensing material could be replaced by other sensing material such as VO_x to investigate it's performance.

All these sensors were characterized on flat substrate. This sensors need to characterized on curved surface and the results could be compared with the results measured on flat substrate. The easy release layer could be incorporate to facilitate easy removal of sensors from rigid silicon substrate as well as to increase the yield.

It was observed that for bolometer, substrate and superstrate were separated from each other when attempt was taken to dice the wafer. An adhesion promoter can be used in such case before depositing superstrate layer.

The bolometer can be characterized to measure 'view angle' compared with the IR source and analyzed how the bolometer responds in such situation. It could be done by packaging a die on a flat package and placing it an angle with the optical bench so that radiation falls on the detector at a particular angle.

The bolometer could be also fabricated without the long-pass optical filter in order to compare it's performance with other bolometer found in literature.

The bolometer with nanomesh absorber was designed but it was not fabricated. The nanomesh bolometer can be fabricated by utilizing e-beam lithography.

Since the concepts behind the bolometer design works, the design can be used for fabricating pyroelectric infrared detector. One of the major challenges in fabricating pyroelectric infrared detector is that the detecting material requires high temperature for deposition and annealing. The minimum temperature, that the pyroelectric material was deposited, was 550 ^{o}C (PCT). The glass transition temperature of the polyimide sacrificial layer is below this temperature. In order to deposit a sacrificial layer that can withstand such temperature, chromium could be used as a sacrificial layer. But before removing the sacrificial layer, the pyroelectric material needs to be poled.

The flexible substrate also needs to be replaced by either polyimide (that can survive in such high temperature) or thin (35-40 μm thick) silicon as substrate. In order to use silicon as substrate, SOI wafer could be used where the detector can be fabricated on top surface and once the fabrication is done the oxide can etched to get the detectors on flexible silicon substrate.

The entire research also raises some other questions which may give future directions of research:

- What are the alternatives for high temperature flexible substrate and how to apply those to current fabrication technology?
- Is it possible to fabricate μm-sized device directly on flexible substrate without using a rigid carrier wafer?
- How to bond the flexible circuitry on a curved medium?

- How to engineering the curvature of flexible substrate for specific applications?
- How does heat dissipate on the flexible substrate compared to their rigid counterparts in case of denser fabrication of devices?
- If some devices are fabricated on flexible substrate and some on rigid substrate, how do they interact with each other, how can unequal stretch or heat affect each other?
- What would be the stretching effect on multi-layer device? What conditions make those devices to fail?
- Is it possible to fabricate bio-degradable flexible substrate and sensors?
- How to fabricate CMOS electronics on flexible substrate without extensive modification?

Appendix A

Equations and Parameters for Calculating Responsivity, Detectivity and *NEP* Used in the Microbolometer Simulation

Constants used in calculations

n_{al} = 34.46 -105.600i complex refractive index of aluminum [113]

n_{alu}= 0.624 -1.0307i complex refractive index of alumina [114]

$n_{silicon}$= 3.42 - 8 × 10^{-5}i complex refractive index of silicon [115]

n_{Ge}= 3.905 - 2 × 10^{-5}i complex refractive index of Germanium [115]

β=0.0281 %/K temperature coefficient of resistance

Calculating intrinsic impedance of a certain material

$$\eta = \sqrt{\frac{\mu'}{\varepsilon}} \quad \text{(A.1)}$$

where

μ' complex permeability

ε permittivity of a certain material, which could be calculated by

$$\varepsilon = \varepsilon_0 . n^2 \quad \text{(A.2)}$$

where

n refractive index of that particular material

ε_0 permittivity of air.

Calculating voltage responsivity for a bolometer

$$R_v = \frac{-R_o}{(R_o + R_d)} V_{bias} R_d \beta \frac{\eta_{eff}}{G_{eff}\sqrt{1+\omega^2 {\tau_{th}}^2}} \quad \text{(A.3)}$$

where

η_{eff} absorption coefficient of the detector

V_{bias} biasing voltage

R_d resistance of the detector

R_o reference resistance

ω modulating frequency of IR radiation (Chopper frequency)

τ_{th} thermal time constant

G_{eff} effective thermal conductance of the detector

G_{eff} could be calculated as:

$$G_{eff} = G_{th} + G_{rad} - V_{bias}^2 \left(\frac{R_o - R_d}{\left(R_o + R_d\right)^2} \right) \beta R_d \qquad \text{(A.4)}$$

where

G_{th} thermal conductance due to conduction process

G_{rad} thermal conductance due to radiative cooling

Calculating 1/f noise voltage:

$$V_{1/f} = \sqrt{\frac{K_{1/f} V_{dc} \Delta f}{f}} \qquad \text{(A.5)}$$

where

f frequency

Δf frequency bandwidth

V_{dc} biasing voltage

$K_{1/f}$ normalized Hooge coefficient

Calculating Johnson noise voltage:

$$V_J = \sqrt{4 K_B T R_d \Delta f} \qquad \text{(A.6)}$$

where

k_B Boltzmann constant

T room temperature

Calculating thermal fluctuation noise voltage:

$$V_{TF} = \frac{R_v}{\eta_{eff}} \sqrt{4K_B T^2 G_{th} \Delta f} \tag{A.7}$$

Calculating background noise voltage:

$$V_{BG} = \frac{R_v}{\eta_{eff}} \sqrt{4K_B T^2 G_{rad} \Delta f} \tag{A.8}$$

Calculating total noise voltage:

$$V_n = \sqrt{V_{1/f}{}^2 + V_J{}^2 + V_{TF}{}^2 + V_{BG}{}^2} \tag{A.9}$$

Calculating noise equivalent power:

$$NEP = \frac{V_n}{R_v} \tag{A.10}$$

Calculating detectivity of the detector:

$$D^* = \frac{\sqrt{A_d \Delta f}}{NEP} \tag{A.11}$$

where

A_d area of the detector

References

[1] Z. Celik-Butler and D. P. Butler, “Flexible sensors- a review,” *J. of. Nanoelec. & Optoelec.,* vol. 1, pp. 194-202, 2006.

[2] A. Hanson, British Patent 4,681, 1903.

[3] I. C. Cheng and S. Wagner, “Overview of flexible electronics technology,” *Electron. Mat. : Sci. & Technol.,* vol. 11, pp. 1-28, 2009.

[4] V. J. Lumelsky, M. S. Shur, and S. Wagner, “Sensitive skin,” *IEEE Sensors J,* vol. 1, no. 1, pp. 41-51, 2001.

[5] D. H. Kim, J. H. Ahn, W. M. Choi, H. S. Kim, T. H. Kim, J. Song, Y. Y. Huang, Z. Liu, C. Lu and J. A. Rogers, “Stretchable and foldable silicon integrated circuits,” *Science*, vol. 320, pp. 507-511, 2008.

[6] H. Kim and K. Najafi, "Characterization of aligned wafer-level transfer of thin and flexible parylene membranes," *J. Microelectromech. Syst.*, vol. 16, no. 6, pp. 1386-1396, 2007.

[7] A. Drost, G. Klink, M. Feil and K. Bock, "Studies of fine pitch patterning by reel-to-reel processes for flexible electronic systems," *Proc. Int. Symp. Adv. Packaging Maters: Processes, Properties and Interfaces,* pp. 130-135, Irvine, CA, 16-18 March 2005.

[8] G. S. Nadvi, D. P. Butler, Z. Celik-Bulter, I. E. Gonenli, “Micromachined force sensors using thin film nickel-chromium piezoresistors, ” *J. Micromech. Microeng.*, vol. 22, no. 6, pp. 065002, 2012.

[9] F. B. Kiewiet, M. P. Bruijn, H. F. C. Hoevers, A. C. Bento, W. A. Mels and P. A. J. Korte, “Fabrication and characterization of infrared and sub-mm spiderweb bolometers with low-T_c superconducting transition edge thermometers, ” *IEEE T.*

Appl. Supercon., vol. 9, no. 2, pp. 3862-3865, 1999.Korte, “Fabrication and characterization of infrared and sub-mm spiderweb bolometers with low-T_c superconducting transition edge thermometers, ” *IEEE T. Appl. Supercon.*, vol. 9, no. 2, pp. 3862-3865, 1999.

[10] P. D. Maushkopf, J. J. Bock, H. D. Castillo, W. L. Holzapfel and A. E. Lange, “Composite infrared bolometers with Si_3N_4 micromesh absorbers, ” *Appl. Optics*, vol. 36, no. 4, pp. 765-771, 1997.

[11] J. J. Bock, H. M. D. Castillo, A. D. Turner, J. W. Beeman, A. E. Lange and P. D. Mauskopf, “Infrared bolometers with silicon nitride micromesh absorbers,” *Proc. 30th EsLAB Symp.*, pp. 119-122, 1996.

[12] J. M. Gildemeister, A. T. Lee and P. L. Richards, “A fully lithographed voltage-biased superconducting spiderweb bolometer, ” *Appl. Phys. Lett.*, vol. 74, no. 6, pp. 868-870, 1996.

[13] A. T. Lee, S. F. Lee, J. M. Gildemeister and P. L. Richards, “Voltage-biased superconducting bolometers for infrared and mm-wave astronomy,” *Proc. 7th Intl. Work. Low-Temp. Det.*, pp. 123-125, 1997.

[14] W. H. Han, X. K. Chen, E. Q. Xie, G. Wu, J. P. Yang, R. Wang, S. Z. Cao and Y. L. Wang, “High negative temperature coefficient of resistance of heteroepitaxial (Ba, Sr) TiO_3 single crystal films prepared by pulsed laser deposition”, *Surface & Coatings Tech.*, vol. 209, pp. 5680-5683, 2007.

[15] F. J. Gonzalez, M. Abdel-Rahman and G. D. Boreman, “Antenna-coupled VOx thin-film microbolometer array,” *Microwave & Optical Tech. Lett.,* vol. 38, no. 3, pp. 235-237, August 5, 2003.

[16] E. Mottin, A. Bain, J. L. Martin, J. L. Ouvrier-Buffet, S. Bisotto, J. J. Yon and J.L. Tissot, “Uncooled amorphous silicon technologyenhancement for 25 μm pixel pitch achievement,” *Proc. SPIE*, vol. 4820, pp. 200-207, 2003.

[17] E. Obermeier and P. Kopystynski, “Polysilicon as a material for microsensor applications,” *Sens. Actuat. A-Phys.*, vol. 30, no. 1-2, pp. 149-155, January 1992.

[18] A. Mahmood, D. P. Butler and Z. Celik-Butler, “Micromachined bolometers on polyimide,” *Sensors and Actuators A*, vol. 132, no. 2, pp. 452-459, 2006.

[19] M. M. Rana and D. P. Butler, “Radio frequency sputtered $Si_{1-x}Ge_x$ and $Si_{1-x}Ge_x O_y$ thin films for uncooled infrared detectors, ” *Thin Solid Films*, vol. 514, pp. 355-360, 2006.

[20] R. Ambrosio, M. Moreno, J. Mireles, A. Torres, A. Kosarev and A. Heredia, “An overview of uncooled infrared sensors technology based on amorphous silicon and silicon germanium alloys,” *Phys. Status Solidi C*, vol. 7, no. 3-4, pp.1180-1183, 2010.

[21] M. R. Madani and P. K. Ajmera, “Low temperature oxidation of silicon”, *Elect. Letts.*, vol. 24, no.14, pp. 856- 857, 1988.

[22] G. Radnoczi, A. Robertsson, H. T. G. Hentzell. S. F. Gong and M. A. Hasan, “Al induced crystallization of a-Si,” *J. Appl. Phys.,* vol. 69, no. 9, pp. 6394-6399, 1991.

[23] M. Ahmed, M. M.Chitteboyina, D. P. Butler and Z. Celik-Butler, “Temperature sensor in a flexible substrate,” *IEEE Sensors J.,* vol. 12, no. 5, pp. 864-869, May 2012.

[24] Z. Celik-Butler, *1/f Noise in semiconductor devices,* Ph.D, Thesis, University of Rochester, 1987.

[25] F. N. Hooge, “1/f noise sources,” *IEEE Trans. Elec. Dev.*, vol. 41, no. 11, pp. 1926-1935, 1994.

[26] F. N. Hooge, T. G. M. Kleinpenning and L. K. J. Vandamme, “Experimental studies on 1/f noise,” *Rep. Prog. Phys.*, vol. 44, pp. 479-532, 1981.

[27] C. D. Motchenbacher and J. A. Connelly, “Fundamental noise mechanisms,” in *Low-Noise Electronic System Design*, 1st ed., New York: John Wiley & Sons, Inc, 1993, pp. 5-37.

[28] A. Barlian, W. T. Park, J. R. Mallon Jr., A. J. Rastegar and B. L. Pruitt, “Review: semiconductor piezoresistance for microsystems,” in *Proc. of IEEE*, vol. 97, no. 3, 2009.

[29] W. Thomson, “On the electrodynamic qualities of metals:-effects of magnetization on the conductivity of nickel and of iron,” in *Proc. of the Royal society of London*, vol. 8, pp. 546-550, 1857.

[30] M. Elwenspoek and R. Wiegerink, “Mechanical microsensors,” in *Force and Pressure Senosrs,* 1st Ed.,Springer –verlandg Berlain Heidelberg NewYork, 2001, pp. 106-119.

[31] G. C Hill, R. Melamud, F. E. Declercq, A.A. Davenport, I. H. Chan, P.G. Hartwell and B. L. Pruitt, “SU-8 MEMS fabry-perot pressure sensor,” *Sensor Actuat. A-Phys*., vol. 138, pp. 52-62, 2007.

[32] Y. Zhu, A. Wang, “Minuature fiber-optic pressure Sensor,” *IEEE Photonic Tech. L.*, vol. 17, no. 2, pp. 447-449, 2005.

[33] H. Bartelt, H. Unzeitig, “Design and investigation of micromechanical bridge structures for an optical pressure sensor with temperature compensation,” *Sensor Actuat. A-Phys*., vol. 37-38, pp. 167-170, 1993.

[34] K. Peterson, F. Pourahmadi, J. Brown, “Resonant beam pressure sensor fabricated with silicon fusion bonding,” in *Proc. 6th Int. Conf Solid-State Sensor Actuat (Transducers ’91*), pp. 664-667, 1991.

[35] C. J. Welham, J. W. Gardner and J. Greenwood, “A laterally driven micromachined resonant pressure sensor,” *Sensor Actuat. A-Phys*., vol. 52, pp. 86-91, 1996.

[36] R. L. Parker and A. Krinsky, “Electrical resistance –strain characteristics of thin evaporated metal films,” *J. Appl. Phys.,* vol. 34, no. 9, 1963.

[37] G. C. Kuczynski, “Effect of elastc strain on the electrical resistance of metals,” *Phys. Rev.*, vol. 94, no. 1, pp. 61-64, 1954.

[38] C. Grimaldi, P. Ryser and S. Strassler, “Gauge factor enhancement driven by heterogeneity in thick-film resistors,” *J. Appl. Phys.,* vol. 90, no. 1, pp. 322-327, 2001.

[39] M. Prudenziati, M. Morten, F. Cilloni and G. Ruffi, “Very high strain sensitivity of thick film resistor: real and false gauge factors,” *Sensor Actuat. A-Phys*., vol. 19, pp. 401-414, 1989.

[40] S. Tamborin, S. Piccinini, M. Prudenziati, B. Morten, “Piezoresistive properties of RuO_2-based thick-film resistors: the effect of RuO_2 grain size,” *Sensor Actuat. A-Phys*., vol. 58, pp. 159-164, 1997.

[41] O. J. Gregory and T. You, “Atability and piezoresistive properties of indium-tin-oxide ceramic strain gages,” in *Proc. 2nd Int. IEEE Sens. Conf.*, pp. 801-806, 2003.

[42] H. Chiriac, M. Urse, F. Rusu, C. Hison and M. Neagu, "Ni-Ag thin films as strain-sensitive materials for piezoresistive sensors," *Sensor Actuat. A-Phys*., vol. 76, pp. 376-380, 1999.

[43] S. U. Jen, C. C. Yu, C. H. Liu and G. Y. Lee, "Piezoresistance and electrical resistivity of Pd, Au, and Cu films," *Thin Solid Films,* vol. 434, pp. 316-322, 2003.

[44] C. M. Wang, J. H. Hsieh and C. Li, "Electrical and piezoresistive properties of TaN-Cu nanocomposite thin films," *Thin Solid Films,* vol. 469-470, pp. 455-459, 2004.

[45] W. D. Edwards and R. P. Beaulieu, "Germanium piezoresistive element on a flexible substrate," *J. Scientific Ins.,* vol. 2, no. 2, pp 613-615, 1969.

[46] E. Piener, A. Tibrewala, R. Bandorf, S. Biehl, H. Luthje and L. Doering, "Micro force sensor with piezoresistive amorphous carbon strain gauge," *Sensor Actuat. A-Phys*., vol. 130-131, pp. 75-82, 2006.

[47] S. K. Patil, Z. Celik-Butler and D. P. Butler, "Nanocrystalline piezoresistive polysilicon film by aluminum-induced crystallization for pressure sensing applications," *IEEE Trans. Nanotech.*, vol. 9, no. 5, pp. 640-646, 2010.

[48] I. H. Kazi, P. M. Wild, T. N. Moore and M. Sayer, "Characterization of sputtered nichrome films for strain gauge applications," *Thin Solid Films*, vol. 515, pp. 2602-2606, 2006.

[49] M. Ahmed, M. M. Chitteboyina, D. P. Butler and Z. Celik-Butler, "MEMS force sensor in a flexible substrate using nichrome piezoresistors," *IEEE Sensors J.*, vol. 13, no. 10, pp. 4081-4089, 2013.

[50] M. Ahmed, D. P. Butler and Z. Celik-Butler, "MEMS relative pressure sensor on flexible substrate ," in *Proc. 10th Int. IEEE Sens. Conf.*, pp. 460-463, 2011.

[51] T. B. Gabrielson, “Mechanical-thermal noise in micromachined acoustic and vibration sensors, ” *IEEE Trans. Elec. Dev.*, vol. 40, no. 5, pp. 903-910, 1993.

[52] Z. Djuric, “Mico-and nanosystems based on vibrating structures,” in *Proc 26th Int. Conf. Microelec.*, pp. 1-8, 2008.

[53] L. A. Rocha, E. Cretu and R. F. Wolffenbuttel, “Measuring and interpreting the mechanical-thermal noise spectrum in a MEMS,” *J. Micromech. Microeng.,* vol. 15, pp. S30-38, 2005.

[54] Y. Wang, X. Zheng, L. Liu and Z. Li, “A novel structure of pressure sensors,” *IEEE Trans. Elect. Dev.*, vol. 38, no. 8, pp. 1797-1802, 1991.

[55] S. K. Clark and K. D. Wise, “Pressure sensitivity in anisotropically etched thin-diaphragm pressure sensors,” *IEEE Trans. Elec. Dev.*, vol. 26, no. 1, pp. 1887-1896, 1979.

[56] H. Bartelt and H. Unzeitig, “Design and investigation of micromechanical bridge structures for an optical pressure sensors with temperature compensation,” *Sensor Actuators A-Phys.,* vol. 37-38, pp. 167-170, 1993.

[57] J. Zhou, S. Dasgupta, H. Kobayashi, J. M. Wolff, H. E. Jackson and J. T. Boyd, “Optically interrogated MEMS pressure sensors for propulsion applications,” *Opt. Eng.*, vol. 40, no. 4, pp. 598-604, 2001.

[58] C. S. Sander, J. W. Knutti and J. D. Meidl, “A monolithic capacitive pressure sensor with pulse-period output,” *IEEE Trans. Elec. Dev.*, vol. 27, no. 5, pp. 927-930, 1980.

[59] A. Jornod and F. Rudolf, “High-precission capacitive absolute pressure sensor,” *Sensor Actuat. A-Phys.*, vol. 17, pp. 415-421, 1989.

[60] Y. S. Lee and K. D. Wise, “A Batch-fabricated silicon capacitive pressure transducer with low temperature sensitivity,” *IEEE Trans. Elec. Dev.*, vol. 29, no. 1, pp. 42-48, 1982.

[61] M. Esashi, S. Sugiyama, K. Ikeda, Y. Wang and H. Miyashita, “Vacuum-sealed silicon micromachined pressure sensors,” in *Proc. of IEEE*, vol. 86, no. 8, pp. 1627-1639, 1998.

[62] J. N. Palasagaram and R. Ramadoss, “MEMS-capacitive pressure sensor fabricated using printed-circuit-processing techniques,” *IEEE Sensors J.*, vol. 6, no. 6, pp. 1374-1375, 2006.

[63] E. Kalvesten, L. Smith, L. Tererz and G. Stemme, “The first surface micromachined pressure sensor for cardiovascular pressure measurements,” in *Proc. 11th Int. Workshop on MEMS.*, pp. 574-579, 1998.

[64] M. Ahmed, D. P. Butler and Z. Celik-Butler, “MEMS absolute pressure sensor on flexible substrate ,” in *Proc. 25th Int. IEEE MEMS Conf.*, pp. 575-578, 2012.

[65] M.Esashi, Y. Matshumoto and S. Shoji, “Absolute pressure sensors by air-tight feedthrough structure,” *Sensor Actuat. A-Phys.,* vol. 21-23, pp. 1048-1052, 1990.

[66] A. C. Rastogi, S. R. Darvish and P. K. Bhatnagar, “Phase evolution of electron-beam evaporated $Pb(Zr,Ti)O_3$ thin films,” *Mat. Chem. Phys.*, vol. 73, pp. 135-143, 2002.

[67] E. L. Derenik and G. D. Boreman, “Infrared detectors and systems,” in *Thermal detectors*, 1st ed., New York: JohnWilley & Sons, Inc, 1996, pp. 424-427.

[68] L. F. Malmonge and J. A. Malmonge, W. K. Sakamoto, “Study of pyroelectric activity of PZT/PVDF-HFP composite,” *Mats. Research*, vol. 6, no. 4, pp. 469-473, 2003.

[69] M. Natali, D. Garoli, V. Rigato and F. Romanato, “Structural characterization of lead zirconium titanate thin films prepared on different electrodes and on silicon substrates,” *J. Vac. Sci. Technol. A*, vol. 29, no. 6, pp. 061505-1-6, 2011.

[70] G. Yi, Z. Wu and M. Sayer, “Preparation of Pb(Zr, Ti)O_3 thin films by sol gel processing: electrical, optical , and electrooptic properties,” *J. Appl. Phys.*, vol. 64, pp. 2717-2724, 1988.

[71] M. Tyunina, J. Levoska and S. Leppavuori, “Experimental studies and modeling of Pb-Zr-Ti-O film growth in pulsed laser deposition,” *J. Appl. Phys.*, vol. 83, pp. 5489-5496, 1998.

[72] X. Zheng, J. Li and Y. Zhou, “X-ray diffraction measurement of residual stress in PZT thin films prepared by pulsed laser deposition,” *Act. Mat. Inc.*, vol. 52, pp. 3313-3322, 2004.

[73] X. G Tang, Q. F. Zhou and Z. X. Jhang, “Growth and characterization of oriented $Pb_{1-x}Ca_XTiO$ thin films,” *Thin Solid Films,* vol. 375, pp. 159-162, 2000.

[74] D. Viehland, J. F. Li, X. Dai and Z. Xu, “Structural and property studies of high Zr-content lead zirconate titanate,” *J. Phys. Chem. Solids*, vol. 57, no. 10, pp. 1545-1554, 1996.

[75] J. Friend, E. Jamison, M. Pennell and W. Huebner, “Ultrasonic characterization of poling in lead zirconatetitanateceramics,” *Appl. Phys. Lett.*, vol. 79, no. 17, pp. 2794-2796, 2001.

[76] J. M. Marshall, Q. Zhang and R. W. Whatmore, “Corona poling of highly (001)/(100)-oriented lead zirconate titanate thin films,” *Thin Solid Films*, vol. 516, pp. 4679-4684, 2008.

[77] Z. Huang, Q. Zhang and R. W. Whatmore, "Low temperature crystallization of lead zirconium titanate thin films by a sol-gel method," *J. Appl. Phys.*, vol. 85, pp. 7355-7361, 2001.

[78] D. H. Kang, K. W. Kim, S. Y. Lee, Y. H. Kim and S. K. Gil, "Influencing factors on the pyroelectric properties of $Pb(Zr,Ti)O_3$ thin film for uncooled infrared detector," *Mat. Chem. Phys.*, vol. 90, pp. 411-416, 2005.

[79] C. Ye, T. Tamagawa, P. Schiller and D. L. Polla, "Pyroelectric $PbTiO_3$ thin films for microsensor applications," *Sensor Actuat. A-Phys.*, vol. 35, pp. 77-83, 1992.

[80] C. C. Chang and Y. C. Lai, "The fabrication and characterization of $(Pb,Ca)TiO_3$ pyroelectric thin films with different Ca contents," *J. Appl. Phys.*, vol. 101, pp. 104106-104106-7, 2007.

[81] S. Chopra, S. Sharma, T. C. Guel and R. G. Mendiratta, "Ca Substituted $PbTiO_3$ Thin Films for Infrared Detectors," *J. Electroceram.*, vol. 13, no. 1-3, pp. 155-158, 2004.

[82] X. G. Tang, H. L. W. Chan and A. L. Ding, "Electrical properties of compositionally graded lead calcium titanate thin films," *Solid State Commun.*, vol.127, pp. 625-628, 2003.

[83] M. Copycinska, C. Ziebert, H. Schmitt, U. Rabe, S. Hirsekorn and W. Arnold, "Nanoscale imaging of elastic and piezoelectric properties of nanocrystalline lead calcium titanate," *Surf. Sci.*, vol. 532-535, pp. 450-455, 2003.

[84] Q. Cao, H. S. Kim, N. Pimparkar, J. P. Kulkarni, C Wang, M. Shim, K. Roy, M. A. Alam and J. A. Rogers, "Medium-scale carbon nanotube thin-film integrated circuits on flexible plastic substrates," *Nature Lett.*, vol. 454, pp. 494-500, 2008.

[85] M. Kotera, T. Nishino and K. Nakamae, "Imidization processes of aromatic polyimide by temperature modulated DSC," *Polymer*, vol. 41, pp. 3615-3619, 2000.

[86] K. J. Lee, M. J. Motala, M. A. Metil, W. R. Childs, E. Menard, A. K. Shim, J. A. Rogers and R. Z. Nuzzo, "Large-area, selective transfer of microstructured silicon: a printing-based approach to high-performance thin-film transistors supported on flexible substrate," *Adv. Mater.*, vol. 17, pp. 2332-2336, 2005.

[87] Y. Sun and J. A. Rogers, "Inorganic semiconductor for flexible electronics," *Adv. Mater.*, vol. 19, pp. 1897-1916, 2007.

[88] M. Ahmed and D. P. Butler, "Flexible substrate and release layer for flexible MEMS devices," *J.Vac. Sci. Technol. Lett.*, vol. 31, no. 5, pp. 050602-050602-4, 2013.

[89] PI-2600 series product bulletin, HD Microsystems (2009).

[90] PI5878 G product bulletin, HD Microsystems (2009).

[91] W. W. Y. Chow, K. F. Lei, G. Shi, W. J. Li and Q. Huang, "Microfluidic channel fabrication by PDMS-interface bonding," *SmartMater. Struct.*, vol. 15, pp. S112-S116, 2006.

[92] J. Biros, T. Larina J. Trekoval and J. Pouchly, "Dependence of glass transition temperature of poly on their tacticity," *Colloid & Polymer Sci.*, vol. 260, pp. 27-30, 1982.

[93] Estane Thermoplastic Polyuthrane, general brochure, Lubrizol Advance Material Inc.

[94] H. S. Noh, Y. Huang and P. J. Hesketh, "Parylene micromolding, a rapid and low-cost fabrication method for parylene microchannel," *Sensor Actuat. B-Chem.*, vol. 102, no. 1, pp. 78–85, Sep. 2004.

[95] Z. Suo, E. Y. Ma, H. Gleskova and S. Wagner, "Mechanics of rollable and foldable film-on-foil electronics," *Appl. Phys. Lett.*, vol. 74, pp. 1177-1179, 1999.

[96] PI-4100 series product bulletin, HD Microsystems, 2009.

[97] Y. Okada and Y. Tokumaru, "Precise determination of lattice parameter and thermal expansion coefficient of silicon between 300 and 1500 K," *J. Appl. Phys.*, vol. 56, no. 2, pp. 314-320, 1984.

[98] M. T. Kim, "Influence of substrates on the elastic reaction of films for the microindentation tests" *Thin Solid Films*, vol. 283, no. 1-2, pp. 12- 16, 1996.

[99] E. L. Derenik and G. D. Boreman, "Optical-detection processes," in *Infrared detectors and systems*, 1st ed., New York: John Wiley & Sons, Inc, 1996, ch. 3, sec. 3.1-3.3, pp. 86-123.

[100] H. Rafla-Yuan, J. D. Rancourt and M. J. Cumbo, "Ellipsometric study of thermally evaporated germanium thin film," *Appl. Optics*, vol. 36, no. 25, pp. 6360-6363, 1997.

[101] J. J. Bock, D. Chen, P. D. Mauskopf and A. E. Lange, "A novel bolometer for infrared and millimeter-wave astrophysics," *Space Sci. Rev.*, vol. 74, pp. 229-235, 1995.

[102] K. E. Petersen, "Silicon as a mechanical material," in *Proc. of IEEE*, vol. 70, no. 5, pp. 420-456, 1982.

[103] T. Dhaene and D. D. Zutter, “Selection of lumped element models for coupled lossy transmission lines,” *IEEE T. Comp. Aid. D.*, vol. 11, no. 7, pp. 805-815, 1992.

[104] D. M. Pozar, “Transmission lines and microwave networks, ” *in Microwave and RF design of wireless systems*, 1st ed., New York: John Wiley & Sons, Inc, 2000, ch. 2, sec. 2.1-2.4, pp. 29-67.

[105] S. Ramo, J. R. Whinnery and T. V. Duzar, “Transmission lines” in *Fields and waves in communcation electronics*, 3rd Ed., 1994, New York: John Wiley & Sons, Inc, 2000, ch. 5, sec. 5.1-5.8, pp. 213-235.

[106] C. J. F. T. Braak, “A Markov chain Mote Carlo version of the genetic algorithm differential evolution: easy Bayesian computing for real parameter spaces,” *Stat. Computat.*, vol. 16, pp. 239-249, 2006.

[107] M. J. M. E. D. Nivelle, M. P. Buijn, P. A. J. D. Korte, S. Sanchez, M. Elwekspoek, T. Heidenbult, B. Schwierzi, W. Michalke and E. Steinbeiss, “High-T_c bolometers with silicon-nitride spiderweb suspension for far-infrared detection, ” *IEEE T. Appl. Supercon.*, vol. 9, no. 2, pp. 3350-3353, 1999.

[108] A. Mahmood, D. P. Butler and Z. Celik-Butler, “A device level vacuum packaging scheme for microbolometers on rigid and flexible substrate,” *IEEE Sensors J.*, vol. 7, no. 7, pp. 1012-1019, 2007.

[109] P. E. Ciddor and L. B. Whitbourn, “Equivalent thin film of a periodic metal grid,” *Appl. Optics*, vol. 28, no. 6, pp. 1228-1230, 1989.

[110] R. Ulrich, T. J. Bridges and M. A. Pollack, “Variable metal mesh coupler for far infrared lasers,” *Appl. Optics*, vol. 9, no. 11, pp. 2511-2516, 1970.

[111] L. B. Whitbourn and R. C. Compton, “Equivalent-circuit formulas for metal grid reflectors at a dielectric boundary,” *Appl. Optics*, vol. 24, no. 2, pp. 217-220, 1985.

[112] M. M. Rana, D. P. Butler, “High responsivity a-$Si_xGe_{1x}O_y$:H microbolometers,” *IEEE Sensors J.*, vol.7, no.10, pp.1413-1419, 2007.

[113] M. A. Ordal, L. L. Long, R. J. Bell, S. E. Bell, R. R. Bell, R. W. Alexander and C. A. Ward, “Optical properties of the metals Al, Co, Cu, Au, Fe, Pb, Ni, Pd, Pt, Ag, Ti, and W in the infrared and far infrared,” *Appl. Optics*, vol. 22, no. 7, pp. 1099-1119, 1983.

[114] A. Mahmood, “Device level vacuum packaged microbolometer on flexible substrate,” PhD. Dissertation, The University of Texas, Arlington, 2005, p. 87.

[115] E. D. Palik, “Handbook of optical constants of solid,” in *Semiconductors*, 2nd Ed., Academic Press, LTD, 1998, pp. 465-547.

Biographical Information

Moinuddin Ahmed received his B. Sc. degree in electrical and electronic engineering from Bangladesh University of Engineering and Technology (BUET), Dhaka, Bangladesh, in 2009. He started his direct BS to Ph. D. degree in electrical engineering in University of Texas at Arlington, TX, USA, in Fall 2009.

Since Fall 2009, he has been working in Microsensors Laboratory and the Nanotechnology Research Center, UTA. His research interests include design, fabrication and characterization of MEMS sensors on flexible substrates and pyroelectric infrared detector. He has authored four journal papers and five conference papers in this area. Several other journal papers are under review. He has submitted several invention disclosures in bolometer field of research.

Moinuddin Ahmed is a member of IEEE, American Vacuum Society, Tau Beta Pi and Eta Kappa Nu. He was awarded Talentpole scholarship in 1995 (from Bangladesh Govt.), BUET Technical scholarship in 2004, ‘Dean’ award in 2008 (BUET, Dhaka), ‘Dean Doctoral’ fellowship in 2009-2013 from UT Arlington, ‘Contact Travel’ award in 2012 and several other scholarships.